A Multi-scale Stochastic Filter Based Approach to Inverse Scattering for 3D Ultrasound Soft Tissue Characterization

by

Patrick P. C. Tsui

A thesis
presented to the Univsersity of Waterloo
in fulfillment of the
thesis requirement for the degree of
Doctor of Philosophy
in
Electrical and Computer Engineering

Waterloo, Ontario, Canada, 2009

I hereby declare that I am the sole author of this thesis. This is a true copy of the thesis, including any required final revisions, as accepted by my examiners.

I understand that my thesis may be made electronically available to the public.

Abstract

The goal of this research is to achieve accurate characterization of multi-layered soft tissues in three dimensions using focused ultrasound. The characterization of the acoustic parameters of each tissue layer is formulated as recursive processes of forward- and inverse- scattering.

Forward scattering deals with the modelling of focused ultrasound wave propagation in multi-layered tissues, and the computation of the focused wave amplitudes in the tissues based on the acoustic parameters of the tissue as generated by inverse scattering. The model for mapping the tissue acoustic parameters to focused waves is highly nonlinear and stochastic. In addition, solving (or inverting) the model to obtain tissue acoustic parameters is an ill-posed problem. Therefore, a nonlinear stochastic inverse scattering method is proposed such that no linearization and mathematical inversion of the model are required.

Inverse scattering aims to estimate the tissue acoustic parameters based on the forward scattering model and ultrasound measurements of the tissues. A multi-scale stochastic filter (MSF) is proposed to perform inverse scattering. MSF generates a set of tissue acoustic parameters, which are then mapped into focused wave amplitudes in the multi-layered tissues by forward scattering. The tissue acoustic parameters are weighted by comparing their focused wave amplitudes to the actual ultrasound measurements. The weighted parameters are used to estimate a weighted Gaussian mixture as the posterior probability density function (PDF) of the parameters. This PDF is optimized to achieve minimum estimation error variance in the sense of the posterior Cramer-Rao bound. The optimized posterior PDF is used to produce minimum mean-square-error estimates of the tissue acoustic parameters. As a result, both the estimation error and uncertainty of the parameters are minimized.

PDF optimization is formulated based on a novel multi-scale PDF analysis framework. This framework is founded based on exploiting the analogy between PDFs and analog (or digital) signals. PDFs and signals are similar in the sense that they represent characteristics of variables in their respective domains, except that there are constraints imposed on PDFs. Therefore, it is reasonable to consider a PDF as a signal that is subject to amplitude constraints, and as such apply signal processing techniques to analyze the PDF.

The multi-scale PDF analysis framework is proposed to recursively decompose an arbitrary PDF from its fine to coarse scales. The recursive decompositions are designed so as to ensure that requirements such as PDF constraints, zero-phase shift and non-creation of artifacts are satisfied. The relationship between the

PDFs at consecutive scales is derived in order for the PDF optimization process to recursively reconstruct the posterior PDF from its coarse to fine scales. At each scale, PDF reconstruction aims to reduce the variances of the posterior PDF Gaussian components, and as a result the confidence in the estimate is increased. The overall posterior PDF variance reduction is guided by the posterior Cramer-Rao bound.

A series of experiments is conducted to investigate the performance of the proposed method on ultrasound multi-layered soft tissue characterization. Multi-layered tissue phantoms that emulate ocular components of the eye are fabricated as test subjects. Experimental results confirm that the proposed MSF inverse scattering approach is well suited for three-dimensional ultrasound tissue characterization. In addition, performance comparisons between MSF and a state-of-the-art nonlinear stochastic filter are conducted. Results show that MSF is more accurate and less computational intensive than the state-of-the-art filter.

Acknowledgements

First and foremost, I express my sincerest gratitude to my supervisor, Dr. Otman A. Basir, for his support, guidance, precious time and endless patience throughout this research. His depth of knowledge in the research field and skills in scientific communication are invaluable to the accomplishment of this thesis. I am honoured to gain excellent research experience under his supervision.

I would like to thank Dr. Gauri Mittal from the University of Guelph, who gave me expert advice on the biological aspects of my research. I benefited greatly from his extensive knowledge and experience in biological and food engineering.

I am grateful for all the help given by Dr. Vivian Choh from the School of Optometry, who guided me on the development of the eye phantom in my research. In addition, she generously provided the ultrasound equipment to realize the physical experiments of my research.

I would also like to thank my examining committee, Dr. O. Basir, Dr. V. Choh, Dr. M. Kamel, Dr. O. Michailovich and Dr. R. Rudra, who carefully reviewed my work and gave valuable suggestions to refine my thesis.

The staff at the graduate office of the department of Electrical and Computer Engineering (ECE), especially Lisa Hendel, Annette Dietrich and Wendy Boles, helped me tremendously in processing various administrative documents for my PhD program. They are treasures of the department.

I like to give thanks to the Natural Sciences and Engineering Research Council of Canada, University of Waterloo and the ECE department for supporting my research with NSERC Postgraduate Scholarship, University of Waterloo Graduate Scholarship and President's Graduate Scholarship.

It has been my pleasure to meet friendly, hard working fellow colleagues at the PAMI laboratory. We often had interesting discussions on both academic and non-academic topics during lunch breaks and social gatherings. They also taught me about different cultures. I am thankful to Miriam Heynen, Elizabeth Heikkila and a number of graduate students from the School of Optometry for their helpful discussions on the development of the eye phantom. Appreciations also go to the supervisors at the student machine shop, Kwai Chan and John Potzold, who helped me with the machining work needed for my research.

Last but not least, I owe many many thanks to my wife, Winnie, who put up with me for the past few years. My mind was constantly preoccupied by my research work, even though I was physically at home. More importantly, Winnie

gave birth to our first child, Kristen, in the course of this research. She truly makes this research more memorable.

This research would not have been possible without the support and encouragement from the people and institutions acknowledged above.

Contents

List of Figures

List of Tables

Nomenclature

The following symbols and abbreviations are used in this thesis.

α	Attenuation coefficient
m	Slope of attenuation coefficient model for soft tissues
b	Y-intercept of attenuation coefficient model for soft tissues
c	Sound speed
ρ	Mass density
f	Frequency
ω	Angular frequency
i	Complex number; i also has other meanings when used as a superscript or subscript depending on the context
ψ	Acoustic wave pressure function in space-time domain
Ψ	Acoustic wave pressure function in frequency domain
∇^2	Laplacian operator
λ_e, μ_e	Lame's constants
B, G, Y	Bulk, shear and Young's modulus, respectively
k, $\overrightarrow{k}$	Wave number and wave vector, respectively
u	Particle velocity in space-time domain
U	Particle velocity in frequency domain

Z	Specific acoustic impedance
θ_i, θ_r, θ_t	Angles of incident, reflected and transmitted waves, respectively
R	Reflection coefficient
T	Transmission coefficient
u_0	Speed amplitude of the radially vibrating sphere source
$\overline{r}$	Average radius of radially vibrating sphere source
ψ^v	Wave pressure attenuated due to the viscous drag of particles
ν_s, ν_b	Shear and compressional viscosities, respectively
γ	Ratio of specific heats
C_p	Heat capacity at constant pressure
κ	Thermal conductivity
$\Psi^P_{r,i}$, $\Psi^P_{r,s}$	Incident and scattered plane wave at point r, respectively
n_r	Refractive index at point r
g_r	Free-space Green's function at point r
Ψ^p_{r,B^j}	j^{th} order Born approximation of $\Psi^P_{r,s}$
J_0	Zeroth order complex Bessel function
$J_{0,re}$, $J_{0,im}$	Real and imaginary part of J_0, respectively
d	Thickness of tissue layer
$a_{n,f}$	Measurement of the n^{th} echo amplitudeat frequency f
N	Gaussian distribution
η_f	Measurement noise of frequency f
n_η	Number of Gaussian components used to represent measurement noise distribution
w^η_j, μ^η_j, v^η_j	Weight, mean and variance of a Gaussian component of measurement noise PDF, respectively

p_s	PDF at scale s
p_{s+1}	PDF at scale s+1 (or a low-pass version of p_s)
l_s	Low-pass filter for PDF at scale s
v_s^{lp}	Covariance matrix of l_s
x_n	Vector of tissue acoustic parameters
$p\left(x_n \mid a_{n,1:f}\right)$	Posterior PDF of x_n given $a_{n,1:f}$
n_x	Number of Gaussian components used to represent $p\left(x_n \mid a_{n,1:f}\right)$
$w_{n,f,j}^x$	Weight of the j^{th} Gaussian component of $p\left(x_n \mid a_{n,1:f}\right)$
$\mu_{n,f,j}^x$	Mean of the j^{th} Gaussian component of $p\left(x_n \mid a_{n,1:f}\right)$
$v_{n,f,j}^x$	Covariance matrix of the j^{th} Gaussian component of $p\left(x_n \mid a_{n,1:f}\right)$
$p\left(a_{n,f} \mid x_n\right)$	Likelihood PDF of $a_{n,f}$ given x_n
$p\left(x_n \mid a_{n,1:f-1}\right)$	Prior PDF of x_n before the current measurement
$w_{n,f-1,j}^x$	Weight of the j^{th} Gaussian component of $p\left(x_n \mid a_{n,1:f-1}\right)$
$\mu_{n,f-1,j}^x$	Mean of the j^{th} Gaussian component of $p\left(x_n \mid a_{n,1:f-1}\right)$
$v_{n,f-1,j}^x$	Covariance matrix of the j^{th} Gaussian component of $p\left(x_n \mid a_{n,1:f-1}\right)$
F_n	Posterior Fisher information matrix
AIM	Acoustic Impedance Mismatch
EKF	Extended Kalman Filter
FIR	Finite Impulse Response
GMM	Gaussian Mixture Model
GPF	Gaussian Particle Filter
GSPF-II	Gaussian Sum Particle Filter type two
MMSE	Minimum Mean-Square Error

MSF	Multi-scale Stochastic Filter
NSF	Nonlinear Stochastic Filter
PF	Particle Filter
PDF	Probability Distribution Function
PD	Propagation Direction
PCRB	Posterior Cramer-Rao Bound
SNR	Signal-to-Noise Ratio
UKF	Unscented Kalman Filter
UPF	Unscented Particle Filter
ZMG	Zero-Mean Gaussian

Chapter 1

Introduction

Tissue characterization is the estimation of quantitative information of tissues from their measurements. Characterization of tissues is essential for many real-world medical applications such as eye examination, anatomies detection, tumor type (benign or malignant) identification, intraoperative tissue assessment and coronary artery calcification measurement. Generally speaking, techniques of tissue characterization can be classified as invasive and noninvasive. Noninvasive techniques are more desirable for patient comfort and are lower risk operations than the invasive counterparts. Common noninvasive tissue characterization techniques include magnetic resonance imaging, positron emission tomography, ultrasound and X-Ray. Among these techniques, ultrasound is the most cost effective and safe measurement modality. Therefore, this research is interested in ultrasound based tissue characterization.

1.1 Ultrasound Tissue Characterization

Ultrasound tissue characterization is defined by Thijssen as [1]:

> *"The assessment by ultrasound of quantitative information about the characteristics of biological tissues, and pathological changes thereof".*

Ultrasound tissue characterization is a research field with rich history. The first publication on computer analysis of scattered ultrasound waveforms was in 1972 by Mountford and Wells [2]. The first symposium on ultrasound tissue characterization was organized by the National Bureau of Standards in 1975 and the proceedings

were published in 1976 [3]. A large volume of scientific publications has been devoted to this topic ever since.

Medical ultrasound research accounts for more than one quarter of medical imaging studies in the world [4]. This popularity mainly comes from the safety aspect of medical ultrasound. In addition, ultrasonic equipment is, in general, low cost, mobile and convenient to use compared to other medical imaging modalities such as MRI and X-ray. Moreover, ultrasound imaging has the advantage of visualizing the interior of a biological body in real-time without invasion, and hence it is highly desirable for medical practices. The propagation of ultrasound waves depends on the tissue acoustic properties. Anomalies affect these properties, for example, tumors tend to have higher mass density than the corresponding normal tissue. Taking advantage of the effect of anomalies on tissue acoustic properties, quantitative imaging of the tissue acoustic properties is a potentially useful technique for diagnosing cancer and other diseases.

The conventional approach to ultrasound image formation is the pulse-echo method, which simply displays the absolute value (commonly known as envelop) of echoes to be the acoustic reflectivity distribution of the tissue [5]. This approach ignores the phase information of the echoes. Another limitation of conventional ultrasound image analysis is its heavy dependency on the operator. Ultrasound image acquisition and interpretation require highly trained medical professionals such as physicians and radiologists, and as such it tends to be a subjective process. Different medical professionals may suggest different diagnosis for the same image.

The drawbacks of conventional ultrasound imaging can be relaxed using inverse scattering methods. Instead of taking the envelop of echoes as the acoustic distribution, inverse scattering methods reconstruct the tissue acoustic properties by exploiting their relation to the echoes and the complete echo waveform. It has been reported that ultrasound tissue characterization using inverse scattering methods achieve an order of magnitude improvement in image resolution compared to conventional image based approaches [6]. Also, high degree of correlation between the reconstructed acoustic property profile and the tissue pathology is reported [6]. According to Thijssen, inverse scattering methods that produce high resolution and accuracy quantitative images of the tissue acoustic properties are the ultimate goal of innovation in medical ultrasound [1]!

Although diffraction tomographic methods reported in the literature have demonstrated high resolution and quantitative accuracy, these methods have not yet been incorporated into commercially successful medical ultrasound imaging systems. This is because these methods are based on narrow-band frequency reconstruction in the spectral domain, while current diagnostic ultrasound scanners employ

wide-band time-domain signals and time-domain reconstruction is known to provide increased point and contrast resolution [7].

1.2 Forward and Inverse Scattering

Forward scattering (also known as direct scattering) is a process of determining the distribution of radiation waves in a medium based on the medium properties and the physics of interaction between the waves and the medium. In the context of medical ultrasound, the acoustic properties of a tissue and the mechanics of propagating particle vibrations in the tissue are used to determine the distribution of ultrasound waves in the tissue. Scatterings of the waves are caused by inhomogeneities or scatterers, such as tumors and fat-muscle layer interfaces, in the tissue.

The distributions of scattered waves are modelled as multi-dimensional integral equations. Therefore, forward scattering can be formulated as computing the equations given the knowledge of the tissue acoustic properties. The challenge of forward scattering is to compute the equations efficiently. The problem of ultrasound tissue characterization is to estimate the tissue acoustic properties given the knowledge of the scattered waves. To solve this problem, an inverse process of forward scattering is needed. This process is inverse scattering.

Inverse scattering is defined by Norton and Linzer as the task of deriving the structure of an object from scattered radiations [8]. According to Colton *et al.*, all the inverse scattering problems that are of significance in practical applications belong to the class of so-called ill-posed problems[1] in the sense of Hadamard [9, 10]. Traditionally, ill-posed problems involving partial differential equations of mathematical physics, including inverse scattering, are considered to be of purely academic interest and not worthwhile for extensive study [11].

[1] In the 1920's, a French mathematician named Hadamard formulated that a mathematical model of a physical phenomenon is well-posed if it satisfies the following three criteria [9]:

1. Existence: Every observation of the physical phenomenon has at least one corresponding solution of the model
2. Uniqueness: For every observation of the physical phenomenon, the solution of the model is unique
3. Continuity: The dependence of the solution of the model on the observation is continuous

Problems of solving models that are not well-posed based on the formulation of Hadamard are called ill-posed problems.

This view of inverse scattering problem has changed dramatically after the successful development of the radar and sonar sensors during the Second World War. Scientists and engineers then pose the following question: could more information about a scattering object be inferred from its scattered waves than simply its location? Subsequently, this problem has received considerable interest. However, its progress has been rather slow due to the lack of a mathematical theory of inverse problems and computational capabilities to facilitate solution attempts, until the introduction of regularization methods for solving linear ill-posed problems by Tikhonov in the mid-1960's [12].

Inverse scattering has been applied in various fields of nondestructive testing using acoustics, such as sonar and ultrasound; electromagnetic, such as microwave; and optical waves [13, 14]. Since the governing equations of these wave types are mathematically equivalent, the same inverse scattering techniques apply. This research is interested in inverse scattering in the context of ultrasound soft tissue characterization. In the field of medical ultrasound, there are two main types of inverse scattering, namely, reflection and diffraction tomography. Reflection tomography operates on the waves reflected (also referred to as backscattered signals or echoes) from the object, while diffraction tomography performs inversion based on the wave transmitted through the object.

1.3 Three-dimensional Ultrasound

In addition to the disadvantages discussed in Section 1.1, other major limitations of conventional ultrasound images, as reported in [15, 16, 17], are listed as follows:

- The inherently low dimensionality of ultrasound images constrains the representation of three-dimensional (3D) human anatomy as two-dimensional (2D) slices. Accurate geometric information of the anatomy in 3D is important for many medical applications such as tumor development monitoring, surgery and therapy planning. In order to develop a volumetric picture of the 3D anatomy, diagnosticians must mentally integrate a series of 2D images. This is a tiring and time-consuming process, which is prone to inaccuracy and inconsistency.

- The size of tumors are currently estimated using its height, width, and length measured from a few selected 2D images, which may not provide sufficient spatial resolution to establish consistent and accurate estimates.

- The poses (i.e., positions and orientations) of image planes are controlled manually. Localizing the image planes and reproducing the exact poses at a later time is practically impossible. This makes conventional ultrasound imaging undesirable for monitoring disease progression, surgery and therapy planning.
- Some 2D imaging poses are not possible because of patients' anatomies, which degrades the accuracy of diagnosis or staging of patients' conditions.

The goal of 3D ultrasound (US) is to overcome the limitations of conventional 2D US images by providing an imaging technique that reduces the variability of the conventional technique and allows the diagnostician to view the anatomy in 3D [18]. 3D US imaging permits the segmentation of the desired structure in 3D allowing for accurate and consistent estimates of anatomical geometry. It facilitates diagnosis by providing an accurate volume measurement of the anatomy. It is especially useful for tracking the evolution of lesion shape change in 3D, which enables much more detailed analysis of complex lesions to identify whether they are benign or malignant. Moreover, 3D US allows interactive viewing of the patient's interior at any arbitrary pose to improve the diagnosis and staging of cancer. Furthermore, 3D US improves 2D segmentation of an image [19]. The continuity of data in the third dimension allows a more robust detection of object boundaries.

For these reasons, this research is interested in using wide-band incident waves and time-domain based reflection tomography to achieve 3D ultrasound soft tissue characterization.

1.4 Challenges

The challenges of ultrasound tissue characterization include the following.

- Nonlinearity:

  Scattered fields in inhomogeneous media is modeled as a non-homogeneous partial differential equation, which is highly nonlinear with respect to the tissue acoustic properties. Solving this nonlinear equation for the tissue acoustic properties is a challenging undertaking.

- Weak scattering assumption:

  To relax the nonlinearity of the scattered field model, some characteristics of scattered fields are assumed to be small and can thus be ignored (i.e., weak

scattering assumption). However, this assumption is invalid for strong scattering, for instance in tissue anomalies such as tumors and lesions which produce strong scattered fields. Ignoring certain characteristics of the scattered fields degrades the accuracy of tissue characterization.

- Ill-posed problem:

  As mentioned earlier, inverse scattering is an ill-posed problem, and as an implication the mathematical inversion of the scattered field model does not exist. Regularization methods have been introduced to alleviate this problem. However, these methods rely on prior knowledge or asserted conditions that may not be realistic. Also, a small amount of measurement noise may be translated into large variations (or instability) in the results.

- Prior knowledge:

  Prior knowledge of the tissue acoustic properties is typically required as initial values for inverse scattering methods, especially for iterative methods. In practice, such knowledge may be inaccurate or unavailable. Inappropriate initial values for these methods often lead to slow convergence and sub-optimal solutions.

- Speckle noise:

  Speckle noise is an inherent characteristic of ultrasound imaging. It appears as an interference pattern or texture, which does not entirely correspond to the underlying tissue structure. Many speckle noise reduction methods consider speckle noise as purely random noise. However, it is well-understood that the formation of speckle noise is both random and deterministic [20]. The deterministic part of speckle noise is caused by a physical phenomenon known as reverberation. Modeling and filtering speckle noise are still on-going research areas.

- Information loss and ambiguities in conventional ultrasound images:

  As mentioned in Section 1.1, many existing ultrasound imaging systems discretize the envelope of backscattered signals and display the discretized values as grey levels. Substantial information of the signal waveform is lost in the process of signal to image conversion. Complex biological materials are represented as grey levels only. As a result, severe ambiguities of tissue structures and properties are present in conventional ultrasound images, and hence hinder accurate physical interpretation.

1.5 Problem Formulation

The formulation of the inverse scattering problem for 3D ultrasound tissue characterization considered in this research is presented in this section. A wideband spherically focused ultrasound transducer is employed to illuminate a volume of multi-layered soft tissue and to measure backscattered signals from the tissue. The transducer sensing surface and the tissue layers are aligned to the x-y plane of the coordinate system as shown in Figure 1.1. The tissue is discretized along the x-z and y-z planes into a set of multi-layered tissues. The transducer is mounted on a x-y manipulator (omitted from Figure 1.1) to perform B-scan of the tissue in discrete intervals.

The tissue acoustic impedance mismatches are located at the layer interfaces. For each discretized multi-layered tissue, the locations of its layers in the 3D space are identified by the triplet x, y, z. The acoustic property of each layer is assumed to be homogeneous, isotropic and characterized by three parameters, namely attenuation coefficient ($\alpha_{x,y,z}$), sound speed ($c_{x,y,z}$) and mass density ($\rho_{x,y,z}$). It is well known that the tissue attenuation coefficient is approximately a first order function of frequency [21, 22, 23],

$$\alpha_{x,y,z} = m_{x,y,z}\ f + b_{x,y,z} \tag{1.1}$$

where f is the frequency of ultrasound wave; $m_{x,y,z}$ and $b_{x,y,z}$ are the slope and y-intercept of the attenuation coefficient model for soft tissues, respectively. It should be noted that the attenuation coefficient of water is proportional to f^2, unlike that of soft tissues. The water attenuation coefficients in the relevant frequency range are assumed known. No assumption is made on the prior statistics of $m_{x,y,z}$, $b_{x,y,z}$, $c_{x,y,z}$ and $\rho_{x,y,z}$.

Let $a_{x,y}$ be a time series of backscattered signals measured by the transducer at location x, y in the $x - y$ plane. Given $a_{x,y}$, the problem of inverse scattering for 3D ultrasound tissue characterization is to reconstruct $m_{x,y,z}$, $b_{x,y,z}$, $c_{x,y,z}$ and $\rho_{x,y,z}$. Note that there is no restriction on the number of layers in this problem formulation.

Reconstruction of the tissue acoustic parameters is achieved by solving a forward problem and an inverse problem recursively. In the forward problem, backscattered signals of the multi-layered tissues are computed based on a set of estimated tissue acoustic parameters. This problem is traditionally regarded as the "easy" problem. However, computing the propagation of focused waves in a multi-layered medium with planar interfaces is a complicated undertaking. This makes the forward problem a "hard" problem.

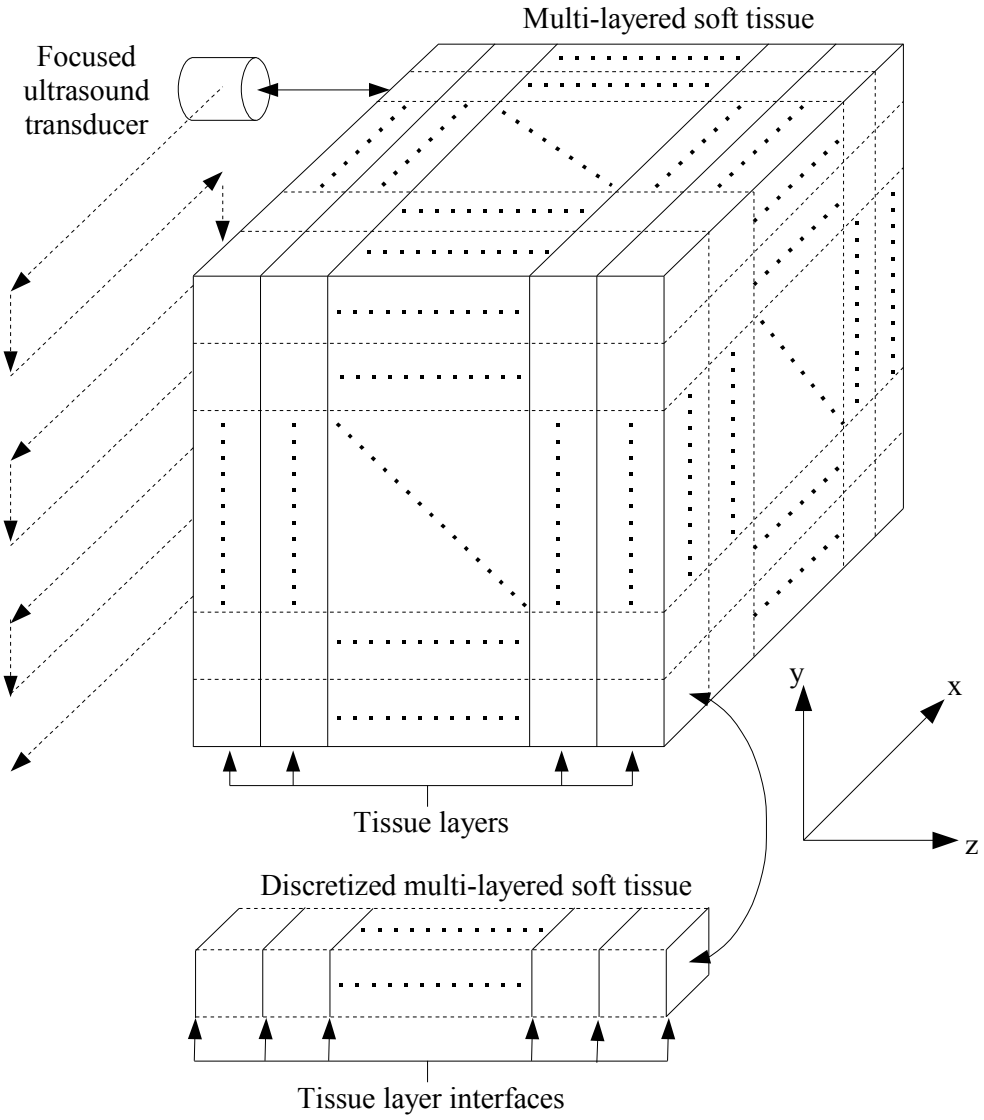

Figure 1.1: Configuration of 3D ultrasound testing

The inverse problem, traditionally regarded as the "hard" problem, aims to estimate a set of tissue acoustic parameters based on the actual measurements. The inverse problem compares the backscattered signals produced by the forward problem to the actual measurements, and adjusts the proposed tissue acoustic parameters based on an error criterion. The adjusted values replace the proposed ones in the forward problem and another cycle begins until certain error criterion is achieved.

Furthermore, reverberated echoes in the backscattered signals may severely degrade the accuracy of tissue characterization. Thus, the complex wave reverberation phenomenon in the multi-layered tissue are modelled and a filter for the reverberated echoes are developed.

1.6 Objectives

The primary goal of this research is to develop an ultrasound tissue characterization method that reconstructs accurate 3D maps of tissue acoustic parameters in multi-layered soft tissues. In order to achieve the goal, the proposed method must be designed to overcome the challenges identified in Section 1.4. The research objectives are then defined as:

1. To improve estimation accuracy, the proposed method must be designed as a nonlinear solver in which no linearization is involved. The wave propagation equation is severely nonlinear with respect to the tissue acoustic parameters. Some existing inverse scattering approaches linearize the equation to simplify derivations but compromise the accuracy of acoustic parameter estimates.

2. To be applicable to tissues of various scattering characteristics, the proposed method must be designed to eliminate the assumption of weak scattering. Existing inverse scattering methods are commonly developed based on the weak scattering assumption. However, this assumption limits the type of tissues that can be examined.

3. As discussed previously, inverse scattering is an ill-posed problem, which implies that mathematical inversion of the wave equation is not readily achievable. To tackle this problem, the proposed method must be designed to estimate the tissue acoustic parameters without performing mathematical inversion of the wave equation.

4. To eliminate the need for prior knowledge of the tissues, instead of inverting the wave equation, the proposed method must be designed to search for the tissue acoustic parameters solution space. The initial search point is critical to the search accuracy, and this point is topically determined based on the prior knowledge of the tissues. However, the prior knowledge may be unavailable or inaccurate in practice. Therefore, the proposed method must also be designed to generate the initial search point based on criteria other than the prior knowledge.

5. To reduce speckle noise in the measurement signals, the proposed method must be designed to model wave reverberations in multi-layered media and to filter reverberated echoes from the signals. Speckle noise in the ultrasound signals hinders the ability for inverse scattering methods to resolve tissue structures.

6. To minimize information loss in input data, the proposed method must be designed to analyze the signal waveforms rather than ultrasound images to estimate the tissue acoustic parameters. Conventional ultrasound imaging ignores the phase information of the measured signals and merely displays the signal magnitudes. Since signal magnitudes are not unique representations of tissue structures, conventional ultrasound imaging is unable to convey accurate information about the tissue acoustic parameters.

1.7 Thesis Organization

The remainder of this thesis is organized as follows:

- Chapter 2 presents the reviews of relevant background materials and literature.

- Chapter 3 introduces the overview of the proposed approach to inverse scattering. This approach consists of preprocessing, modeling and a multi-scale nonlinear stochastic filter. Descriptions of the preprocessing and derivations of the models needed for the filter are also provided in this chapter.

- Chapter 4 demonstrates the derivations of the forward scattering problem and the multi-scale nonlinear stochastic filter to solve the inverse scattering problem.

- Chapter 5 evaluates the performance of multi-scale nonlinear stochastic filter using simulated data.
- Chapter 6 describes details of multi-layered tissue phantom development, experimental conditions, tissue characterization results produced by the filter and result analysis.
- Chapter 7 concludes this research work and discusses future work related to this research.

Chapter 2

Background and Literature Review

This chapter presents the background materials and literature review relevant to this research. The background materials provide derivations of important equations that model forward scattering in fluids and elastic media. The propagation of waves at the media interfaces, the attenuation of waves and focused wave beam pattern are also discussed. In addition to forward scattering, scattered field approximations widely used in inverse scattering are described in detail, and the major drawbacks of the approximations are highlighted.

The literature review gives an overview of existing ultrasound tissue characterization and inverse scattering methods. Variations of the inverse scattering methods and their applications to ultrasound tissue characterization are described. One of the major problems of ultrasound inverse scattering is the presence of speckle noise. Review on speckle noise modelling and methods of speckle noise reduction are also presented.

2.1 Background

2.1.1 Forward Scattering

Forward scattering is the modelling and computing the scattered wave patterns in a medium with the knowledge of the properties of the medium.

Plane waves and spherical waves are commonly utilized in forward scattering problems, since they are simple to model and can be used to represent complicated

waves. The propagation of these waves in fluids and elastic media, as well as the effect of viscosity in the media are reviewed.

Plane Waves in Fluids and Elastic Media

Let ψ^p be acoustic plane wave pressure in space-time form. The propagation of ψ^p in a homogeneous, isotropic, nonattenuating medium can be described by the following equation [24],

$$\nabla^2 \psi^p - \frac{1}{c^2} \frac{\partial^2 \psi^p}{\partial t^2} = 0 \tag{2.1}$$

where $\nabla^2 = \frac{\partial^2}{\partial x^2} + \frac{\partial^2}{\partial y^2} + \frac{\partial^2}{\partial z^2}$; x, y and z are Cartesian coordinates; c is the sound speed of a homogeneous isotropic medium; t is time.

Equation 2.1 can also be expressed in terms of the elasticity of the medium,

$$(\lambda_e + 2\mu_e) \nabla^2 \psi^p = \rho \frac{\partial^2 \psi^p}{\partial t^2} \tag{2.2}$$

where ρ is the mass density; λ_e and μ_e are the Lame's constants [25],

$$\lambda_e = B - \frac{2}{3} G = \frac{Y v}{(1+v)(1-2v)}, \tag{2.3}$$

$$\mu_e = G = \frac{Y}{2(1+v)}, \tag{2.4}$$

v is the ratio of transverse to axial deformations known as the Poisson's ratio; B, G and Y are the bulk, shear and Young's moduli, respectively.

The propagations of plane waves in fluids and elastic media differ in the shear support. In fluids, the normal components of stress are equal in all directions and directional stress (i.e., shear stress) is not supported. Therefore, the shear modulus for fluids is zero ($G = 0$). Substituting Equations 2.3 and 2.4 into Equation 2.2 and comparing the result to Equation 2.1, it can be easily deduced that the sound speed of plane wave in a fluid is,

$$c_f = \sqrt{\frac{B_f}{\rho_f}} \tag{2.5}$$

where c_f, B_f and ρ_f are the sound speed, bulk modulus and density of the fluid, respectively.

For elastic media, the sound speed of plane wave propagation can be obtained as,

$$\begin{aligned} \frac{1}{c_e^2} &= \frac{\rho_e}{B_e + \frac{4}{3}G_e} \\ c_e &= \sqrt{\frac{B_e + \frac{4}{3}G_e}{\rho_e}} \end{aligned} \tag{2.6}$$

where c_e, B_e, G_e and ρ_e are the sound speed, bulk modulus, shear modulus and density of the elastic medium, respectively.

For elastic media like soft tissues, shear waves attenuate rather quickly such that they are insignificant [26, 21]. Therefore, the sound speed of plane wave in a soft tissue can be similar to that in a fluid,

$$c_t = \sqrt{\frac{B_t}{\rho_t}} \tag{2.7}$$

where c_t, B_t and ρ_t are the sound speed, bulk modulus and density of the soft tissue, respectively.

The harmonic form of ψ^p is often a more convenient representation since most forward and inverse wave approaches operate on each frequency component of the wave individually. A frequency component of ψ^p can be obtained by taking the Fourier transform of Equation 2.1 [27],

$$\left(\nabla^2 + k^2\right) \Psi^p = 0 \tag{2.8}$$

where k is the wave (or propagation) number, $k = \omega/c$; ω is the angular frequency; Ψ^p is the ω component of ψ^p. Since the wave equation in Equation 2.1 is linear in ψ^p, the solution for ψ^p can be readily obtained as the superposition of the frequency components' solutions. It should be noted that Equation 2.8 is the celebrated Helmholtz equation.

The solution of Equation 2.8 is,

$$\Psi^p = \Psi^p_+ + \Psi^p_- \tag{2.9}$$

where

$$\Psi^p_+ = P^p_+ \, e^{-i\,\vec{k}\cdot\vec{r}}; \tag{2.10}$$

$$\Psi^p_- = P^p_- \, e^{+i\,\vec{k}\cdot\vec{r}}; \tag{2.11}$$

Ψ_+^p and Ψ_-^p are the ω components of ψ^p propagating in opposite directions; P_+^p and P_+^p are pressure amplitudes of Ψ_+^p and Ψ_-^p, respectively; $\overrightarrow{k}$ is a vector normal to the wave front and is commonly known as the wave or propagation vector,

$$\overrightarrow{k} = k_x\,\widehat{x} + k_y\,\widehat{y} + k_z\,\widehat{z}, \tag{2.12}$$

k_x, k_y and k_z are projections of $\overrightarrow{k}$ onto the x, y and z axes, respectively; and these projections satisfy the condition,

$$\left\| \overrightarrow{k} \right\| = k = \sqrt{k_x^2 + k_y^2 + k_z^2} = \frac{\omega}{c}; \tag{2.13}$$

$\overrightarrow{r}$ is a position vector,

$$\overrightarrow{r} = x\,\widehat{x} + y\,\widehat{y} + z\,\widehat{z}, \tag{2.14}$$

$\widehat{x}$, $\widehat{y}$ and $\widehat{z}$ are unit vectors parallel to the x, y and z axes, respectively.

The inner products in Equations 2.10 and 2.11 are,

$$\overrightarrow{k} \cdot \overrightarrow{r} = kr = k_x\,x + k_y\,y + k_z\,z,$$

and the notations of Ψ_+^p and Ψ_-^p are simplified as,

$$\Psi_+^p = P_+^p\; e^{-ikr} \tag{2.15}$$

$$\Psi_-^p = P_-^p\; e^{+ikr} \tag{2.16}$$

The particle velocity caused by Ψ_+^p can be obtained as,

$$\overrightarrow{U}_+^p = \frac{P_+^p}{\rho c}\; e^{-ikr} \tag{2.17}$$

where ρ is the mass density of a homogeneous isotropic medium.

The specific acoustic impedance associated with Ψ_+^p is,

$$\begin{aligned} Z_+^p &= \frac{\Psi_+^p}{\overrightarrow{U}_+^p} \\ &= \rho c \end{aligned} \tag{2.18}$$

When a plane wave propagates normal to the z axis, the wave equation is reduced to

$$\frac{\partial^2}{\partial z^2}\psi^p - \frac{1}{c^2}\frac{\partial^2 \psi^p}{\partial t^2} = 0$$

It follows that the solutions of the wave in Equations 2.15 and 2.16 are also reduced to

$$\Psi_+^p = P_+^p \, e^{-ik_z z} \tag{2.19}$$
$$\Psi_-^p = P_-^p \, e^{+ik_z z} \tag{2.20}$$

where $k_z = k = \omega/c$.

The specific acoustic impedances associated with Equations 2.19 and 2.20 are identical to Equation 2.18.

Plane Wave Reflection and Transmission at an Elastic Solid-to-solid Planar Interface

When a plane wave impinges a planar interface between two elastic solids of different specific acoustic impedances, the wave is reflected at and/or transmitted through the interface depending on the acoustic impedances of the solids and the angle of incident. Figure 2.1 illustrates plane wave reflection and transmission at a planar interface parallel to the x-y plane. Let Ψ_i, Ψ_r and Ψ_t respectively be the incident, reflected and transmitted plane waves at the interface; $\overrightarrow{U}_i$, $\overrightarrow{U}_r$ and $\overrightarrow{U}_t$ be the particle velocities associated with Ψ_i, Ψ_r and Ψ_t, respectively; P_i, P_r and P_t be pressure magnitudes of Ψ_i, Ψ_r and Ψ_t, respectively, at the interface; Z_0 and Z_1 be the specific acoustic impedances of the solids; θ_i, θ_r and θ_t be the angles of incident, reflection and transmission (or refraction), respectively; they are defined as angles between the plane waves propagation directions and the z axis (i.e., normal vector of the interface).

It is assumed that θ_i is not large enough to produce total internal reflection. The angle of reflection, θ_r, is equal to the incident wave angle, θ_i,

$$\theta_r = \theta_i \tag{2.21}$$

The angle of transmission is determined by Snell's law,

$$\frac{\sin(\theta_i)}{\sin(\theta_t)} = \frac{c_0}{c_1} \tag{2.22}$$

where c_0 and c_1 are the sound speeds of the solids shown in Figure 2.1.

At the interface, the wave pressures and particle velocities of the two solids must be identical. Otherwise, the media will be tear apart from each other at the

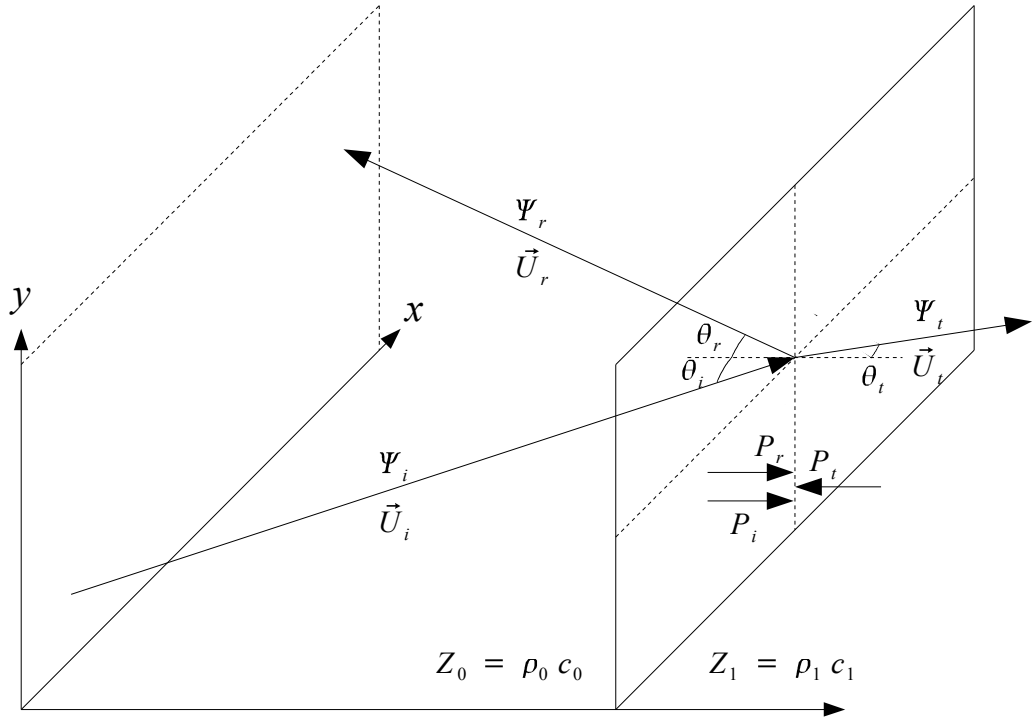

Figure 2.1: Plane wave reflection and transmition at a planar interface

interface. The LHS of the interface contains the incident and reflected waves, and the RHS contain the transmitted one. The wave pressures and particle velocities at the interface can be modelled as,

$$P_i + P_r = P_t \tag{2.23}$$

$$\overrightarrow{U}_i \, cos\,(\theta_i) - \overrightarrow{U}_r \, cos\,(\theta_r) = \overrightarrow{U}_t \, cos\,(\theta_t) \tag{2.24}$$

It should be noted that, pressures act in all directions and they are independent of the angles. The converse is true for the particle velocities.

The pressure magnitudes of Ψ_r and Ψ_t are directly proportional to that of Ψ_i,

$$P_r = R \, P_i \tag{2.25}$$

$$P_t = T \, P_i \tag{2.26}$$

where R and T are the reflection and transmission coefficients, respectively.

The relationship between R and T can be obtained by substituting Equations 2.25 and 2.26 into Equation 2.23,

$$\begin{aligned} P_i + R \, P_i &= T \, P_i \\ 1 + R &= T \end{aligned} \tag{2.27}$$

It follows that the acoustic impedances of the two media must also be identical at the interface,

$$\frac{P_i + R \, P_i}{\overrightarrow{U}_i \, cos\,(\theta_i) - \overrightarrow{U}_r \, cos\,(\theta_r)} = \frac{T \, P_i}{\overrightarrow{U}_t \, cos\,(\theta_t)} \tag{2.28}$$

From Equation 2.17, the particle velocities are expressed in terms of wave pressures,

$$\begin{aligned} \frac{Z_0\,(P_i + R \, P_i)}{P_i \, cos\,(\theta_i) - R \, P_i \, cos\,(\theta_r)} &= \frac{T \, P_i \, Z_1}{T \, P_i \, cos\,(\theta_t)} \\ \frac{Z_0\,(1 + R)}{cos\,(\theta_i) - R \, cos\,(\theta_r)} &= \frac{Z_1}{cos\,(\theta_t)} \\ R &= \frac{Z_1/cos\,(\theta_t) - Z_0/cos\,(\theta_i)}{Z_0/cos\,(\theta_i) + Z_1/cos\,(\theta_t)} \end{aligned} \tag{2.29}$$

$$\begin{aligned} T &= 1 + R \\ &= \frac{2Z_1/cos\,(\theta_t)}{Z_0/cos\,(\theta_i) + Z_1/cos\,(\theta_t)} \end{aligned} \tag{2.30}$$

where $Z_0 = \rho_0 c_0$; $Z_1 = \rho_1 c_1$.

It is straight forward to see that when the plane wave propagates perpendicular to the interface(i.e., $\theta_i = 0$), R and T are simplified to

$$R = \frac{Z_1 - Z_0}{Z_0 + Z_1} \tag{2.31}$$

$$T = \frac{2Z_1}{Z_0 + Z_1} \tag{2.32}$$

When $R < 0$, phase of the reflected wave is shifted 180° relative to the incident wave. Also, when $T > 1$, it may be strange at first to learn that the transmitted waves have higher magnitude than the incident waves. In this case, the transmitted wave power is only a fraction of that of the incident wave [28].

Plane Wave Reflection and Transmission at an Elastic Fluid-to-solid Planar Interface

The transmission of plane waves at a fluid-solid planar interface may be different from that at a solid-solid planar interface as discussed in Section 2.1.1. The porosity and elastic of the solid determine the nature of wave transmission as one of the following three refraction types [24],

1. when the solid is isotropic and its sound speed is much lower than that of the fluid, the transmitted wave propagates perpendicular to the interface since θ_t is effectively 0 for $c_0 \gg c_1$,

2. when the acoustic impedance of the solid is similar to that of the fluid, the transmitted wave propagates in the same manner as that at the solid-to-solid interface, and

3. when the solid is rigid, the transmitted wave is divided into a compressional and a transverse wave that travel at different speeds and in different directions.

In this work, the solid is a soft tissue that has similar acoustic properties as water, so that plane wave transmission at the water and soft tissue interface belongs to the second refraction type. Detail discussions of the first and third refraction types are out of the scope of this work.

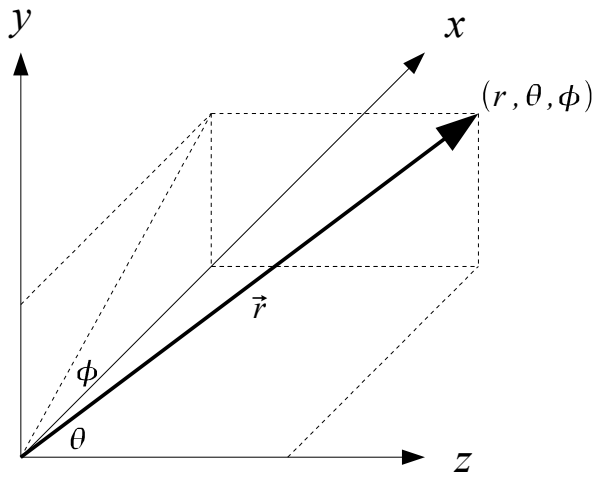

Figure 2.2: Spherical coordinate system

Spherical Waves

In addition to plane waves, background knowledge of spherical waves is needed in the derivation of focused wave propagation in multi-layered tissues later.

Waves of spherical shape can be modelled more conveniently in a spherical coordinate system as illustrated in Figure 2.2. Let ψ^s be the spherical wave pressure. Since ψ^s is symmetrical about all axes, ψ^s is function of $\overrightarrow{r}$ but not of ϕ and θ [24],

$$\nabla^2\psi^s - \frac{1}{c^2}\frac{\partial^2\psi^s}{\partial t^2} = 0 \tag{2.33}$$

where $\nabla^2 = \frac{\partial^2}{\partial r^2} + \frac{2}{r}\frac{\partial}{\partial r}$; $r = \|\overrightarrow{r}\| = \sqrt{x^2+y^2+z^2}$, $\overrightarrow{r} = (r, \theta, \phi)$.

The general solution of Equation 2.33 consists of a diverging wave from the point source and a converging wave to the source. In most applications, the diverging wave is of interests. The harmonic form of the diverging spherical wave is,

$$\Psi^s = i\rho c u_0 \, \frac{\overline{r}}{r} \, k\overline{r} \, e^{-ikr} \tag{2.34}$$

where ρ is the mass density of a homogeneous isotropic medium; u_0 is the speed amplitude of the radially vibrating sphere source with angular frequency ω and average radius of the vibrating sphere source $\overline{r}$, $u = u_0 e^{i\omega t}$. It is assumed that the

displacement of the sphere surface vibration is much less than r (i.e., $u_0/\omega \ll \overline{r}$), and u can be measured at $\overline{r}$; $\overrightarrow{k} = (k, \theta, \phi)$.

The specific acoustic impedance associated with spherical waves, Z^s, is of great interests since it determines the reflection and transmission of the waves. It can be obtained through the relationship between wave pressure and particle velocity, $\overrightarrow{U}^s$,

$$Z^s = \frac{\Psi^s}{\overrightarrow{U}^s} \tag{2.35}$$

where

$$\overrightarrow{U}^s = \left(1 - \frac{i}{kr}\right) \frac{\Psi^s}{\rho c} \widehat{r} \tag{2.36}$$

It should be noted that the particle speed of spherical wave is out of phase with the pressure. It then follows from Equations 2.34 to 2.36 that,

$$Z^s = \rho c \frac{(kr)^2 + ikr}{1 + (kr)^2} \tag{2.37}$$

The complex acoustic impedance implies that the diverging wave front dilutes the wave energy as the wave propagates. The angle between the real and complex axis can be interpreted as the phase difference between Ψ^s and $\overrightarrow{U}^s$.

Wave Attenuation Due to Viscosity in Elastic Media

When acoustic waves propagate in elastic media like soft tissues, some of the waves' energy is transferred into heat. This phenomenon is also known as absorption. In Sections 2.1.1 and 2.1.1, the wave equations are derived under the assumption of viscosity-free tissue so that no loss of waves' energy was taken into account. In actual elastic media, however, some wave energy must be consumed to overcome the resistance due to viscosity in order for the wave to propagate. The following derivations of wave attenuation are valid for both plane and spherical waves. The loss of energy is modeled as an attenuation of wave pressure, which is realized by introducing a term for loss of pressure in the wave equation as [21],

$$\nabla^2 (\psi - \psi^v) - \frac{1}{c^2} \frac{\partial^2}{\partial t^2} (\psi - \psi^v) = 0 \tag{2.38}$$

where ψ^v is the wave pressure attenuated due to the viscous drag of particles. This pressure is dependent on the tissue viscosity and the spatial variation of particle velocity [29] as

$$\psi^v = \left(\frac{4\nu_s}{3} + \nu_b + \frac{\gamma - 1}{C_p}\kappa\right) \nabla u \tag{2.39}$$

where ν_s and ν_b are the dynamic coefficients of shear and compressional viscosities, respectively; γ, C_p and κ are the ratio of specific heats, heat capacity at constant pressure and thermal conductivity of the medium, respectively; since $\kappa \ll \nu_s$ (and ν_b), it is customary to neglect the term, $\kappa(\gamma - 1)/C_p$,

$$\psi^v \simeq \left(\frac{4\nu_s}{3} + \nu_b\right) \nabla u \tag{2.40}$$

Using the relation between particle velocity and pressure, $\nabla u = -\frac{1}{\rho c^2}\frac{\partial \psi}{\partial t}$, ψ^v can be expressed in terms of pressure as,

$$\psi^v \simeq -\left(\frac{4}{3}\nu_s + \nu_b\right) \frac{1}{\rho c^2}\frac{\partial \psi}{\partial t} \tag{2.41}$$

Let $\beta = \left(\frac{4}{3}\nu_s + \nu_b\right)\frac{1}{\rho c^2}$ to simplify notation, and substitute Equation 2.41 into Equation 2.38,

$$\nabla^2\left(\psi + \beta\frac{\partial \psi}{\partial t}\right) - \frac{1}{c^2}\frac{\partial^2}{\partial t^2}\left(\psi + \beta\frac{\partial \psi}{\partial t}\right) = 0 \tag{2.42}$$

As mentioned above, the frequency component of ψ is more desirable for subsequent analysis. It can be obtained by taking the Fourier transform of Equation 2.42,

$$\begin{aligned}
\nabla^2(\Psi + i\omega\beta\Psi) - \frac{1}{c^2}\left(i^2\omega^2\Psi + i^2\omega^2\beta\Psi\right) &= 0 \\
\left[\nabla^2(1 + i\omega\beta) + \frac{1}{c^2}\left(\omega^2 + \omega^2\beta\right)\right]\Psi &= 0 \\
\left[\nabla^2 + \frac{\omega^2}{c^2}\frac{1+\beta}{1+i\omega\beta}\right]\Psi &= 0 \\
\left[\nabla^2 + k^2\frac{(1+\beta)(1-i\omega\beta)}{1+\omega^2\beta^2}\right]\Psi &= 0
\end{aligned} \tag{2.43}$$

For media such as water and soft tissues, the values β is much smaller than 1. For instance, the value of β for water is $\beta = \left(\frac{4}{3}0.7 \times 10^{-3} + 2 \times 10^{-3}\right)/1500^2 = 1.3 \times 10^{-9}$. Therefore, Equation 2.43 can be simplified as,

$$\left[\nabla^2 + k^2\frac{1 - i\omega\beta}{1 + \omega^2\beta^2}\right]\Psi = 0 \tag{2.44}$$

The solutions of Ψ are exponential functions of the coefficient, $k^2\frac{1-i\omega\beta}{1+\omega^2\beta^2}$. This coefficient should be written as follows to facilitate solving for Ψ,

$$\begin{aligned}(k-i\alpha)^2 &= k^2\frac{1-i\omega\beta}{1+\omega^2\beta^2}\\ k^2-2ik\alpha-\alpha^2 &= \frac{k^2}{1+\omega^2\beta^2}-i\frac{k^2\omega\beta}{1+\omega^2\beta^2}\end{aligned} \tag{2.45}$$

where α is the attenuation coefficient for the wave at frequency ω.

The solutions of Ψ can be written as,

$$\begin{aligned}\Psi &= \Psi_+ + \Psi_-\\ \Psi_+ &= P_+\, e^{-i(k-i\alpha)r}\\ \Psi_- &= P_-\, e^{+i(k-i\alpha)r}\end{aligned}$$

α can be derived from the imaginary component of Equation 2.45,

$$\begin{aligned}2k\alpha &= \frac{k^2\omega\beta}{1+\omega^2\beta^2}\\ \alpha &= \frac{k\omega\beta}{2\left(1+\omega^2\beta^2\right)}\end{aligned} \tag{2.46}$$

Substitute β into Equation 2.46,

$$\begin{aligned}\alpha &= \frac{k\omega\left(\frac{4}{3}\nu_s+\nu_b\right)\frac{1}{\rho c^2}}{2\left(1+\omega^2\left(\frac{4}{3}\nu_s+\nu_b\right)^2\frac{1}{\rho^2c^4}\right)}\\ &= \frac{\omega^2\left(\frac{4}{3}\nu_s+\nu_b\right)\rho c}{2\rho^2c^4+2\omega^2\left(\frac{4}{3}\nu_s+\nu_b\right)^2}\end{aligned} \tag{2.47}$$

For low frequency waves, $2\rho^2c^4 \gg 2\omega^2\left(\frac{4}{3}\nu_s+\nu_b\right)^2$ and α can be simplified as,

$$\alpha = \frac{\left(\frac{4}{3}\nu_s+\nu_b\right)\omega^2}{2\rho c^3} \tag{2.48}$$

The effect of wave attenuation can be incorporated in the plane and spherical wave equations simply by replacing k with $k-i\alpha$,

$$k \rightarrow k-i\alpha, \tag{2.49}$$

$$k_x \rightarrow k_x-i\alpha_x, \tag{2.50}$$

$$k_y \rightarrow k_y-i\alpha_y, \tag{2.51}$$

$$k_z \rightarrow k_z-i\alpha_z, \tag{2.52}$$

where α_x, α_y and α_z are projections of α normal to the wave front on the x, y and z axes, $\alpha^2 = \alpha_x^2 + \alpha_y^2 + \alpha_z^2$.

Some remarks on wave attenuation are in order. In Section 2.1.1, the acoustic impedance in Equation 2.18 is a real number assuming lossless plane wave. However, in this section wave pressure is attenuated due to viscosity. The question posed is as follows: does the acoustic impedance now become a complex number? In this case, the particle velocity and wave pressure are slightly out of phase since some wave's energy is spent to combat the viscosity effect. Consequently, the acoustic impedance should be complex. This phase mismatch is often quite small for soft tissues, so that the complex component is negligible. Therefore, the acoustic impedance is considered as a real number.

Another remark is regarding the relationship between attenuation coefficient and frequency of waves. Due to the relaxation effects for most soft tissues, ν_s and ν_b have different frequency characteristics and can be modelled as,

$$\nu_s = \frac{\nu_l}{1 + (\omega/\omega_s)^2}, \ \nu_b = \frac{\nu_l}{1 + (\omega/\omega_b)^2} \tag{2.53}$$

where ν_l is the low-frequency viscosity; ω_s and ω_b are respectively the angular frequencies at which ν_s and $\nu_b = 0.5\ \nu_l$.

Equation 2.53 is only applicable to soft tissues. The attenuation coefficient for viscous fluids (not tissues) shown in Equation 2.48 is proportional to the square of frequency. This explains why the depth of wave penetration decreases exponentially as frequency increases. On the other hand, for soft tissues (i.e., Equation 2.53 is valid), the viscosity are not constant and decrease as frequency increases. The decreasing viscosities counteract the increasing frequency (i.e., ω^2) in Equation 2.48. As a result, the attenuation coefficient is roughly linearly proportional to frequency. This implies high frequency acoustic waves are able to convey material property information of greater depths in soft tissues than in viscous fluids.

Focused Wave Beam Pattern

In this research, soft tissues are characterized using focused ultrasound produced by a spherically focused ultrasound transducer as mentioned in Section 1.5. Modelling of the wave beam pattern radiated by a spherically focused ultrasound transducer is essential for forward scattering. The model describing focused waves propagation in a homogenous soft tissue is derived in this section. The wave beam pattern produced by a spherically focused ultrasound transducer is modelled based on the following assumptions.

- Pressure field sources[1] are mounted on a baffle, which is a perfectly rigid boundary, so that the pressures generated by the pressure field sources and reflected by the baffle are in phase and have twice the amplitude in the half-space of the source [24],
- the radiating surface of the transducer vibrates uniformly with speed $u_0 e^{i\omega t}$ normal to the surface [30],
- since the pressure amplitude level is low, cavitation and/or nonlinear effects of the tissue can be ignored, and
- no Lamb waves propagate on the radiating surface of the transducer [31].

The radiating surface of the transducer can be considered as a composition of many pressure field sources emitting spherical waves of the same amplitude and phase. The harmonic form of the focused waves at any point in a homogeneous, isotropic tissue in front of the transducer surface is described by the Rayleigh-Sommerfeld integral [31],

$$\Psi^f(r,\theta,t) = i\frac{\rho_0 \omega u_0 r_c^2}{2\pi} e^{i\omega t} \int_0^{2\pi} \int_0^a \frac{e^{-i(k-i\alpha)r'}}{r'} sin(\theta_0)\ d\theta_0\ d\phi_0 \tag{2.54}$$

where $\Psi^f(r,\theta,t)$ is the focused wave pressure at angular frequency ω, which is suppressed to simplify notations; r is the distance between the transducer surface center and a point of interest in the tissue; r_c is the radius of curvature of the transducer; θ, θ_0 and ϕ_0 are angles used in focused wave modelling as shown in Figure 2.3; $k = \omega/c$; c and α are the sound speed and attenuation coefficient of the tissue;

$$r' = \left\{ r^2 + 2r_c^2 \left[\left(1 - \frac{r\, cos\theta}{r_c} \right) (1 - cos\theta_0) - \frac{r\, sin\theta}{r_c}\, sin\theta_0\, cos\phi_0 \right] \right\}^{1/2}$$

The tissue attenuation coefficient can be expressed as a first order function of the frequency of ultrasound wave as in Equation 1.1.

The Rayleigh-Sommerfeld integral in Equation 2.54 can be approximated as a single integral equation to gain computational efficiency [31],

$$\begin{aligned} \Psi^f(r,\theta,t) &= i\frac{\rho_0 \omega u_0 r_c^2}{2\pi r} e^{i(\omega t - kr) - \alpha r} \times \\ &\int_0^a e^{(-ik-\alpha)r''} J_0\left((k - i\alpha)\ r_c\, sin\theta\, sin\theta_0 \right)\ sin\theta_0\ d\theta_0 \end{aligned} \tag{2.55}$$

[1] A pressure field source is small compared to a wavelength of the field produced.

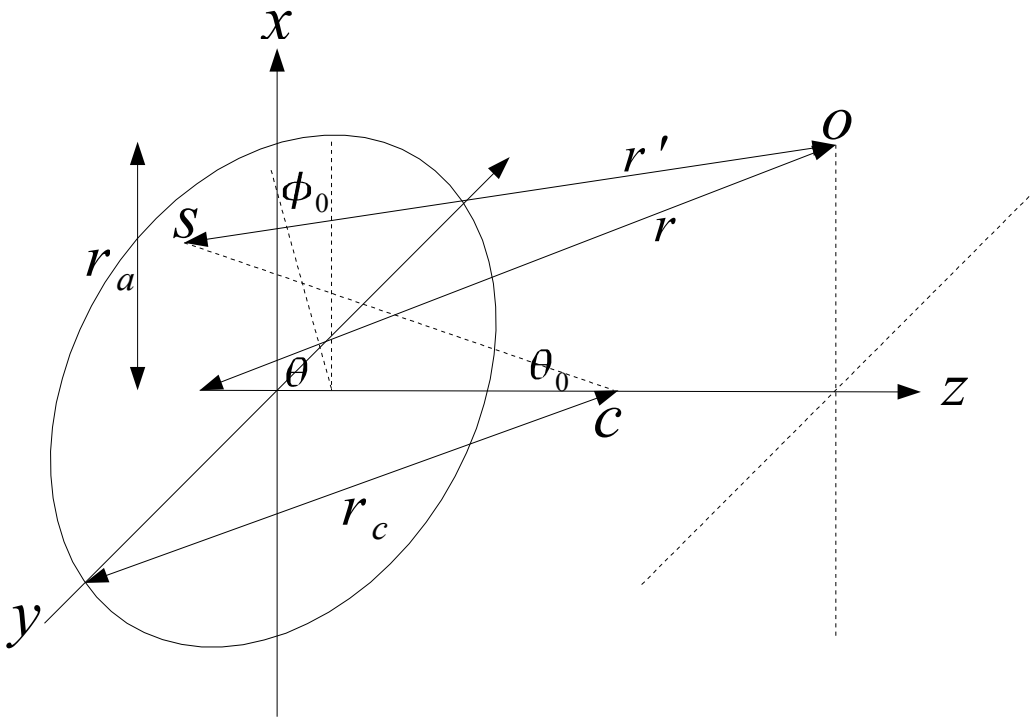

Figure 2.3: Configuration of spherically focused transducer in homogeneous medium

where $r'' = \frac{r_c^2}{r}\left(1 - \frac{r}{r_c}cos\theta\right)(1 - cos\theta_0)$; $J_0(\cdot)$ is the zeroth order complex Bessel function [30].

The focused wave pressure amplitude in the Cartesian coordinates is of interest, since the tissue layers are flat. The focused wave pressure is the magnitude of Ψ^f in Equation 2.55, and Ψ^f is transformed to Cartesian coordinates as,

$$\left|\Psi^f(z,x)\right| = \frac{\rho_0 \omega u_0 r_c^2}{\sqrt{z^2+x^2}} e^{-\alpha\sqrt{z^2+x^2}} \sqrt{J_{0,re}^2(z,x) + J_{0,im}^2(z,x)} \tag{2.56}$$

where $J_{0,re}(\cdot)$ and $J_{0,im}(\cdot)$ are respectively the real and imaginary parts of $J_0(\cdot)$,

$$\begin{aligned} J_{0,re}(z,x) &= \int_0^a e^{-\alpha r''} \left[U_0(\gamma,\varphi)\ sin(kr'') - \right. \\ &\quad \left. V_0(\gamma,\varphi)\ cos(kr'')\right]\ sin\theta_0\, d\theta_0 \\ J_{0,re}(z,x) &= \int_0^a e^{-\alpha r''} \left[U_0(\gamma,\varphi)\ cos(kr'') - \right. \\ &\quad \left. V_0(\gamma,\varphi)\ sin(kr'')\right]\ sin\theta_0\, d\theta_0 \end{aligned}$$

$U_0((\theta),\varphi)$ and $V_0((\theta),\varphi)$ are respectively the real and imaginary parts of the zeroth order complex Bessel function [30]; $\gamma = \frac{k\, r_c\, sin\theta_0\, x}{cos\varphi\sqrt{z^2+x^2}}$; $\varphi = tan^{-1}(-\alpha/k)$; $r'' = \frac{-zr_c+r_c^2}{\sqrt{z^2+x^2}}(1 - cos\theta_0)$.

The focused wave pressure amplitude of a circular surface having an area πr_a^2 on the X-Y plane located at $(0,0,z)$ can be computed as,

$$\left|\Psi^f(z)\right| = \pi\left(\int_0^{r_a} \left|\Psi^f(z,x)\right| dx\right)^2 \tag{2.57}$$

The wave beam is modelled as the sum of many pressure field sources emitting spherical waves on the transducer surface. The spherical waves interfere each other causing extensive fluctuations in the wave beam amplitude and phase in the region near the transducer surface known as the near field (or Fresnel zone). As the spherical waves propagate further away from the transducer surface, the spherical wave fronts become more similar to each other. Hence, fluctuations in the wave beam are reduced. The region beyond the near field, where the wave beam pattern becomes uniform, is known as the far field (or Fraunhofer zone) [32].

2.1.2 Inverse Scattering

Inverse scattering is the reverse of forward scattering. Given the measurements of scattered waves from a medium, inverse scattering determines the properties of the

medium.

A major challenge of inverse scattering is solving the nonlinear equation describing the relationship between the scattered waves and medium properties. It is well known that this equation cannot be solved analytically. Born approximation is developed to linearize the equation enabling analytical solution based on the assumption of weak scattering. Ever since Born approximation was developed, it has become the basis of most inverse scattering methods. Therefore, understanding Born approximation is the first step to review existing inverse scattering methods.

Born Approximation

The wave satisfying the Helmholtz equation in Equation 2.8 for homogeneous media is reprinted here for convenience,

$$\left(\nabla^2 + k_r^2\right)\ \Psi_r^P = 0 \tag{2.58}$$

where the subscript r denotes a point in the medium; Ψ_r^P and k_r are the wave and wave number at point r; specification of the point is needed for later use.

For inhomogeneous media, Ψ_r^p and k_r can be explicitly expressed in terms of their components as,

$$\begin{aligned} \Psi_r^p &= \Psi_{r,i}^P + \Psi_{r,s}^P & (2.59)\\ k_r &= k n_r = k\left(1 + n_{r,\delta}\right) & (2.60) \end{aligned}$$

where $\Psi_{r,i}^P$ and $\Psi_{r,s}^P$ are the incident and scattered waves, respectively; $\Psi_{r,i}^P$ represents the Ψ_r^P component that corresponds to the medium's homogeneities, while $\Psi_{r,s}^P$ is associated with the inhomogeneities; k is the average wave number of the medium; n_r is the refractive index of the medium at r, $n_r = \frac{c}{c_r}$; c is the average sound speed of the media; $n_{r,\delta}$ is the deviation of refractive index at r.

Substituting Equations 2.59 and 2.60 into Equation 2.58, the Helmholtz equation becomes,

$$\begin{aligned} \left(\nabla^2 + k^2\right)\ \left(\Psi_{r,i}^P + \Psi_{r,s}^P\right) &= -k^2\left(n_{r,\delta}^2 - 2n_{r,\delta}\right)\ \left(\Psi_{r,i}^P + \Psi_{r,s}^P\right) & (2.61)\\ &= -k^2\left(n_r^2 - 1\right)\ \left(\Psi_{r,i}^P + \Psi_{r,s}^P\right) \end{aligned}$$

Due to the homogeneities of media, the incident field in Equation 2.61 is equivalent to Equation 2.58,

$$\left(\nabla^2 + k^2\right)\ \Psi_{r,i}^p = 0 \tag{2.62}$$

Based on Equation 2.15, the solution of $\Psi^p_{r,i}$ can be written as,

$$\Psi^p_{r,i} = P^p_+ \; e^{-ikr} \tag{2.63}$$

Consequently, Equation 2.61 can be simplified as,

$$\left(\nabla^2 + k^2\right) \; \Psi^p_{r,s} = -k^2 \left(n_r^2 - 1\right) \; \Psi^p_r \tag{2.64}$$

Now the objective is to solve the scattered field, $\Psi^p_{r,s}$, in Equation 2.64. However, no known method is available to solve $\Psi^p_{r,s}$ directly. According to [33], the solution of $\Psi^p_{r,s}$ can be expressed in terms of the free-space Green's function as,

$$\Psi^p_{r,s} = \int g_{r-r'} \; k^2 \left(n_{r'}^2 - 1\right) \; \Psi^p_{r'} \; dr' \tag{2.65}$$

$$= \int g_{r-r'} \; k^2 \left(n_{r'}^2 - 1\right) \; \Psi^P_{r',i} \; dr' + \int g_{r-r'} \; k^2 \left(n_{r'}^2 - 1\right) \; \Psi^p_{r',s} \; dr' \tag{2.66}$$

where g_r is the free-space Green's function,

$$g_{r-r'} = \frac{e^{ik(r-r')}}{4\pi \left(r - r'\right)} \tag{2.67}$$

The right-hand side of Equation 2.66 is not readily the solution of $\Psi^p_{r,s}$, since it is a function of the scattered field itself. This solution can be obtained through approximation. Assuming the magnitudes of $\Psi^p_{r',s}$ are small relative to that of $\Psi^p_{r',i}$, the integral associated with $\Psi^p_{r',s}$ can be ignored and Equation 2.66 can be approximated as,

$$\Psi^p_{r,s} \approx \Psi^p_{r,B^1} = \int g_{r-r'} \; k^2 \left(n_{r'}^2 - 1\right) \; \Psi^p_{r',i} \; dr' \tag{2.68}$$

where Ψ^ω_{r,B^1} is the first order Born approximation of the scattered field. Higher order Born approximation may be used to obtain better approximation,

$$\Psi^p_{r,B^2} = \int g_{r-r'} \; k^2 \left(n_{r'}^2 - 1\right) \left(\Psi^p_{r',i} + \Psi^p_{r',B^1}\right) \; dr'$$

$$\Psi^p_{r,B^{j+1}} = \int g_{r-r'} \; k^2 \left(n_{r'}^2 - 1\right) \left(\Psi^p_{r',i} + \Psi^p_{r',B^j}\right) \; dr' \tag{2.69}$$

where Ψ^p_{r,B^j} is the j^{th} order Born approximation.

In addition to Born approximation, the solution of scattered field can be approximated by the Rytov approximation [34]. Although it is derived based on slightly different assumptions compared to Born approximation, their resulting form of approximations are quite similar [35].

Extended Born Approximation

The extended Born approximation [36] is developed to overcome some of the limitations associated with the Born and Rytov approximations. The extension involves incorporating a high-frequency approximation of the scattered field to the scattering measurements at more than one frequency. The extended Born approximation begins with invoking the far-field form of the Green's function. The far-field version of the scattered field in Equation 2.65 can be written as,

$$\Psi^p_{\widehat{r},s} = \int e^{ik\widehat{r}\cdot r'}\ k^2\left(n^2_{r'}-1\right)\ \Psi^p_{r'}\ dr' \tag{2.70}$$

where $\widehat{r} = \frac{r-r'}{|r-r'|}$.

Equation 2.70 is manipulated into the form of a Fourier integral to take advantage of the numerical efficiency of the fast Fourier transform (FFT),

$$\Psi^p_{\widehat{r},s} = \int e^{ik(r-r')}\ k^2\left(n^2_{r'}-1\right)\ \Psi^p_{r'}\ e^{ikr'}\ e^{-ikr'}\ dr' \tag{2.71}$$

where $\Psi^p_{r'}\ e^{ikr'}$ is defined as a distorting function denoted as $\Psi^p_{r',D}$, which compensates for the difference between the incident field and the total field. Equation 2.71 is rewritten as,

$$\begin{aligned}
\Psi^p_{\widehat{r},s} &= \int e^{ik(r-r')}\ k^2\left(n^2_{r'}-1\right)\ \Psi^p_{r',D}\ e^{-ikr'}\ dr' \\
&= k^2\int\left(n^2_{r'}-1\right)\ \Psi^p_{r',D}\ e^{-ik\left(\widehat{k}-\widehat{r}\right)r'}\ dr' \\
&= k^2\ \mathcal{F}\left[\left(n^2_{r'}-1\right)\ \Psi^p_{r',D}\right]
\end{aligned}$$

where $\widehat{k}$ is the direction of wave propagation; $\mathcal{F}[\cdot]$ denotes Fourier transform in domain of $k\left(\widehat{k}-\widehat{r}\right)$.

It is important to note that when the Born approximation is valid (i.e., scattering is weak and can be ignored), the distorting function is constant due to Equation 2.63,

$$\begin{aligned}
\Psi^p_{r,D} &= \Psi^p_r\ e^{ikr} \\
&= P\ e^{-ikr}\ e^{ikr} \\
&= P
\end{aligned}$$

and an inverse Fourier transform can be used to reconstruct the refractive index distribution. However, when the Born approximation is invalid the distorting function must be estimated for inversion. Based on the WKB high-frequency approximation [37], the total field can be represented as,

$$\Psi_r^p = e^{-ikS_r}$$

, and the distorting function becomes,

$$\Psi_{r,D}^p = e^{-ik\left(S_r - \widehat{k}r\right)}$$

where S_r is the wavefront of Ψ_r^p and is a function of $\widehat{k}$.

The problem of far-field scattered field approximation is now transformed to the approximation of the quantity $S_r - \widehat{k}r$. To simplify $S_r - \widehat{k}r$, it is expressed in the form of a power series

$$S_r - \widehat{k}r = \sum_{j=0}^{n} a_j r^j, \quad n = \infty$$

where a_j is a coefficient of the power series. A convenient way to approximate this quantity is to assume only the coefficient a_0 is significant, such that all other coefficients can be ignored. The distorting function and the scattered field are approximated as

$$\begin{aligned} \Psi_{r,D}^p &= e^{-ika_0} \\ \Psi_{\widehat{r},s}^p &= k^2\, e^{-ika_0}\, \mathcal{F}\left[n_{r'}^2 - 1\right] \end{aligned}$$

The coefficient a_0 can be estimated based on the phase difference between the measured far-field scattered data at two wave numbers, k_1 and k_2, in the forward direction, $\widehat{r} = \widehat{k}$ [36]. This may be expressed as

$$a_0 = -k_1 \frac{\phi_{k_2} - \phi_{k_1}}{k_2 - k_1}$$

where ϕ_{k_1} and ϕ_{k_2} are the phases of the measured far-field scattered data at k_1 and k_2, respectively; $k_2 - k_1$ is assumed to be small.

Note that a_0 is dependent on $\widehat{k}$ and frequency. After estimating a_0 for each $\widehat{k}$ in each frequency, the entire spectrum is then inverse Fourier transformed to reconstruct the refractive index, n_r, distribution of the medium. In practice, the validity of the extended Born approximation depends on the medium. Nevertheless, it is expected to be a better approximation than the conventional Born approximation in which the distorting function is simply taken as a constant.

2.2 Literature Review

2.2.1 Ultrasound Tissue Characterization

Conventional ultrasound imaging uses the pulse-echo method which can only resolve structures that are larger than the wavelength of the incident wave. Inverse scattering of the ultrasound signals, on the other hand, is capable of reconstructing structural details smaller than the wavelength. This leads to significant improvements in resolution and has many potential applications in tissue characterization.

Some of the recent applications of ultrasound tissue characterization are reviewed in the following. Parsons *et al.* [38] employ the normalized power spectrum of backscattered signals to study the development of changes occurring in venous thrombosis. Davison *et al.* [39] delineate the effects of treatment with enzyme inhibitors on the material properties of the heart using the integrated backscatter (IB) obtained through acoustic microscopy. Stetson and Sommer [40] investigate the correlations between the backscattered signal frequency contents and both benign and malignant liver anomalies. Noritomi *et al.* [41] distinguish among the components of advanced carotid plaques based on spectral analysis of echoes. Lin *et al.* [42] detect multi-vessel coronary artery diseases and the recanalization of infract-related artery with IB, and identify viable myocardium and residual ischemia with IB and echocardiography [43]. They in [44] delineate the alterations in the cyclic changes of myocardial ultrasonic IB in patients who received angioplasty. Lee *et al.* [45] discriminate between the carotid plaques between asymptomatic and symptomatic patients according to three parameters of the backscattered signal power spectrum. Schmitz *et al.* [46] perform prostatic carcinoma detection by processing radiofrequency ultrasonic echo signals. Cespedes *et al.* [47] propose the addition of local compliance information to intravascular ultrasound to determine the composition of atheroma. Lin *et al.* [48] utilize weighted amplitude of the cyclic modulation of IB to detect jeopardized or salvageable myocardium in patients having chronic coronary artery disease. Huber *et al.* [49] evaluate the diagnostic value of computer-assisted texture analysis in the examination of solid breast masses. Kondo *et al.* [50] demonstrate the analysis of transeptal variation IB to predict the efficacy of beta-blocker treatment in dilated cardiomyopathy. Masuyama *et al.* [51] monitor the chaotic behavior of damaged myocardium in dilated cardiomyopathy patients by a time-delay embedding technique. Scheipers *et al.* [52] propose a system for prostate diagnosis based on multi-feature ultrasound tissue characterization. Kutay *et al.* [53] investigate the parameters of the power-law shot noise model for ultrasound RF echoes proposed in [54] as features for breast cancer detection.

2.2.2 Inverse Scattering Techniques

Kechribaris *et al.* [55] present a comprehensive overview of techniques for inverse scattering. Part of their discussions on the progress in this field is adopted here. Born and extended Born approximations provide a linear relationship between the measured scattered data and the scattering object material properties for the case of weak scattering. This linear relationship is a basis for the Fourier diffraction and reflection theorems (FDT and FRT) [27]. Subsequently, many spectral based inverse scattering techniques including the filtered back-propagation [56] and direct Fourier algorithms [57] have been developed in the light of FDT and FRT. Although mathematically straightforward and computationally efficient, these algorithms perform poorly for strong scattering media reconstruction [58] due to the underlying weak scattering assumption. Examples of strong scattering soft tissues are microvasculature (arterioles), collagen matrix of parenchymal tissues and fat lobes near the surface of the breast tissue.

Attempts have been made to improve the accuracy of approximation based methods using iterative optimization. The approximated scattered field integral equation is first discretized into a more solvable system of equations. Common means of producing a discrete representation of integral equation are finite difference and moment methods [59]. Each equation in the discretized representation is solved through iterative optimization with the objective of minimizing the difference between the measured and the estimated scattered fields. Borup *et al.* [60] develop a reconstruction technique based on the Gaussian-Newton iteration method. Roger [61] presents a Newton-Kantorovich (NK) method in which a Newton-type iterative optimization scheme is used to adjust an *a priori* contrast distribution. Wang and Chew propose a Born iterative method (BIM) that successively and independently solves each of the system equations [62]. They in [63] develop a distorted Born iterative method (DBIM) to improve BIM by updating the Green's function at every iteration. Numerical simulations show that DBIM is capable of faster convergence, but is less robust to noise contamination compared to BIM. Convergence and stability assessments are conducted on NK and show that it is equivalent to DBIM [64]. Liu *et al.* [65] introduce the coarse resolution initial value (CRIV) and quadriphase source (QS) methods to increase the rate of convergence of the BIM. CRIV uses BIM for a coarse grid of the object to quickly estimate the initial solution. The solution of a coarse grid is used as the initial value of the next finer grid with additional iterations until the solution of the finest grid is obtained. QS performs four reconstructions in parallel based on the fields measured from each side of the object. The four reconstruction results are averaged to obtain the final image.

It has been shown that both BIM and DBIM diverge for strongly scatter media.

Haddadin and Ebbini [66] alleviate this problem by extending DBIM in a multi-frequency sense. At low frequencies, DBIM converges to solutions that are close to the actual values, but with a poor spatial resolution. These solutions serve as the initial point at higher frequencies to improve the spatial resolution.

The formulation of inverse scattering in high frequency bands is quite different from that of the low frequency bands due to the significant change in the physics of wave propagation. Yang *et al.* [67] modify the extended Born approximation (EBA) to emphasize the material property that contributes to considerable scattered field variations in the microwave spectrum. The feasibility of the modified EBA for high frequencies is demonstrated through simulations. They in [68] incorporate the modified EBA in a wavelet based inversion algorithm [69] that is designed for low frequency cases, and apply it to a high frequency application. Their simulations results demonstrate the computational effectiveness of the algorithm.

Mast *et al.* [7] present a time-domain inverse scattering method that reconstructs the sound speed contrast of a medium directly in the time domain. They show that time-domain inverse scattering method is more efficient than multi-frequency diffraction tomography methods and is more efficient than single-frequency based methods in some cases. Results of synthetic data demonstrate that the accuracy of time-domain reconstruction method is superior to single-frequency reconstructions for objects whose size and contrast are similar to those found in medical applications. However, time-gain compensation and aberration correction [70] methods are needed to reduce error associated with medium absorption and weak scattering approximations.

2.2.3 Inverse Scattering Techniques for Ultrasound Tissue Characterization

Recent techniques of inverse scattering developed for ultrasound tissue characterization are reviewed. Santosh *et al.* [71] propose the use of iterative distorted wave Born approximation (IDWBA) method to analyze high frequency (10MHz) ultrasound reflection data to reconstruct high resolution images of human eye *in vivo*. They are able to resolve profiles of the acoustic impedance of 300um thick retina with features of 50um. Unlike retina, most tissue structures of interest including small tumors and arterial plaque deposits are of greater thickness and are obstructed by intervening tissues that have large attenuation coefficients and acoustic impedance differences. In [72], they model a fatty plaque deposit on the wall of a carotid artery under a 2.5 cm thick layer of tissue. A plane-wave Born approximation (PWBA) inverse scattering method is used instead of the IDWBA method,

which is more accurate but more cumbersome to implement, since the targeted tissue is weakly scattered. Compensation for the attenuation of the intervening tissue is also implemented.

Tobocman *et al.* [73] analyze backscattered signals from aorta specimens that are shielded from the ultrasound transducer by a human tissue specimen, which is about 1.25 cm thick. A PWBA deconvolved inverse scattering [74] method in conjunction with compensation for the distortion due to the frequency dependent attenuation of the intervening tissue are used. Visual examinations of the resultant acoustic impedance profiles show definite correlation to the specimens' pathology. Bedekar *et al.* [75] also utilize the PWBA deconvolved inverse scattering method to estimate relative acoustic impedance from the reflected pulses of some left anterior descending coronary artery specimens. Based on relative acoustic impedance values, they are able to distinguish between fibrolipidic and lipid core regions.

Yamada [76, 77] presents a technique to reconstruct quasi 3D sound velocity slices of a weak scattering spherical object based on backward propagation of Rytov approximation and a spatial filter. The measurement system collects 3D data of the object by transmitting and receiving acoustic waves over the cylindrical aperture around a single rotational axis. Simulations of a lossless medium demonstrate satisfactory results for practical condition of the sound velocity variation (+/-10%) and potential for actual clinical breast cancer screening test.

Kwon and Jeong [78] point out that many inverse scattering techniques consider simple models that describe the measured field as functions of tissue inhomogeneities in terms of only the sound speed (or refractive index) [76, 77], or density and compressibility fluctuations [79, 80, 81, 82, 83]. Kuroiwa and Yamada [84] extend the previous work [76, 77] to emphasize on the reconstruction of tissue attenuation. However, for larger values of sound velocity and attenuation contrast (i.e., strong scattering), their estimated sound velocity and attenuation images become imprecise. Yamada then in [85, 86] presents a compensation method for extending the limit of the weak scattering approximation. Kim and Yamada [87] realize that acquiring scattered fields at 360° around soft tissues such as organs in Yamada's previous work is impractical for clinical applications. They mitigate this issue by placing a reflection plate behind the tissue and modifying the inverse scattering technique accordingly. Simulated data from an elliptical object show that the precision of the reconstructed parameters is not yet satisfactory for the purposes of medical diagnostic applications.

Berggren *et al.* [88] suggest to reconstruct separate images of tissue sound speed, density and absorption through a nonlinear formulation of the inverse scattering problem in order to obtain the accuracy for quantitative clinical ultrasound

imaging. They present a method of inverting the Helmholtz equation based on moment discretizations and iterative techniques. Kwon and Jeong [78] carry out computer simulations to solve the three acoustic parameters as the solution of an inhomogeneous Helmholtz equation using the sinc basis moment method and Newton-Raphson method. They find out that tissue density is rather difficult to reconstruct compared to the other two parameters.

2.2.4 Speckle Noise Modelling and Reduction Methods

When an ultrasound impulse penetrates a medium with multiple inhomogeneities, part of the impulse energy is reflected by an inhomogeneity and the rest transmits through it creating multiple impulses with various propagation directions, phase characteristics and attenuated amplitudes. These impulses are repeatedly divided into their reflection and transmission components when they encounter other inhomogeneities. This process is known as reverberation and it continues until the energy levels of the impulses become negligible. As a result, multiple reflected impulses (i.e., echoes) from nearby inhomogeneities arrive at the transducer with small differences in phase and amplitude, which are measured as their superposition. Since many of these echoes do not uniquely correspond to the inhomogeneities, they are considered as speckle noise. Anderson and Trahey [20] describe speckle noise as random, deterministic, interference pattern in ultrasound signals formed with coherent radiations of a medium containing many sub-resolution scatterers. It has been shown that the presence of speckle noise reduces the detectability of lesions approximately by a factor of eight [89]. Therefore, speckle noise is responsible for the poor resolution of ultrasound compared to X-ray and MRI.

In the context of biological tissues, reverberation has been described as a random walk of impulses among the inhomogeneities within a mass of tissues. If each step in the random walk is considered to be an independent and identically distributed random variable, the sum over many such steps obeys a Gaussian probability distribution function (PDF) according to the Central Limit Theorem. The envelope magnitude and phase of echoes follow a Rayleigh and uniform PDFs, respectively [90, 91, 1]. At low densities of inhomogeneities, the distribution of magnitudes are changed from Rayleigh to K-distribution [92]. For tissues that have regular patterns such as liver triads, the distribution of speckle noise becomes a Rician PDF instead of a Rayleigh PDF [93, 94, 95].

Many speckle noise reduction methods have been reported in the literatures and some of these methods in recent years are reviewed in the following. Hokland and Taxt [96] develop a harmonic imaging algorithm that suppresses speckle based

on a multi-component scattering model. The backscattered signals are modeled by two orthogonal and independent harmonic oscillation functions. The estimated energies of these functions are presented as gray level values of the resulted image. Results of experiments using phantom and tissues *in vivo* indicate that this algorithm produces high signal-to-noise ratio and tissue contrast but blurrier images than conventional methods. Karaman *et al.* [97] present an adaptive smoothing method based on appropriately shaped and sized local kernels for speckle reduction in B-scan ultrasound images. A kernel is determined using a local statistics based region growing technique for each pixel. Their simulation results show that this method is capable of reducing speckle noise and preserving the resolvable details. Prager *et al.* [98] analyze speckle noise in ultrasound images using fractional order statistics and the homodyned k-distribution instead of second order powers of the homodyned k-distribution, or lower order powers of the more limited k-distribution. They conclude that the discrimination of speckle noise is more effective when the powers of distribution are greater than or equal to one.

Suhm *et al.* [99] investigate the effect of adaptive speckle noise filtering on ultrasound tissue characterization by comparing the characterization results obtained before and after filtering. Two filters are implemented; one is based on a multivariate comparator while the other is a local statistics filter. The characterization results show only slight improvements for the multivariate comparator based filter, but degradation for the local statistics filter since the signal is overly smoothened.

Tobocman *et al.* [100] conduct comparative studies between the traditional pulse-echo method and the Born approximation deconvolved inverse scattering (BADIS) technique developed in [73] for analyzing ultrasound pulse reflections from plastic phantoms and soft tissue specimens. In short, the BADIS technique deconvolves the incident pulse from the reflected pulse, and uses the resulting impulse response to reconstruct a profile of the acoustic impedance distribution of the medium. Their results demonstrate improvements in resolution of the tissue structures that can be fairly well approximated by layered media over the area of the focussed ultrasound beam. However, they report the profiles of acoustic impedance resulted from the BADIS technique are free of speckle noise without any quantitative measure between the actual and reconstructed acoustic impedance profiles. Moreover, no explicit modelling of speckle noise is found in this paper. Furthermore, they intentionally emphasize the free of speckle aspect in the paper titled "Free of speckle ultrasound images of small tissue structures".

Kharin *et al.* [101] combine the BADIS technique developed in [73] and second harmonic backscattered signals to reconstruct the acoustic impedances of plastic film phantoms relative to that of water. In [5], they apply the same technique for

in vitro porcine gastroesophageal junction. Without proofs, they state that the second harmonic of the incident pulse is generated in backscattered signals as a result of incident waveform distortion and accumulation of inhomogeneities in the medium along the propagation path. A model for analyzing the second harmonic signals is developed by including a second harmonic term in the formulation for one-dimensional pulses. In this method, an appropriate tissue attenuation coefficient must be chosen by the user. Similar to [100], they display the reconstructed images of the tissue and claim that less speckle noise is obtained only by inspections. This paper is titled "Free of speckle ultrasonic imaging of soft tissue with account of second harmonic signal". However, there is no description of the effect of speckle noise in the model. The reduction of speckle noise seems to be merely the by-product of this approach.

Saha *et al.* [102] comment on the validity of the integration range for calculating Born reflection amplitude in the BADIS formulation and make modifications to the approach presented in [5] and [100] for a wider range of applications. Numerical comparisons of approximation errors between the modified formulation and that of the previous papers for the case of an one-dimensional homogeneous layer. Results show that the errors produced by [5] and [100] can be quite large even for weak scatterers with thin layers, while the modified formulation yields negligibly small errors even for comparatively thick layers.

In contrast to being an unwanted noise, the change of speckle noise has been used as an indicator of tissue motion. Based on the tissue motion due to external forces, the mechanical properties of tissue can be reconstructed to form an elasticity image of the tissue. Elasticity imaging is proposed as an alternative diagnostic method for many pathologies including breast cancers [103]. O'Donnell *et al.* [104] introduce a method that measures tissue motion and strain fields over a wide dynamic range. Yeung *et al.* [105] develop a multilevel motion model-based approach for speckle tracking that overcomes the problem of the traditional single-level block matching methods. Lawu and Ueda [106] investigate motion artifacts produced by a rotating tissue using a speckle tracking method. Ohashi *et al.* [107] make use of the shift and variation of the speckle noise pattern in the B-mode images to estimate tissue motion for 3D tomographic reconstruction. Carmo *et al.* [108] enhance the positioning accuracy of 3D ultrasound image plane by means of speckle decorrelation. Jeong and Kwon [109] calculate the relative tissue stiffness by determining the standard deviation and/or the range pixel values of speckle noise patterns over a certain number of consecutive B-mode images.

2.3 Summary

This chapter first reviews forward scattering of plane, spherical and focused waves in various homogenous media. Fundamentals of inverse scattering theorems and methods derived based on the Born and extended Born approximations are then discussed. Recent clinical applications and methods of inverse scattering developed for ultrasound soft tissue characterization are also presented. In addition, descriptions of speckle noise formation, its statistical properties and reduction methods are discussed. Based on this review, it can be concluded that the major drawbacks of traditional inverse scattering methods are the weak scattering assumption inherited from Born based approximation, inaccurate modelling of speckle noise, and computational efficiency. In recognition of these drawbacks, an inverse scattering approach is presented in the next chapter that eliminates the reliance on Born based approximation and models speckle noise accurately in a novel way.

Chapter 3

Methodology Overview, Preprocessing and Modeling

A method is proposed to deal with some of the challenges in the field and shortcomings of existing methods discussed in Chapters 1 and 2. The proposed method comprises a number of components, each of which performs tasks designed to solve issues in the problem of ultrasound tissue characterization. Overview of the method is depicted in Figure 3.1. The method begins with conditioning the backscattered signals by filtering noise outside of the transducer frequency range. The design specifications and characteristics of the noise filter are presented in Section 3.1. The backscattered signals contain echoes that carry information of tissues in their propagation paths. It is important to analyze these echoes individually to isolate information associated with different paths. Each of these echoes is detected from the signals in Section 3.2. The resulting echoes are processed by the multi-scale stochastic filter (MSF), which is specifically developed to estimate parameters that are nonlinearly related to the measurements. This is the case of ultrasound tissue characterization. MSF will be discussed in details in Section 4.2.2. The MSF formulation requires models of the measurements and measurement noise. These models are derived in Sections 4.1.1 and 4.1.3. Figure 3.1 shows a much simplified schematics of MSF to maintain clarity of the methodology overview. Some of the echoes in the backscattered signals are the results of reverberation. These echoes convey redundant information, which severely degrade the accuracy of tissue characterization. To solve this problem, a model is developed to describe the relationship between tissue acoustic parameters and propagation paths of each echo in a hierarchical structure called Echotree. Reverberated echoes can be identified based on the tissue acoustic parameters estimated by MSF and the Echotree. The rever-

berated echoes are then removed from the input of MSF. MSF and reverberation filter are executed recursively.

3.1 Noise Filter

All ultrasound signals are first bandpass filtered to remove noise frequency contents out of the transducer frequency range. The bandpass filter is designed using the Parks-McClellan optimal FIR filter algorithm [110] with the following parameters:

- Frequency band edges: 0, 5MHz, 100MHz and 110MHz,
- Stopband ripple: 0.0005V, and
- Passband ripple: 0.0005V.

It should be noted that filter frequency characteristics are commonly specified as cutoff frequencies. However, filter frequency characteristics are specified as band edges in [110]. Therefore, the same filter frequency specification conventions are used here. The resulting filter order is 732. A forward-reverse filtering technique is employed to achieve zero-phase filtering of the ultrasound signals [111]. The magnitude and phase responses are depicted in Figure 3.2.

3.2 Echo Detection

In addition to noise filtering, detection of individual echoes from backscattered signals is needed for sound speed and attenuation coefficient measurements. Echoes are detected based on their oscillation characteristics. The oscillations of echoes can be characterized by the phases and magnitudes of overshoots and undershoots. Since the largest consecutive overshoot and undershoot are convenient to be recognized, their time difference and magnitude ratio are employed as features for echo detection as illustrated in Figure 3.3. The range of these features among echoes are identified experimentally. When a consecutive overshoot-undershoot pair having features within the range is found, an echo is considered detected. The beginning and end of the echo are then identified for subsequent processing. This echo detection method is designed for tissue layers of sufficient thicknesses such that no echoes are superimposed.

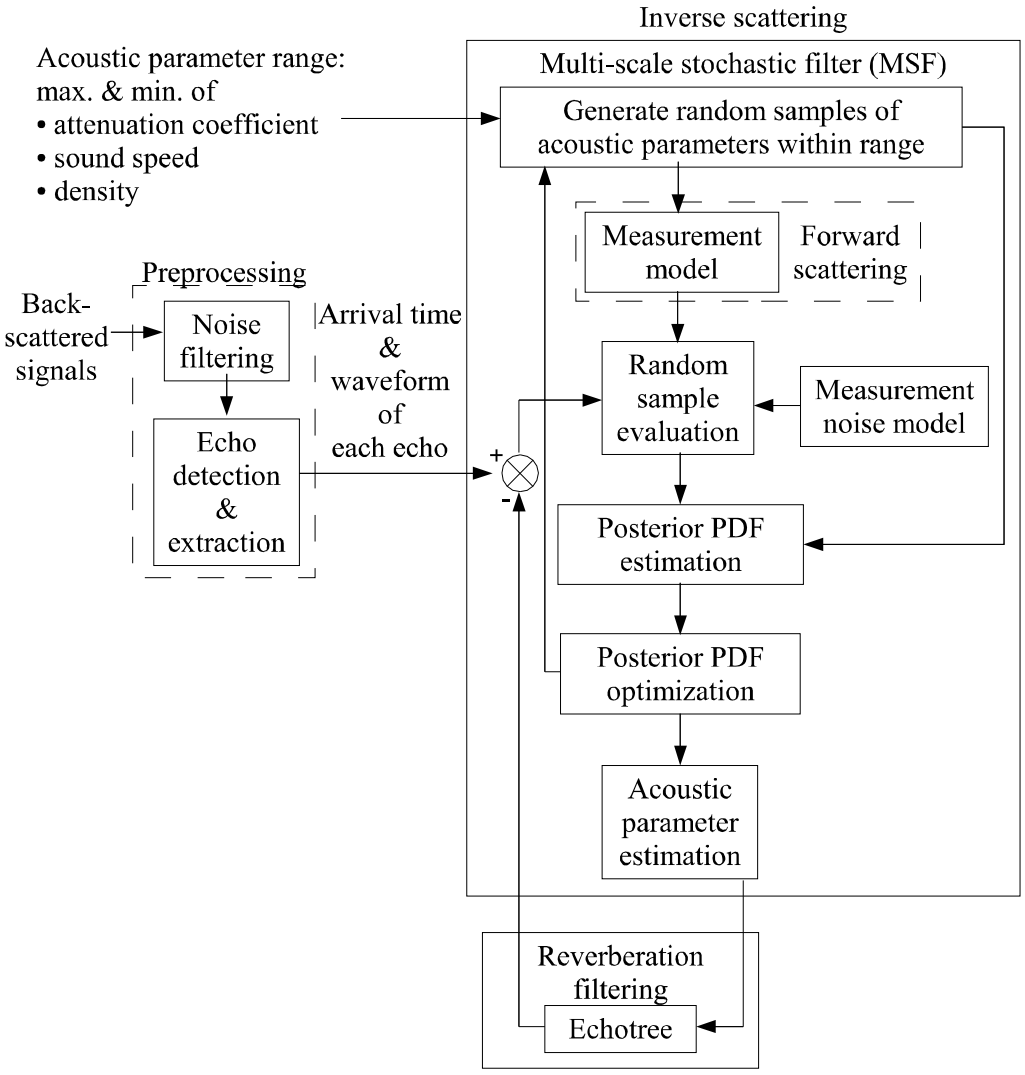

Figure 3.1: Overview of methodology

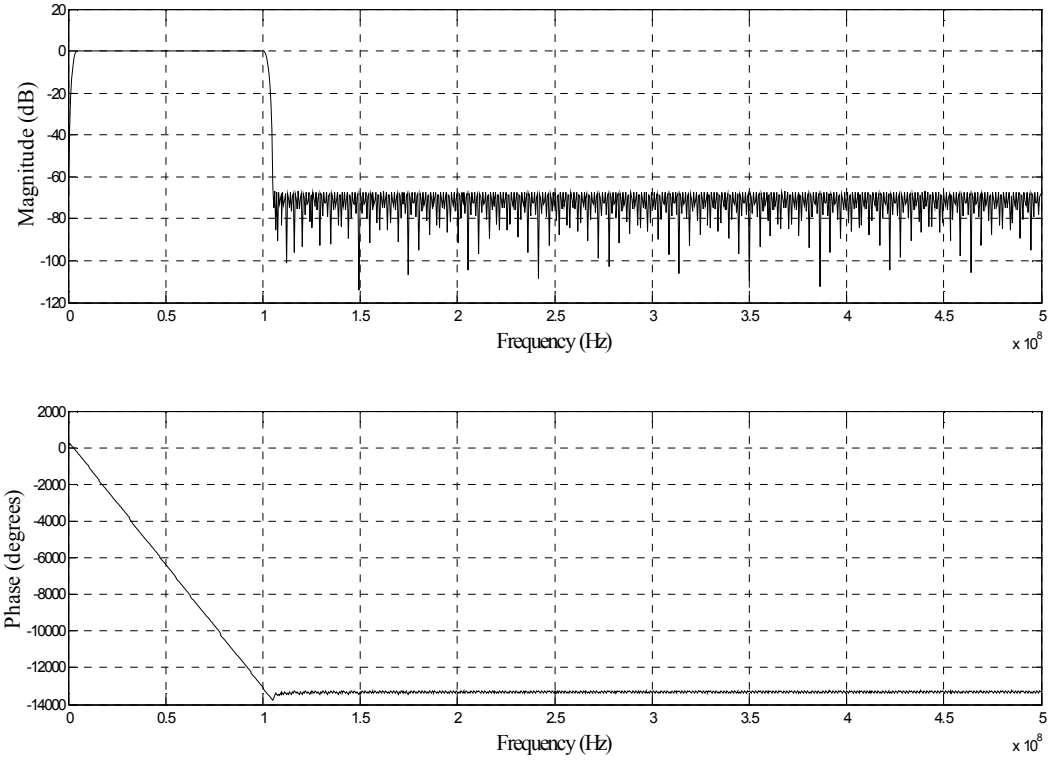

Figure 3.2: Impulse rsponse of bandpass filter

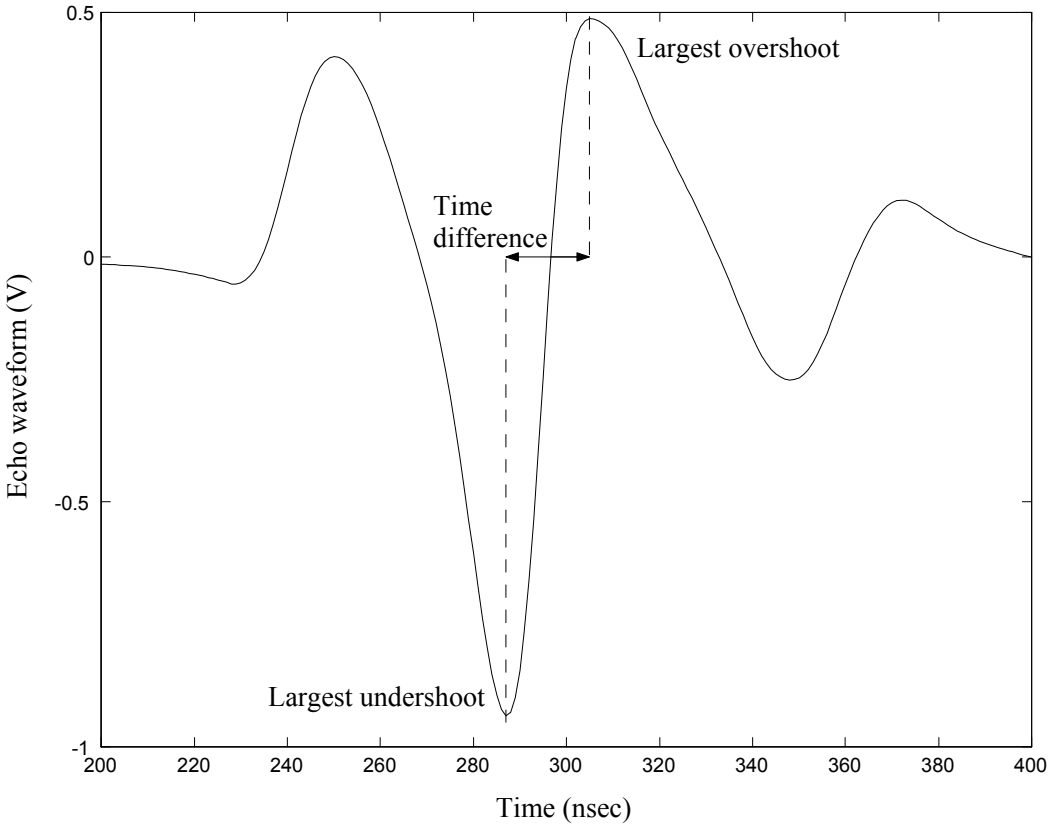

Figure 3.3: Features of echo detection

The algorithm developed for echo detection is presented as follows. Let S be a sequence of backscattered signals; $tmin$ is the minimum time period between a consecutive overshoot-undershoot pair; $rmin$ and $rmax$ are the minimum and maximum values of the ratio between the largest consecutive overshoot and undershoot; $nmax$ be the maximum absolute noise amplitude; $echot$ be the time of arrival of each detected echo in S; $echo$ be the echoes extracted in S;

function $[echot, echo] = EchoDetect\,(S, tmin, rmin, rmax, noise)$

$len = length(S)$

$dS = gradient(S)$;

$i = 1; e = 1$;

while $(i <= len - 1)$,

% Find zero-crossing point

if $(sign\,(S\,(i)) == sign\,(S\,(i+1)))$,

$i = i + 1$;

$continue$;

end

% Search for either undershoot or overshoot before i

$j = i$;

while $(j > 1\ \&\ sign\,(dS\,(j-1)) == sign\,(dS\,(j)))$,

$j = j - 1$;

end

% Search for either undershoot or overshoot after i

$k = i + 1$;

while $(k < len\ \&\ sign\,(dS\,(k)) == sign\,(dS\,(k+1)))$,

$k = k + 1$;

end

$Sj = abs\,(S(j))$

$Sk = abs\,(S(k))$

$r = max\,(Sj, Sk)\,/min\,(Sj, Sk)\,;$

if $(k - j > tmin\ \&\ r > rmin\ \&\ r < rmax\ \&\ Sj > nmax\ \&\ Sk > nmax)$,

% Search for the beginning of echo

$m = j - tmin$;

while $(any\,(S\,(m : j)) > nmax$ & $j > 1)$,

$j = j - 1$;

$m = j - tmin$;

if $(m < 1)$, $m = 1$; end

end

$echot\,(e) = j$;

% Search for the end of echo

$n = k + tmin$;

while $(any\,(S\,(k : n)) > nmax$ & $k < len)$,

$k = k + 1$;

$n = k + tmin$;

if $(n > len)$, $n = len$; end

end

% Extract echo from S to $echo$

$echo\,(e, 1 : k - j + 1) = S\,(j : k)\,;$

$e = e + 1$;

% Remove echo from S

$S\,(j : k) = 0$;

end

$i = k$;

end

3.3 Reverberation Modeling

An inherent characteristic of backscattered ultrasound measurements of multi-layered media is the presence of reverberated echoes. Since reverberated echoes do not uniquely correspond to the media structures, these echoes must be filtered

to improve the accuracy of media characterization. In order to realize reverberated echo filtering, a model of these echoes is needed.

Modeling of reverberated echoes from multi-layered media has been developed in [112, 113]. However, this model has no provision for predicting the number of echoes and the arrival time of each echo, which are important for reverberation filtering. In this research, a reverberated echo modeling approach is proposed to enable the prediction of the number of echoes and echo arrival time. In this approach, a data structure is designed to represent the reverberation path and acoustic parameters involved in the path for each echo.

The acoustic property of each tissue layer is assumed to be homogeneous and isotropic characterized by three parameters, $\alpha_{x,y,z}$, $\rho_{x,y,z}$ and $c_{x,y,z}$. To alleviate demonstration, only the first three tissue layers in the Z axis are considered. The interface between neighboring layers signifies the acoustic interface mismatch (AIM) between them as shown in Figure 3.4.

The pattern of reverberation closely resembles an unbalanced binary tree shown in Figure 3.5. Each node of this tree represents an AIM and has at most two descendents, left and right. The left and right descendents correspond to two AIMs that are closer to and further away from the transducer than the parent as shown in Figure 3.4. For example, the left and right descendents of AIM 2 are always AIM 1 and AIM 3, respectively. AIM 2 is located in between AIM 1 and AIM 3. The number of leaf nodes (i.e., nodes with zero AIM in tree levels greater than one) equals the total number of echoes received by the transducer. These nodes are labeled as E_i for echo number i. Each branch contains information that governs how the wave propagates from a parent to a descendent and the wave characteristics. A label R or T is assigned to each branch to indicate whether the propagation direction (PD) is reflection or transmission from the parent to the descendent, respectively. In addition, each branch is associated with the acoustic property parameters of the tissue layer between the parent and descendent AIMs. For example, the branch connecting between AIM 2 and AIM 3 is associated with $\alpha_{x,y,2}$, $c_{x,y,2}$ and $\rho_{x,y,2}$. These parameters are not shown in Figure 3.5 to maintain clarity. The entire history of wave propagation, reverberated echoes and acoustic parameters of the tissues can be captured in this tree, which is referred to as EchoTree.

The minimum levels in EchoTree required to capture at least one echo from the last AIM (i.e., the AIM furthest away from the transducer) is two times the number of AIM plus one. Figure 3.5 demonstrates an example of four AIMs. In this example, nine levels indexing from zero to eight are needed to describe an echo reflected from the last AIM (i.e., AIM 4). Before E_9 is received by the transducer, it penetrates AIM 0 to 3 twice (in both forward and backward directions) and is

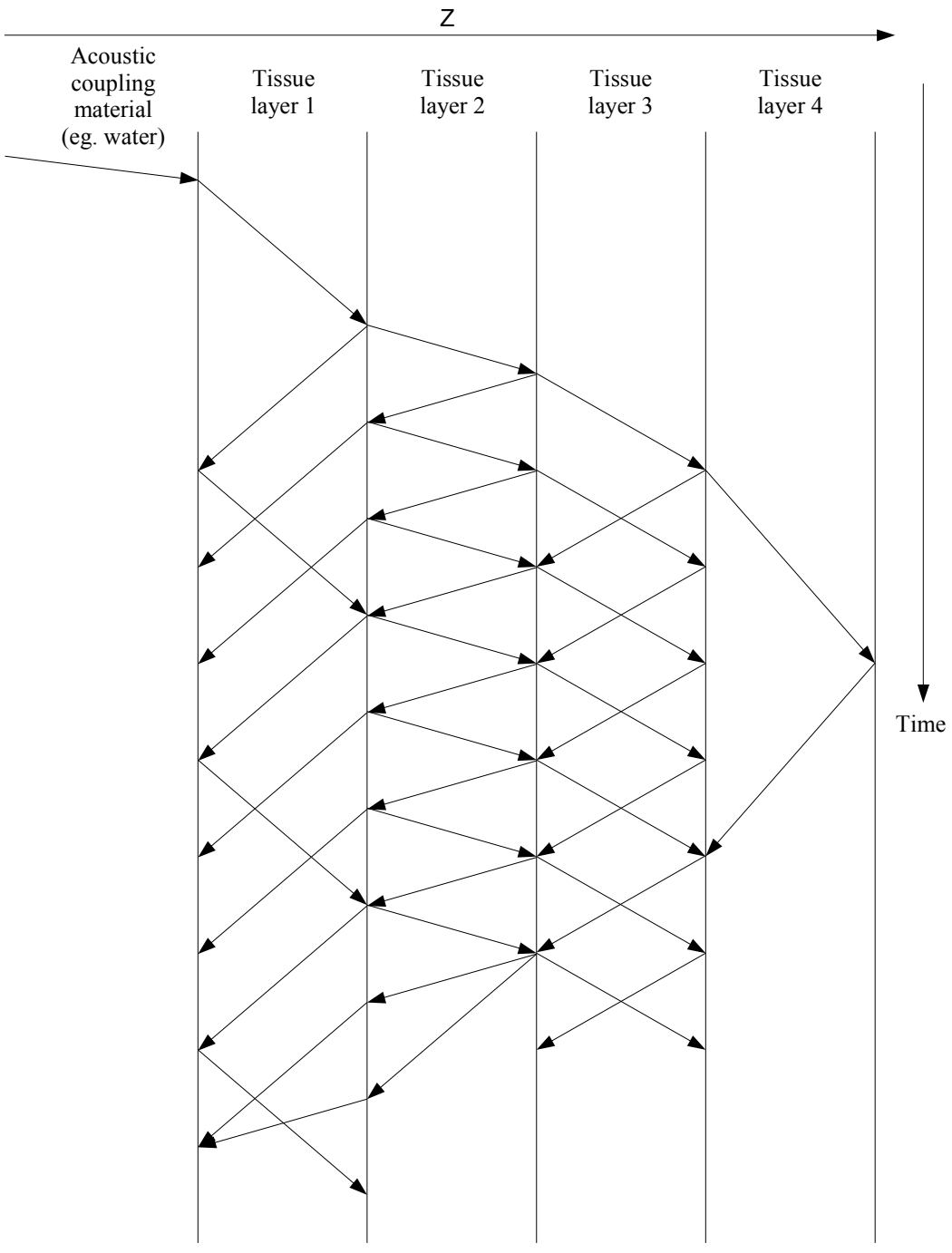

Figure 3.4: Illustration of wave reverberation

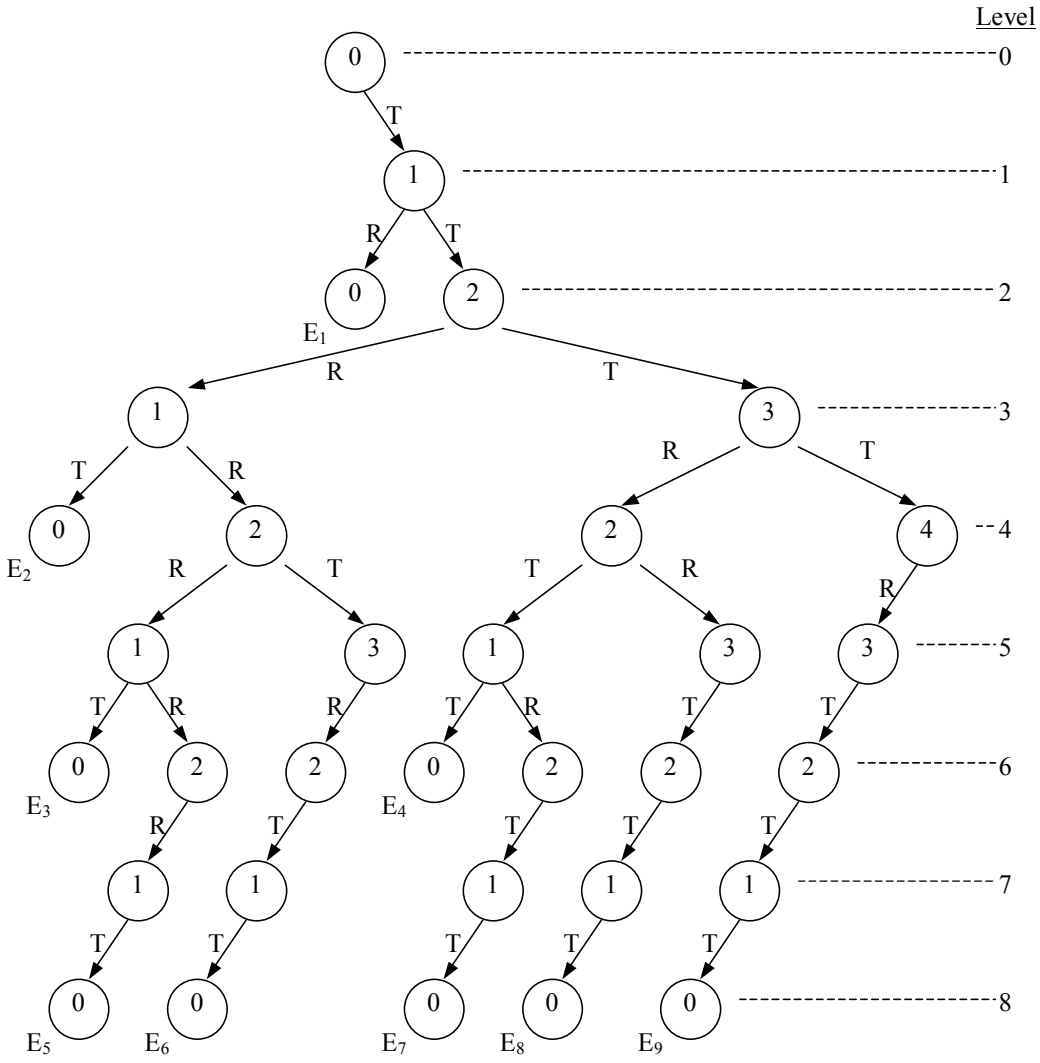

Figure 3.5: Illustration of an Echotree with four acoustic impedance mismatches

Echo	Echo reverberation path & direction								
1	AIM	0	1	0					
	PD	T	R						
2	AIM	0	1	2	1	0			
	PD	T	T	R	T				
3	AIM	0	1	2	1	2	1	0	
	PD	T	T	R	R	R	T		
4	AIM	0	1	2	3	2	1	0	
	PD	T	T	T	R	T	T		
5	AIM	0	1	2	1	2	1	2	1	0
	PD	T	T	R	R	R	R	R	T	
6	AIM	0	1	2	1	2	3	2	1	0
	PD	T	T	R	R	T	R	T	T	
7	AIM	0	1	2	3	2	1	2	1	0
	PD	T	T	T	R	T	R	T	T	
8	AIM	0	1	2	3	2	3	2	1	0
	PD	T	T	T	R	R	T	T	T	
9	AIM	0	1	2	3	4	3	2	1	0
	PD	T	T	T	T	R	T	T	T	

Table 3.1: List of echo reverberation paths and directions in a discretized tissue with four acoustic impedance mismatches

reflected from AIM 4. Therefore, in total nine AIMs are involved in the propagation path. The complete echo reverberation paths and propagation directions can be extracted from EchoTree and is listed in Table 3.1.

A measurement model of backscattered signals that takes reverberation into account can now be derived according to the structure of EchoTree. A backscattered signal comprises a certain number of completely or partially superimposed reverberated echoes. When more than one echo arrive at the transducer at the same time, they are completely superimposed. On the other hand, partial superimposition of echoes occur if one (or more) echo reaches the transducer before the previous echo waveforms thoroughly subside. The number of echoes in a backscattered signal depends on the number of AIMs. As the quantity of AIMs (or tissue layers) considered increases, the number of potential scatterers also increases. Consequently, more echoes are created in the measurement model. An algorithm is implemented to build EchoTrees of various number of AIMs. Experiments on the relationship between the number of echoes in a backscattered signal and that of AIMs are conducted. Figure 3.6 shows the number of these echoes is an exponential function of

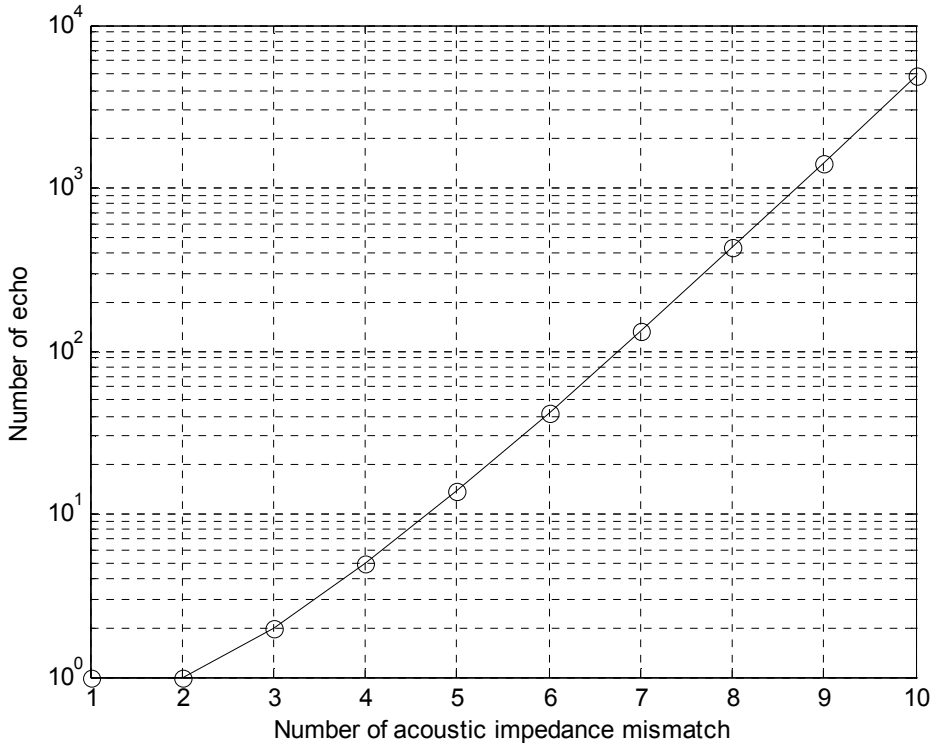

Figure 3.6: Relationship between number of echoes in a backscattered signal and number of acuostic impedance mismatches

the number of AIMs. Notice that the number of echoes grows rapidly to 4862 even with only ten AIMs. Enormous amounts of computational power and resources are required to process and store information of such a large scale of echoes. In practice, the energy of waves attenuates very quickly since the reflection coefficients among soft tissues are likely to be small except for lung tissues because of air sacs. Therefore, it is reasonable to only consider the echoes with a few reflections in their reverberation paths. The number of echoes with three or less reflections in their propagation history as function of AIM size is plotted in Figure 3.7. In this case, the number of echoes grows in a much slower rate compared to that in Figure 3.6, and the computation requirements can be greatly reduced. This model will be adopted hereafter in this research.

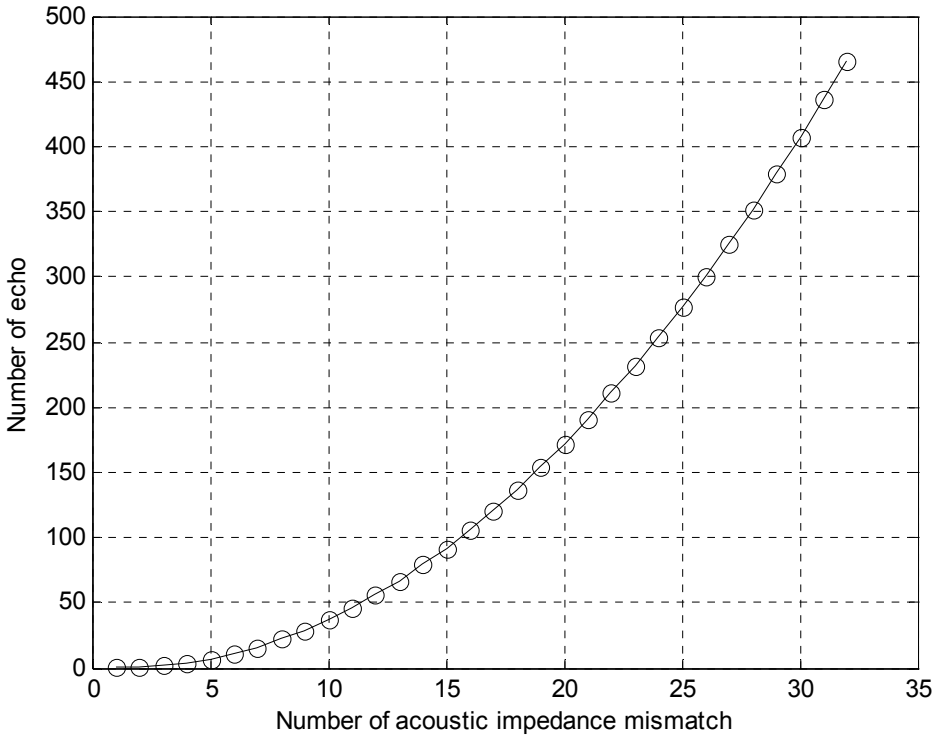

Figure 3.7: Relationship between number of echoes with three or less reflections in a backscattered signal and number of acuostic impedance mismatches

3.4 Reverberation Filtering

Reverberation filtering commences after the second echo, since the first two echoes are not reverberated echoes as shown in Section 3.3. MSF estimates the tissue acoustic parameters of the first two tissue layers estimated based on the first two echoes. The resulting parameters are embedded to the corresponding branches of the Echotree, such that the arrival times and waveforms of all reverberated echoes due to the first two tissue layers can be modeled. These arrival times and waveforms compared to that of the echoes detected in Section 3.2. If the difference between the arrival time (and waveform) of a detected echo and that of any modeled counterparts within the user defined tolerances, the echo is discarded from the MSF input. The operations of reverberation filtering are repeated upon the completion of the acoustic parameter estimation for every subsequent tissue layer by MSF.

3.5 Summary

The overview of method developed for tissue characterization provides a map of the components involved and their relationships. The method is organized as three major parts: preprocessing, MSF and reverberation filtering. Preprocessing deals with bandpass filtering the backscattered signal to noise outside of the ultrasound transducer's frequency range. In addition to noise filtering, individual echoes in the backscattered signals are detected as inputs of MSF. It is a statistics based nonlinear filter that estimates tissue acoustic parameters based on the echo inputs and models of the measurement, measurement noise, acoustic parameter transition and transition noise. The MSF acoustic parameter estimates of each tissue layer is used to model subsequent reverberation echoes in conjunction with the Echotree. Filtering of reverberated echoes is achieved by removing the MSF input echoes that match the modeled echoes. MSF and reverberation filtering are interconnected processes that are executed recursively. Details of preprocessing, derivations of models and reverberation filtering are reported in this chapter. The formulation and operations of MSF will be presented in the next chapter.

Chapter 4

Forward and Inverse Scattering

Forward and inverse scattering are dual processes in the context of ultrasound tissue characterization. Forward scattering is a task of computing wave pressures in tissues of known acoustic parameters. The estimation of the tissue acoustic parameters based on the wave pressures is known as inverse scattering. The proposed forward and inverse scattering methods are presented in this chapter.

4.1 Forward Scattering

This research employs focused ultrasound to characterize multi-layered soft tissues. The forward scattering of focused waves in the tissues is modeled in this section.

4.1.1 Focused Transducer and Multi-layered Tissue

A wide-band spherically focused ultrasound transducer is employed to illuminate multi-layered soft tissues and to measure backscattered signals from the tissues as shown in Figure 4.1. Since the dimensions of cells are small relative to the ultrasound wave lengths used in this research, each tissue layer is modeled as a homogenous, isotropic medium. Soft tissues support the propagations of both longitudinal[1] and shear[2] waves. However, shear waves attenuate quickly in soft tissue like media, such that they are insignificant for the purpose of ultrasound [26, 21]. Therefore, only longitudinal waves are considered. The transducer sensing surface

[1]Longitudinal (also known as compressional) waves propagate parallel to the Z-axis

[2]Shear (also known as transverse) waves propagate perpendicular to the Z-axis

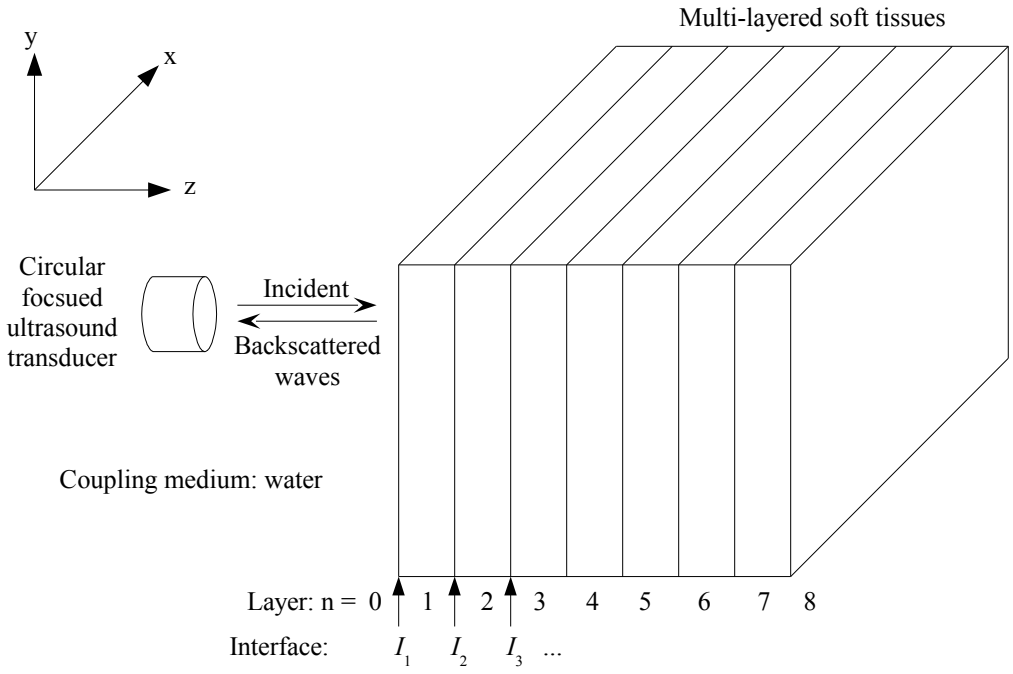

Figure 4.1: Configuration of ultrasound characterization of a multi-layered medium

and all tissue layer interfaces are normal to the Z axis. Ultrasound waves propagate through the layers and reflect at the interfaces back to the transducer along the Z axis. The X-Y dimensions of each layer is larger than the ultrasound beam width, so that the tissue layers are considered as unbounded media.

4.1.2 Modeling of Focused Waves in Multi-layered Soft Tissues

The forward problem is viewed in this research work as modelling of the wave beam produced by the spherically focused transducer and the wave pressures reflected at the interfaces of tissue layers. The model describing focused waves propagation in a homogeneous soft tissue is derived in Section 2.1.1. This model is extended to accommodate the reflections and transmissions of focused waves at the interfaces of the tissue layers in this section.

Methods of computing reflection and transmission coefficients for focused waves in multi-layered soft tissues have been proposed, for instance, in [114] and [115].

However, as discussed in Section 2.1.1, it is well known that computing these coefficients for plane waves in planar layered media is the most efficient. The establishment of focused wave pressure amplitude on the X-Y plane in Equation 2.57 lends itself to model the focused waves as amplitude modulated plane waves. The computations of reflection and transmission coefficients for plane waves in multi-layered soft tissues are presented in the following.

The wave propagation paths are described by the Echotree in Section 3.3. When the wave propagates from a parent node (i.e., AIM) to one of its two descendants, the wave pressure amplitude is attenuated and is scaled by either a reflection or a transmission coefficient associated with the Echotree branch. For instance, the overall reflection-transmission coefficient of the first echo shown in Figure 3.4 can be modeled as follows:

$$S_1 = T_{t\to 0}\, R_{0\leftarrow 1}\, T_{0\to t} \tag{4.1}$$

where

- $T_{t\to 0}$ and $T_{0\to t}$ are the transmission coefficients from the ultrasound transducer to the coupling material and vice versa: $T_{t\to 0}$ and $T_{0\to t}$ are close to 1,
- $R_{0\leftarrow 1}$ is the reflection coefficient from layer 1 to the coupling material: $R_{0\leftarrow 1} = (Z_1 - Z_0) / (Z_1 + Z_0)$,
- Z_0 and Z_1 are the acoustic impedances of layers 0 and 1, respectively: $Z_0 = c_0\rho_0$ and $Z_1 = c_1\rho_1$,
- c_0 and c_1 are the sound speeds of the coupling material and layer 1, respectively,
- ρ_0 and ρ_1 are the densities of the coupling material and layer 1, respectively,

It follows that the overall reflection-transmission coefficient of the second echo in Figure 3.4 can be modeled as,

$$S_2 = T_{t\to 0}\, T_{0\to 1}\, R_{1\leftarrow 2}\, T_{1\to 0}\, T_{0\to t} \tag{4.2}$$

where

- $T_{0\to 1}$ and $T_{1\to 0}$ are the transmission coefficients from the coupling material to layer 1 and vice versa: $T_{0\to 1} = 2Z_1/ (Z_1 + Z_0)$, $T_{1\to 0} = 2Z_0/ (Z_1 + Z_0)$,
- $R_{1\leftarrow 2}$ is the reflection coefficient from layer 2 back to layer 1: $R_{1\leftarrow 2} = (Z_2 - Z_1) / (Z_2 + Z_1)$,

- Z_2 is the acoustic impedance of layer 2: $Z_2 = c_2\rho_2$,
- c_2 and ρ_2 are the sound speed and density of layer 2, respectively.

Once the overall coefficients of the first two layers are estimated, all reverberated echoes due to these layers (eg. the third and fourth echoes) can be filtered by searching the Echotree as described in Section 3.4. Reverberated echoes due to subsequent layers can also be filtered in a similar way. Therefore, models of reverberated echoes are unnecessary. The third non-reverberated echo can be modelled as,

$$S_3 = T_{t\to 0}\, T_{0\to 1}\, T_{1\to 2}\, R_{2\leftarrow 3}\, T_{2\to 1}\, T_{1\to 0}\, T_{0\to t} \tag{4.3}$$

where

- $T_{1\to 2}$ and $T_{2\to 1}$ are the transmission coefficients from layers 1 to 2 and vice versa: $T_{1\to 2} = 2Z_2/\left(Z_2 + Z_1\right)$, $T_{2\to 1} = 2Z_1/\left(Z_1 + Z_2\right)$,
- $R_{2\leftarrow 3}$ is the reflection coefficient from layer 3 back to layer 2: $R_{2\leftarrow 3} = \left(Z_3 - Z_2\right)/\left(Z_3 + Z_2\right)$,
- Z_3 is the acoustic impedance of layer 3: $Z_3 = c_3\rho_3$,
- c_3 and ρ_3 are the phase velocity and mass density of layer 3, respectively.

Equations 4.1 to 4.3 show that the overall reflection-transmission coefficients of non-reverberated echoes follow certain patterns and can be generalized as,

$$\begin{aligned} S_{n+1} &= \prod_{j=1}^{n} \left(T_{j-1\to j}\, T_{j\to j-1}\right)\, R_{n\leftarrow n+1} \\ &= \prod_{j=1}^{n} \left(\frac{2Z_j}{Z_j + Z_{j-1}} \frac{2Z_{j-1}}{Z_{j-1} + Z_j}\right) \frac{Z_{n+1} - Z_n}{Z_{n+1} + Z_n} \end{aligned} \tag{4.4}$$

where n is the index of layer at which an wave is reflected.

The overall reflection-transmission coefficient is expressed in terms of acoustic impedances rather than the products of sound speeds and densities. This is because non-unique combinations of sound speeds and densities can produce the same acoustic impedance. If a feasible combination is found to yield a pressure amplitude that is very closed to the measurement, it may be far away from the

true combination. Therefore, it is more desirable to perform estimation in terms of acoustic impedance. In addition to reflections and transmissions, focused wave pressure amplitudes are affected by the attenuation and diffraction in each layer of the multi-layered tissues. Computing the attenuations and diffractions of focused waves in multi-layer tissues is a challenge, since the angles of diffraction change as the waves propagate through layers at various sound speeds. This also has an impact on attenuation as the diffraction angle is related to the wave traveling distance within a layer. However, Equation 2.57 only describes attenuation and diffraction of focused wave in a homogeneous soft tissue.

A method is proposed based on Equation 2.57 to compute the attenuation and diffraction of focused waves in a multi-layered tissue. This method divides the propagation path of each echo into segments, and computes the attenuation and diffraction of focused waves in each segment individually. The resulting waves in these segments are combined to obtain the waves in the entire propagation path. For instance, the second echo propagates from the transducer through layers 0 and 1, and is reflected at the layer 1-2 interface back to the transducer through layers 1 and 0 as shown in Figure 4.2. The propagation path of this echo is divided into four segments. The first and fourth segments of the path have opposite directions and are located in layer 0. The second and third path segments reside in layer 1 with opposite directions. The attenuation and diffraction of focused waves in each of these path segments are computed as:

1.
$$\left|\Psi^f_{p1}\right| = \left|\Psi^f_0\left(d_0\right)\right| \tag{4.5}$$

where $\left|\Psi^f_{p1}\right|$ is the focused wave amplitude at the end of the first path segment; the subscript 0 of $\left|\Psi^f_0\left(\cdot\right)\right|$ denotes that the acoustic parameters of layer 0 are used in this equation, the subscript is explicitly shown here, but is implicit in Equation 2.57; d_0 is the thickness of layer 0, $d_0 = t_0 c_0/2$; t_0 is the arrival time of the first echo.

2.
$$\left|\Psi^f_{p2}\right| = \frac{\left|\Psi^f_1\left(d_0 + d_1\right)\right|}{\left|\Psi^f_1\left(d_0\right)\right|} \tag{4.6}$$

where $\left|\Psi^f_{p2}\right|$ is the focused wave amplitude at the end of the second path segment; the subscript 1 of $\left|\Psi^f_1\left(\cdot\right)\right|$ denotes that the acoustic parameters of

layer 1 are used in this equation, the subscript is explicitly shown here, but is implicit in Equation 2.57; d_1 is the thickness of layer 1, $d_1 = (t_1 - t_0)\, c_1/2$; t_1 is the arrival time of the second echo.

3.
$$\left|\Psi^f_{p3}\right| = \frac{\left|\Psi^f_1\left(d_0 + 2d_1\right)\right|}{\left|\Psi^f_1\left(d_0 + d_1\right)\right|} \tag{4.7}$$

where $\left|\Psi^f_{p3}\right|$ is the focused wave amplitude at the end of the third path segment.

4.
$$\left|\Psi^f_{p4}\right| = \frac{\left|\Psi^f_0\left(2d_0 + 2d_1\right)\right|}{\left|\Psi^f_0\left(d_0 + 2d_1\right)\right|} \tag{4.8}$$

where $\left|\Psi^f_{p4}\right|$ is the focused wave amplitude at the end of the fourth path segment.

It should be noted that $\left|\Psi^f_{p2}\right|$, $\left|\Psi^f_{p3}\right|$ and $\left|\Psi^f_{p4}\right|$ are calculated as ratios of the focused wave amplitudes. These ratios represent the reduction of focused wave amplitudes in the respective path segments. In addition, path segments three and four are reflection paths. These segments are treated as transmission paths with appropriate distances from the transducer, since the reduction of focused wave amplitudes for reflection and transmission paths are equivalent. The wave pressure amplitude of the second echo can be computed based on the path segment results as,

$$\left|\Psi^f_{e2}\right| = \prod_{j=1}^{2}\left(T_{j-1\rightarrow j}\, T_{j\rightarrow j-1}\right)\, R_{2\leftarrow 2+1} \prod_{j=1}^{4}\left|\Psi^f_{pj}\right| \tag{4.9}$$

It follows that the wave pressure amplitude of the n^{th} non-reverberated echo can be generalized as,

$$\left|\Psi^f_{en}\right| = \prod_{j=1}^{n}\left(T_{j-1\rightarrow j}\, T_{j\rightarrow j-1}\right)\, R_{n\leftarrow n+1} \prod_{j=1}^{2n}\left|\Psi^f_{pj}\right| \tag{4.10}$$

The acoustical vibrations of echoes are transformed into electronic signals. The measurement of electronic signals are linearly proportional to the pressure ampli-

tudes. Also, the inevitable measurement noise is assumed additive. The measurement model of echo pressure amplitude is defined as,

$$a_n \propto \left|\Psi_{en}^f\right| + \eta \tag{4.11}$$

where η is the measurement noise, the model of η is described in Section 4.1.3. It should be noted that $\left|\Psi_{en}^f\right|$ and η are frequency dependent.

4.1.3 Measurement Noise Modelling

The measurement noise model describes the statistical characteristics of the signals measured without tissue samples. As the measurement model is frequency specific, the noise model becomes the statistical model of the noise frequency content. This model is assumed to be a Gaussian mixture,

$$\eta \sim \sum_{j=1}^{n_\eta} w_j^\eta \; N\left(\eta; \mu_j^\eta, v_j^\eta\right) \tag{4.12}$$

where n_η is the number of Gaussian component; w_j^η is the weight of each Gaussian component, $w_j^\eta > 0$ and $\sum_j^{n_\eta} w_j^\eta = 1$; $N\left(\eta; \mu_j^\eta, v_j^\eta\right)$ is a Gaussian distribution with mean, μ_j^η, and variance, v_j^η.

The parameters of the Gaussian mixture are estimated using the expectation maximization algorithm [116]. Determining the optimal number of Gaussian components for modelling is out of the scope of this research. The experiment conducted to acquire signals for measurement noise modeling and the resulting Gaussian mixture parameters are reported in Section 6.4.3.

4.2 Inverse Scattering

Inverse scattering aims to estimate the tissue acoustic parameters based on the forward scattering model and ultrasound measurements of the tissues. The forward scattering model is nonlinear with respect to the tissue acoustic parameters and stochastic. The task of estimating parameters in a nonlinear stochastic model based on measurements related to the parameters is known as nonlinear stochastic filtering (NSF). The goal of NSF is to obtain parameter estimates that minimizes the estimation errors and uncertainties. NSF can be formulated into estimating a posterior PDF of the parameters that minimizes the estimation errors and error

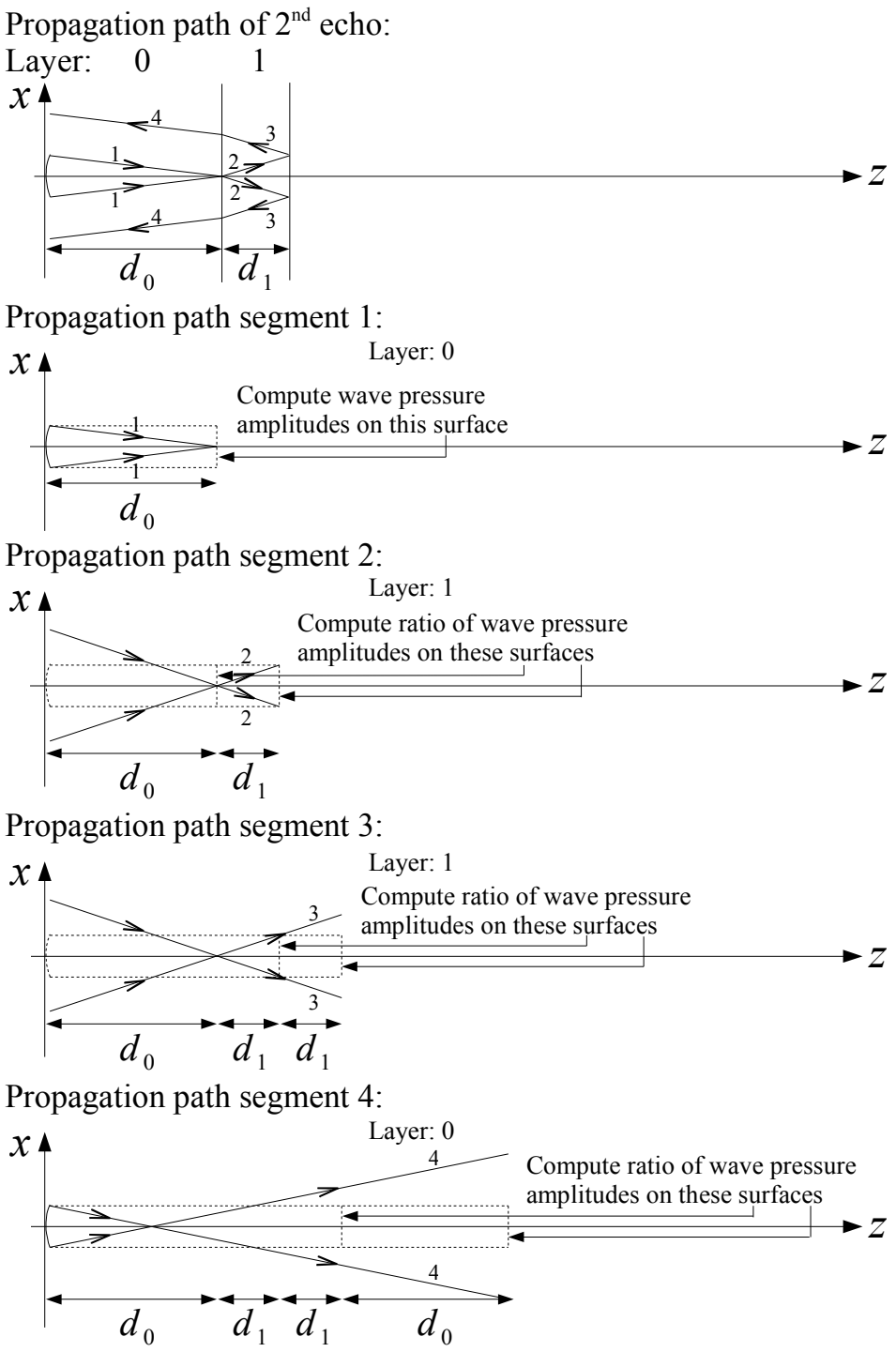

Figure 4.2: Forward scattering of focused waves in multi-layered medium

covariance. Bayesian based approaches can be applied to solve NSF problems since the Bayes' theorem provides a framework for incorporating new measurements to update the posterior probability density function (PDF). However, the posterior PDF, generally speaking, cannot be analytically determined in the Bayesian formulation. Since the mid-1960's a great deal of work in the field of NSF has been devoted to realizing the estimation schemes of the posterior PDF. These schemes include: Gaussian sum filters, grid-based methods, extended Kalman filter (EKF), unscented Kalman filter (UKF) and particle filter (PF) [117]. EKF and UKF have been embedded in the formulation of PF to create unscented particle filter (UPF) [118], Gaussian particle filter (GPF) [119, 120] and Gaussian sum particle filter (GSPF) [121]. Although optimal density functions have been derived for some special cases [122, 123, 124], devising methods for obtaining optimal posterior PDFs that minimize estimation error covariance in general remains an open problem. Hence, developing a filter that constructs such optimal posterior PDF for the general case, and for tissue acoustic parameter estimation as a special case, constitutes a significant focus of this thesis.

In the proposed filter formulation, the scale-space theory for signals [125] is adopted as a framework for representing a posterior PDF in multiple scale levels. In the context of PDF, a scale describes the spread of the function or covariance of the random variables. In Section 4.2.1, a framework of multi-scale PDF analysis is developed with the goal to decompose a PDF from fine to coarse scales and to reconstruct the PDF from coarse to fine scales. The framework employs multi-scale PDF reconstruction to optimize posterior PDF, and is referred to as the Multi-scale Stochastic Filter (MSF). The formulations of MSF and the optimization of posterior PDF are presented in Section 4.2.2.

4.2.1 Multi-scale Probability Density Function analysis

Let p_s be a PDF of x, such that

$$\int_{-\infty}^{+\infty} p_s(x)\ dx = 1 \tag{4.13}$$

$$p_s(x) \geqslant 0 \tag{4.14}$$

where the subscript s denotes the scale level of the PDF, which will be discussed in detail later.

In this thesis, a nontraditional view of PDF is adopted. Mathematically speaking, a PDF conveys probabilistic information on a random variable in the domain

of the random variable analogous to the way a physical model conveys characteristics of the physical quantity commonly in the form of electrical signals in time, space and/or frequency domains. This analogy leads to the interpretation of p_s as a signal subject to the constraints in Equations 4.13 and 4.14 in the domain of x. Therefore, it is logical and conceivable to treat and analyze p_s using signal processing techniques.

Low-pass filtering of p_s can be defined as,

$$\int_{-\infty}^{+\infty} l_s(\tau)\ p_s(x-\tau)\ d\tau = p_{s+1}(x) \tag{4.15}$$

where l_s is a low-pass kernel; p_{s+1} is the low frequency component of p_s obtained as a response of l_s. For the purpose of PDF frequency analysis, the desired properties of p_{s+1} are defined next. These properties serve as the bases for designing l_s.

Properties of PDF Low Frequency Components

The desired properties of p_{s+1} are defined as follows:

1. PDF characteristics inheritance: p_{s+1} inherits the PDF characteristics of p_s,

$$\int_{-\infty}^{+\infty} p_{s+1}(x)\ dx = 1 \tag{4.16}$$

$$p_{s+1}(x) \geqslant 0 \tag{4.17}$$

   where p_{s+1} is also a PDF.

2. Zero phase shift: p_{s+1} is defined to be a linear phase response of p_s. It preserves the integrity of the probabilistic information of x,

$$\theta_{s+1}(f) = \theta_s(f) \tag{4.18}$$

   where f is the spatial frequency of x; $\theta_{s+1}(f)$ and $\theta_s(f)$ are the phase angles of the Fourier transforms of p_{s+1} and p_s, at f, respectively.

3. Strict smoothing[3] of probabilistic information: p_{s+1} is delineated as the strictly smoothed representation of p_s. The significant of strict smoothing is that all features of p_{s+1} originate from and correspond to that of p_s. In other words,

[3]Strict smoothing refers to suppression of sharp features such as, peaks and valleys, (i.e. high frequency components) without generating such features in the smoothing process.

this property also preserves the integrity of probability information. Let p'_s and p'_{s+1} respectively be the 1^{st} derivatives of p_s and p_{s+1} with respect to x. Assuming p'_s and p'_{s+1} exist, strict smoothing implies that both p'_s and p'_{s+1} must be zero at all peaks and valleys of p_s,

$$p_s^{'}(x) = p_{s+1}^{'}(x) = 0, \ \forall x \in \{x_{peak}\} \cup \{x_{valley}\} \tag{4.19}$$

Design of PDF Low-pass Kernel

The design of a low-pass kernel, l_s, is organized into two steps: 1) deriving the constraints imposed on l_s based on the properties of p_{s+1}, and 2) identifying and selecting the kernel generating functions that satisfy the derived constraints.

PDF Low-pass Kernel Constraints The constraints imposed on l_s are derived as follows:

1. To obtain the property in Equation 4.16, l_s must satisfy:

$$\int_{-\infty}^{+\infty} l_s(\tau) \ d\tau = 1 \tag{4.20}$$

2. To obtain the property in Equation 4.17, l_s must satisfy:

$$l_s(x) \geqslant 0 \tag{4.21}$$

3. To obtain the property in Equation 4.18, l_s must satisfy:

$$l_s(x) = l_s(-x) \tag{4.22}$$

4. To obtain the property in Equation 4.19, l_s must satisfy:

$$l'_s(x) = \begin{cases} \geq 0, & x < 0 \\ = 0, & x = 0 \\ \leq 0, & x > 0 \end{cases} \tag{4.23}$$

Constraints on l_s in Equations 4.20, 4.21 and 4.22 imply that l_s must be increasing from $-\infty$ to 0 and decreasing from 0 to $+\infty$. Derivations of the PDF low-pass kernel constraints are presented in Appendix 7.1.

Identification and selection of low-pass kernel generating function The constraints in Equations 4.20, 4.21, 4.22 and 4.23 infer l_s to be,

1. a PDF,
2. symmetric about $x = 0$,
3. first order differentiable,
4. a unimodal function that has the maximum at $x = 0$, and
5. asymptotically and monotonically decreasing to 0 as x approaches $+\infty$ and $-\infty$ from 0.

Some candidate functions that satisfy the constraints and characteristics above are identified below. Let β be an appropriate coefficient,

- Exponential[4]: $\beta \exp\left(-x^2\right)$
- Hyperbolic[4]: $\beta\, sech^2\left(\pi x\right),\ \beta\, sech^2\left(\pi x\right),\ \beta x\, cosech\left(\pi x\right)$
- Inverse trigonometric[4]: $\beta\, arctan\left(1/2\pi^2 x^2\right)$
- Reciprocal[4]: $\beta\, /1 + x^2$
- Student's t distribution: $\frac{\Gamma\left(\frac{\iota+1}{2}\right)}{\Gamma\left(\frac{\iota}{2}\right)\sqrt{\pi\iota}\left(1+\frac{x^2}{\iota}\right)^{\frac{\iota+1}{2}}}$, where $\iota \in \mathbb{R}^1_{\geq 0}$ is a constant; $\Gamma\left(n\right) = (n-1)!$ is a gamma function.
- Zero-mean Gaussian PDF: $\frac{1}{\sqrt{2\pi\sigma^2}} \exp\left(-\frac{x^2}{2\sigma^2}\right)$, where $\sigma \in \mathbb{R}^1_{\geq 0}$ is the standard deviation of x.
- Zero-mean generalized Gaussian PDF: $\frac{\Gamma(3/\gamma)^{1/2}}{\sigma(2/\gamma)\Gamma(1/\gamma)^{3/2}} \exp\left(-\left(\frac{\Gamma(3/\gamma)}{\Gamma(1/\gamma)}\right)^{\gamma/2} \left\|\frac{x}{\sigma}\right\|^{\gamma}\right)$, where γ is a positive constant.

Although these functions are valid candidates for the low-pass kernel in theory, however, some of them are more advantageous in practice. The desirable practical criteria are such that l_s should be:

[4]Sketches of these functions are displayed in [126]

- computationally tractable,
- readily expandable to multi-dimensions,
- a continuous function to facilitate analytical analysis for continuous PDFs,
- expedient for Fourier transform (i.e., l_s has known closed-form solution for Fourier transform), and
- facilitating closed-form solutions for filtering arbitrary PDFs, which can be represented by Gaussian mixture models (GMMs).

Among the candidate functions, the zero-mean Gaussian (ZMG) PDF meets all the desirable practical criteria. Therefore, ZMG PDF is selected as the low-pass kernel generating function,

$$\begin{aligned} l_s(x) &= N\left(x; 0, v_s^{lp}\right) \\ &= \frac{1}{(2\pi)^{d_x/2}\left|v_s^{lp}\right|^{1/2}} \exp\left(-\frac{1}{2}x^T {v_s^{lp}}^{-1} x\right) \end{aligned} \tag{4.24}$$

where v_s^{lp} is the covariance matrix that determines the width of l_s (i.e., the frequency characteristics of l_s); superscripts T and -1 are transpose and matrix inversion, respectively; $|\cdot|$ denotes matrix determinant.

Multi-scale Decomposition and Reconstruction of PDF

The properties of the low frequency PDF component defined in Section 4.2.1 lead to the formulation of ZMG PDF as the low-pass kernel generating function. Coincidently, ZMG PDF is also derived as the low-pass kernel based on different properties in a multi-scale representation of signals known as scale-space. In 1983, Witkin first proposed the scale-space representation for 1D signals [125]. This representation has been extended for discrete 2D signals (or images) by Koenderink [127]. Since then it has been extensively used in the areas of computer vision and image processing.

According to Lindeberg, the utmost important feature of scale-space is the non-creation of new structure, which stipulates that the disappearance of fine-scale features must be monotonic as the scale increases [128]. This feature corresponds to the strict smoothing property defined in Section 4.2.1. Non-creation of a new structure is formulated based on the characteristics of zero-crossings in the second

order derivative of the signal with increasing scale [129, 130, 131], and based on a structure of low-pass kernel called semi-group [132, 133]. In the proposed multi-scale PDF analysis formulation, the strict smoothing property is formalized as the relationship between the first order derivative of the original PDF and its low frequency component shown in Equation 4.19. Other properties inherited from the scale-space theory are described in [128].

The multi-scale decomposition of PDF in the sense of scale-space is presented here. To facilitate a generic analysis, p_s is represented by a GMM,

$$\begin{aligned} p_s(x) &= \sum_{j=1}^{n_x} w_{s,j}\ p_{s,j}(x) \qquad (4.25)\\ &= \sum_{j=1}^{n_x} w_{s,j}\ N\left(x;\mu_{s,j}^x, v_{s,j}^x\right)\\ &= \sum_{j=1}^{n_x} w_{s,j} \frac{\exp\left(-\frac{1}{2}\left(x-\mu_{s,j}^x\right)^T\ {v_{s,j}^x}^{-1}\left(x-\mu_{s,j}^x\right)\right)}{(2\pi)^{d_x/2}\left|v_{s,j}^x\right|^{1/2}} \end{aligned}$$

where n_x is the number of Gaussian PDFs used to represent p_s; $w_{s,j}$ is the weight of the j^{th} component of p_s, $\sum_{j=1}^{n_x} w_{s,j} = 1$; $p_{s,j}$ denotes a Gaussian component of p_s; $\mu_{s,j}$ and $v_{s,j}$ are the mean and covariance matrix of the j^{th} Gaussian component of p_s, respectively.

A set of n_x low-pass filters is defined as,

$$\begin{aligned} &\{l_{s,1}(x)\ ,\ \cdots\ ,\ l_{s,n_x}(x)\} \qquad (4.26)\\ =\ &\left\{N\left(x;0,v_{s,1}^{lp}\right)\ ,\ \cdots\ ,\ N\left(x;0,v_{s,n_x}^{lp}\right)\right\} \qquad (4.27) \end{aligned}$$

A coarser scale of p_s is defined as the decomposition of each Gaussian component of p_s using a respective low-pass filter,

$$\begin{aligned} p_{s+1}(x) &= \sum_{j=1}^{n_x} w_{s,j}\ l_{s,j}(x) \circledast p_{s,j}(x) \qquad (4.28)\\ &= \sum_{j=1}^{n_x} w_{s+1,j}\ p_{s+1,j}(x)\\ &= \sum_{j=1}^{n_x} w_{s+1,j}\ N\left(x;\mu_{s+1,j}^x, v_{s+1,j}^x\right) \end{aligned}$$

where $\circledast$ denotes a convolution operator; $w_{s+1,j}$ is the weight of the j^{th} component of p_{s+1}, $\sum_{j=1}^{n_x} w_{s+1,j} = 1$; $p_{s+1,j}$ denotes a Gaussian component of p_{s+1}; $\mu_{s+1,j}$ and $v_{s+1,j}$ are the mean and covariance matrix of the j^{th} Gaussian component of p_{s+1}, respectively.

The closed-form solution of p_{s+1} can be derived as,

$$\begin{aligned} P_{s+1}(f) &= \sum_{j=1}^{n_x} w_{s,j}\ L_{s,j}(f)\ P_{s,j}(f) \qquad (4.29) \\ &= \sum_{j=1}^{n_x} \Big(w_{s,j}\ \exp\left(-2\pi^2\ f^T\ v_{s,j}^{lp}\ f\right) * \\ &\qquad \exp\left(-i2\pi\mu_{s,j} - 2\pi^2 f^T\ v_{s,j}^{x}\ f\right)\Big) \\ p_{s+1}(x) &= \sum_{j=1}^{n_x} w_{s,j}\ \frac{\exp\left(-\frac{1}{2}\Delta x_{s,j}^T\ \left(v_{s,j}^x + v_{s,j}^{lp}\right)^{-1}\ \Delta x_{s,j}\right)}{(2\pi)^{n_x/2}\left|v_{s,j}^x + v_{s,j}^{lp}\right|^{1/2}} \qquad (4.30) \\ &= \sum_{j=1}^{n_x} w_{s+1,j}\ N\left(x; \mu_{s+1,j}^x, v_{s+1,j}^x\right) \end{aligned}$$

where $L_{s,j}$, $P_{s,j}$ and P_{s+1} are the Fourier transforms of $l_{s,j}$, $p_{s,j}$ and p_{s+1}, respectively; $\Delta x_{s,j} = x - \mu_{s,j}^x$. Based on Equations 4.25 and 4.30, the coarse scale weight, mean and covariance are related to their counter parts in a finer scale can be derived as,

$$w_{s+1,j} = w_{s,j} \qquad (4.31)$$
$$\mu_{s+1,j}^x = \mu_{s,j}^x \qquad (4.32)$$
$$v_{s+1,j}^x = v_{s,j}^x + v_{s,j}^{lp} \qquad (4.33)$$

As mentioned above, $p_{s+1,j}$ is the low frequency component of $p_{s,j}$ and $l_{s,j}$ is the low-pass kernel at scale level s, $s \in \{0, 1, 2, \cdots, c\}$; the finest and coarsest scales are indicated by $s = 0$ and $s = c$, respectively. The coarsest scale of $p_{s,j}$ can be obtained by recursive strict smoothing,

$$\cdots \circledast\ l_{s+2,j}\ \circledast\ l_{s+1,j}\ \circledast\ l_{s,j}\ \circledast\ p_{s,j} = p_{c,j} = u \qquad (4.34)$$

where u is a uniform PDF; x is suppressed for clarity.

The intended application of tissue acoustic parameter estimation requires reconstructing a fine scale PDF from its coarse scale components. With the information

of p_{s+1} and $l_{s,1:n_x}$, p_s can be reconstructed based on Equations 4.31, 4.32 and 4.33. Figure 4.3 illustrates multi-scale PDF decompositions and reconstructions, in which single low-pass filters are depicted for simplicity. An alterative p_s reconstruction method is based on p_{s+1} and the corresponding high frequency PDF components. However, computing these components is not of interest of this research work.

Relationship Between Scale and Filter Frequency

Although scale-space operations are heavily dependent on frequency filtering, the relationship between scale and the filter's 3dB cutoff frequency is not explicitly stated in scale-space literatures. This relationship can be derived from the Fourier transform of l_s,

$$\begin{aligned} L_s &= \exp\left(-2\pi^2 \ f^T \ v_s^{lp} \ f\right) \\ 1/\sqrt{2} &= \exp\left(-2\pi^2 \ f_{3db}^T \ v_s^{lp} \ f_{3db}\right) \\ 0.0176 &= f_{3db}^T \ v_s^{lp} \ f_{3db} \end{aligned} \tag{4.35}$$

where f_{3db} is the cutoff frequency of l_s. For $d_x = 1$, it is straightforward to obtain a unique solution,

$$\begin{aligned} 0.0176 &= f_{3db}^2 \sigma_s^2 \\ f_{3db} &= \frac{0.133}{\sigma_s} \end{aligned} \tag{4.36}$$

where σ_s is the standard deviation of l_s. For $d_x > 1$, f_{3db} is a coordinate that satisfies Equation 4.35 on a contour in 2D, a surface in 3D, a volume in 4D, and so on. For 1D case, Equation 4.36 shows that the 3dB cutoff frequency is inversely proportional to scale parameter, σ_s. In other words, at each scale level the low-pass kernel standard deviation controls the frequency attenuation rate of the low-pass filter. The frequency characteristics of l_s in relation to σ_s in 1D are illustrated in Figure 4.4.

4.2.2 Multi-scale Stochastic Filtering

MSF is formulated to achieve optimal estimation of tissue acoustic parameters based on the information available. In the preprocessing stage, the waveform of each ultrasound echo is extracted from the backscattered signals. Each waveform contains multiple measurements of backscattered signals and information on the acoustic parameters of each tissue layer along the wave propagation path. The

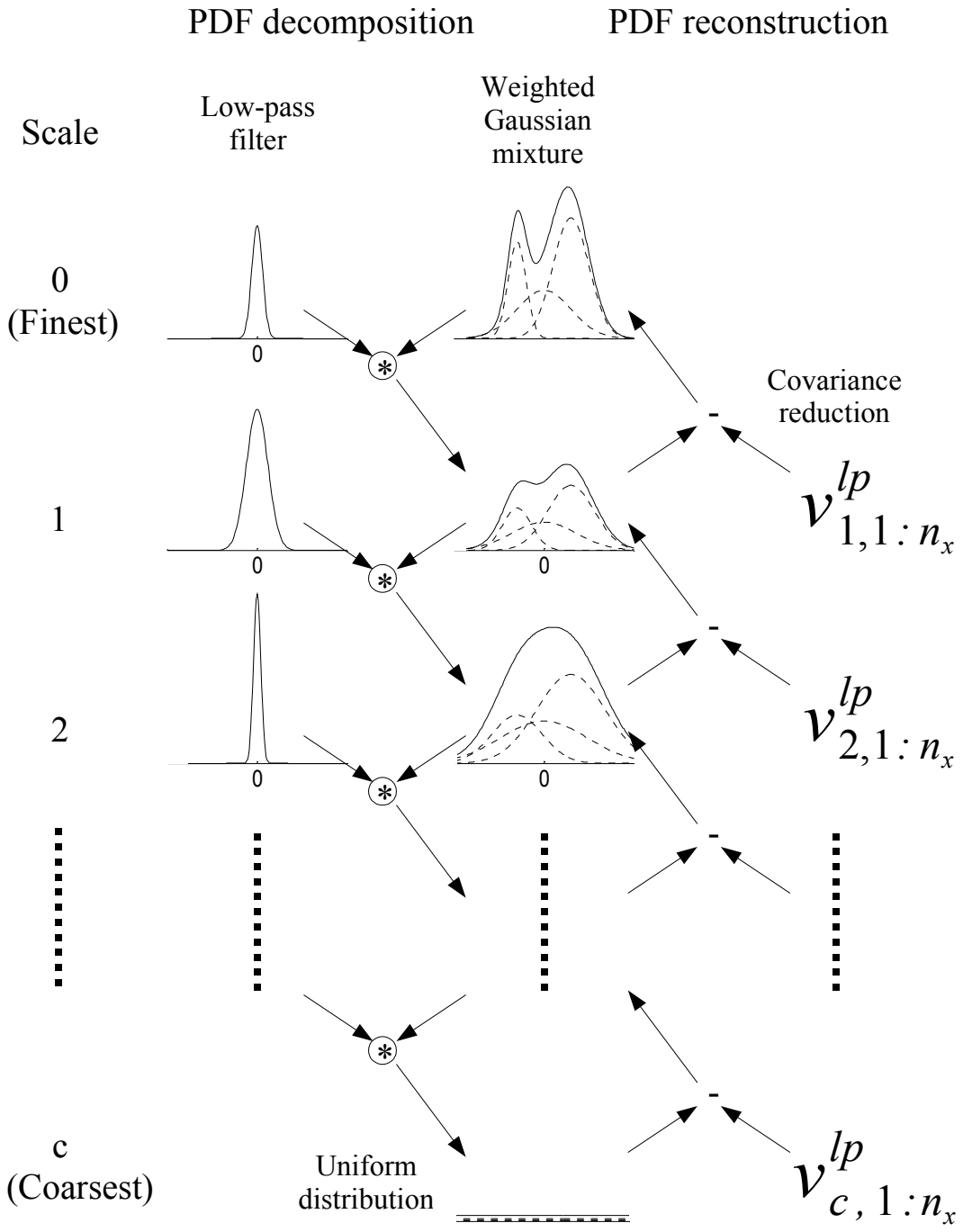

Figure 4.3: Multi-scale PDF decompositions and reconstructions.

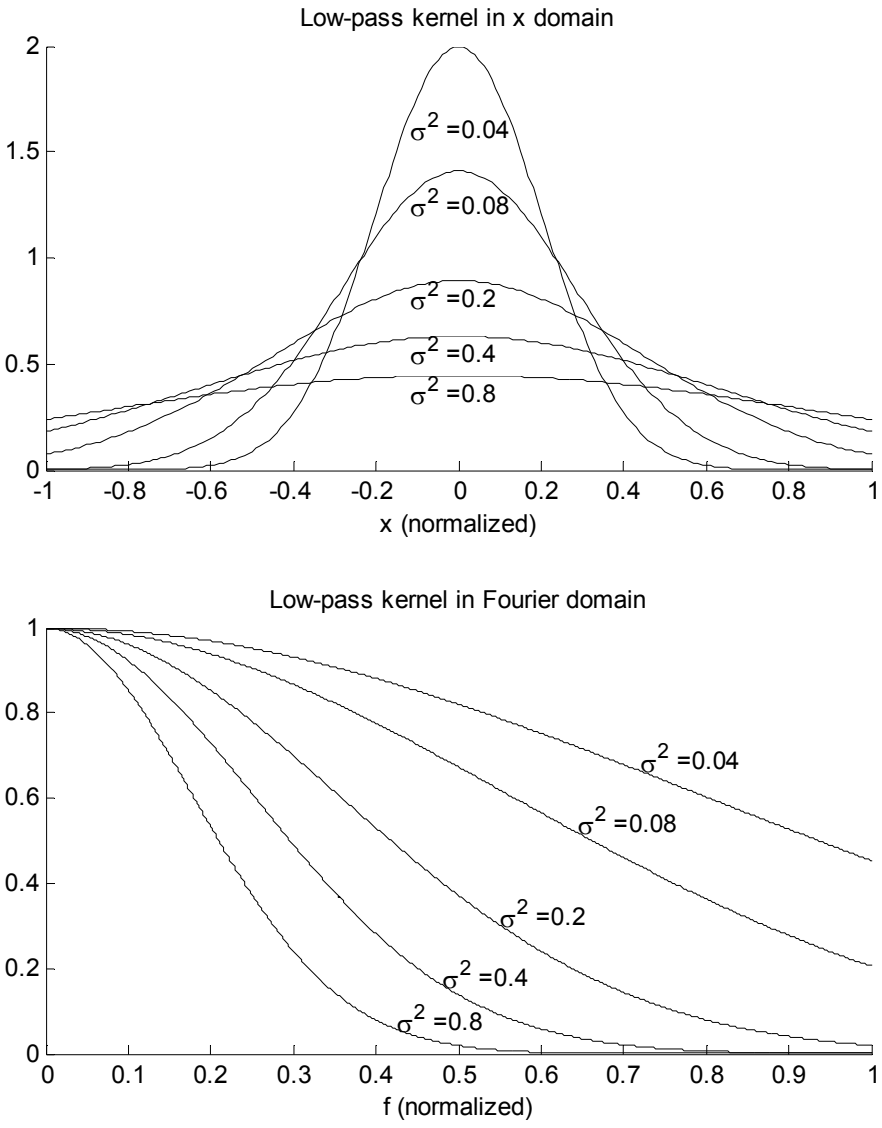

Figure 4.4: Characteristics of scale-space low-pass kernels in 1D

attenuation coefficients vary with frequencies, and as such the frequency contents of the measurements are considered. The measurement model in Equation 4.11 used in the MSF formulation is recalled below for convenience,

$$\begin{aligned} a_{n,f} &= \left|\Psi_{en}^{f}\right| + \eta_f \\ &= h\left(x_n\right) + \eta_f \end{aligned}$$

where the frequency dependencies of a_n and η are shown explicitly; $\left|\Psi_{en}^{f}\right|$ is a function of the parameters $m_{0:n-1}$, $b_{0:n-1}$,$c_{0:n}$ and $Z_{0:n}$; the only unknown parameters in $\left|\Psi_{en}^{f}\right|$ are m_{n-1}, b_{n-1}, c_n and Z_n; the rest of the parameters are either determined in the preprocessing stage or are previous estimation results; $\left|\Psi_{en}^{f}\right|$ is expressed as a function, $h\left(x_n\right)$, of x_n for notation convenience; η is the measurement noise and its statistical model is shown in Equation 4.12.

Here the acoustic parameters to be estimated are denoted as x_n to simplify notation, $x_n = \left[\begin{array}{cccc} m_{n-1} & b_{n-1} & c_n & Z_n \end{array}\right]^T$. The objective of MSF is to achieve optimal estimation of x_n in the sense of minimum mean-square error (MMSE) and minimum estimation covariance. Let $\{a_{n,_1}, \cdots, a_{n,f}\}$ be a set of echo frequency amplitudes related to tissue layer n, and the frequencies of the amplitudes are indexed from 1 to f. The set is denoted as $a_{n,1:f}$ to compact the notation, $a_{n,1:f} \triangleq \{a_{n,_1}, \cdots, a_{n,f}\}$. The MMSE estimate of x_n can be formulated as a minimization problem,

$$\min_{\widehat{x}_n} \int \left[x_n - \widehat{x}_n\right]^T \left[x_n - \widehat{x}_n\right] \; p\left(x_n | a_{n,1:f}\right) \; dx_n \tag{4.37}$$

where $\widehat{x}_n$ is the MMSE estimate of x_n; $p\left(x_n | a_{n,1:f}\right)$ is the posterior PDF of x_n. It is straightforward to derive the solution of Equation 4.37 as,

$$\widehat{x}_n = \int x_n \; p\left(x_n | a_{n,1:f}\right) \; dx_n \tag{4.38}$$

Since $p\left(x_n | a_{n,1:f}\right)$ is unknown for this application, deriving MSF is transformed into a problem of finding $p\left(x_n | a_{n,1:f}\right)$. In general, $p\left(x_n | a_{n,1:f}\right)$ can be expressed in a recursive form [134],

$$p\left(x_n | a_{n,1:f}\right) = \frac{p\left(a_{n,f} | x_n\right) \; p\left(x_n | a_{n,1:f-1}\right)}{\int p\left(a_{n,f} | x_n\right) \; p\left(x_n | a_{n,1:f-1}\right) \; dx_n} \tag{4.39}$$

where

- $p\left(x_n | a_{n,1:f}\right)$ is also represented as a GMM to substantiate a general formulation as discussed in Section 4.2.1,

$$p\left(x_n | a_{n,1:f}\right) = \sum_{j=1}^{n_x} w_{n,f,j}^{x} \; N\left(x_n; \mu_{n,f,j}^{x}, v_{n,f,j}^{x}\right) \tag{4.40}$$

where n_x is the number of Gaussian PDFs used to represent $p\left(x_n|a_{n,1:f}\right)$; $w^x_{n,f,j}$, $\mu^x_{n,f,j}$ and $v^x_{n,f,j}$ are the weight, mean and covariance matrix of the j^{th} Gaussian component of $p\left(x_n|a_{n,1:f}\right)$, respectively; $w^x_{n,f,j} > 0$, $\sum_{j=1}^{n_x} w^x_{n,f,j} = 1$.

- $p\left(a_{n,f}|x_n\right)$ is the likelihood PDF, which can be derived based on Equations 4.11 and 4.12,

$$p\left(a_{n,f}|x_n\right) = \sum_{j=1}^{n_\eta} w^\eta_{n,f,j}\ N\left(a_{n,f}; h\left(x_n\right) + \mu^\eta_{n,f,j}, v^\eta_{n,f,j}\right) \tag{4.41}$$

  where the parameters except for x_n in h are suppressed to simplify the notations.

- $p\left(x_n|a_{n,1:f-1}\right)$ is the prior PDF of x_n given the set of measurements in the frequency domain, $a_{n,1:f-1}$. Since x_n is frequency independent, it follows that $p\left(x_n|a_{n,1:f-1}\right)$ is the previous posterior PDF of x_n,

$$p\left(x_n|a_{n,1:f-1}\right) = \sum_{j=1}^{n_x} w^x_{n,f-1,j}\ N\left(x_n; \mu^x_{n,f-1,j}, v^x_{n,f-1,j}\right) \tag{4.42}$$

The prior PDF is required in order to compute the posterior PDF given the first measurement (i.e., $p\left(x_n|a_{n,1}\right)$). $p\left(x_n|a_{n,1}\right)$ can be estimated using the following steps:

1. Generate uniformly distributed random samples of x_n within the user defined range.

2. Evaluate the samples by calculating the likelihoods of them causing $a_{n,1}$ using Equation 4.41. These likelihoods are normalized and used as sample weights.

3. $p\left(x_n|a_{n,1}\right)$, is estimated as a Gaussian mixture using the expectation maximization algorithm [116] based on the samples and their weights.

The posterior PDF is proportional to the product of $p\left(a_{n,f}|x_n\right)$ and $p\left(x_n|a_{n,1:f-1}\right)$. The analytical expression of the posterior PDF, in general, cannot be obtained due to the nonlinearity of the measurement model (i.e., $h\left(x_n\right)$) in $p\left(a_{n,f}|x_n\right)$. However, the posterior PDF can be computed numerically. Recall that $p\left(a_{n,f}|x_n\right)$ produces probability densities that reveal how likely the actual measurement to appear given the values of x_n. From another perspective, these probability densities can be interpreted as indications of how close are the estimated x_n (i.e., $h\left(x_n\right)$) and the actual

measurement. In other words, $p\left(a_{n,f}|x_n\right)$ weights x_n according to the similarity between $a_{n,f}$ and $h\left(x_n\right)$. Therefore, $p\left(x_n|a_{n,1:f}\right)$ can be computed numerically based on random samples of x_n generated by $p\left(x_n|a_{n,1:f-1}\right)$ and the normalized weights of the samples produced by $p\left(a_{n,f}|x_n\right)$. These random samples and weights are then employed to estimate the n_x component GMM as $p\left(x_n|a_{n,1:f}\right)$ using expectation maximization [116].

Although MMSE estimates can be obtained using $p\left(x_n|a_{n,1:f}\right)$, $p\left(x_n|a_{n,1:f}\right)$ is not the optimal distribution for minimizing the state estimation covariance. In recognition of this issue, a method is proposed to find the optimal distribution for minimizing estimation error covariance based on $p\left(x_n|a_{n,1:f}\right)$, posterior Cramer-Rao bound and multi-scale PDF analysis.

Optimal PDF for Minimum Estimation Covariance

Assuming the random samples drawn from $p\left(x_n|a_{n,1:f}\right)$ are independent, $\widehat{x}_n$ is an unbiased estimate and converges to the true x_n according to the law of large numbers [135],

$$E\left(x_n - \widehat{x}_n\right) = 0 \tag{4.43}$$

$$pr\left(|x_n - \widehat{x}_n| < \varepsilon\right) \geq 1 - \frac{1}{4n_s\varepsilon} \underset{n_s\to\infty}{\longrightarrow} 1 \tag{4.44}$$

where $pr\left(\cdot\right)$ denotes probability; ε is a positive constant; n_s denotes number of random samples.

For an unbiased estimate, the posterior Cramer-Rao bound (PCRB) is well known as the lower bound of the estimation covariance. Therefore, it is logical to evaluate the estimation uncertainty of MSF based on PCRB. The optimal MSF uncertainty is achieved when the difference between estimation covariance and PCRB are minimized. This can be formulated as a problem of PDF optimization as follows,

$$\min_{q\left(x_n|a_{n,1:f}\right)} tr\left(E\left\{\Delta\widehat{x}_n\ \Delta\widehat{x}_n^T\right\} - F_{n,f}^{-1}\right) \tag{4.45}$$

where $q\left(x_n|a_{n,1:f}\right)$ is the conditional PDF of x_n that minimizes the difference between the estimation covariance and the PCRB; $\Delta\widehat{x}_n = \widehat{x}_n - x_n$; $tr\left(\cdot\right)$ denotes a trace operator; F_n^{-1} is the inverse of the posterior Fisher information matrix.

The Fisher information matrix is defined as,

$$F_{n,f} = -E\left\{\nabla\ \nabla^T\ \log p\left(a_{n,f}|x_n\right)|_{x_n}\right\} \tag{4.46}$$

$$= -\int\left\{\nabla\ \nabla^T \log\ p\left(a_{n,f}|x_n\right)|_{x_n}\right\} p\left(x_n|a_{n,1:f}\right)\ dx_n \tag{4.47}$$

It should be noted that for applications whose transition model of x_n is stochastic, $F_{n,f}$ can be obtained recursively based on the work of Tichavsky in [136].

The solution of Equation 4.45 is $q\left(x_n|a_{n,1:f}\right)$ that satisfies,

$$E\left\{\left[\widehat{x}_n - x_n\right]\left[\widehat{x}_n - x_n\right]^T\right\} = F_{n,f}^{-1} \tag{4.48}$$

The unbiased estimate property in Equation 4.43 implies that $E\left(x_n\right) = \widehat{x}_n$. The expectation term in Equation 4.48 can be written as,

$$\begin{aligned} & E\left(\widehat{x}_n\widehat{x}_n^T - \widehat{x}_n x_n^T - x_n\widehat{x}_n^T + x_n x_n^T\right) \\ = \;& \widehat{x}_n\widehat{x}_n^T - \widehat{x}_n E\left(x_n^T\right) - E\left(x_n\right)\widehat{x}_n^T + E\left(x_n x_n^T\right) \\ = \;& \widehat{x}_n\widehat{x}_n^T - \widehat{x}_n\widehat{x}_n^T - \widehat{x}_n\widehat{x}_n^T + E\left(x_n x_n^T\right) \\ = \;& E\left(x_n x_n^T\right) - \widehat{x}_n\widehat{x}_n^T \end{aligned} \tag{4.49}$$

Substituting Equation 4.49 into Equation 4.48 and denoting $\widehat{x}_n$ as $\widehat{\mu}_{n,f}^q$, we have,

$$E\left\{x_n\; x_n^T\right\} - \widehat{\mu}_{n,f}^q\; \widehat{\mu}_{n,f}^{qT} = F_{n,f}^{-1} \tag{4.50}$$

The expectation in Equation 4.50 can be calculated as,

$$E\left\{x_n\; x_n^T\right\} = \int x_n\; x_n^T\; q\left(x_n|a_{n,1:f}\right)\; dx_n \tag{4.51}$$

Similar to $p\left(x_n|a_{n,1:f}\right)$, $q\left(x_n|a_{n,1:f}\right)$ is represented by a GMM for general formulation,

$$\begin{aligned} q\left(x_n|a_{n,1:f}\right) &= \sum_{j=1}^{n_x} w_{n,f,j}^q\; q_j\left(x_n|a_{n,1:f}\right) \\ &= \sum_{j=1}^{n_x} w_{n,f,j}^q\; N\left(x_n; \mu_{n,f,j}^q, v_{n,f,j}^q\right) \end{aligned} \tag{4.52}$$

where q_j is the j^{th} Gaussian component of q; $w_{n,f,j}^q$, $\mu_{n,f,j}^q$ and $v_{n,f,j}^q$ are the weight, mean and covariance matrix of q_j, respectively; $\sum_{j=1}^{n_x} w_{n,f,j}^q = 1$.

Based on Equation 4.52, Equation 4.51 can be written as,

$$\begin{aligned} E\left\{x_n\ x_n^T\right\} &= \int x_n\ x_n^T \sum_{j=1}^{n_x} w_{n,f,j}^q\ N\left(x_n; \mu_{n,f,j}^q, v_{n,f,j}^q\right)\ dx_n \\ &= \sum_{j=1}^{n_x} w_{n,f,j}^q \int x_n\ x_n^T\ N\left(x_n; \mu_{n,f,j}^q, v_{n,f,j}^q\right)\ dx_n \\ &= \sum_{j=1}^{n_x} \frac{w_{n,f,j}^q}{\sqrt{2\pi}^{d_x-1}}\ \left(v_{n,f,j}^q + \mu_{n,f,j}^q\, \mu_{n,f,j}^{qT}\right) \\ &= \sum_{j=1}^{n_x} w_{n,f,j}^q\ \left(v_{n,f,j}^q + \mu_{n,f,j}^q\, \mu_{n,f,j}^{qT}\right) \end{aligned} \tag{4.53}$$

where $1/\sqrt{2\pi}^{d_x-1}$ is a constant for all n_x Gaussian components and therefore it vanishes in the process of weight normalization.

Substituting Equation 4.53 into Equation 4.50, we have,

$$\sum_{j=1}^{n_x} w_{n,f,j}^q \left(v_{n,f,j}^q + \mu_{n,f,j}^q\ \mu_{n,f,j}^{qT}\right) - \widehat{\mu}_{n,f}^q\ \widehat{\mu}_{n,f}^{qT} = F_{n,f}^{-1} \tag{4.54}$$

Since $q\left(x_n|a_{n,1:f}\right)$ is optimized to minimize the estimation error covariance with respect to $F_{n,f}^{-1}$, which is computed based on $p\left(x_n|a_{n,1:f}\right)$. This implies the overall covariance of $q\left(x_n|a_{n,1:f}\right)$ must be less than that of $p\left(x_n|a_{n,1:f}\right)$ while retaining similar properties of $p\left(x_n|a_{n,1:f}\right)$ to preserve estimation integrity. Mathematically, it can be modelled as low-pass filtering $q\left(x_n|a_{n,1:f}\right)$ to produce $p\left(x_n|a_{n,1:f}\right)$ subject to the constraint that the difference between the covariances of $p\left(x_n|a_{n,1:f}\right)$ and that of $q\left(x_n|a_{n,1:f}\right)$ is positive definite. Realizing that the mathematical model and constraints are satisfied by the multi-scale PDF decomposition from a fine scale s to a coarser scale $s+1$ in Equation 4.28. Therefore, the framework of multi-scale PDF analysis in Section 4.2.1 is well suited for the formulation of $q\left(x_n|a_{n,1:f}\right)$ optimization,

$$l_{n,f,j}\left(x_n\right)\ \circledast\ q_j\left(x_n|a_{n,1:f}\right) = p_j\left(x_n|a_{n,1:f}\right),\ \forall\ j = \{1, \cdots, n_x\} \tag{4.55}$$

where $l_{n,f,j}$ is a PDF low-pass filter,

$$l_{n,f,j}\left(x_n\right) = N\left(x_n; 0, v_{n,f,j}^{lp}\right) \tag{4.56}$$

The weight and mean of each $q\left(x_{n,f}|a_{n,1:f}\right)$ Gaussian component are reconstructed based on the relations in Equations 4.31 and 4.32 to preserve estimation integrity,

$$\begin{aligned} w^q_{n,f,j} &= w^x_{n,f,j} && (4.57)\\ \mu^q_{n,f,j} &= \mu_{n,f,j} && (4.58) \end{aligned}$$

The expectation of x_n (i.e., $E\left(x_n\right)$) or $\widehat{\mu}^q_{n,f}$ in Equation 4.54 can be obtained as,

$$\widehat{\mu}^q_{n,f} = \sum_{j=1}^{n_x} w^q_{n,f,j}\ \mu^q_{n,f,j} \tag{4.59}$$

Rearranging Equation 4.54, we have,

$$\sum_{j=1}^{n_x} w^q_{n,f,j}\ v^q_{n,f,j} = F^{-1}_{n,f} + \widehat{\mu}^q_{n,f}\ \widehat{\mu}^{qT}_{n,f} - \sum_{j=1}^{n_x} w^q_{n,f,j}\ \mu^q_{n,f,j}\ \mu^{qT}_{n,f,j} \tag{4.60}$$

Equation 4.60 shows the solution of the weighted sum of $v^q_{n,f,j}$ instead of the individual $v^q_{n,f,j}\ \forall\ j = \{1, \cdots, n_x\}$. To ensure each $v^q_{n,f,j}$ is positive definite and is reconstructed to preserve estimation integrity, the relationship between a coarse scale covariance and its finer scale counterpart in Equation 4.33 is imposed,

$$\begin{aligned} v^x_{n,f,j} &= v^q_{n,f,j} + v^{lp}_{n,f,j}\\ v^q_{n,f,j} &= v^x_{n,f,j} - v^{lp}_{n,f,j} && (4.61) \end{aligned}$$

subject to Equation 4.60 and the positive definite constraints as follows,

$$\begin{aligned} v^{lp}_{n,f,j} &> 0 && (4.62)\\ v^x_{n,f,j} - v^{lp}_{n,f,j} &> 0 && (4.63) \end{aligned}$$

Substituting Equation 4.61 into Equation 4.60, yields

$$\begin{aligned} &\sum_{j=1}^{n_x} w^q_{n,f,j}\left(v^x_{n,f,j} - v^{lp}_{n,f,j}\right) && (4.64)\\ = \ & F^{-1}_{n,f} + \widehat{\mu}^q_{n,f}\ \widehat{\mu}^{qT}_{n,f} - \sum_{j=1}^{n_x} w^q_{n,f,j}\ \mu^q_{n,f,j}\ \mu^{qT}_{n,f,j} \end{aligned}$$

$$\sum_{j=1}^{n_x} w^q_{n,f,j} v^{lp}_{n,f,j} \tag{4.65}$$
$$= \sum_{j=1}^{n_x} w^q_{n,f,j}\ v^x_{n,f,j} - F^{-1}_{n,f} - \widehat{\mu}^q_{n,f}\ \widehat{\mu}^{qT}_{n,f} + \sum_{j=1}^{n_x} w^q_{n,f,j}\ \mu^q_{n,f,j}\ \mu^{qT}_{n,f,j}$$

Let $V_{n,f} = \sum_{j=1}^{n_x} w^q_{n,f,j}\ v^x_{n,f,j} - F^{-1}_{n,f} - \widehat{\mu}^q_{n,f}\ \widehat{\mu}^{qT}_{n,f} + \sum_{j=1}^{n_x} w^q_{n,f,j}\ \mu^q_{n,f,j}\ \mu^{qT}_{n,f,j}$ for conciseness,

$$\sum_{j=1}^{n_x} w^q_{n,f,j}\ v^{lp}_{n,f,j} = V_{n,f} \tag{4.66}$$

Expanding $V_{n,f}$ to a n_x component weighted sum,

$$\begin{aligned} \sum_{j=1}^{n_x} w^q_{n,f,j}\ v^{lp}_{n,f,j} &= \sum_{j=1}^{n_x} w^V_{n,f,j}\ V_{n,f} \\ v^{lp}_{n,f,j} &= \left(w^V_{n,f,j}/w^q_{n,f,j}\right) V_{n,f} \end{aligned} \tag{4.67}$$

where $w^V_{n,f,j}$ is a weight satisfying the constraint,

$$\sum_{j=1}^{n_x} w^V_{n,f,j} = 1 \tag{4.68}$$

In addition, $w^V_{n,f,j}$ must be positive in order to satisfy constraint in Equation 4.62,

$$w^V_{n,f,j} > 0 \tag{4.69}$$

To ensure that the constraint in Equation 4.63 is satisfied, we substitute Equation 4.67 into Equation 4.63 to determine any further constraint must be imposed on $w^V_{n,f,j}$,

$$\begin{aligned} v^x_{n,f,j} - \left(w^V_{n,f,j}/w^q_{n,f,j}\right) V_{n,f} &> 0 \\ w^q_{n,f,j}\ v^x_{n,f,j}\ V^{-1}_{n,f} &> w^V_{n,f,j} I \\ w^V_{n,f,j} I - w^q_{n,f,j}\ v^x_{n,f,j}\ V^{-1}_{n,f} &< 0 \end{aligned} \tag{4.70}$$

where I is an identity matrix.

The inequality in Equation 4.70 reveals that $w^V_{n,f,j}$ must be less than any eigen value of the positive definite matrix $w^q_{n,f,j}\ v^x_{n,f,j}\ V^{-1}_{n,f}$,

$$w^V_{n,f,j} < \lambda_{n,f,j} \tag{4.71}$$

where $\lambda_{n,f,j}$ is an eigen value of $w^q_{n,f,j}\ v^x_{n,f,j}\ V^{-1}_{n,f}$.

The task of optimizing the posterior PDF now is transformed into finding the set $\left\{w^V_{n,f,1}, \cdots, w^V_{n,f,n_x}\right\}$ that satisfies Equations 4.68, 4.69 and 4.71. A bisection search is used to obtaining $\left\{w^V_{n,f,1}, \cdots, w^V_{n,f,n_x}\right\}$ instead of the computational intensive $V^{-1}_{n,f}$ and $\lambda_{n,f,j}$.

The filtering scheme of MSF is illustrated in Figure 4.5. Analysis on the convergence of estimation covariance is presented in Section 4.2.2. Algorithms of posterior PDF optimization and the proposed MSF are presented in Sections 4.2.2 and 4.2.2, respectively.

Convergence of estimation covariance

This section demonstrates how the MSF formulation reduces the error covariance of the estimated acoustic parameters within a tissue layer. At each frequency, two filtering processes are carried out recursively, namely, correction and PDF optimization. The correction process employs the actual measurement information to obtain the posterior PDF by adjusting the prior PDF. The covariance matrix in each Gaussian component of the prior PDF is that of the previous posterior PDF. The posterior PDF is linearly proportional to the product of the likelihood and prior PDFs,

$$p\left(x_n|a_{n,1:f}\right) \propto p\left(a_{n,f}|x_n\right)\ p\left(x_n|a_{n,1:f-1}\right) \tag{4.72}$$

Both likelihood and prior PDFs in Equations 4.41 and 4.42 are represented by GMMs and are reprinted here for convenience,

$$\begin{aligned} p\left(a_{n,f}|x_n\right) &= \sum_{j=1}^{n_\eta} w^\eta_{n,f,j}\ N\left(a_{n,f}; h\left(x_n\right) + \mu^\eta_{n,f,j}, v^\eta_{n,f,j}\right) \\ p\left(x_n|a_{n,1:f-1}\right) &= \sum_{j=1}^{n_x} w^x_{n,f-1,j}\ N\left(x_n; \mu^x_{n,f-1,j}, v^x_{n,f-1,j}\right) \end{aligned}$$

The nonlinear measurement model is linearized around the previous estimate of x_n (i.e., $\widehat{x}'_n$) in order to express $p\left(a_{n,f}|x_n\right)$ in terms of x_n explicitly. Let H_n be the Jacobian of $h\left(x_n\right)$ (i.e., $\partial h/\partial x_n|_{\widehat{x}'_n}$). The linearized measurement model is,

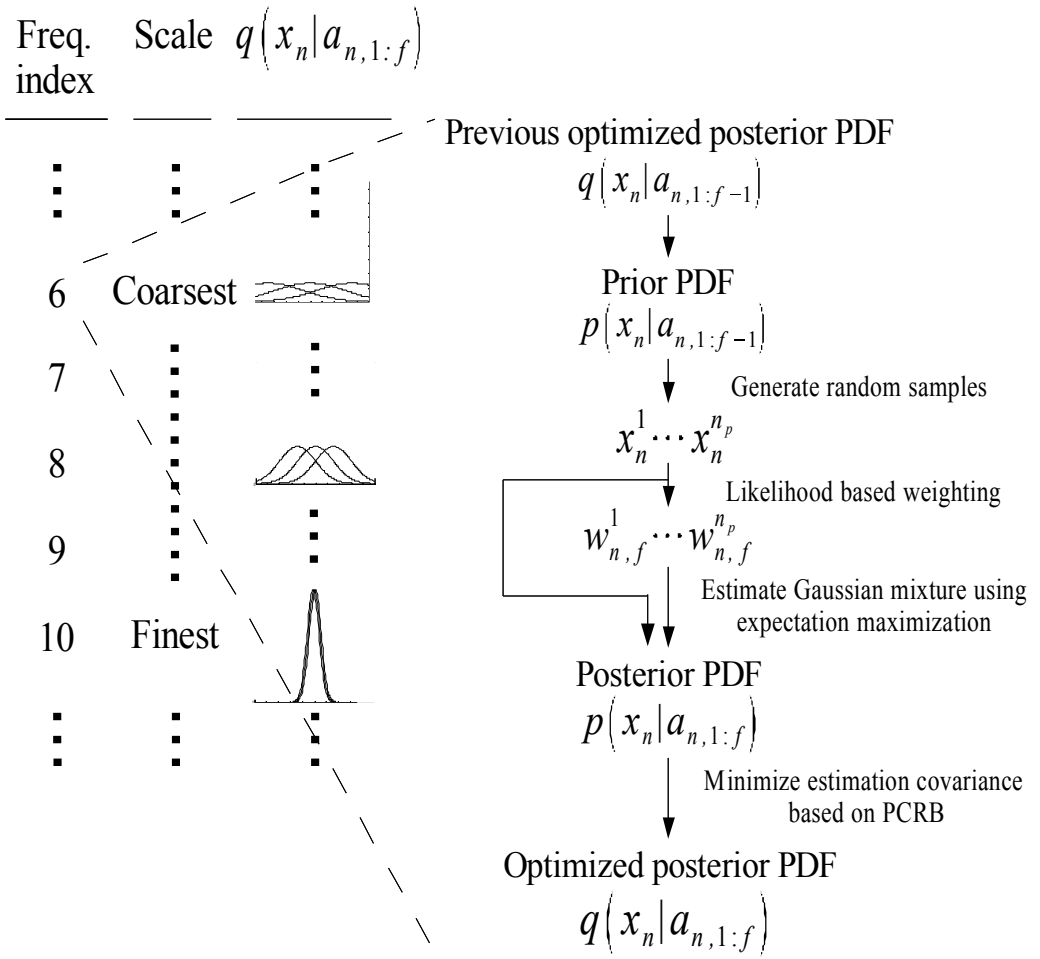

Note: the filtering processs of the tissue acoustic parameters, x_n, is conducted in the frequency domain.

Figure 4.5: Schematic of multi-scale stochastic filtering

$$\Delta a_{n,f} = H_n \; x_n + \eta_f \tag{4.73}$$

where $\Delta a_{n,f} = a_{n,f} - h\left(\widehat{x}'_n\right) + H_n \; \widehat{x}'_n$.

The likelihood PDF of the linearized measurement model can be written as,

$$p\left(\Delta a_{n,f} | x_n\right) = \sum_{j=1}^{n_\eta} w^\eta_{n,f,j} \; N\left(\Delta a_{n,f}; H_n \; x_n + \mu^\eta_{n,f,j}, v^\eta_{n,f,j}\right) \tag{4.74}$$

Substituting Equations 4.74 and 4.42 into Equation 4.72, we have,

$$\begin{aligned} p\left(x_n | a_{n,1:f}\right) \quad \propto \quad & \sum_{i=1}^{n_\eta} \sum_{j=1}^{n_x} w^\eta_{n,f,i} \; w^x_{n,f-1,j} \; N\left(\Delta a_{n,f}; H_n \; x_n + \mu^\eta_{n,f,i}, v^\eta_{n,f,i}\right) * & (4.75) \\ & N\left(x_n; \mu^x_{n,f,j-1}, v^x_{n,f-1,j}\right) & (4.76) \end{aligned}$$

The product of Gaussian PDFs in Equation 4.75 can be expressed as,

$$\begin{aligned} & \frac{\exp\left\{-\frac{1}{2}\left[\Delta a_{n,f} - H_n \; x_n - \mu^\eta_{n,f,i}\right]^T {v^\eta_{n,f,i}}^{-1} \left[\Delta a_{n,f} - H_n \; x_n - \mu^\eta_{n,f,i}\right]\right\}}{(2\pi)^{d_z/2} \left|v^\eta_{n,f,i}\right|^{1/2}} \\ * \quad & \frac{\exp\left\{-\frac{1}{2}\left[x_n - \mu^x_{n,f-1,j}\right]^T {v^x_{n,f-1,j}}^{-1} \left[x_n - \mu^x_{n,f-1,j}\right]\right\}}{(2\pi)^{d_x/2} \left|v^x_{n,f-1,j}\right|^{1/2}} \end{aligned} \tag{4.77}$$

Let $M_n = H_n \; \left(H_n^T \; H_n\right)^{-1}$. The term x_n in the first Gaussian PDF in Equation 4.77 can be separated by multiplying $M_n^T M_n$ and $\left[M_n^T \; M_n\right]^{-1}$ in its exponent term. The product in Equation 4.77 is proportional to,

$$\begin{aligned} \propto \quad & \frac{\exp\left\{-\frac{1}{2}\left[x_n - \mu^{\eta'}_{n,f,i}\right]^T \left[M_n^T \; v^\eta_{n,f,i} \; M_n\right]^{-1} \left[x_n - \mu^{\eta'}_{n,f,i}\right]\right\}}{(2\pi)^{d_x/2} \left|M_n^T \; v^\eta_{n,f,i} \; M_n\right|^{1/2}} & (4.78) \\ & * \frac{\exp\left\{-\frac{1}{2}\left[x_n - \mu^x_{n,f-1,j}\right]^T {v^x_{n,f-1,j}}^{-1} \left[x_n - \mu^x_{n,f-1,j}\right]\right\}}{(2\pi)^{d_a/2} \left|v^x_{n,f-1,j}\right|^{1/2}} \\ \propto \quad & \frac{\exp\left\{-\frac{1}{2}\left[x_n - \mu^x_{n,f,i,j}\right]^T {v^x_{n,f,i,j}}^{-1} \left[x_n - \mu^x_{n,f,i,j}\right]\right\}}{(2\pi)^{d_x/2} \left|v^x_{n,f,i,j}\right|^{1/2}} & (4.79) \end{aligned}$$

where

$$\mu^x_{n,f,i,j} = v^x_{n,f,i,j}\left\{\left[M_n^T\ v^\eta_{n,f,i}\ M_n\right]^{-1}\ \mu^{\eta'}_{n,f,i} + {v^x_{n,f-1,j}}^{-1}\ \mu^x_{n,f-1,j}\right\} \quad (4.80)$$

$$\mu^{\eta'}_{n,f,i} = M_n\ \left(\Delta a_{n,f} - \mu^\eta_{n,f,i}\right) \quad (4.81)$$

$$v^x_{n,f,i,j} = \left[v^x_{n,f-1,j} + M_n^T\ v^\eta_{n,f,i}\ M_n\right]^{-1}\ M_n^T\ v^\eta_{n,f,i}\ M_n\ v^x_{n,f-1,j} \quad (4.82)$$

Equations 4.80 and 4.81 show that the posterior PDF Gaussian mixture means $\left(\text{i.e., } \mu^x_{n,f,1\cdots n_\eta,1\cdots n_x}\right)$ are weighted sums of the measurement noise PDF Gaussian mixture means $\left(\text{i.e., } \mu^\eta_{n,f,1\cdots n_\eta}\right)$ and the previous posterior PDF Gaussian mixture means $\left(\text{i.e., } \mu^x_{n,f-1,1\cdots n_x}\right)$. When the variation of $\mu^\eta_{n,f,1\cdots n_\eta}$ is less than that of $\mu^x_{n,f-1,1\cdots n_x}$, which is true particularly at coarse scales, the variation of $\mu^x_{n,f,1\cdots n_\eta,1\cdots n_x}$ is less than that of $\mu^x_{n,f-1,1\cdots n_x}$. Therefore, the covariances of posterior PDF Gaussian mixture means do not increase as the scale becomes finer (or as more measurements are available),

$$E\left\{\Delta\mu^x_{n,f-1,j}\ \Delta\mu^{xT}_{n,f-1,j}\right\} - E\left\{\Delta\mu^x_{n,f,i,j}\ \Delta\mu^{xT}_{n,f,i,j}\right\} \geqslant 0 \quad (4.83)$$

where $\Delta\mu^x_{n,f-1,j} = \mu^x_{n,f-1,j} - E\left(\mu^x_{n,f-1,j}\right), \forall\ j$; $\Delta\mu^x_{n,f,i,j} = \mu^x_{n,f,i,j} - E\left(\mu^x_{n,f,i,j}\right), \forall\ i,j$; $\geqslant 0$ denotes positive semi-definiteness.

The covariance matrices of the posterior PDF Gaussian mixture, $v^x_{n,f,1\cdots n_\eta,1\cdots n_x}$, are products of $M_n^T\ v^\eta_{n,f,1\cdots n_\eta}\ M_n$ and $v^x_{n,f-1,1\cdots n_x}$ and the inverse of their sum. It is straight forward to realize that,

$$\begin{aligned} M_n^T\ v^\eta_{n,f,i}\ M_n - v^x_{n,f,i,j} &> 0 \\ v^x_{n,f-1,j} - v^x_{n,f,i,j} &> 0 \end{aligned} \quad (4.84)$$

where > 0 denotes positive definiteness.

This implies that the uncertainty of each posterior PDF Gaussian component is less than that of the previous posterior PDF due to the information gain from the measurement despite its own uncertainty (i.e., measurement noise).

The optimized PDF (i.e., $q\left(x_n|a_{n,1:f}\right)$) is obtained based on the inverse of the Fisher information matrix $\left(\text{i.e., } F^{-1}_{n,f}\right)$, which is a function of $p\left(x_n|a_{n,1:f}\right)$. $p\left(x_n|a_{n,1:f}\right)$ is dependent on $p\left(x_n|a_{n,1:f-1}\right)$. Thus, $p\left(x_n|a_{n,1:f}\right)$ is also dependent on $q\left(x_n|a_{n,1:f-1}\right)$. These recursive dependences are represented as,

$$q\left(x_n|a_{n,1:f}\right) \longleftarrow F^{-1}_{n,f} \longleftarrow p\left(x_n|a_{n,1:f}\right) \quad (4.85)$$

$$p\left(x_n|a_{n,1:f}\right) \longleftarrow q\left(x_n|a_{n,1:f-1}\right) \quad (4.86)$$

As the mean covariance reduces in the correction process in Equation 4.83, $p\left(x_n|a_{n,1:f}\right)$ converges to a unimodal distribution. Based on Equations 4.57, 4.58 and 4.85, $q\left(x_n|a_{n,1:f}\right)$ approaches a unimodal distribution,

$$\lim_{f\to\infty}\sum_{j=1}^{n_x} w_{n,f,j}^{q}\ \mu_{n,f,j}^{q}\ \mu_{n,f,j}^{qT} - \widehat{\mu}_{n,f}^{q}\ \widehat{\mu}_{n,f}^{qT} = 0 \tag{4.87}$$

Based on Equation 4.87, the overall covariance of $q\left(x_n|a_{n,1:f}\right)$ decreases as the number of measurement increases. It follows from Equations 4.85 and 4.86 that $F_{n,f}^{-1}$ is smaller than that of the previous frequency,

$$F_{n,f-1}^{-1} - F_{n,f}^{-1} \geq 0 \tag{4.88}$$

Substituting Equation 4.87 into Equation 4.60, we have,

$$\lim_{f\to\infty}\sum_{j=1}^{n_x} w_{n,f,j}^{q}\ v_{n,f,j}^{q} \tag{4.89}$$

$$= \lim_{f\to\infty} F_{n,f}^{-1} + \widehat{\mu}_{n,f}^{q}\ \widehat{\mu}_{n,f}^{qT} - \sum_{j=1}^{n_x} w_{n,f,j}^{q}\ \widehat{\mu}_{n,f,j}^{q}\ \widehat{\mu}_{n,f,j}^{qT}$$

$$= F_{n,f}^{-1} \tag{4.90}$$

Expand $F_{n,f}^{-1}$ to a weighted sum,

$$\begin{aligned}\lim_{f\to\infty}\sum_{j=1}^{n_x} w_{n,f,j}^{q}\ v_{n,f,j}^{q} &= \sum_{j=1}^{n_x} w_{n,f,j}^{q}\ F_{n,f}^{-1} \\ \lim_{f\to\infty} v_{n,f,j}^{q} &= F_{n,f}^{-1}\end{aligned} \tag{4.91}$$

The results derived for the convergence of estimation error covariance in Equations 4.88 and 4.91 are consistent with the reduction of covariance in the multi-scale PDF reconstruction in Equation 4.33 and in the PDF reconstruction in Equation 4.61.

PDF Optimization Algorithm

Optimization of posterior PDF is implemented by the following algorithm.

$[F_{n,f}, q\left(x_n|a_{n,1:f}\right)] = OptimizePDF\left(f, n_x, F_{n,f-1},\ p\left(x_n|a_{n,1:f}\right)\right)$

{

If $f == 1$ {

$F_{n,f} = -\int \left\{\nabla x_n \nabla x_n^T \log\ p\left(x_n|a_{n,f}\right)\right\} p\left(x_n|a_{n,f}\right)\ dx_{n,f}$ }

Else {

Compute $F_{n,f}$ using Equation 4.46}

$F_{n,f}^{-1} = inv\left(F_{n,f}\right)$

For $j = 1, \cdots, n_x$ {

$w_{n,f,j}^q = w_{n,f,j}^x$

$\mu_{n,f,j}^q = \mu_{n,f,j}$ }

$\widehat{\mu}_{n,f}^q = \sum_{j=1}^{n_x} w_{n,f,j}^q \mu_{n,f,j}^q$

$V_{n,f} = \sum_{j=1}^{n_x} w_{n,f,j}^q\, v_{n,f,j}^x - F_{n,f}^{-1} - \widehat{\mu}_{n,f}^q\, \widehat{\mu}_{n,f}^{qT} + \sum_{j=1}^{n_x} w_{n,f,j}^q\, \mu_{n,f,j}^q\, \mu_{n,f,j}^{qT}$

For $j = 1, \cdots, n_x$ {

$w_{n,f,j}^V = w_{n,f,j}^q$

$low = 0;\ high = 1$

$V_{n,f,j}^V = \left(w_{n,f,j}^V / w_{n,f,j}^q\right) V_{n,f}$ }

while $\left|v_{n,f,j}^x - V_{n,f,j}^V\right| \leq 0 \cup \min\left(diag\left(V_{n,f,j}^V\right)\right) \leq 0$ {

If $\left|v_{n,f,j}^x - V_{n,f,j}^V\right| > 0 \cup \min\left(diag\left(V_{n,f,j}^V\right)\right) > 0$ {

$low = w_{n,f,j}^V$ }

Else {

$high = w_{n,f,j}^V$ }

$w_{n,f,j}^V = 0.5(low + high)$

$V_{n,f,j}^V = \left(w_{n,f,j}^V / w_{n,f,j}^q\right) v_{n,f}^x$ }

For $j = 1, \cdots, n_x$ {

$w_{n,f,j}^V = w_{n,f,j}^V / \sum_{k=1}^{n_x} w_{n,f,k}^V$

$V_{n,f,j}^V = \left(w_{n,f,j}^V / w_{n,f,j}^q\right) V_{n,f}$

$v_{n,f,j}^q = v_{n,f,j}^x - V_{n,f,j}^V$ }

$q\left(x_n|a_{n,1:f}\right) = \sum_{j=1}^{n_x} w_{n,f,j}^q N\left(x_n; \mu_{n,f,j}^q, v_{n,f,j}^q\right)$

}

Multi-scale Stochastic Filter Algorithm

MSF is realized by the following algorithm.

$[\widehat{x}_n] = MSF\left(x_n^{\min}, x_n^{\max}, n_s, a_{n,1:n_f}, n_f, p\left(\eta_f\right)\right)$

{

For $f = 1 : n_f$

If $f == 1$ {

$x_n^{1:n_s} \sim u\left(x_n^{\min}, x_n^{\max}\right)\}$

Else {

$p\left(x_n|a_{n,1:f-1}\right) = \sum_{j=1}^{n_x} w_{n,f-1,j}^{x}\ N\left(x_n; \mu_{n,f-1,j}^{x}, v_{n,f-1,j}^{x}\right)$

$x_n^{1:n_s} \sim p\left(x_n|a_{n,1:f-1}\right)$ }

$w = 0$

For $i = 1 : n_s$ {

$w_f^i = \sum_{j=1}^{n_\eta} w_{n,f,j}^{\eta}\ N\left(a_{n,f}; h\left(x_n^i\right) + \mu_{n,f,j}^{\eta}, v_{n,f,j}^{\eta}\right)$

$w = w + w_f^i$ }

$w_f^{1:n_s} = w_f^{1:n_s}/w$

$n_f^{1:n_s} = round\left(n_s\ w_f^{1:n_s}\right)$

$indices = find\left(n_f^{1:n_s} > 0\right)$

$w_f^{indices} = w_f^{indices}/sum\left(w_f^{indices}\right)$

$n_x = length\left(indices\right)$

$p\left(x_n|a_{n,1:f}\right) = EM\_GM\left(w_f^{indices}, x_n^{indices}\right)$

$[F_{n,f}, q\left(x_n|a_{n,1:f}\right)] = OptimizePDF\left(\cdots\right)$

$\widehat{x}_n = \sum_{j=1}^{n_x} w_{n,f,j}^{q}\ \mu_{n,f,j}^{q}$

filter reverberated echoes using the method discussed in Section 3.4

$p\left(x_n|a_{n,1:f}\right) = q\left(x_n|a_{n,1:f}\right) = \sum_{j=1}^{n_x} w_{n,f,j}^{x}\ N\left(x_n; \mu_{n,f,j}^{x}, v_{n,f,j}^{x}\right)$

}

This algorithm does not assume the distribution $p\left(x_0\right)$ to be known. A set of n_s random samples are generated by a uniform distribution and are mapped in the range between the maximum and minimum of x_n (defined by the user). These samples are weighted by the likelihood function. The weighted samples are employed

to estimate a n_x component GMM as $p(x_n)$, using expectation maximization [116], which is implemented by the function EM_GM. The value of n_x is determined by the number of samples that have significant normalized weights.

It is important to note that, unlike particle filtering, the MSF algorithm does not propagate random samples along with time. Therefore, MSF eliminates the particle filtering inherent problem of degeneracy and sample impoverishment, which lead to poor estimates as only one particle contributes to the estimation.

4.2.3 Quantitative Evaluation of Multi-scale Stochastic Filter

In order to conduct a quantitative evaluation of the proposed method, MSF is compared to a state-of-the-art NSF (i.e., Gaussian sum particle filter (GSPF)) reported in [121]. There are three types of GSPF, namely, GSPF-I, GSPF-II and GSPF-III. GSPF-I is designed for systems with Gaussian noise models. GSPF-II and GSPF-III are developed for systems with Gaussian mixture noise models using different approaches. Since the noise model considered in this research is a Gaussian mixture model, as discussed in Section 4.1.3, and GSPF-II has been tested thoroughly in [121], GSPF-II is implemented to compare against MSF.

GSPF-II employes a bank of Gaussian particle filters (GPFs) to estimate the posterior PDF. Each GPF estimates one Gaussian component of the posterior PDF [119]. Each GPF requires the so-called importance density to generate random samples for estimating the parameters of a posterior PDF Gaussian component. The importance density is problem dependent and is unknown in general. A Unscented Kalman filter (UKF) is used to estimate the importance density as a Gaussian PDF by each GPF. UKF applies unscented transformation in the extended Kalman filtering framework to obtain the importance density that represents local statistics of the parameters to be estimated [137].

Since GSPF-II was applied to estimation problems in the literature other than tissue characterization, the performance of MSF is first compared to that of GSPF-II based on these applications. The performance of MSF on tissue characterization is then compared to that of GSPF-II later in Sections 6.4.5 and 6.4.6. Two estimation problems reported in [121] are bearing-only tracking and univariate nonstationary growth and frequency demodulation.

Bearings-only Tracking

Bearings-only tracking (BT), also known as target motion analysis [117], is a practical problem of particular interests in surveillance applications [138, 139, 140]. The objective of BT is to estimate the kinematics of a moving target, typically positions and velocities, based on noisy angle measurements relative to the sensor. The distance between the target and the sensor, however, is not measured. Problems of BT can be classified into two categories: non-maneuvering and maneuvering targets. The main difference between them is that the kinematic models of non-maneuvering targets remain unchanged, while the kinematics of maneuvering targets may be modelled by several regimes [141, 142]. For each of these categories, tracking algorithms using single and multiple sensors have been proposed [117]. Since a GPF based method has been applied to non-maneuvering target BT [119] with single sensor, a similar application is employed in this paper to facilitate performance comparison.

Let x_t be the relative target kinematics with respect to that of a sensor, $x_t = \begin{bmatrix} o_{x,t} & o_{y,t} & o_{s,t} \end{bmatrix}^T$, where $o_{x,t}$ and $o_{y,t}$ are the relative x and y Cartesian coordinates of the target at time t; $o_{s,t}$ is the relative speed at which the object travels in both x and y directions at time t. The relative kinematics of the target are governed by,

$$x_t = \begin{cases} A_{t-1}\ x_{t-1} + \xi_{t-1}, & \forall\ t-1 = i\ n_z \\ x_{t-1}, & \forall\ t-1 \neq i\ n_z \end{cases} \tag{4.92}$$

where A_{t-1} describes the dynamics of the parameters to be estimated; ξ_{t-1} is white noise with stationary statistics, $\xi_{t-1} \sim N\left(\xi_{t-1}; 0, \Phi_\xi\right)$; 0 is a zero vector; Φ_ξ is a covariance matrix;

$$A_{t-1} = \begin{bmatrix} 1 & 0 & 0.3\,(13-t) \\ 0 & 1 & -1 \\ 0 & 0 & 1 \end{bmatrix},\ \Phi_\xi = \begin{bmatrix} \sigma_\xi^2 & 0 & 0 \\ 0 & \sigma_\xi^2 & 0 \\ 0 & 0 & 2\sigma_\xi^2 \end{bmatrix}$$

The measurements of the sensor are modelled as,

$$z_t = \arctan\left(o_{y,t}/o_{x,t}\right) + \eta_t \tag{4.93}$$

where z_t is the measurement acquired at time t; η_t is white noise with stationary statistics, $\eta_t \sim 0.5N\left(\eta_t; 0, \sigma_\eta^2\right) + 0.5N\left(\eta_t; 0, 2\sigma_\eta^2\right)$; the values of σ_ξ and σ_η are shown in Tables 4.1, 4.2, 4.3 and 4.4.

The objective of the BT problem is to estimate x_t based on the models in Equations 4.92 and 4.93, z_t and noise statistics. This BT problem is simulated for

24 time steps, $t \in \{1, \cdots, 24\}$, with the prior PDF, $p(x_0) = n_x^{-1} \sum^{n_x} N(x_0; \mu_0, \Phi_0)$, $\mu_0 = \begin{bmatrix} 0 & 2 & 0.08 \end{bmatrix}^T$, Φ_0 is a 3×3 diagonal matrix with 0.1 as its diagonal elements. The maximum and minimum of x_t are $\begin{bmatrix} 2 & 2 & 0.09 \end{bmatrix}^T$ and $\begin{bmatrix} 0 & 0 & 0.07 \end{bmatrix}^T$.

A set of experiments are designed to test the performances of MSF and GSPF-II under various conditions:

1. numbers of Gaussian PDFs and samples used to estimate posterior PDF and states,
2. low and high noise levels,
3. known and unknown prior PDF, in case of unknown prior PDF, the prior PDF estimated by MSF is applied to GSPF-II, and
4. number of measurements available in the time period between state transitions (only applicable for MSF). The numbers of these measurements tested are one and five, which are denoted by $n_z = 1$ and $n_z = 5$, respectively.

For each of these conditions, MSF and GSPF-II are executed 50 times to obtain performance statistics. Let $\widehat{o}_{x,t,e}$, $\widehat{o}_{y,t,e}$ and $\widehat{o}_{s,t,e}$ be the estimates of $o_{x,t}$, $o_{y,t}$ and $o_{s,t}$, respectively, from either MSF or GSPF-II. The mean square error (MSE) of $\widehat{o}_{x,t,e}$, $\widehat{o}_{y,t,e}$ and $\widehat{o}_{s,t,e}$ are computed as:

$$\begin{array}{l} \widetilde{o}_x = E\left\{E\left[\left(o_{x,t} - \widehat{o}_{x,t,e}\right)^2 |t\right] |e\right\}, \\ \widetilde{o}_y = E\left\{E\left[\left(o_{y,t} - \widehat{o}_{y,t,e}\right)^2 |t\right] |e\right\}, \\ \widetilde{o}_s = E\left\{E\left[\left(o_{s,t} - \widehat{o}_{s,t,e}\right)^2 |t\right] |e\right\}, \end{array} \quad \begin{array}{l} \forall\ t \in \{1, \cdots, 24\} \\ \forall\ e \in \{1, \cdots, 50\} \end{array}$$

where $\widetilde{o}_x$, $\widetilde{o}_y$ and $\widetilde{o}_s$ are the averaged MSE of $\widehat{o}_{x,t,e}$, $\widehat{o}_{y,t,e}$ and $\widehat{o}_{s,t,e}$, respectively.

The resulting $\widetilde{o}_x$, $\widetilde{o}_y$ and $\widetilde{o}_s$ from MSF and GSPF-II under various conditions are presented in Tables 4.1, 4.2, 4.3 and 4.4. Let $\widehat{o}_{x,t}$, $\widehat{o}_{y,t}$ and $\widehat{o}_{s,t}$ be the averaged $\widehat{o}_{x,t,e}$, $\widehat{o}_{y,t,e}$ and $\widehat{o}_{s,t,e}$ with respect to e; $\delta_{x,t}$, $\delta_{y,t}$ and $\delta_{s,t}$ be the standard deviations of $\widehat{o}_{x,t,e}$, $\widehat{o}_{y,t,e}$ and $\widehat{o}_{s,t,e}$ with respect to e. The resulting $\widehat{o}_{x,t}(\pm\delta_{x,t})$, $\widehat{o}_{y,t}(\pm\delta_{y,t})$ and $\widehat{o}_{s,t}(\pm\delta_{s,t})$ from MSF and GSPF-II at $n_x = 8$ and $n_s = 100$ under various conditions are shown in Figures 4.6, 4.7, 4.8 and 4.9.

Univariate Nonstationary Growth Model

The univariate nonstationary growth model (UNGM) is a highly nonlinear function, which is of interest in many areas including econometrics, control and aerospace

$n_z = 1$		$\sigma_\xi = 0.01$, $\sigma_\eta = 0.005$					
		MSF			GSPF-II		
n_x	n_s	$\widetilde{o}_x$	$\widetilde{o}_y$	$\widetilde{o}_s$	$\widetilde{o}_x$	$\widetilde{o}_y$	$\widetilde{o}_s$
4	20	5.17e-2	1.17e-2	1.37e-5	1.13	1.45e-1	8.48e-3
	100	5.84e-3	1.17e-3	3.64e-6	1.24	1.57e-1	1.14e-2
8	20	1.97e-2	4.43e-3	1.14e-5	9.17e-1	1.12e-1	7.26e-3
	100	2.40e-3	4.59e-4	1.83e-6	1.04	1.30e-1	8.41e-3
16	20	1.14e-2	2.08e-3	1.05e-5	7.41e-1	9.08e-2	5.34e-3
	100	1.17e-3	2.24e-4	9.99e-7	8.17e-1	1.01e-1	6.43e-3

Table 4.1: BT MSE of MSF and GSPF-II with low noise intensity and known prior PDF

$n_z = 1$		$\sigma_\xi = 0.1$, $\sigma_\eta = 0.05$					
		MSF			GSPF-II		
n_x	n_s	$\widetilde{o}_x$	$\widetilde{o}_y$	$\widetilde{o}_s$	$\widetilde{o}_x$	$\widetilde{o}_y$	$\widetilde{o}_s$
4	20	6.62e-2	1.41e-2	3.96e-6	4.41	7.05e-1	5.72e-2
	100	7.34e-3	1.78e-3	8.73e-7	2.75	3.62e-1	2.89e-2
8	20	3.95e-2	7.50e-3	1.81e-6	1.86	2.60e-1	2.01e-2
	100	3.81e-3	7.65e-4	3.78e-7	1.81	2.35e-1	2.12e-2
16	20	4.45e-2	7.22e-3	7.48e-7	1.22	1.85e-1	1.43e-2
	100	4.55e-3	6.86e-4	1.72e-7	1.30	1.84e-1	1.36e-2

Table 4.2: BT MSE of MSF and GSPF-II with high noise intensity and known prior PDF

$n_z = 5$		$\sigma_\xi = 0.01$, $\sigma_\eta = 0.005$			$\sigma_\xi = 0.1$, $\sigma_\eta = 0.05$		
		MSF			MSF		
n_x	n_s	$\widetilde{o}_x$	$\widetilde{o}_y$	$\widetilde{o}_s$	$\widetilde{o}_x$	$\widetilde{o}_y$	$\widetilde{o}_z$
4	20	1.14e-2	2.13e-3	5.72e-6	3.18e-2	5.74e-3	3.16e-6
	100	1.27e-3	2.45e-4	1.59e-6	9.80e-3	1.91e-3	1.08e-6
8	20	3.64e-3	6.96e-4	4.40e-6	3.52e-2	5.52e-3	2.07e-6
	100	4.55e-4	9.39e-5	9.33e-7	5.69e-3	1.04e-3	6.43e-7
16	20	1.80e-3	3.70e-4	3.07e-6	2.90e-2	4.47e-3	9.57e-7
	100	2.58e-4	5.41e-5	5.05e-7	8.69e-3	1.12e-3	4.04e-7

Table 4.3: BT MSE of MSF with nz=5, low and high noise intensity and known prior PDF

$n_z = 1$		$\sigma_\xi = 0.01$, $\sigma_\eta = 0.005$					
		MSF			GSPF-II		
n_x	n_s	$\widetilde{o}_x$	$\widetilde{o}_y$	$\widetilde{o}_s$	$\widetilde{o}_x$	$\widetilde{o}_y$	$\widetilde{o}_s$
8	100	3.10e-3	1.57e-2	1.59e-6	2.26	0.33	0.01

Table 4.4: BT MSE of MSF and GSPF-II with low noise intensity and unknown prior PDF

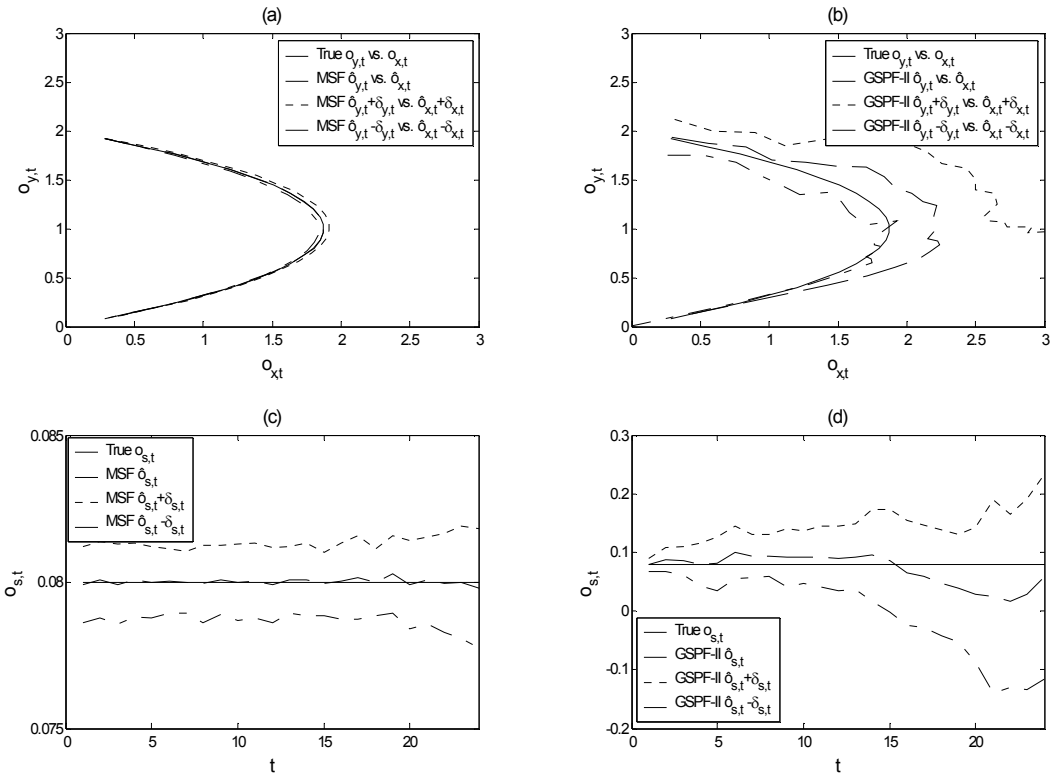

Figure 4.6: BT x and y coordinates of target estimated by a) MSF and b) GSPF-II, target speed estimated by c) MSF and d) GSPF-II with low noise intensity, known prior PDFs, $n_z = 1$, $n_x = 8$ and $n_s = 100$.

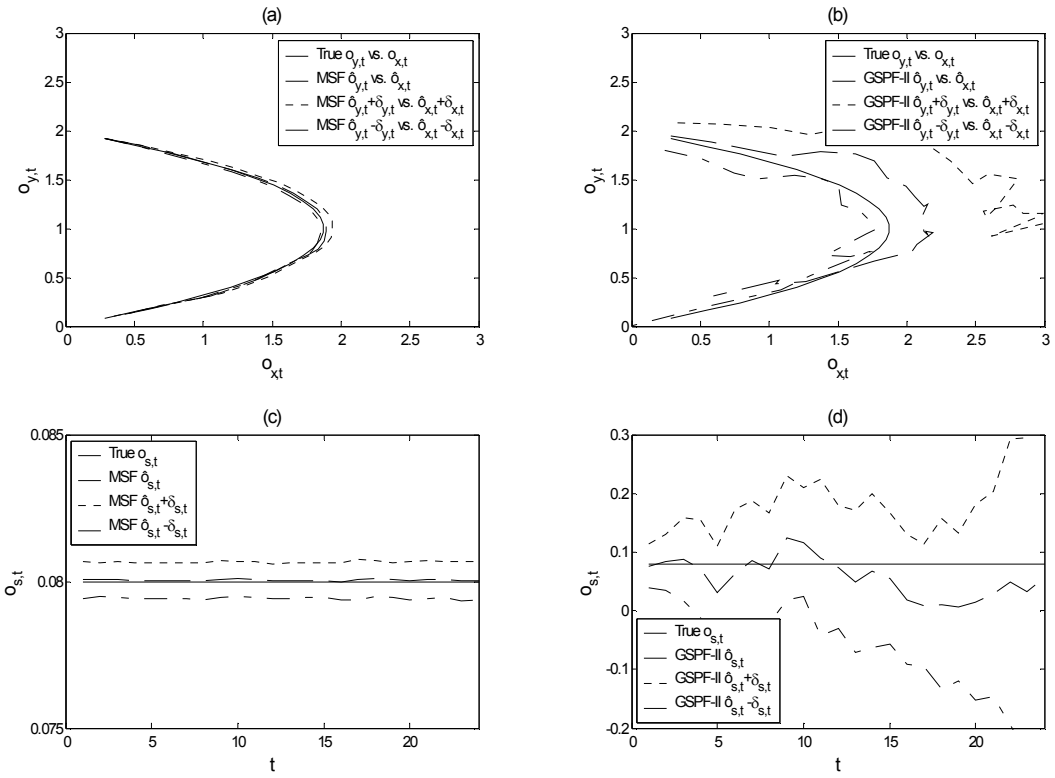

Figure 4.7: BT x and y coordinates of target estimated by a) MSF and b) GSPF-II, target speed estimated by c) MSF and d) GSPF-II with high noise intensity, known prior PDFs, $n_z = 1$, $n_x = 8$ and $n_s = 100$.

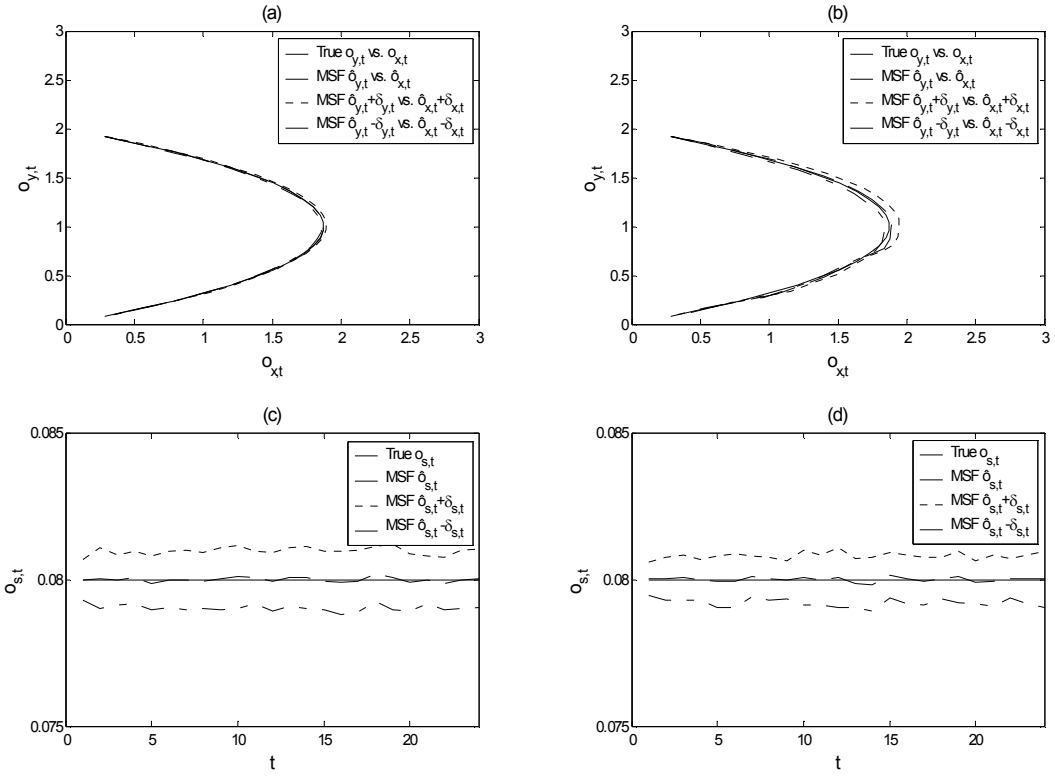

Figure 4.8: BT x and y coordinates of target estimated by MSF with a) low and b) high noise intensities, target speed estimated by MSF with c) low and d) high noise intensities, known prior PDFs, $n_z = 5$, $n_x = 8$ and $n_s = 100$

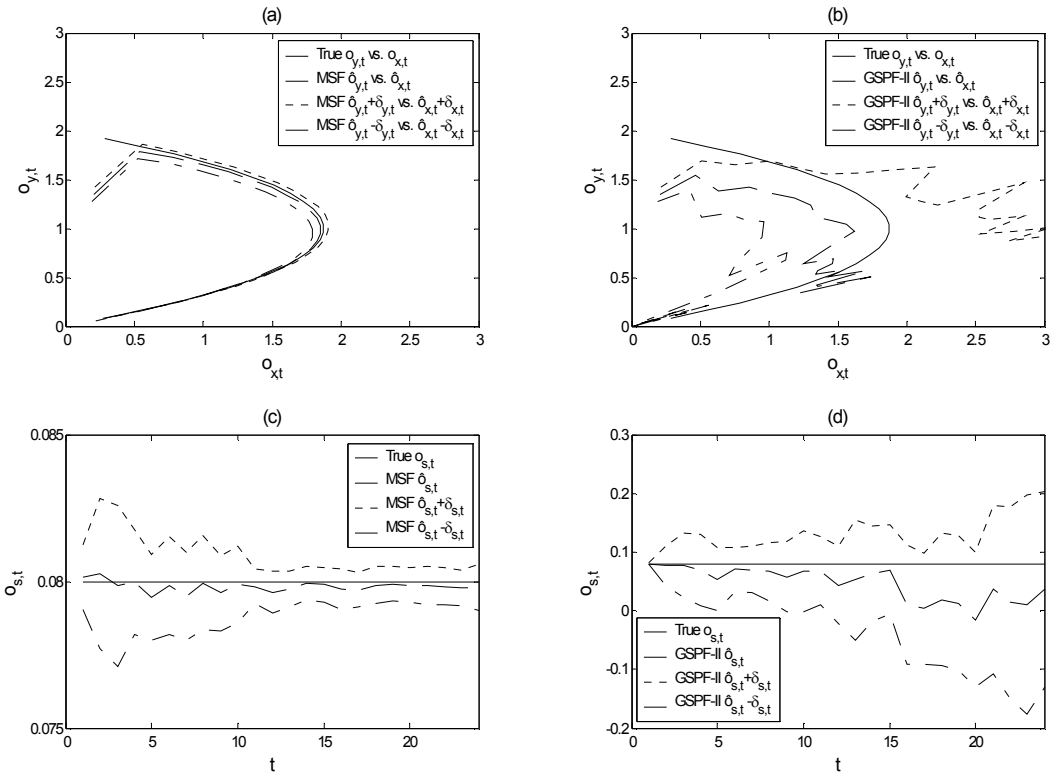

Figure 4.9: BT x and y coordinates of target estimated by a) MSF and b) GSPF-II; target speed estimated by c) MSF and d) GSPF-II with low noise intensity, unknown prior PDFs, $n_z = 1$, $n_x = 8$ and $n_s = 100$

[143, 144, 145]. The UNGM is defined as,

$$x_t = \begin{cases} 0.5x_{t-1} + 25\frac{x_{t-1}}{1+x_{t-1}^2} + 8\cos(1.2(t-1)) + \xi_{t-1}, \\ \qquad\qquad \forall\ t-1 = i\ n_z \\ \chi_{t-1}, \qquad \forall\ t-1 \neq i\ n_z \end{cases} \tag{4.94}$$

$$z_t = \frac{x_t^2}{20} + \eta_t \tag{4.95}$$

where x_t is a parameter to be estimated; z_t is the measurement acquired at time t; ξ_{t-1} and η_t are white noise with stationary statistics, $\xi_{t-1} \sim 0.8N\left(\xi_{t-1}; 0, 0.1\right) + 0.2N\left(\xi_{t-1}; 0, 1\right)$ and $\eta_t \sim N\left(0, 1\right)$.

This UNGM problem is simulated for 50 time steps, $t \in \{1, \cdots, 50\}$, with the prior PDF, $p\left(x_0\right) = n_x^{-1} \sum^{n_x} N\left(x_0; 0.1, 0.1\right)$. The maximum and minimum of x_t are 16 and -18. A set of experiments are designed to test the performances of MSF and GSPF-II under similar conditions as in Section 4.2.3. For each condition, MSF and GSPF-II are executed 50 times to obtain performance statistics. Let $\widehat{x}_{t,e}$ be the estimates of x_t from either MSF or GSPF-II. The MSE of $\widehat{x}_{t,e}$ is computed as:

$$\widetilde{x} = E\left\{E\left[\left(x_t - \widehat{x}_{t,e}\right)^2 |t\right] |e\right\}, \begin{array}{l} \forall\ t \in \{1, \cdots, 50\} \\ \forall\ e \in \{1, \cdots, 50\} \end{array}$$

where $\widetilde{x}$ is the averaged MSE of $\widehat{x}_{t,e}$.

The resulting $\widetilde{x}$ from MSF and GSPF-II under various conditions are presented in Table 4.5. The resulting averaged $\widehat{x}_{t,e}$ with respect to e from MSF and GSPF-II at $n_x = 16$ and $n_s = 100$ under various conditions are shown in Figures 4.10 and 4.11. The standard deviations of $\widehat{x}_{t,e}$ with respect to e are plotted as error bars in these figures.

Discussion

The performances of MSF and GSPF-II are analyzed based on the simulation results.

- Posterior PDF Estimation Method

  The effects of posterior PDF estimation method on estimation accuracy for both filters are indicated by the averaged MSE below computed from Tables 4.1, 4.2 and 4.4 for BT; from Table 4.5 for UNGM,

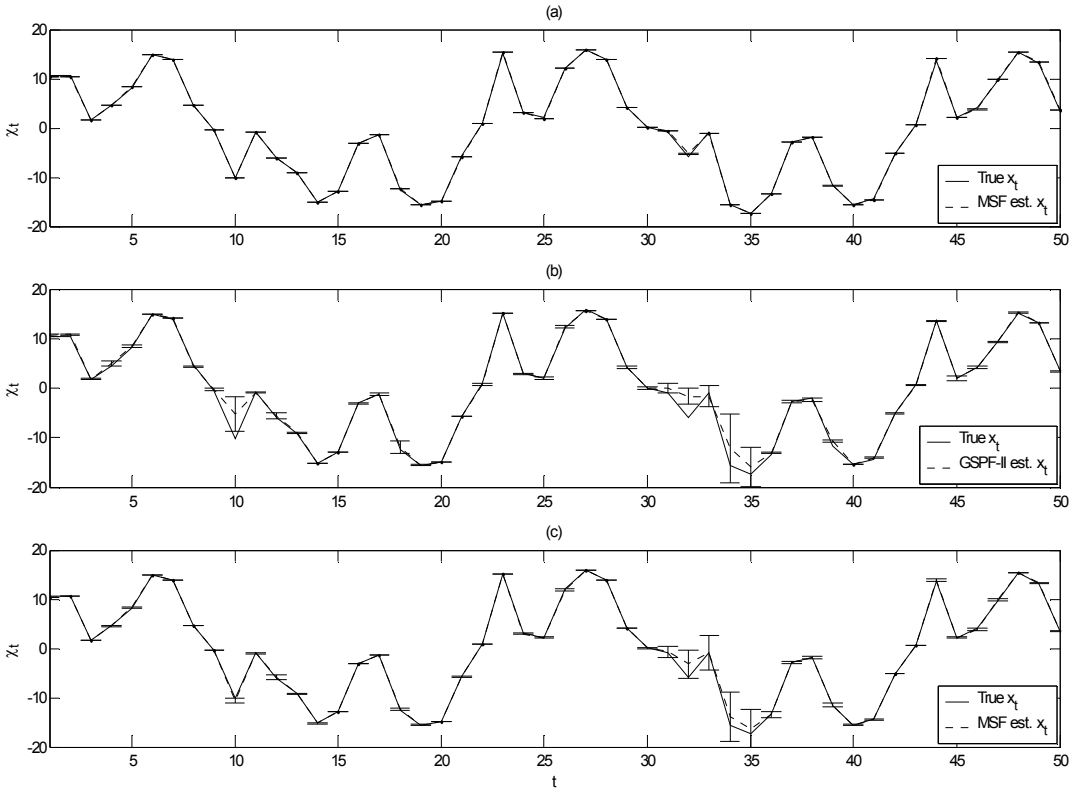

Figure 4.10: BT x and y coordinates of target estimated by a) MSF and b) GSPF-II; target speed estimated by c) MSF and d) GSPF-II with low noise intensity, unknown prior PDFs, $n_z = 1$, $n_x = 8$ and $n_s = 100$

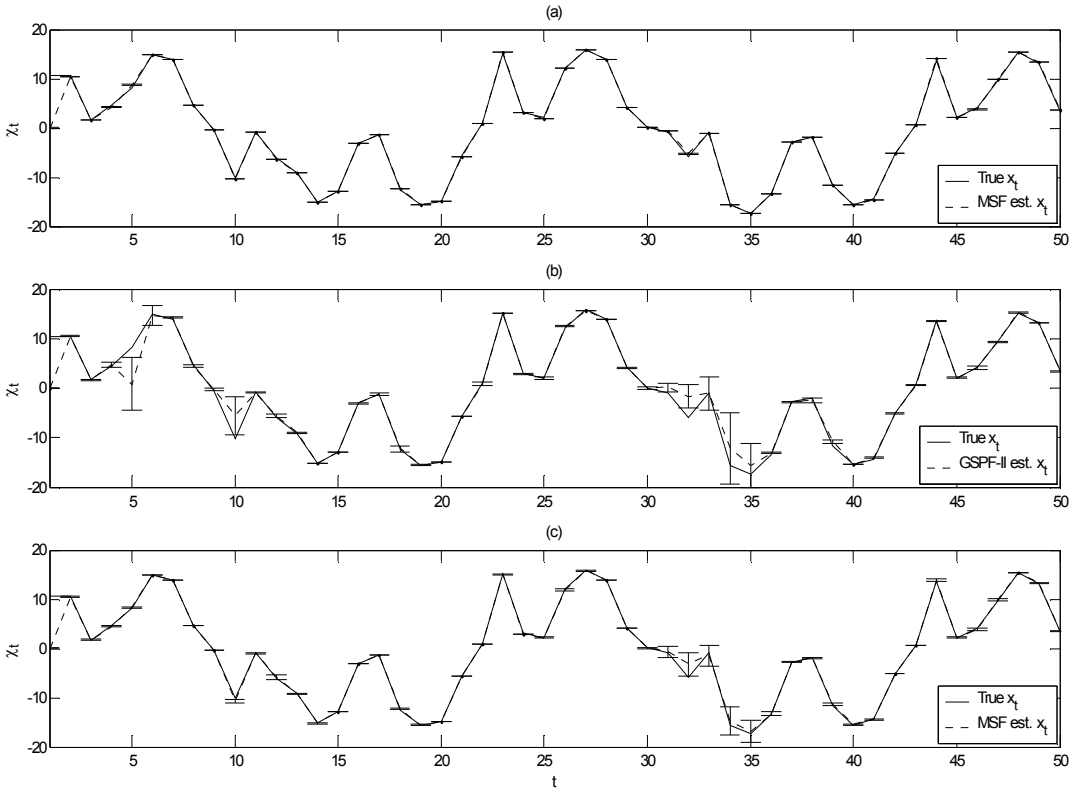

Figure 4.11: BT x and y coordinates of target estimated by a) MSF and b) GSPF-II; target speed estimated by c) MSF and d) GSPF-II with low noise intensity, unknown prior PDFs, $n_z = 1$, $n_x = 8$ and $n_s = 100$

$\widetilde{x}$		Known Prior PDF			Unknown Prior PDF		
		$n_z = 1$		$n_z = 5$	$n_z = 1$		$n_z = 5$
n_x	n_s	MSF	GSPF-II	MSF	MSF	GSPF-II	MSF
8	20	3.82e-2	4.99	2.05	2.26	10.96	3.41
	100	3.92e-2	5.09	2.94	2.26	10.78	5.69
16	20	3.43e-2	3.41	0.79	2.25	8.22	3.79
	100	2.32e-2	2.94	1.50	2.26	7.16	2.92
32	20	4.48e-2	1.63	3.05e-1	2.26	4.92	2.60
	100	2.91e-2	1.20	3.34e-1	2.26	5.50	2.59

Table 4.5: UNGM MSE of MSF (nz=1 and nz=5) and GSPF-II with known and unknown prior PDF

Application	Avg. MSE	
	MSF	GSPF-II
BT	8.44e-3	6.33e-1
UNGM	1.15	5.57

It is apparent that the average MSE produced by MSF are only a small fraction relative to that of GSPF-II for BT (also see Figures 4.6, 4.7 and 4.9) and UNGM (also see Figures 4.10 and 4.11).

The method of posterior PDF estimation is considered as one of the most critical elements in NSF. GSPF-II employes a bank of GPF to estimate a Gaussian mixture as the posterior PDF. Each GPF independently estimates a Gaussian component of the mixture based on an importance density, which is generated by an UKF to capture local statistics of the state.

MSF estimates the posterior PDF using a sampling technique. The posterior PDF is then optimized based on multi-scale PDF reconstruction to achieve minimum estimation error variance in the sense of posterior Cramer-Rao bound. In addition, all Gaussian components of the posterior PDF are collectively optimized to capture the state statistics globally. Therefore, the posterior PDF estimation method of MSF is able to produce more accurate estimates than that of GSPF-II.

- Number of Gaussian Components and Samples

  The number of Gaussian components (i.e., n_x) and samples (i.e., n_s) used to estimate the posterior PDF and state estimate for both filters are of great practical interests. The averaged MSE rates, $E\left(d\widetilde{x}/dn_x\right)$ and $E\left(d\widetilde{x}/dn_s\right)$, for

both filters are calculated based on data in Tables 4.1 and 4.2 for BT and Table 4.5 for UNGM as follows,

Application	$E\left(d\widetilde{x}/dn_x\right)$		$E\left(d\widetilde{x}/dn_s\right)$	
	MSF	GSPF-II	MSF	GSPF-II
BT	-8.82e-4	-5.68e-2	-1.74e-4	-1.16e-3
UNGM	-2.61e-4	-2.24e-1	-3.29e-5	-3.04e-3

The negative MSE rates indicate that the estimation errors decrease as n_x and/or n_s increase. These results are expected, since the posterior PDF can be estimated more accurately using more Gaussian components. Also, the convergence of state estimation requires large number of samples as suggested by Monte-Carlo integration and the law of large numbers. The error rates produced by MSF are consistently smaller than that of GSPF-II by about two orders of magnitude on average. This reveals an advantageous characteristic of MSF over GSPF-II in practice. That is, the estimation accuracy of MSF is relatively less sensitive to n_x and n_s, so that small n_x and n_s can be used in MSF to relax computation power needed while maintaining the estimation accuracy.

- Noise Level

  The impacts of noise level on both filters are analyzed by the average MSE computed from Tables 4.1 and 4.2 as follows,

Noise level	Avg. MSE	
	MSF	GSPF-II
Low	6.24e-3	3.70e-1
High	1.10e-2	8.58e-1
High/Low	1.76	2.32

  These results convey that the estimates yielded by MSF are two orders of magnitude more accurate than GSPF-II even in the case of high noise level. In addition, the ratios between the averaged MSE at high and low noise levels show that MSF is less sensitive to noise compared to GSPF-II. This is confirmed by Figures 4.6 and 4.7.

- Dependency on Prior PDF

  Prior PDF of the state is required for both filters. However, the prior PDF may be inaccurate or unknown in real world applications. Therefore, the filter

dependency on prior PDF is an important practical issue ones must address. The average MSE for both filters with and without prior PDF are obtained based on Tables 4.1 and 4.4 for BT, and Table 4.5 for UNGM,

Application	Known prior PDF		Unknown prior PDF	
	Avg. MSE		Avg. MSE	
	MSF	GSPF-II	MSF	GSPF-II
BT	6.24e-3	3.70e-1	6.27e-3	8.67e-1
UNGM	3.48e-2	3.21	2.26	7.92

For BT, the average MSF estimation errors are almost the same regardless of the prior PDF availability. However, the averaged GSPF-II estimation error without prior PDF is more than twice of that with prior PDF. When the prior PDF is unknown, MSF employs the expectation maximization algorithm to estimate a GMM as the prior PDF based on uniform random samples and the measurement at the first time step. The same prior PDF estimated by MSF is applied to GSPF-II. As illustrated in Figure 4.9, the estimation error is large at the first time step due to noisy measurement and insufficient number of samples. MSF is able to reduce the estimation error very quickly at the second time step. On the contrary, GSPF-II is unable to correct the estimation errors and it propagates the errors throughout the rest of the simulation. This demonstrates the effectiveness of optimizing the posterior PDF at every time step.

For UNGM, there is a large difference of the average MSE between known and unknown prior PDF for both filters. The likelihood function of UNGM bimodal because of the square term in the measurement model (i.e., Equation 4.95). At the first time step, the EM_GM function is able to estimate the bimodal prior PDF. However, the state is estimated as the weighted sum of samples generated by the bimodal PDF, which is equal to the value in between the two peaks. The estimated prior PDF for UNGM peaks at 10 and -10, which causes the state estimate to be 0 at the first time step. Figure 4.9 shows the large estimation errors for both filters are mainly contributed from the first time step.

- Estimation Consistency

  Both filters compute state estimates based on random samples. Deviations of the state estimates among trials are expected. It is highly desirable to produce consistent estimates, or estimates with small deviations. The +/- one

standard deviations of state estimates for both filters are plotted in Figures 4.6, 4.7 and 4.9 for BT and Figures 4.10 and 4.11 for UNGM.

These figures clearly show that the deviations of the estimates produced by MSF are consistently smaller than that of GSPF-II for all cases of noise levels and the availability of prior PDF. The highly consistent MSF estimates are achieved by the minimization of estimation error variance through the covariance reduction in the process of posterior PDF optimization derived based on multi-scale PDF reconstruction.

- Number of Scales

  Number of scale refers to the number of measurements available in between state transitions. The performances of MSF using one and five scales are calculated based on Tables 4.1 to 4.5 as follows,

Application	MSF	
	Avg. MSE	
	$n_z = 1$	$n_z = 5$
BT	8.62e-3	4.51e-3
UNGM	1.15	2.41

The average MSE produced by MSF with five scales is about two times lower than that with one scale for BT. The converse is true for UNGM due to the multimodal likelihood distributions in these applications as mentioned previously. This will be discussed in more details later. The MSF performances with respect to the number of scales for BT are discussed in more details in the following.

Application: BT		MSF	
Filter char.	Performance	$n_z = 1$	$n_z = 5$
n_x	$E\left(d\widetilde{x}/dn_x\right)$	-8.82e-4	-1.59e-4
n_s	$E\left(d\widetilde{x}/dn_s\right)$	-1.74e-4	-7.02e-5
Noise: Low	Avg. MSE	6.24e-3	1.25e-3
Noise: High	Avg. MSE	1.10e-2	7.78e-3
Known[5]	Avg. MSE	9.54e-4	1.83e-4
Unknown[6]	Avg. MSE	6.27e-3	-

[8]Known prior PDF
[6]Unknown prior PDF

The performance of MSF with five scales improve about four times compared to that with one scale on average. The estimation consistencies of MSF with one and five scales can be observed from Figures 4.6, 4.7 and 4.8. For low noise level, the state estimates produced by MSF with five scales are clearly more consistent than that with one scale. In the case of high noise level, the estimation consistencies are similar for both number of scales.

These results correspond well to the convergence of estimation covariance in Section 4.2.2. At each scale, the estimation error covariance is minimized to improve the estimation consistency. As the number of scale increases, more such minimizations are allowed to take place. Consequently, the estimation covariance reduces asymptotically and the state estimate converges to the true state.

- Time complexity

  In addition to estimation accuracy, time complexity is an important performance measure for a filtering algorithm. The time complexities of MSF and GSPF-II can be described in terms of the big-O complexity index (also commonly known as big-O notation) [146]. Let d_x and n_s, respectively, be the dimension of the tissue acoustic parameter vector and number of random samples of the parameters; n_x and n_η, respectively, be the number of Gaussian components representing the posterior and measurement noise PDFs. The big-O time complexities of MSF and GSPF-II are expressed in terms of d_x, n_s, n_x and n_η. Tables 4.6 and 4.7 depict the big-O time complexity analyses of the filters. The time complexities of MSF and GSPF-II are respectively derived as $O(n_x\, n_s)$ and $O\left(n_x\, (d_x^3 + n_s)\right)$ based on the assumptions stated in the tables. These assumptions are valid for the parameter estimation problems discussed above and the tissue characterization problem formulated in this thesis. The time complexity of MSF is smaller than that of GSPF-II by $O\left(n_x\, d_x^3\right)$, since GSPF-II executes UKF n_x times to estimate the importance densities in the posterior PDF estimation process and the time complexity of UKF is d_x^3 [147]. On the other hand, MSF does not require UKF in its posterior PDF estimation process. For problems where d_x is large such that $d_x^3 \simeq n_s$, $O\left(n_x\, d_x^3\right)$ is significant relative to $O\left(n_x\, n_s\right)$. As a result, the time complexity of GSPF-II is significantly larger than that of MSF for these problems.

MSF		
Operation	Description	Complexity
Random sample generation	n_s number of random samples are generated from the posterior PDF of the previous iteration.	$O(n_s)$
Sample evaluation	Probability densities of n_s number of random samples are computed from a n_η component Gaussian mixture likelihood PDF.	$O(n_s\, n_\eta)$
Posterior PDF estimation	A posterior PDF is estimated using an expectation maximization algorithm, which consists of two main steps in each iteration, - expectation: computes probability densities of n_s number of random samples from a n_x component Gaussian mixture - maximization: computes means and covariance matrices of a n_x component Gaussian mixture based on the random samples	 $O(n_s\, n_x)$ $O(n_s\, n_x)$
Posterior PDF optimization	A PDF is obtained to minimize estimation uncertainty based on posterior Cramer-Rao bound, which involves - computing a Fisher information matrix based on n_s number of random samples from a n_x component Gaussian mixture, - inverting the matrix using the Coppersmith–Winograd algorithm, and - solving Equation 4.84 for $W^V_{n,f,1:n}$.	 $O(n_s)$ $O(d_x^{2.376})$ $O(n_x)$
Estimation computation	The estimates of parameter are computed as the weighted sum of the optimized posterior PDF Gaussian component means.	$O(n_x)$
Overall time complexity: $O(n_s\, n_x)$ for $n_\eta \ll n_s\, n_x$ and $d_x^{2.376} \ll n_s\, n_x$		

Table 4.6: Time complexity of MSF

GPF		
Operation	Description	Complexity
Importance density estimation	A UKF is used to estimate the importance density as a Gaussian PDF based on unscented transformation.	$O\left(d_x^3\right)$
Random sample generation	n_s number of random samples are generated from the importance density.	$O\left(n_s\right)$
Sample weight computation	n_s number of random samples are weighted using the n_η component Gaussian mixture likelihood PDF, importance density and respective posterior PDF Gaussian component of the previous iteration.	$O\left(n_s\, n_\eta\right)$
Weight normalization	The weights of n_s number of random samples are normalized.	$O\left(n_s\right)$
Mean and covariance estimation	The mean and covariance of the respective Gaussian component of the posterior PDF are estimated.	$O\left(n_s\right)$
Overall time complexity: $O\left(d_x^3 + n_s\right)$ for $n_\eta \ll d_x^3$		
GSPF-II		
Gaussian mixture posterior PDF estimation	A bank of n_x GPFs are executed to estimate a n_x component Gaussian mixture posterior PDF.	$O\left(n_x \left(d_x^3 + n_s\right)\right)$
Estimation computation	The estimates of parameter are computed as the weighted sum of the optimized posterior PDF Gaussian component means.	$O\left(n_x\right)$
Overall time complexity: $O\left(n_x \left(d_x^3 + n_s\right)\right)$ for $n_\eta \ll d_x^3$		

Table 4.7: Time complexity of GSPF-II

4.3 Summary

Forward scattering of focused waves in multi-layered tissues is formulated as the propagation of pressure amplitude modulated plane waves through the tissues. The pressure amplitudes of plane waves are computed by a set of sub-problems, which compute the reductions of wave pressure amplitude in the layers individually. The models developed for these problems are combined as the measurement model used in the inverse scattering method. In addition, Gaussian mixture is employed to model the statistics of measurement noise.

MSF is developed to achieve not only MMSE estimate, but also minimum estimation error variance by optimizing the posterior PDF. The optimal posterior PDF is determined based on a novel framework of multi-scale PDF analysis, which is embedded in the MSF formulation to minimize the estimation error covariances subject to the Cramer-Rao bounds. The multi-scale PDF analysis is developed to examine the frequency characteristics of any arbitrary PDF that can be represented by a GMM. It is decomposed recursively using a set of low-pass filters. Based on the criteria and constraints imposed to retain the properties of PDF, these filters are derived as Gaussian PDFs. The use of Gaussian PDFs as low-pass filters is well known in the scale-space theory. Each decomposition can be considered as a scale. In addition to multi-scale PDF decomposition, the reconstruction of PDF in the multi-scale framework is also established.

The MSF formulation specifically for tissue acoustic parameter estimation is presented. For each ultrasound echo frequency measurement, a minimization of estimation error covariance is performed in which the posterior PDF is reconstructed based on multi-scale PDF reconstruction. In each scale of PDF reconstruction, the covariance of each Gaussian component of the posterior PDF is guaranteed to reduce. As more measurements become available, the estimation error covariance converges to the inverse of Fisher information matrix.

Performance comparisons between MSF and a state-of-the-art NSF, GSPF-II, are performed on parameter estimation problems reported in the literature. Results show that MSF is over 3.5 times more accurate than GSPF-II. In addition, MSF is relatively less sensitive to noise level, prior knowledge of the parameters, numbers of random samples and Gaussian components representing the posterior PDF compared to GSPF-II. Furthermore, the time complexity of MSF is smaller than that of GSPF-II. The time complexity difference between these filters become significant as the dimension of the parameters to be estimated increases.

Chapter 5

Analysis of MSF Based on Plane Wave Simulation

This chapter analyzes the behavior and performance of MSF based on simulated data. Simulation based analysis has the advantage of isolating errors due to modeling from MSF. In addition, simulation allows the control of signal-to-noise ratio (SNR) in order to evaluate the robustness of MSF. SNR control may not be possible to realize in physical experiments. In what follows, the simulation of wave propagation in a multi-layered tissue (i.e., the forward scattering problem) is first described. The MSF estimates of the acoustic parameters of the tissue using various random sample sizes and SNR values are then presented. The behavior and performance of MSF are analyzed under various sample sizes and SNR values.

5.1 Plane Wave Modelling of Forward Scattering Problem

The incident wave of the seven-layered tissue shown in Figure 4.1 is simulated as a plane wave, which can be represented in harmonic form,

$$\psi^p_{inc} = \mathcal{IF}\left\{\sum_{\omega} \Psi^p_{inc,\omega}\right\} \tag{5.1}$$

where ψ^p_{inc} is the incident wave pressure in the time domain; $\Psi^p_{inc,\omega}$ is the incident plane wave pressure at frequency ω, the subscript ω is suppressed to simplify notations, $\Psi^p_{inc,\omega} \rightarrow \Psi^p_{inc}$; $\mathcal{IF}$ denotes inverse Fourier transform.

The incident wave is simulated using plane wave instead of focused wave used in Section 4, since the computations of plane wave are much more efficient than that of focused wave. Also, plane wave based simulations of wave propagation in multi-layered media have been widely accepted in the research community. The measurement model for plane wave is different from that for focused wave. Let α_i, c_i, ρ_i respectively be the attenuation coefficient, sound speed and density of layer number i of the tissue. After the plane wave penetrates through layer i, the magnitude of the wave is attenuated based on α_i and the thickness of the layer. At the interface between layers i and $i+1$, part of the wave magnitude is reflected and the rest is transmitted proportional to the reflection and transmission coefficients. For example, the magnitude of the wave reflected at the interface between layers 1 and 2 is computed as,

$$|\Psi_1^p| = exp\left(-\alpha_0\, c_0 \Delta t_0 - \alpha_1\, c_1 \Delta t_1\right)\ T_{0\rightarrow 1}\ T_{1\rightarrow 0}\ R_{1\leftarrow 2}\ \ |\Psi_{inc}^p| \tag{5.2}$$

where $\Delta t_0 = t_0 - t_{inc}$; $\Delta t_1 = t_1 - t_0$; t_{inc} is the time at which the incident wave is transmitted; t_0 and t_1 are respectively the arrival time of waves reflected at the layer 0-1 and 1-2 interfaces; α_0 is the attenuation coefficient of water, the coupling material between the transducer and tissue; $T_{0\rightarrow 1}$ and $T_{1\rightarrow 0}$ are the transmission coefficients from layer 0 to 1 and from layer 1 to 0, respectively; $R_{1\leftarrow 2}$ is the reflection coefficient from layer 2 to 1. $T_{0\rightarrow 1}$, $T_{1\rightarrow 0}$ and $R_{1\leftarrow 2}$ are functions of c_0, c_1, c_2, ρ_0, ρ_1 and ρ_2.

At each frequency, the magnitude of the wave reflected from the interface between layers i and $i+1$ can be derived as,

$$|\Psi_i^p| = exp\left(-\sum_{j=0}^{i} \alpha_j\, c_j \Delta t_j\right)\ \prod_{j=1}^{i} \left(T_{j-1\rightarrow j}\ T_{j\rightarrow j-1}\right)\ R_{i\leftarrow i+1}\ \ |\Psi_{inc}^p| \tag{5.3}$$

A multi-layered tissue is simulated based on the acoustic properties of the tissue phantoms developed in this research. Details of tissue phantom development will be presented in Section 6.3. A seven-layered tissue phantom is developed to mimic the tissue layers of mammalian eye along the optical axis. The sound speeds and densities of the tissue phantoms are presented in Tables 5.1 and 5.2. As mentioned in Section 1.5 that attenuation coefficients of soft tissues are approximately first order functions of frequency. α_i is expressed as,

$$\alpha_i = m_i\ f + b_i \tag{5.4}$$

where f is the frequency of the simulated ultrasound wave; m_i and b_i are the slope and y-intercept of the attenuation model, respectively. m_i and b_i of the tissue

Tissue phantom	Sound speed (m/s)	
	Mean	Std
Cornea	1585.6	2.087
Aqueous humor	1518.4	3.978
Lens	1597.7	4.513
Vitreous humor	1534.6	9.865
Retina	1550.0	8.204
Choroid	1551.0	4.382
Sclera	1597.2	5.738

Table 5.1: Sound speeds of tissue phantoms

Tissue phantom	Density (g/ml)	
	Mean	Std
Cornea	1.060	1.863e-3
Aqueous humor	1.007	4.775e-3
Lens	1.112	4.757e-3
Vitreous humor	1.010	1.508e-3
Retina	1.032	4.676e-3
Choroid	1.047	8.406e-3
Sclera	1.077	2.471e-3

Table 5.2: Mass densities of tissue phantoms

Tissue phantom	Slope (1/(m MHz))	Y-intercept (1/m)
	Mean	Mean
Cornea	2.48e-6	40.6600
Aqueous humor	2.48e-6	3.0871
Lens	2.47e-6	77.1070
Vitreous humor	2.46e-6	8.2263
Retina	2.49e-6	16.9776
Choroid	2.50e-6	26.1580
Sclera	2.50e-6	47.2794

Table 5.3: Slopes and y-intercepts of attenuation coefficient models of tissue phantoms

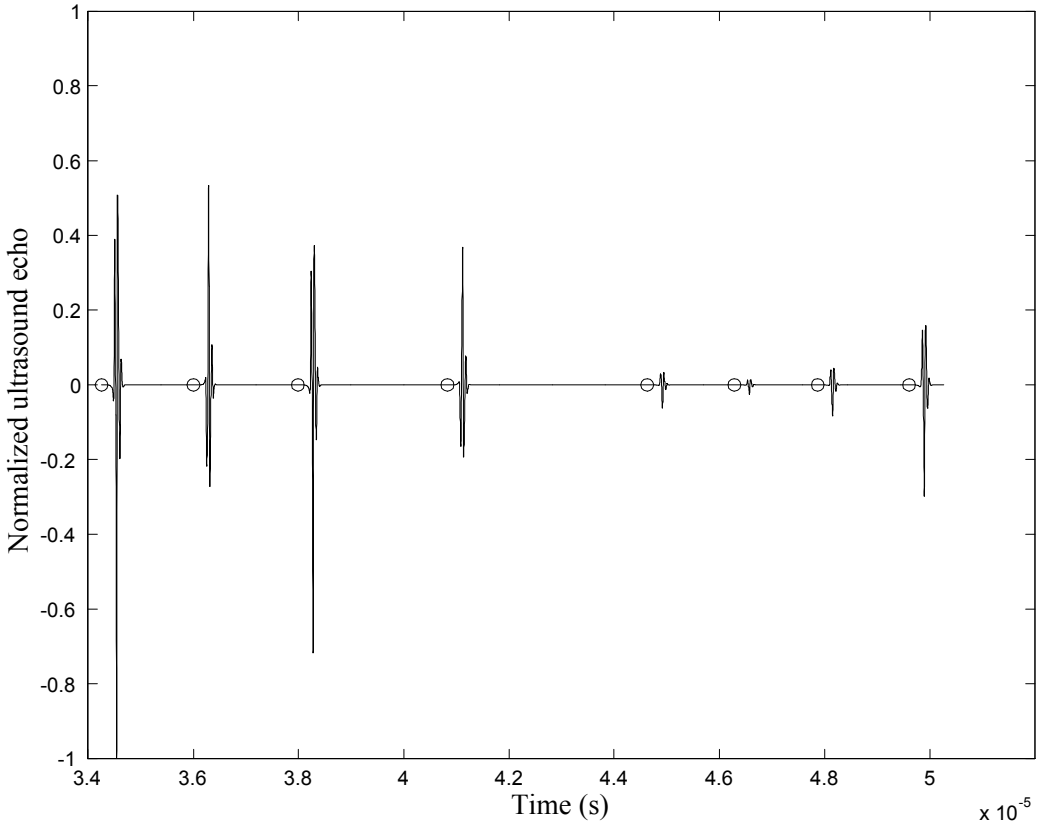

Figure 5.1: Simulated echoes of the seven-layered eye phantom

phantoms are listed in Table 5.3. It is noted that the standard deviations of m_i and b_i are unavailable since they are model fitted parameters.

Based on the acoustic parameters of the tissue and the wave propagation paths of the Echotree, the simulated echoes of the tissue are shown in Figure 5.1. The amplitudes of the echoes are normalized with respect to the absolute maximum amplitude of the echo signals. The beginning of each echo is detected by the algorithm discussed in Section 3.2 and is marked by a circle. It should be noted that eight echoes are detected. The propagation paths of these echoes are investigated. Each of these paths involves only one reflection, which implies that the echoes uniquely correspond to the layer interfaces and no reverberation echo is detected.

5.2 MSF Inverse Scattering of the Simulated Problem

Given the simulated ultrasound echoes of the multi-layered tissue, estimation of the tissue acoustic parameters is an inverse scattering problem. As discussed in Section 4.1.1, it is advantageous to first estimate acoustic impedances instead of densities and then compute densities based on the estimated acoustic impedances and sound speeds. Therefore, the parameters to be estimated for each layer of the tissue are defined as m_i, b_i, c_i and Z_i. For each layer, MSF performs recursive estimation of the parameters. In each iteration, the parameter space is randomly sampled. These samples are weighted as their likelihood of producing the new measurement (i.e., echo magnitude in the frequency domain) acquired in the iteration. The weighted samples are used to construct a posterior PDF of the parameters. The posterior PDF is optimized based on the Cramer-Rao bound. Uncertainty of measurements are simulated by adding noise to the ultrasound echoes. Noise is generated using the noise model in Equation 4.12.

5.3 Results and Analysis

MSF is applied to solve the inverse problem described in Section 5.2 using three random sample sizes ($n_s = 50$, 100 and 200) and three SNRs (3db, 6db and 12db). The number of random samples used in the experiments are chosen to be similar to that used by the state-of-the-art filter (i.e., GSPF-II) in [121]. The optimal number of random samples is dependent on the definition of optimality and may vary largely for different optimality definitions. Determining the optimal number of random samples is out of the scope of this research. For each random sample size and SNR, MSF is executed twenty times to obtain the statistics of estimation. The estimation error percentages of the acoustic parameters are presented in Tables 5.4 to 5.12. In addition, the measured and estimated acoustic parameters for 100 random samples and 6db SNR are depicted in Figures 5.2 to 5.5.

MSF estimates four acoustic parameters for each layer of the tissue. The estimation errors of these parameters decrease as either or both of random sample size and SNR increase. The trend of estimation error reduction is expected, since larger amount of random samples is capable of exploring the solution space in higher resolution to achieve more accurate estimates. In addition, when the noise level decreases, the samples closed to the measured values are given higher weights (i.e., likelihoods of the samples being the measured acoustic parameters given the

No. of samples: 50 SNR = 3db	Estimation error percentage							
	Attenuation coef. model				Sound speed		Density	
	Slope		Y-intercept					
Eye layer	Mean	Std	Mean	Std	Mean	Std	Mean	Std
Cornea	0.169	0.652	6.197	0.187	1.186	0.305	-1.171	0.297
Aqueous humor	-0.140	0.738	-1.035	5.313	0.953	0.711	-1.031	0.698
Lens	0.758	0.597	-7.367	5.326	-0.358	1.278	0.443	1.297
Vitreous humor	0.918	0.342	11.602	5.517	-1.147	1.968	1.488	2.115
Retina	-0.405	0.186	12.324	5.675	-1.573	0.700	1.852	0.813
Choroid	-1.008	0.387	4.927	3.442	3.022	0.553	-2.710	0.452
Sclera	-0.766	0.255	-2.737	3.371	0.474	1.509	-0.236	1.499
Absolute average:	0.595	0.451	6.598	4.119	1.245	1.004	1.276	1.025

Table 5.4: MSF acoustic parameter estimation errors based on plane wave simulation, 50 random samples and 3db SNR

No. of samples: 100 SNR = 3db	Estimation error percentage							
	Attenuation coef. model				Sound speed		Density	
	Slope		Y-intercept					
Eye layer	Mean	Std	Mean	Std	Mean	Std	Mean	Std
Cornea	0.200	0.643	-1.090	1.748	0.224	0.185	-0.223	0.184
Aqueous humor	-0.169	0.647	4.192	2.259	1.034	1.019	-1.007	1.017
Lens	0.653	0.498	-5.452	0.831	0.793	0.942	-0.762	0.914
Vitreous humor	0.933	0.284	5.285	6.308	-2.038	0.753	2.269	0.680
Retina	-0.306	0.113	3.826	2.409	-1.304	0.133	1.457	0.155
Choroid	-1.046	0.263	5.478	2.156	1.402	0.682	-1.270	0.644
Sclera	-0.639	0.297	5.749	1.808	0.402	1.313	-0.335	1.320
Absolute average:	0.564	0.392	4.439	2.503	1.028	0.718	1.046	0.702

Table 5.5: MSF acoustic parameter estimation errors based on plane wave simulation, 100 random samples and 3db SNR

No. of samples: 200 SNR = 3db	Estimation error percentage							
	Attenuation coef. model				Sound speed		Density	
	Slope		Y-intercept					
Eye layer	Mean	Std	Mean	Std	Mean	Std	Mean	Std
Cornea	0.022	0.329	2.827	0.928	-0.202	0.297	0.203	0.299
Aqueous humor	0.052	0.152	-5.911	0.432	1.853	0.143	-1.843	0.142
Lens	0.530	0.219	-3.511	1.847	0.030	0.933	-0.001	0.928
Vitreous humor	0.911	0.161	4.754	3.561	-1.222	0.343	1.337	0.294
Retina	-0.557	0.169	2.534	4.020	0.039	0.931	0.047	0.904
Choroid	-1.045	0.203	2.193	3.202	0.309	1.101	-0.228	1.054
Sclera	-0.688	0.319	2.636	3.750	-0.530	1.046	0.579	1.079
Absolute average:	0.543	0.222	3.481	2.534	0.598	0.685	0.606	0.671

Table 5.6: MSF acoustic parameter estimation errors based on plane wave simulation, 200 random samples and 3db SNR

No. of samples: 50 SNR = 6db	Estimation error percentage							
	Attenuation coef. model				Sound speed		Density	
	Slope		Y-intercept					
Eye layer	Mean	Std	Mean	Std	Mean	Std	Mean	Std
Cornea	-0.095	0.650	6.131	0.212	1.265	0.288	-1.243	0.271
Aqueous humor	-0.082	0.803	-1.058	5.422	0.766	0.841	-0.837	0.831
Lens	0.896	1.019	-7.268	3.881	-0.534	0.793	0.622	0.813
Vitreous humor	1.173	0.571	10.235	5.862	-0.839	1.836	1.175	1.912
Retina	-0.334	0.348	10.821	3.615	0.267	0.607	-0.013	0.584
Choroid	-0.916	0.376	7.192	2.923	1.546	1.575	-1.204	1.466
Sclera	-0.404	0.283	-4.145	1.959	-1.546	0.168	1.895	0.233
Absolute average:	0.557	0.579	6.693	3.411	0.966	0.873	0.999	0.873

Table 5.7: MSF acoustic parameter estimation errors based on plane wave simulation, 50 random samples and 6db SNR

No. of samples: 100 SNR = 6db	Estimation error percentage							
	Attenuation coef. model				Sound speed		Density	
	Slope		Y-intercept					
Eye layer	Mean	Std	Mean	Std	Mean	Std	Mean	Std
Cornea	0.134	0.213	-2.929	1.726	0.149	0.367	-0.147	0.366
Aqueous humor	-0.139	0.184	6.662	2.539	1.385	0.111	-1.338	0.111
Lens	0.452	0.056	-4.622	1.763	1.403	0.565	-1.310	0.550
Vitreous humor	1.095	0.128	8.314	2.428	-1.370	0.914	1.601	1.012
Retina	-0.444	0.090	4.925	1.345	0.702	0.419	-0.521	0.411
Choroid	-0.991	0.292	4.019	1.002	0.280	0.462	-0.111	0.455
Sclera	-0.421	0.308	-2.602	3.000	-0.048	1.974	0.236	2.032
Absolute average:	0.525	0.181	4.867	1.972	0.762	0.687	0.752	0.705

Table 5.8: MSF acoustic parameter estimation errors based on plane wave simulation, 100 random samples and 6db SNR

No. of samples: 200 SNR = 6db	Estimation error percentage							
	Attenuation coef. model				Sound speed		Density	
	Slope		Y-intercept					
Eye layer	Mean	Std	Mean	Std	Mean	Std	Mean	Std
Cornea	-0.071	0.426	-3.062	1.238	-1.373	0.257	1.393	0.264
Aqueous humor	0.123	0.480	5.705	2.410	1.699	0.484	-1.600	0.461
Lens	0.426	0.779	-2.459	1.816	0.720	0.811	-0.699	0.808
Vitreous humor	0.917	0.433	4.597	4.947	-0.923	0.945	1.049	0.995
Retina	-0.272	0.159	2.797	4.134	-0.151	0.349	0.235	0.266
Choroid	-0.865	0.308	1.673	3.743	0.389	0.828	-0.308	0.795
Sclera	-0.634	0.301	1.166	4.879	-0.447	1.309	0.505	1.304
Absolute average:	0.473	0.412	3.066	3.310	0.815	0.712	0.827	0.699

Table 5.9: MSF acoustic parameter estimation errors based on plane wave simulation, 200 random samples and 6db SNR

No. of samples: 50 SNR = 12db	Estimation error percentage							
	Attenuation coef. model				Sound speed		Density	
	Slope		Y-intercept					
Eye layer	Mean	Std	Mean	Std	Mean	Std	Mean	Std
Cornea	-0.073	0.358	5.915	0.955	1.506	0.395	-1.483	0.385
Aqueous humor	0.102	0.128	-0.739	5.345	0.782	0.856	-0.861	0.855
Lens	0.456	0.295	-0.832	1.961	-1.344	0.482	1.433	0.510
Vitreous humor	0.817	0.154	-0.597	4.591	0.576	0.569	-0.524	0.537
Retina	-0.527	0.208	5.309	3.361	0.004	0.347	0.111	0.303
Choroid	-0.973	0.223	4.113	4.334	0.261	1.102	-0.106	1.148
Sclera	-0.462	0.200	-7.255	0.447	-1.348	0.719	1.626	0.764
Absolute average:	0.487	0.224	3.537	2.999	0.832	0.639	0.878	0.643

Table 5.10: MSF acoustic parameter estimation errors based on plane wave simulation, 50 random samples and 12db SNR

No. of samples: 100 SNR = 12db	Estimation error percentage							
	Attenuation coef. model				Sound speed		Density	
	Slope		Y-intercept					
Eye layer	Mean	Std	Mean	Std	Mean	Std	Mean	Std
Cornea	-0.094	0.417	-2.042	2.206	0.218	0.248	-0.217	0.248
Aqueous humor	-0.026	0.308	4.184	3.401	1.122	0.435	-1.090	0.416
Lens	0.345	0.591	-4.086	1.728	0.478	0.971	-0.422	0.971
Vitreous humor	0.968	0.261	6.524	4.665	-0.423	0.505	0.613	0.530
Retina	-0.475	0.159	3.759	3.466	0.904	0.509	-0.738	0.550
Choroid	-0.847	0.210	4.035	4.230	0.509	0.514	-0.361	0.492
Sclera	-0.493	0.395	-1.454	5.634	-0.030	1.580	0.180	1.560
Absolute average:	0.464	0.334	3.727	3.619	0.527	0.680	0.517	0.681

Table 5.11: MSF acoustic parameter estimation errors based on plane wave simulation, 100 random samples and 12db SNR

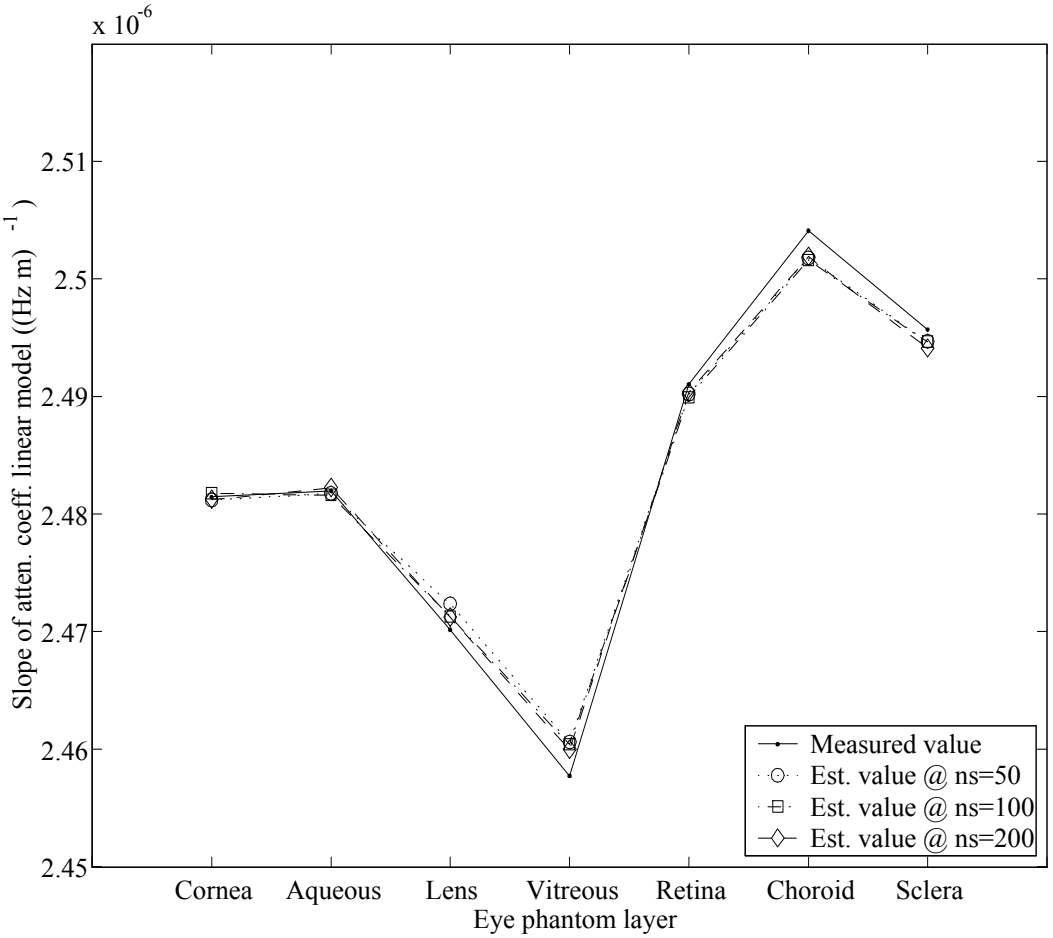

Figure 5.2: Comparison between the measured and MSF estimated slope of attenuation coefficient model based on plane wave simulation, 100 random samples and 6db SNR

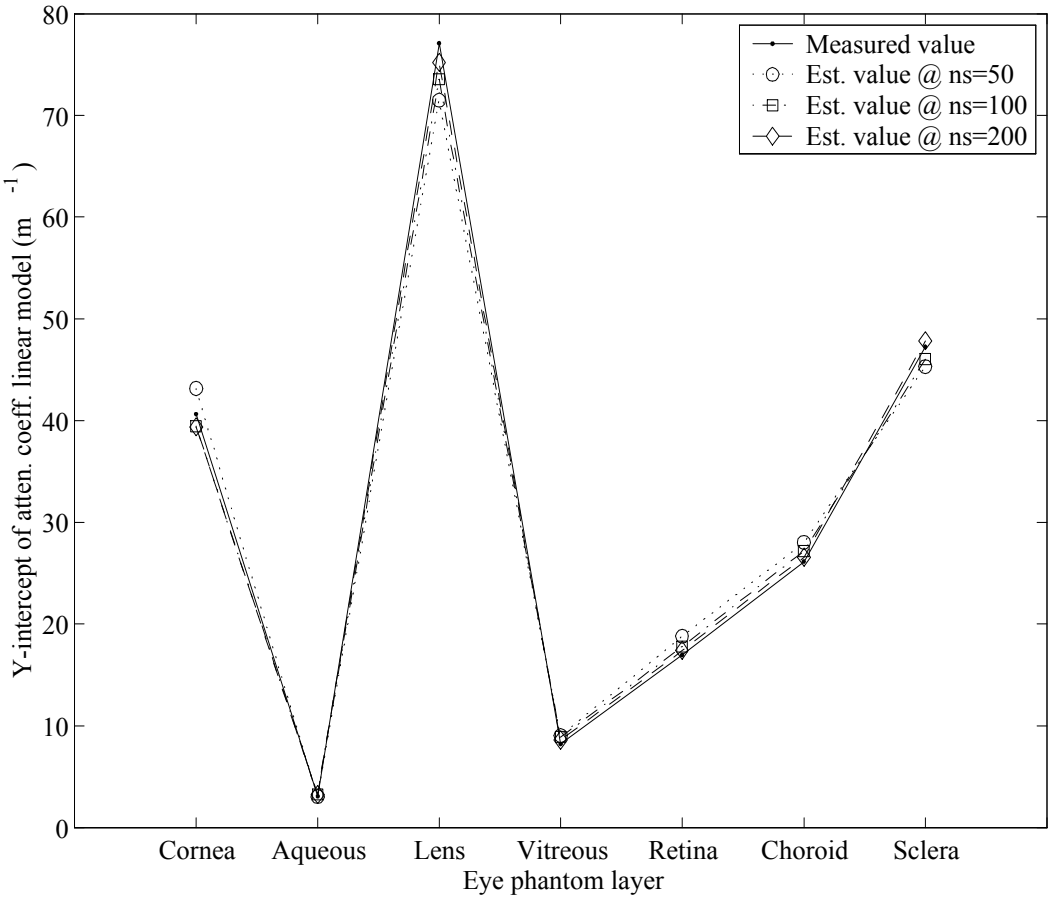

Figure 5.3: Comparison between the measured and MSF estimated y-intercept of attenuation coefficient model based on plane wave simulation, 100 random samples and 6db SNR

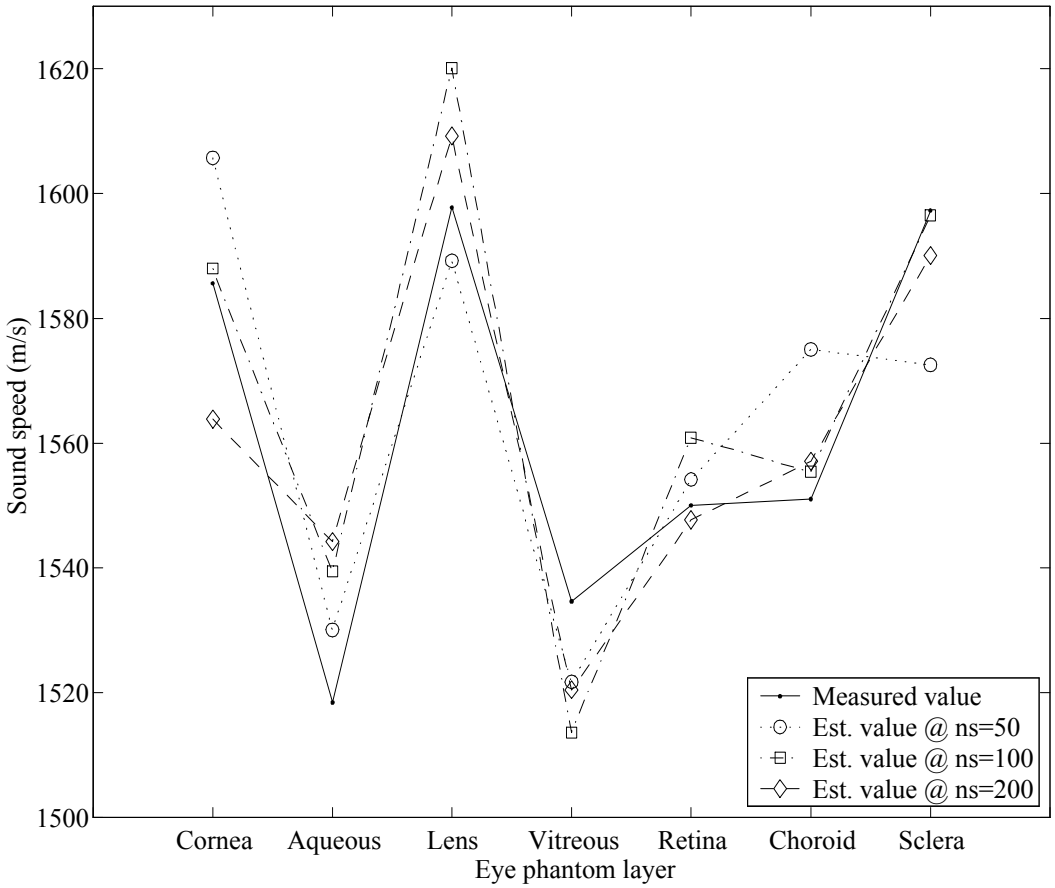

Figure 5.4: Comparison between the measured and MSF estimated sound speed based on plane wave simulation, 100 random samples and 6db SNR

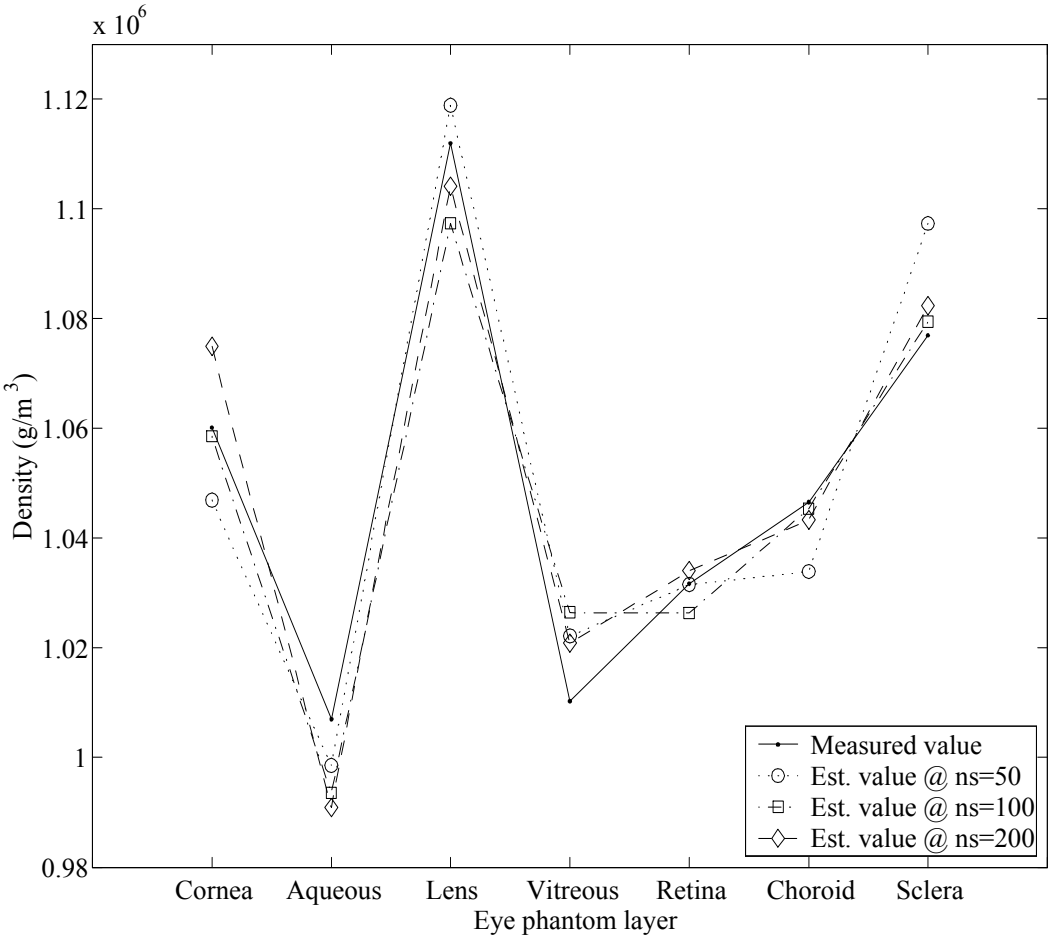

Figure 5.5: Comparison between the measured and MSF estimated density based on plane wave simulation, 100 random samples and 6db SNR

No. of samples: 200 SNR = 12db	Estimation error percentage							
	Attenuation coef. model				Sound speed		Density	
	Slope		Y-intercept					
Eye layer	Mean	Std	Mean	Std	Mean	Std	Mean	Std
Cornea	0.053	0.317	-1.002	0.659	-1.026	0.220	1.037	0.224
Aqueous humor	0.083	0.135	3.212	0.883	0.555	0.801	-0.506	0.803
Lens	0.262	0.261	-1.982	2.664	1.022	0.391	-1.008	0.391
Vitreous humor	0.822	0.179	3.641	4.096	-0.287	0.615	0.349	0.667
Retina	-0.446	0.248	2.238	4.224	0.080	0.932	-0.021	0.848
Choroid	-0.772	0.119	1.214	2.072	0.003	1.298	0.064	1.346
Sclera	-0.692	0.345	-2.231	5.058	-0.247	1.143	0.307	1.083
Absolute average:	0.447	0.229	2.217	2.808	0.460	0.771	0.470	0.766

Table 5.12: MSF acoustic parameter estimation errors based on plane wave simulation, 200 random samples and 12db SNR

information of noisy measurements). The samples with high weights are used to construct the posterior PDF of the parameters. Moreover, the average reduction of estimation error with respect to the increase of random samples is 17% per 50 samples. This error reduction is small relative to the random sample increase of 100% (i.e., increase from 50 to 100 and from 100 to 200). Therefore, the estimation accuracy of MSF can be considered insensitive to the size of random samples. Furthermore, the estimation error of these three parameters increase for later layers of the tissue (i.e., layers further away from the transducer). This is because MSF estimates acoustic parameter recursively, as such the estimation results of the previous layers are used in the estimation of the current layer. Therefore, the estimation error accumulate through the layers.

5.4 Summary

MSF is tested using a simulated inverse scattering problem in order to analyze the behavior and performance of MSF in the absence of physical modeling uncertainties. Results show that MSF achieves an average absolute estimation error of 1.6%. Also, MSF is not heavily dependent on the size of random samples and SNR.

Chapter 6

Investigation on Multi-layered Tissue Phantoms

In order to evaluate the acoustic parameter estimation accuracy of MSF, calibrated test subjects with acoustic characteristics comparable to that of the real tissues are needed. Since ultrasound is widely accepted for clinical eye examination and the eye is a multi-layered organ, ocular tissues are chosen for testing. Although ocular tissues are available, they are inadequate test subjects since their acoustic characteristics can be affected by many factors including freshness and medical conditions of the animals. Therefore, it is necessary to develop tissue phantoms with stable acoustic characteristics as test subjects. The development of tissue phantoms requires the acoustic parameters of real tissues. A brief background on the anatomy of the mammalian eye is presented. Real cow eye tissues are characterized. Tissue phantoms of the cow eye are fabricated based on the tissue characteristics. A series of experiments are conducted to characterize the tissue phantoms using ultrasound. The equipment and its settings used for acquiring ultrasound echoes from the phantoms are presented. They are followed by the phantom acoustic parameter estimation results produced by MSF.

6.1 Anatomy of the Eye

Ultrasound testing of the eye focuses on the ocular structures along the optical axis. For mammalian eyes, there are seven ocular layers along the optical axis, namely cornea, anterior chamber, lens, posterior chamber, retina, choroid and sclera. Brief

descriptions of these layers are presented below. Details of the anatomy of the eye can be found in [148, 149]. These layers are depicted in Figure 6.1[1].

1. Cornea is a avascular, transparent tissue that covers one-sixth of the anterior surface of the eyeball. In addition, it refracts the entering light as part of the eye focusing system.

2. The anterior chamber is filled with a watery liquid from blood filtration known as the aqueous humor. It is absorbed back to the circulation through a venous ring at the base of the cornea. Aqueous humor helps maintaining the intraocular pressure, refracts light, and provides nutrients to the avascular cornea and lens.

3. Lens is a transparent, biconvex, flexible disc attached to the ciliary muscles, which control the curvature of the lens to focus light onto the retina.

4. Posterior chamber occupies four-fifths the eyeball in length. It is filled with a transparent, gelatinous substance known as the vitreous humor. The functions of vitreous humor include maintaining pressure within the eye and holding the lens and the retina in place. Vitreous humor does not circulate like aqueous humor.

5. Retina consists of two layers, namely an outer pigmented layer and an inner sensory layer. The pigmented layer is attached to the choroid, and they prevent light reflection within the eye. The sensory layer contains photoreceptor cells called rods and cones, and numerous neurons. In general, rods are twenty times more prevalent than cones and are responsible for light sensing to provide colorless blurry image. On the other hand, cones produce sharp colored vision given sufficient light source.

6. Choroid is a very thin, highly vascular, heavily pigmented layer firmly attached to the retina. Because of the heavy pigmentation, it appears black in color to absorb entering light and to avoid reflection for vision interference.

7. Sclera is an opaque, white, dense fibrous outer layer of the eye wall. Externally, a small anterior portion of sclera can be seen as the white part of the eye surrounding the cornea, and the posterior of sclera provides attachment sites for the extrinsic muscles involved in eyeball movements. It also helps maintain the shape of the eye. Internally, sclera is loosely attached to choroid and protects the internal structure of the eye.

[1]The source of this figure is http://en.wikipedia.org/wiki/Eye.

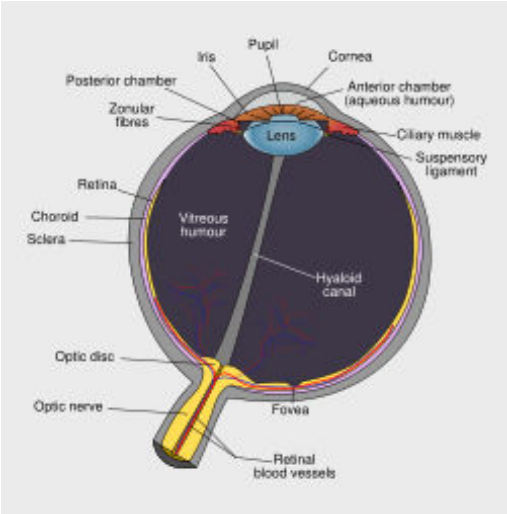

Figure 6.1: Anatomy of the eye

6.2 Characterization of Eye Tissues

The eye tissue acoustic characteristics of interest in this work are sound speed, attenuation coefficient and density. Data of ocular tissue sound speeds and attenuation coefficients found in the literature [150, 151, 152, 23, 153] are summarized in Tables 6.1 and 6.2. However, data of ocular tissue densities are scarce. Experiments on ocular tissue density measurements are conducted by our research collaborators. Bovine eyes are employed because they can be purchased from a beef processing plant nearby (Better Beef Ltd., Guelph, Ontario, Canada). Bovine eyes within a few hours after slaughtered are dissected to extract the seven tissues along the optical path, namely cornea, aqueous humor, lens, vitreous humor, retina, choroid and sclera, as illustrated in Tables 6.3 and 6.4. Except for aqueous humor and vitreous humor, all excised tissues are first preserved in a mixture of Medium 199 (Sigma M3769-1), Fetal Bovine Serum (Sigma F1051), penicillin, L-Glutamine, HEPES and sodium bicarbonate. Densities of these tissues are measured using a solution density comparison method [154]. Brief descriptions of this method are presented here. Solutions of various concentrations are made by dissolving different amounts of sucrose (Sigma S1174) in Medium 199 (Sigma M3769-1). These tissues are carefully immersed in the sucrose solutions of various concentrations. All visible air bubbles on the surface of the immersed tissue are removed. When the tissue floats, its density is less than that of the solution. The converse is true when the

Ocular tissue	Sound speed (m/s)			
	Human		Porcine	
	Mean range	Std range	Mean range	Std range
Cornea	1553.0 - 1632.1	3.0 - 15.5	1555.0 - 1595.0	2.0 - 12.0
Aqueous humor	1510.4 - 1514.3	3.9 - 8.6	-	-
Lens	1538.1 - 1645.0	1.2 - 16	1610.0 - 1677.0	2.0 - 10.7
Vitreous humor	1503.0 - 1530.0	0.5 - 7.3	1497.0 - 1531.0	1.0 - 20.0
Retina	1538.0 - 1576.5	20 - 38	1532.0 - 1548.5	4.0 - 15.1
Choroid	1530.8 - 1527.0	16	1546.8 - 1523.0	19.5
Sclera	1583.0 - 1745.0	10 - 55	1604.0 - 1661.0	2.0 - 11.1

Table 6.1: Sound speeds in normal ocluar tissues taken from the literature

Ocular tissue	Attenuation coefficient (dB/(cm MHz))			
	Human		Porcine	
	Mean	Std	Mean	Std
Cornea	0.78	0.39	1.15	0.14
Aqueous humor	-	-	-	-
Lens	1.19	0.29	1.33	0.15
Vitreous humor	-	-	-	-
Retina	1.15	0.42	0.83	0.31
Choroid	0.95	0.4	1.56	0.29
Sclera	0.97	0.22	1.68	0.31

Table 6.2: Attenuation coefficients of ocluar tissues taken from literature

tissue sinks. The initial concentration of sucrose solution is determined as the concentration at which the bovine eye ball is suspended in the solution. The upper and lower density bounds of each tissue are first determined by testing it with solutions of various concentrations until it floats and sinks. A bisection search of the tissue density is then performed. The search is terminated when the adjustment of the solution concentration is within 1%. The densities of aqueous humor and vitreous humor are gauged based on their weight and volume. The measurements of bovine ocular layer densities are reported in Table 6.5.

Thicknesses of the ocular tissues are also needed for the eye phantom development. Although the thicknesses of some excised ocular tissues can be gauged by a caliber, the measurements are unreliable due to tissue compressibility. Also, aqueous humor and vitreous humor are liquid-like substances, their shapes and thicknesses can only be maintained within intact eyes. A convenient way to access

Step 1 - extract aqueous humor by a syringe

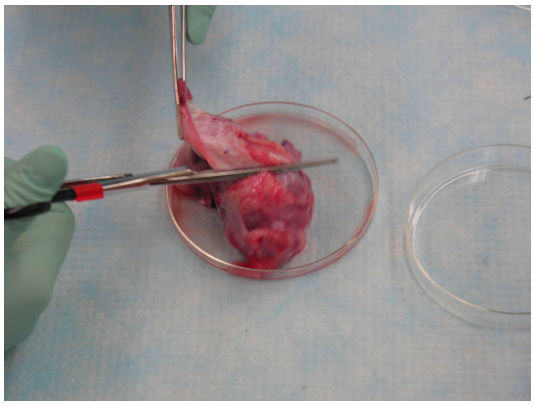

Step 2 - remove muscles surrounding the eye

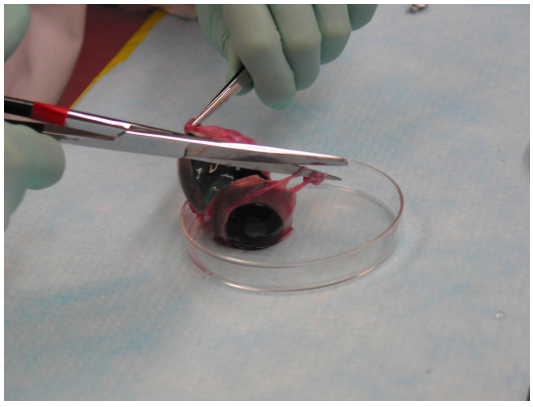

Step 3 - cut the eye in half

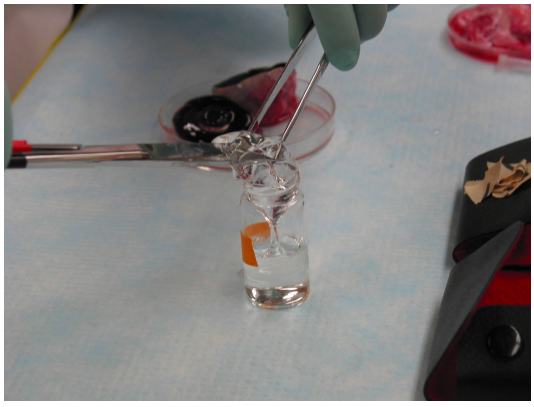

Step 4 - extract vitreous humor

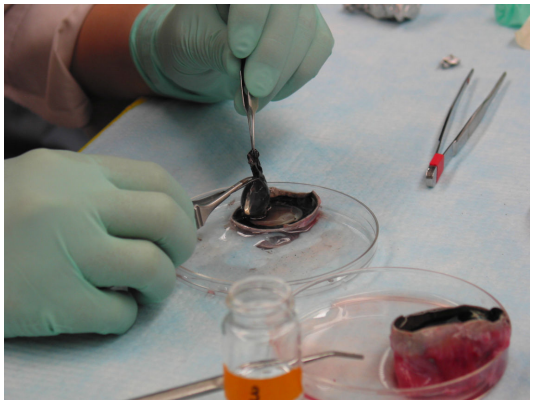

Step 5 - extract lens

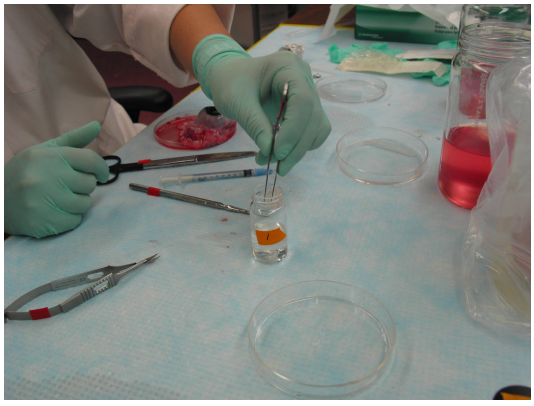

Step 6 - extract Cornea

Table 6.3: Illustration of bovine ocular layer dissections part 1

Step 7 - extract retina

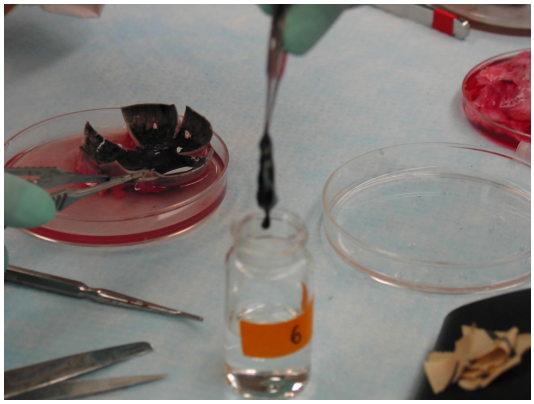

Step 8 - extract choroid

Step 9 - extract sclera

Table 6.4: Illustration of bovine ocular layer dissections part 2

Ocular tissue	Density (g/ml)		Thickness (mm)	
	Mean	Std	Mean	Std
Cornea	1.061	0.004	1.840	0.029
Aqueous humor	1.005	0.012	3.066	0.104
Lens	1.104	0.001	10.695	0.111
Vitreous humor	1.007	0.010	17.142	0.096
Retina	1.033	0.002	0.829	0.039
Choroid	1.052	0.002	0.279	0.004
Sclera	1.076	0.003	1.881	0.043

Table 6.5: Density and thickness measurements of bovine ocluar tissues

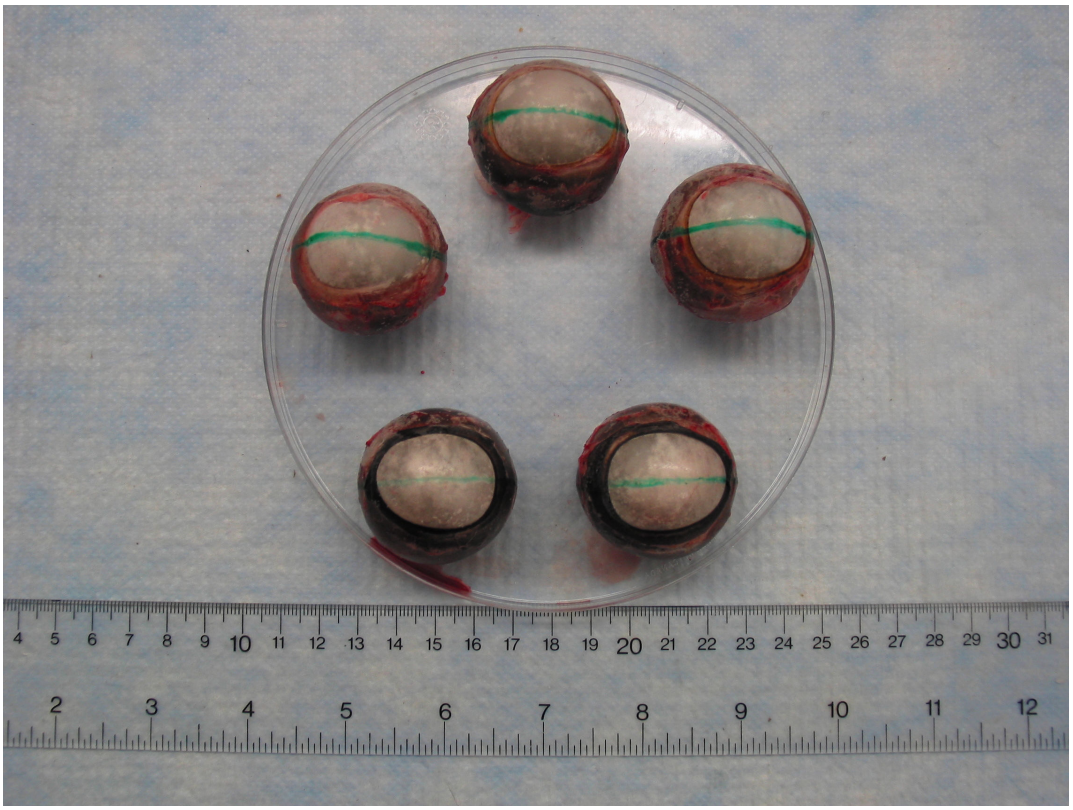

Figure 6.2: Bovine eyes frozen for ocluar layer thickness measurements

all ocular tissues and to maintain their shapes is to cut a frozen eyeball along its optical path. Bovine eyes are frozen, as shown in Figure 6.2, in a cryostat and cut in two halves along their optical paths. The cross sections of eye balls are imaged by a digital camera using four mega pixel resolution as displayed in Figure 6.3. The the ocular thicknesses are measured using a software called ImageJ. The resulting ocular thicknesses are shown in Table 6.5.

6.3 Development of Tissue Phantoms

The development of a tissue phantom involves material selection and fabrication, which are described in the subsequent sections.

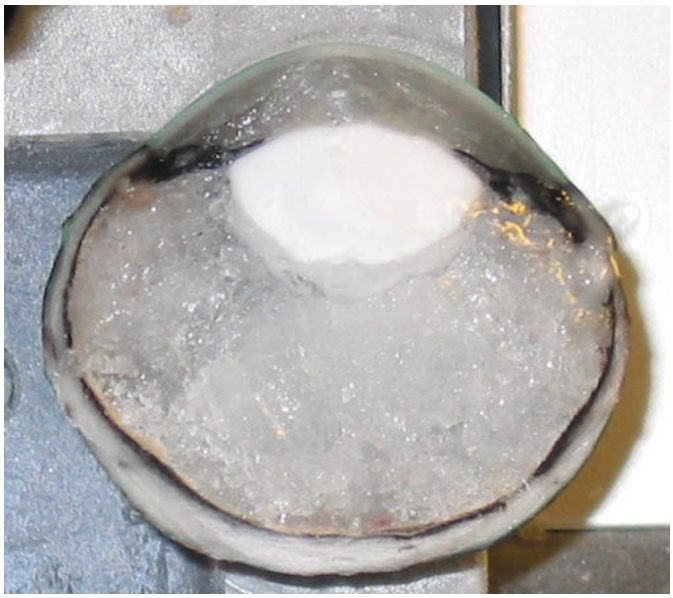

Figure 6.3: Cross section of a bovine eye used for ocluar thickness measurements

6.3.1 Phantom Material Selection

A number of materials have been used to construct phantoms of some ocular tissues in the literature including acrylamide/bis-acrylamide (acrylamide/bis) [155, 156] and silicone based materials [157]. For making non-ocular tissue phantoms, agar [158, 159, 160, 161, 162] and gelatin [163, 164, 165, 166, 167, 168] based materials have been used extensively.

Recipes of tissue phantoms are commonly specified as concentrations by weight, which are equivalent to the densities of materials. These materials are tested to determine if they can be used to fabricate phantoms of the densities of ocular tissues shown in Table 6.5. Protocol two in [155] is implemented using 40% (weight/volume) 29:1 acrylamide/bis solution (VWR) with various amounts of de-ionized water. The highest density obtained is slightly larger than 1.03 g/ml. Higher density acrylamide/bis solutions can be obtained by mixing acrylamide/bis powder with de-ionized water. However, acrylamide/bis powder is a neural toxin and is carcinogenic. To avoid potential health risks, acrylamide/bis powder is not considered in this work. In addition, a silicone elastomer called Sylgard 184 (Dow Corning) is investigated. The density of this material is also approximately 1.03 g/ml. Furthermore, various concentrations of agar and gelatin solutions are made by mixing Agarose (Sigma A9539) and gelatin (Sigma-Aldrich G2500) powders and

de-ionized water. These solutions are heated until the powder is completely dissolved. At high concentrations, both solutions become quite viscous such that air bubbles produced by heating the solutions are trapped.

Although both agar and gelatin solutions are too viscous for our application at high concentrations, it can be observed that gelatin solutions are less viscous than that of agar. For this reason, gelatin is selected as a phantom ingredient. We then investigate making high concentration gelatin solutions with smaller amount of gelatin powder to reduce viscosity. The key to achieving this is to find a chemical that polymerizes with gelatin in water and is water soluble in large quantities without greatly increasing the solution viscosity. One such chemical came to mind is sucrose, which polymerizes with gelatin and hence they are common ingredients of various foods. Also, sucrose is known for its high dissolvability in water without greatly increasing the viscosity of a solution. Therefore, sucrose is selected as another ingredient of the eye phantom. Experimentations are conducted to investigate the effect of the ratio between gelatin and sucrose on polymerization, solution viscosity and phantom consistency. It can be concluded that the mix with equal amounts of gelatin and sucrose yields the best results.

6.3.2 Phantom Fabrication

Each layer of the eye phantom is fabricated by mixing appropriate amounts of gelatin, sucrose and water to obtain the densities of ocular tissues shown in Table 6.5. Powders of gelatin (Sigma-Aldrich G2500) and sucrose (Sigma S1174) are added in a clean, dry 100ml Erlenmeyer flask to the weights specified in Table 6.6. The weights of gelatin and sucrose are gauged by a precision balance (Mettler Toledo AL204 analytical balance). Degased water is added to the flask to reach 100ml. The degased water is also de-ionized and filtered. The gelatin-sucrose-water mixture is heated in a microwave oven until the gelatin and sucrose are completely dissolved (i.e., the powders become transparent) and before boiling. The heated solution is then degased using a vacuum system until no air bubbles are produced. Polymerization takes place in the vacuum system to form a solid as the solution cools down. The solid is heated by a microwave oven until it is just melted.

Two tissue phantoms are fabricated in this work as test subjects. The first is a seven-layered phantom that emulates the mammalian eye along the optical path. The second is a $4 \times 3 \times 4$ phantom array that comprises various combinations of ocular layers. For seven-layered phantom, the procedures described above are performed seven times to fabricate the gelatin-sucrose solutions of the ocular tissue phantoms listed in Table 6.6. This phantom is constructed by dispensing

Tissue phantom	Weight (g)	
	Gelatin	Sucrose
Cornea	9.277	9.269
Aqueous humor	2.522	2.513
Lens	14.578	14.574
Vitreous humor	2.716	2.708
Retina	5.843	5.842
Choroid	8.208	8.210
Sclera	11.120	11.125

Table 6.6: Ingredient weights of tissue phantoms

the solutions of its layers one at a time in a container in the sequence illustrated in Figure 6.4. The container is a well (i.e., cylindrical opening with 35mm diameter) of a 6-well microtiter plate (BD Falcon). After dispensing the solution of each layer, the 6-well plate is placed on a leveling platform (self made) to ensure the tissue phantom surface is parallel to the bottom of the plate. The 6-well plate with the leveling platform is kept in a refrigerator for thirty minutes to facilitate polymerization. The dispensed solution volumes are proportional to the ocular tissue thicknesses shown in Table 6.5. Theoretically, the thinnest phantom (i.e., choroid, 0.279mm thick) requires only 0.268ml ($\pi \times 1.75^2 \times 0.279 \times 0.01$) of the solution to build the thickness in the well. Practically, 0.268ml of the solution is insufficient to sustain a layer at the well center due to meniscus effect. The minimum solution volume needed to sustain a layer at the well center is experimentally determined as 1.18ml. The volumes of the solutions are scaled based on ocular layer thickness measurements, while keeping the thickness of phantom eye less than the height of the well. The actual dispensed solution volumes are listed in Table 6.7. It should be noted that some of the solution is adhered on the inside of the pipette tip due to its viscosity, so that the actual dispensed volumes are less than the value shown.

For the $4 \times 3 \times 4$ phantom array, a 4×3 grid is created by two 6-well microtiter plates (BD Falcon). Each of these plates has six wells arranged in two rows and three columns. Four ocular tissue phantom layers are deposited in each of these twelve wells. The sequence of layers is different for each well. Each layer is formed by 3ml (or 3cm^3) of gelatin and sucrose solution, which is measured and dispensed by a pipette (Eppendorf). The thickness of each layer can be calculated as $3/(\pi \times 1.75^2) = 3.1\text{cm}^2$. As mentioned above, the solution is attached on the inside of the pipette tip due to its viscosity. Therefore, the layer thickness

[2]The radius of each well is 1.75cm.

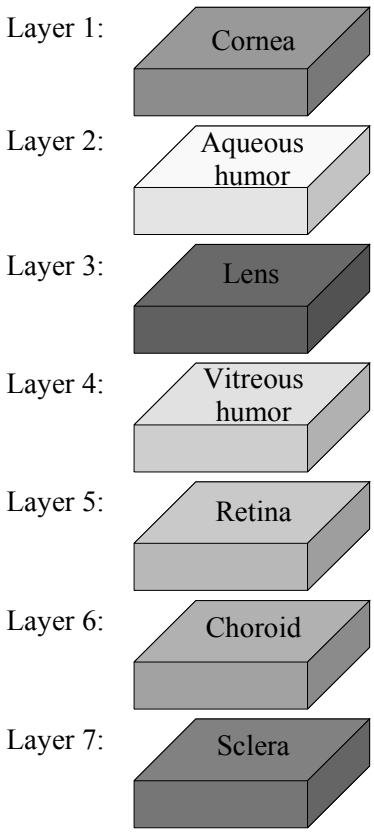

Figure 6.4: The tissue phantom deposit sequence for the second experiment

Tissue phantom	Volume (ml)
Cornea	1.33
Aqueous humor	1.45
Lens	2.18
Vitreous humor	2.80
Retina	1.23
Choroid	1.18
Sclera	1.34

Table 6.7: Volumes of gelatin-sucrose solutions used to fabricate tissue phantoms

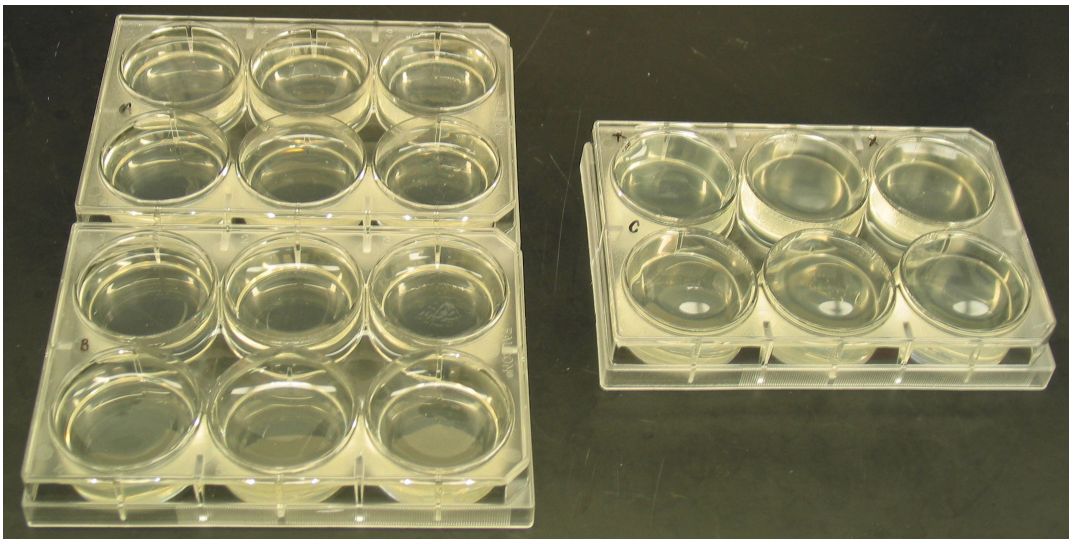

Figure 6.5: Fabricated tissue phantoms: 4x3x4 array on the left and 7-layer on the right

is expect to be less than 31mm. For each layer deposit, the 6-well plate is placed on a leveling platform (self made) to ensure the tissue phantom layer is parallel to the bottom of the plate. The 6-well plate with the leveling platform is kept in a refrigerator for thirty minutes to facilitate polymerization. The sequence of layers and the fabricated phantom array are shown in Figures 6.6 and 6.5, respectively.

6.4 Experimental Validation

As mention previously, the eye phantom is developed as a calibrated model to evaluate the estimation accuracy of MSF. Therefore, the phantom must be characterized to validate the similarity of acoustic parameters between the phantom and real ocular tissues. Experiments are conducted to characterize the phantom using ultrasound. The experimental setup and results are discussed in the following.

6.4.1 Experimental Setup

The experimental setup employed to realize ultrasound characterization of the eye phantom includes A) an electronics system that emits and receives ultrasound signals to and from the phantom, B) a mechanical system that aligns the surfaces

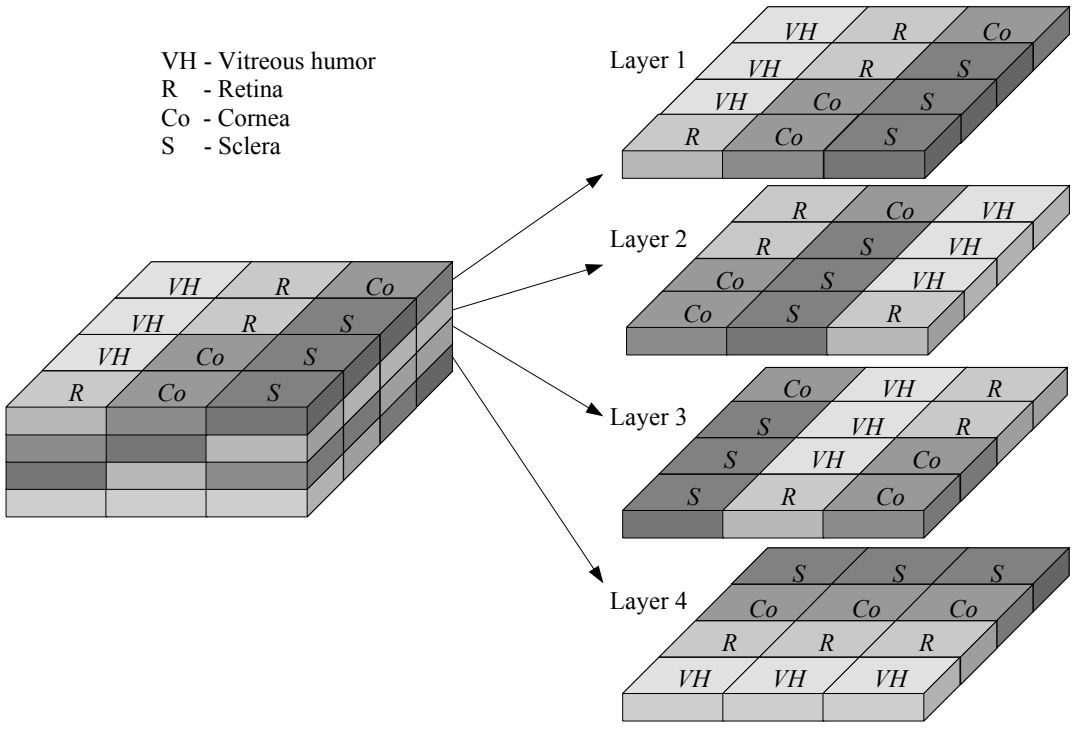

Figure 6.6: Tissue phantom layers chosen and deposit sequences for the first experiment

Pulser-receiver		Oscilloscope	
Pulse frequency:	1kHz	Sampling rate:	1GS/s
Gain:	39db	Coupling:	AC
Energy setting:	4	Sweep average:	500
Damping setting:	3	Bandwidth:	full
Filtering:	none	Probe attenuation:	1
		Noise filter:	none
		offset:	0
		Trigger:	negative edge, -500mV

Table 6.8: Settings of pulser-receiver and oscilloscope

of the ultrasound transducer and phantom, setups that are designed for C) sound speed and D) attenuation coefficient measurements, and E) software that processes ultrasound signals. These systems and setup are described in the following.

A) Ultrasound system

The ultrasound system comprises of three components shown in Figure 6.7: polymer immersion transducer (Olympus PI35-2-R 1.00), pulser-receiver (Olympus 5073PR) and digital oscilloscope (Lecroy WaveRunner 64Xi). These components are connected in series. The transducer converts the high voltage pulses generated by the pulser-receiver to acoustic waves, and transforms acoustic echoes from the tissue phantoms to analog signals. The pulser-receiver also amplifies and filters the signal from the transducer. The oscilloscope serves as an analog-to-digital converter, a signal display device as well as a data logger. The settings of pulser-receiver and oscilloscope used in the experiments are listed in Table 6.8.

B) Mechanical system

The mechanical system consists of four components: transducer mount, five-degree-of-freedom manipulator, water tank and leveling platform. The transducer mount is a circular plate with a transducer fitting at the center and perpendicular to the plate surfaces. The diameter of the circular plate is larger than the opening of the tissue phantom container (i.e., a well of 6-well microtiter plate) to limit the transducer from getting into the opening to protect and to prevent compressing the tissue phantoms. The transducer mount is coupled to the five-degree-of-freedom manipulator that adjusts the pose of the transducer to gain good signal strength. The tissue phantom container

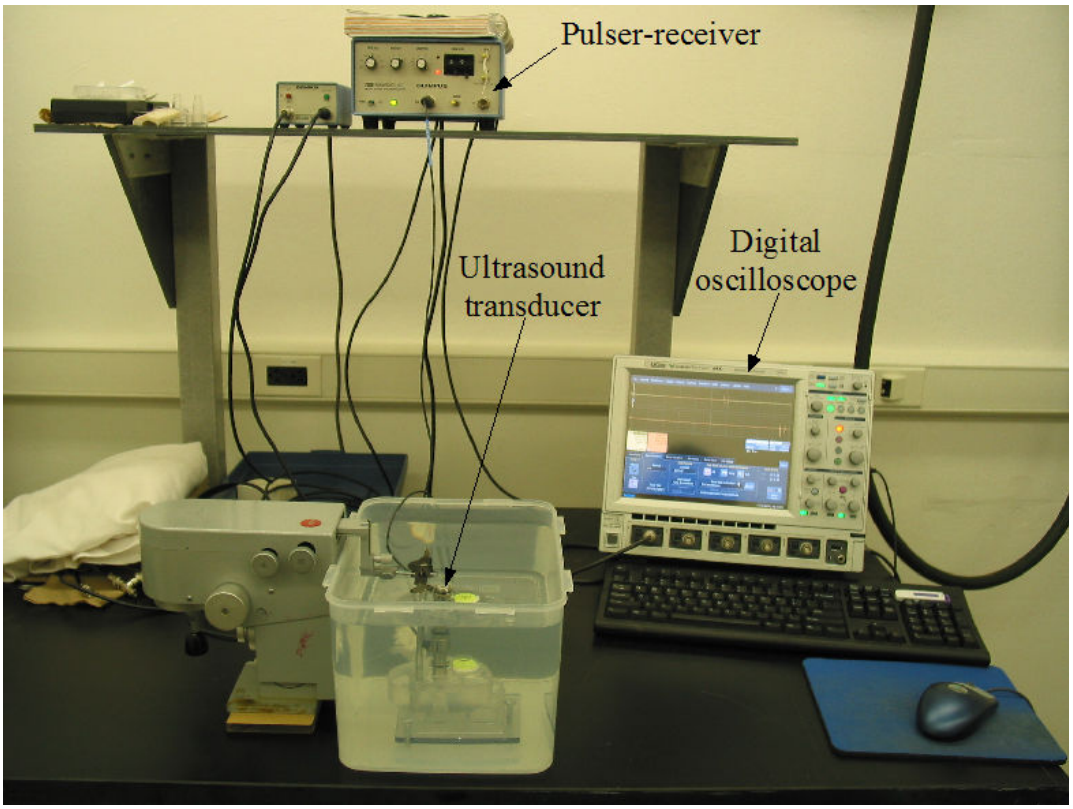

Figure 6.7: Electrical system of the ultrasound echo acquisition equipment

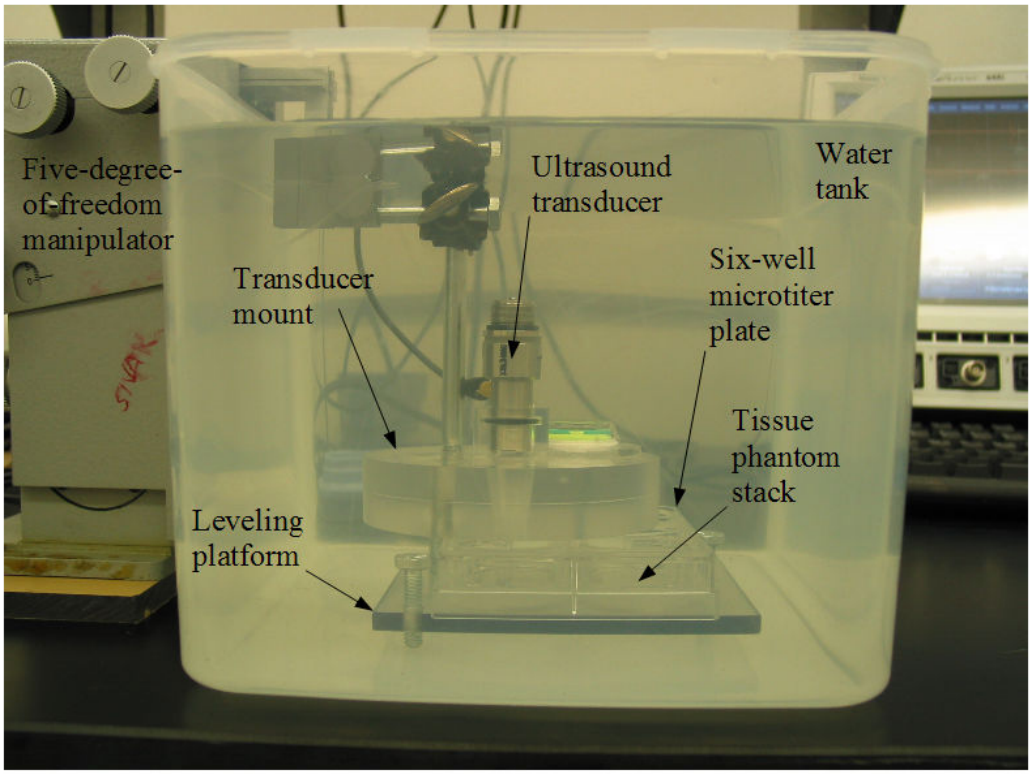

Figure 6.8: Mechanical system of the ultrasound echo acquisition equipment

is placed on the leveling platform for orientation adjustment to improve signal quality. The transducer, transducer mount, tissue phantoms and leveling platform are immersed in distilled and filtered water for acoustic coupling. The mechanical system is depicted in Figure 6.8.

C) Sound Speed Measurement Setup

The thickness of tissue phantom is crucial for its sound speed measurement. Precise thickness of a phantom is obtained by molding it in a special design container depicted in Figure 6.9. This container is made of three layers of lexan and plexiglass, since these materials are widely available and are transparent so that inspection for air bubbles is made possible. The layers are attached together by an adhesive. The middle layer is machined to create an opening of the container. The thicknesses of the layers and container are measured by a digital micrometer to calculate the distance between the in-

ner surfaces of the container. This distance determines the thickness of the phantom. The layer between the phantom and transducer is chosen to be thin, as illustrated in Figure 6.10, to reduce the attenuation of ultrasound signal transmitting through it. Also, lexan is used for this layer instead of plexiglass, since the difference of acoustic impedance between lexan and water is less than that between plexiglass and water. Therefore, the power of ultrasound signal transmits through the water-lexan interface is higher than that of the water-plexiglass interface. On the other hand, thicker pieces of plexiglass are used for other layers to strengthen the container and to increase the power of ultrasound echo at the phantom-plexiglass interface.

D) Attenuation Coefficient Measurement Setup

Attenuation coefficients of an eye phantom layer are measured based on the magnitudes of echoes from the phantom of various thicknesses. Three thicknesses of each eye phantom layer are obtained by depositing 2ml, 3.5ml and 5ml of the corresponding gelatin-sucrose solution into a row of a 6-well plate as demonstrated in Figure 6.11. The thicknesses of these phantoms are determined as 2.079mm, 3.638mm and 5.197mm. The ultrasound transducer active surface is aligned to be parallel to the surfaces of the phantoms using the mechanical system. The same distance is maintained between the ultrasound transducer surface and each phantom surface to eliminate variation of signal attenuation due to the water in between these surfaces.

6.4.2 Frequency Contents of Incident Waves

The wave form of the incident wave is obtained from the backscattered signals from a mirror finished surface of a stainless steel plate. The mirror finished surface is positioned in parallel and one inch from the transducer. Twenty sets of 1024 backscattered signal samples of the stainless steel plate are collected, and the mean of these sets is preprocessed by the bandpass filter described in Section 3.1. The frequency contents of the incident wave are shown in Figure 6.12.

6.4.3 Measurement Noise Characterization

The statistical model of measurement noise data is assumed to be a Gaussian mixture. The parameters of the Gaussian mixture are estimated using expectation maximization [116]. Data of measurement noise are acquired using the equipment described in Section 6.4.1 with the absence of tissue phantom. Twenty sets of 1024

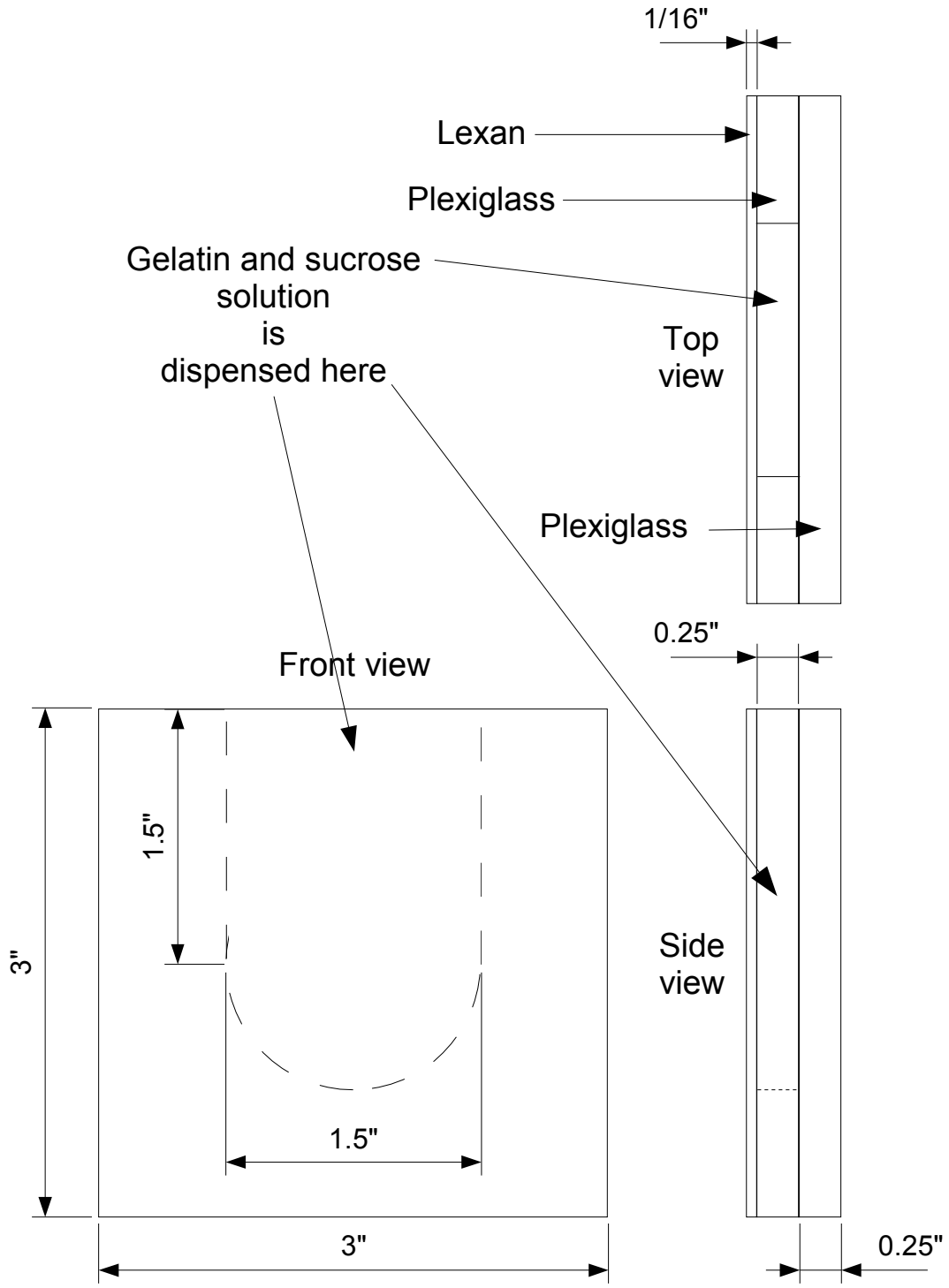

Figure 6.9: Container used for sound speed measurement

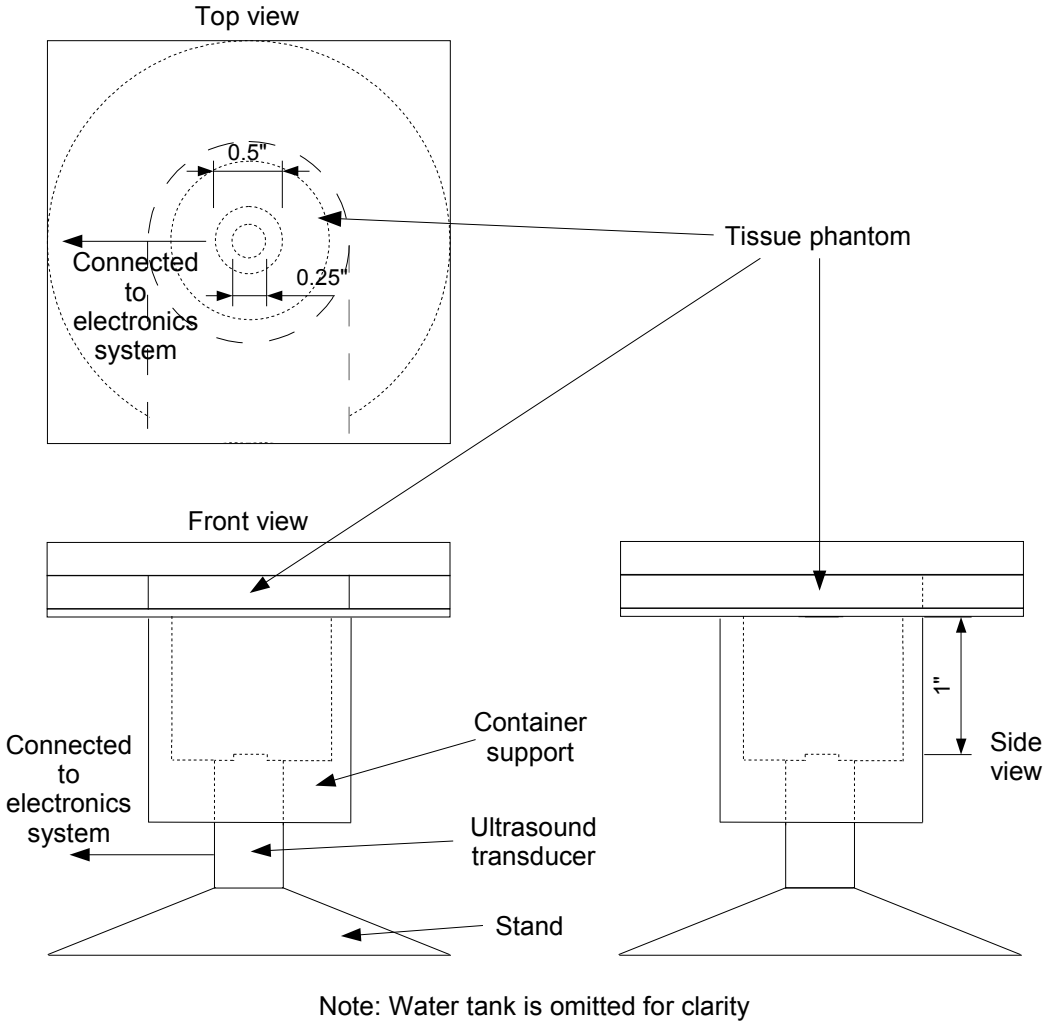

Figure 6.10: Schematics of sound speed measurement setup

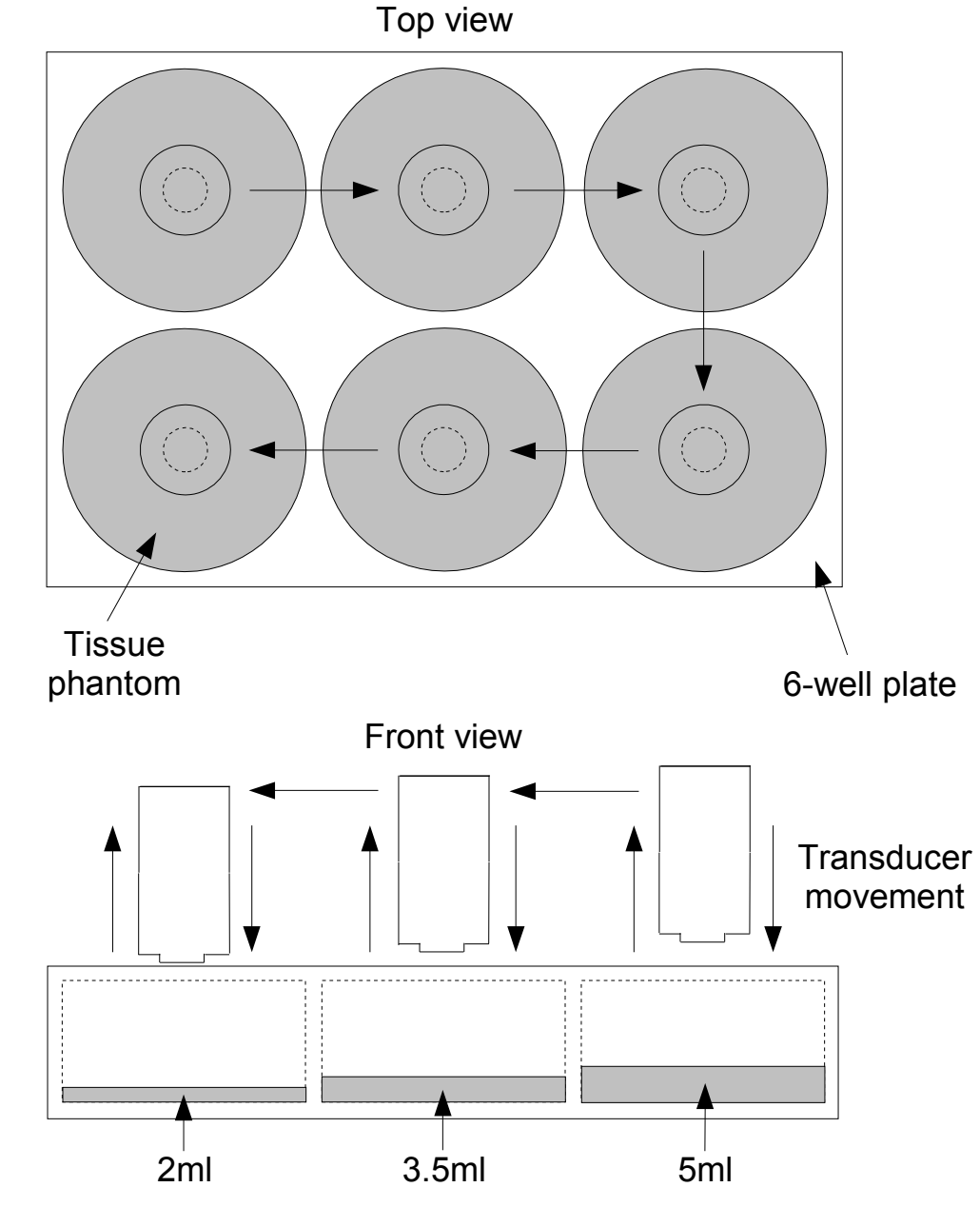

Figure 6.11: Attenuation coefficient measurement setup

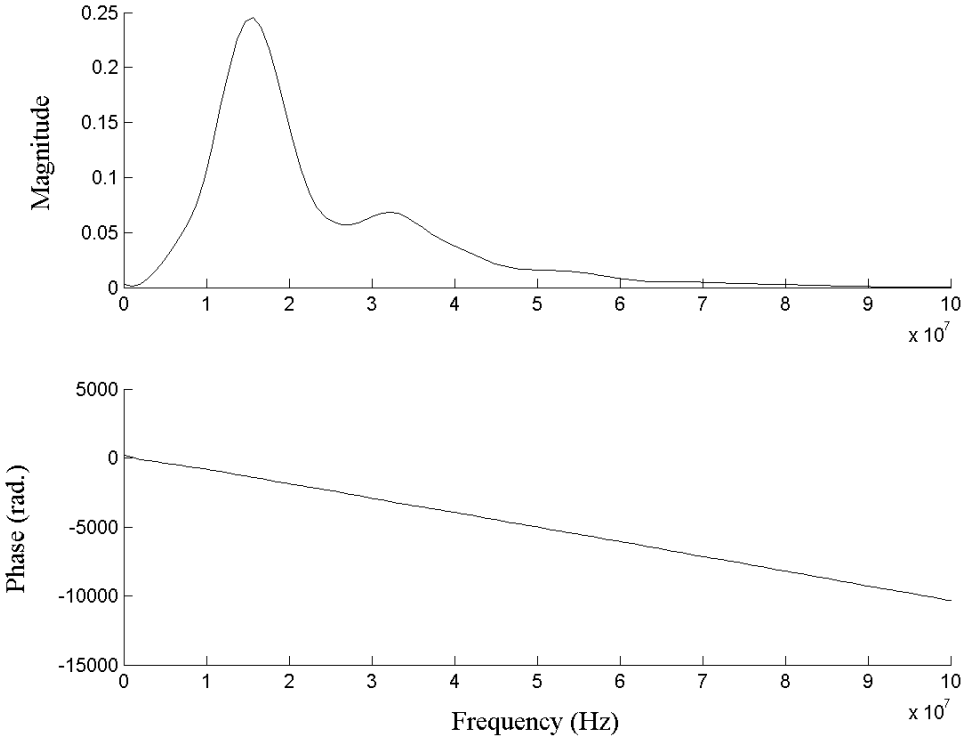

Figure 6.12: Frequency contents of incident wave

Gaussian mixture parameter	Gaussian component	
	1	2
Weight	0.3546	0.6454
Mean	0.3523e-4	0.1905e-4
Variance	1.3956e-10	6.6024e-11

Table 6.9: Parameters of Gaussian mixture for measurement noise model

measurement noise samples are collected, and the mean of these sets is taken for modelling. The resulting mean data (i.e., 1024 samples) is preprocessed by the bandpass filter described in Section 3.1. Since the measurement model is established in the frequency domain, the noise model is the statistical model of the noise frequency content. Ideally, a noise model should be established for each frequency. However, it is a cumbersome undertaking. In addition, fast Fourier transforms of each of these sets (not shown) reveal that the noise frequency contents are fairly uniform in the transducer's frequency range. Therefore, one measurement noise model is applied to all frequencies. Determining the optimal number of Gaussian components for modelling is out of the scope of this research. Experiments of noise model estimation using one to ten Gaussian components are conducted, and for each number of Gaussian component the model estimation is repeated ten times. Figure 6.13 shows the averaged likelihoods, which increase with the number of Gaussian components as expected. The largest likelihood increase is from one to two Gaussian components, and the computing power required for MSF decreases with the number of components. Therefore, Gaussian mixture of two components is selected as the measurement noise model. The Gaussian parameters estimated for this noise model are listed in Table 6.9.

6.4.4 Ultrasound Eye Phantom Layer Characterization

Measurement procedures and results of density, sound speed and attenuation coefficients of the eye phantom layers are presented in the following. The measurement results of these parameters are compared to data in the literature.

A) Sound Speed

Sound speed is measured based on the time for the wave to propagate through the eye phantom layer and the thickness of the layer. Containers are fabricated to mold the phantoms to known thicknesses. The sound speed of each eye

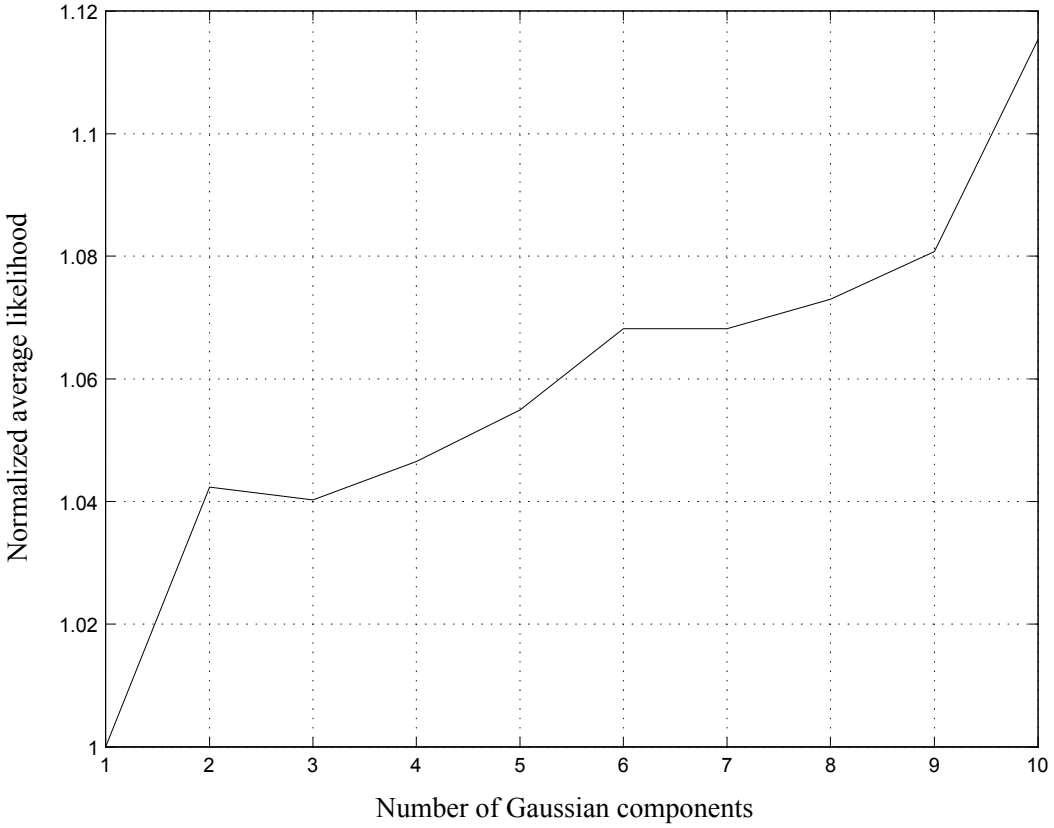

Figure 6.13: Effect of number of Gaussian components on averaged likelihood of measurement noise frequency contents

phantom layer can be calculated as,

$$c = \frac{d}{0.5(t_2 - t_1)} \tag{6.1}$$

where c is the sound speed of an eye phantom layer; d is the distance between the inner lexan and plexiglass surfaces; t_1 and t_2 are the time at which the transducer receives echoes from the inner lexan and plexiglass surfaces. Sound speed measurements of the eye phantom layers are reported in Table 6.10. Reference data of ocular tissue sound speeds and attenuation coefficients are available since the early 60's [169, 170, 171, 172, 151, 152, 23]. The sound speeds and attenuation coefficients of the phantoms are compared to the more recent data in [23]. Since [23] only focuses on the acoustic parameters of human and porcine ocular tissues, the parameters of the phantoms are examined with respect to that of these tissues. The parameters of aqueous humor are not reported in [23]. Therefore, no comparisons to aqueous humor are made. Except for vitreous and choroid, the phantom sound speeds are between that of human and porcine ocular tissues as depicted in Figure 6.14. The sound speed of the choroid phantom is within the range of that of porcine. The average, smallest and largest absolute difference between the sound speeds of eye phantom layers, human and porcine ocular tissues are shown in Table 6.11. It should be noted that the sound speed differences between human and porcine ocular tissues are larger than that between human ocular tissues and phantoms, as well as that between porcine ocular tissues and phantoms. This indicates that the sound speeds of the phantoms are more similar to that of both human and porcine ocular tissues than the ocular tissue sound speeds between these species.

B) Attenuation Coefficient

Attenuation coefficient is frequency dependant. For each frequency f, the attenuation coefficient of an eye phantom layer can be calculated as,

$$\alpha_f = log_{10}\left(\frac{a_{i,f}}{a_{j,f}}\right) / \left(-2\ (d_i - d_j)\right) \tag{6.2}$$

where α_f is the attenuation coefficient of an eye phantom layer at f; d_i and d_j are the thicknesses of the phantom; $a_{i,f}$ and $a_{j,f}$ are the amplitudes of the f component of echoes from the interface between 6-well plate and d_i- and d_j-thick phantoms, respectively.

Tissue phantom	Sound speed (m/s)	
	Mean	Std
Cornea	1585.6	2.087
Aqueous humor	1518.4	3.978
Lens	1597.7	4.513
Vitreous humor	1534.6	9.865
Retina	1550.0	8.204
Choroid	1551.0	4.382
Sclera	1597.2	5.738

Table 6.10: Sound speed measurements of tissue phantoms

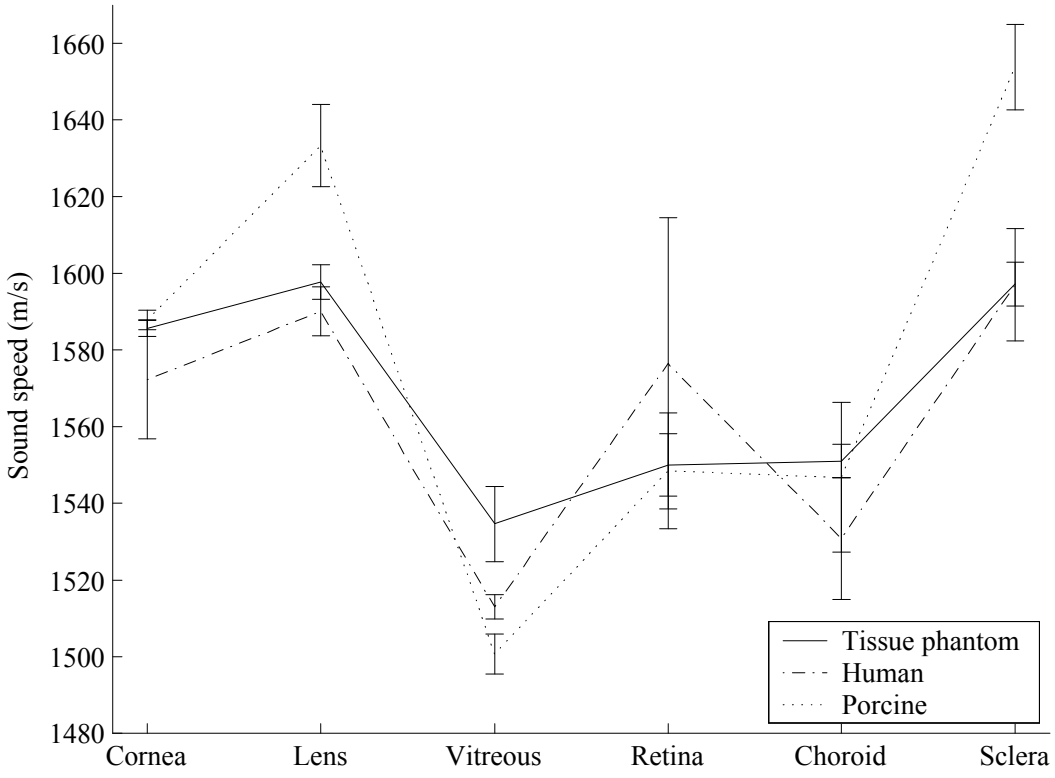

Figure 6.14: Comparisons between the sound speed measurements of eye phantom layers and ocular tissues of human and porcine based on literature data

Sound speed difference (%)			
	Average	Smallest	Largest
HT	0.96	0.013 (sclera)	1.68 (retina)
PT	1.39	0.097 (retina)	3.42 (sclera)
HP	1.82	0.81 (lens)	3.56 (sclera)

Table 6.11: Phase velocity differences between human and tissue phantoms (HT), porcine and tissue phantoms (PT) and human and porcine (HP)

Attenuation coefficient difference (%)			
	Average	Smallest	Largest
HT	38.90	21.38 (cornea)	59.51 (lens)
PT	55.15	36.17 (retina)	69.96 (lens)
HP	52.28	19.39 (lens)	92.70 (choroid)

Table 6.12: Attenuation coefficient differences between human and tissue phantoms (HT), porcine and tissue phantoms (PT) and human and porcine (HP)

The attenuation coefficients of the eye phantom layers are shown in Figure 6.15 and are compared to that of the human and porcine ocular tissues data in [23] as shown in Figure 6.16. The average, smallest and largest absolute difference between the attenuation coefficients of the phantoms, human and porcine ocular tissues are shown in Table 6.12. Similar to sound speed, the attenuation coefficients of the phantoms are more similar to that of both human and porcine ocular tissues than the ocular tissue attenuation coefficients between these species.

The average sound speeds and attenuation coefficients of the phantom and human eye are more similar than that of human and porcine eyes. Porcine eye has been recommended as an animal model for human eye [23, 152]. Therefore, it can be concluded that the eye phantom is a good model of mammalian eyes, and is a better model for human eye than porcine eye for the purpose of ultrasound eye characterization method evaluation.

C) Density

Densities of eye phantom layers are measured using a density meter (Mettler Toledo AL204 analytical balance and density determination kit). Detail procedures of density measurements can be found in the density meter manual. Measurements of the phantom densities are reported in Table 6.13. Since data of ocular tissue densities are scarce, the phantom densities are only compared

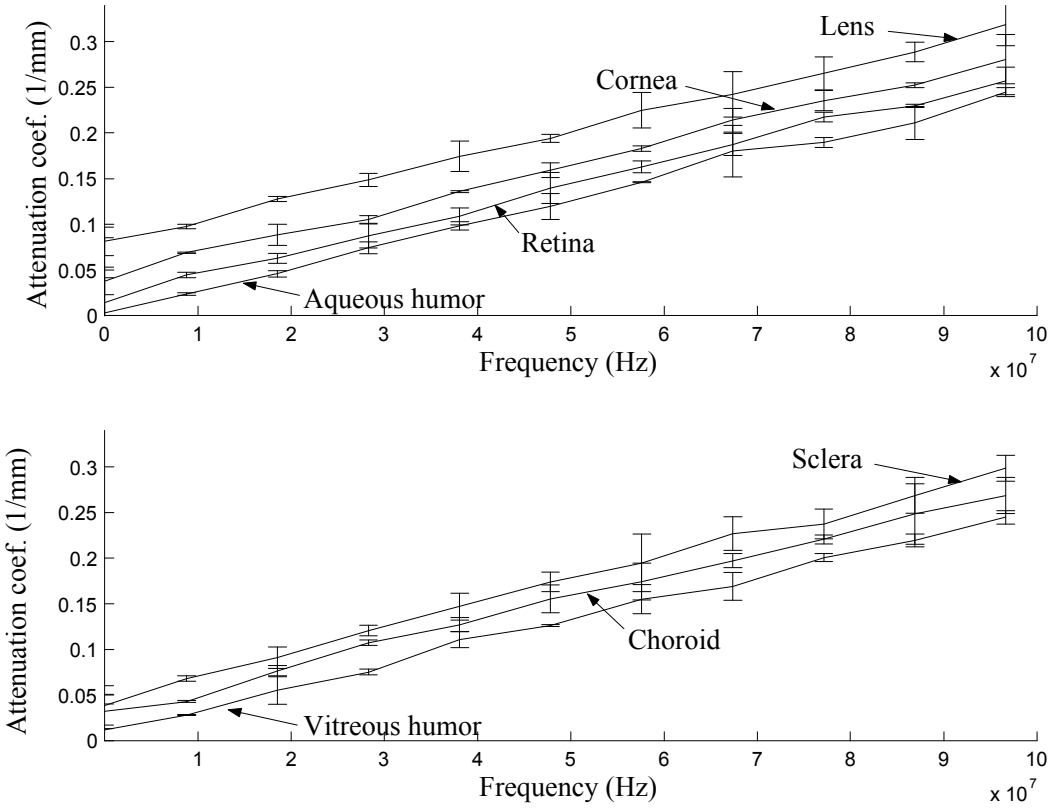

Figure 6.15: Attenuation coefficient measurements of tissue phantoms

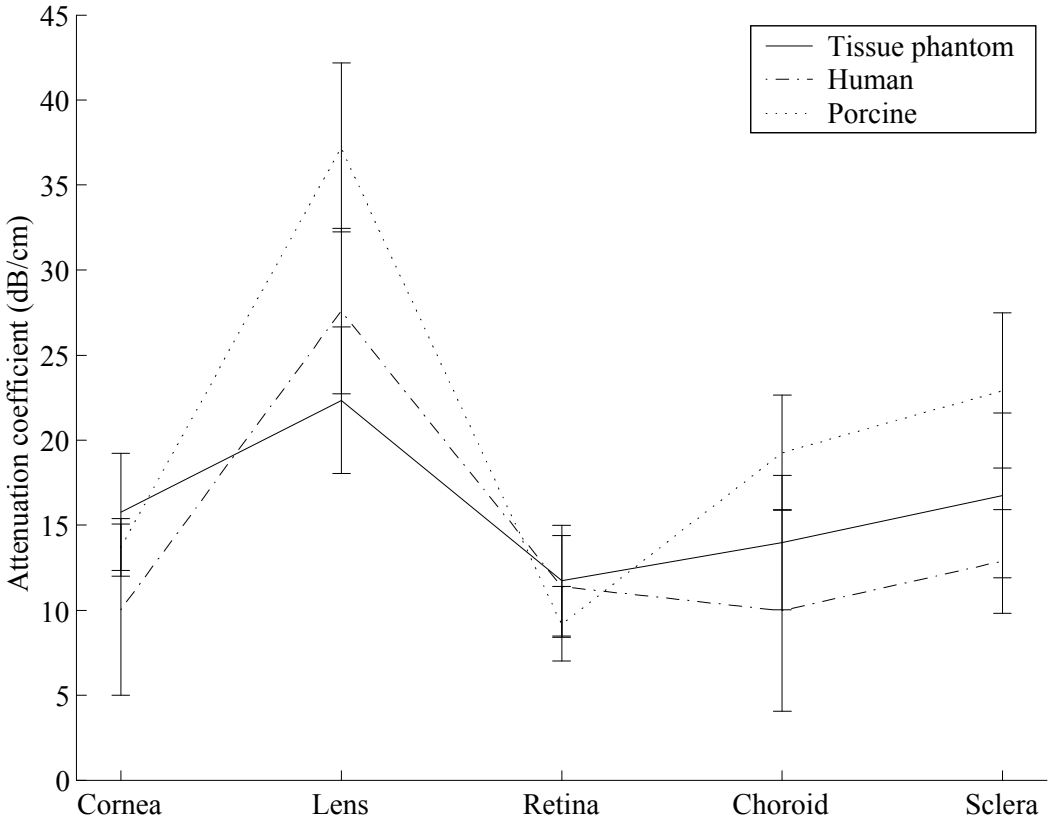

Figure 6.16: Comparisons between the attenuation coefficient measurements of tissue phantoms and ocular tissues of human and porcine at 20 MHz based on literature data

Tissue phantom	Density (g/ml)	
	Mean	Std
Cornea	1.060	1.863e-3
Aqueous humor	1.007	4.775e-3
Lens	1.112	4.757e-3
Vitreous humor	1.010	1.508e-3
Retina	1.032	4.676e-3
Choroid	1.047	8.406e-3
Sclera	1.077	2.471e-3

Table 6.13: Mass density measurements of tissue phantoms

to that of the bovine ocular tissues in Table 6.5. Figure 6.17 shows that phantom densities closely follow to that of the bovine tissues. The average, smallest and largest absolute difference between the densities of the bovine ocular tissues and phantoms are 0.28%, 0.093% (sclera) and 0.72% (lens).

6.4.5 Seven-layered Tissue Phantom Acoustic Parameter Estimation

The seven-layered tissue phantom described in Section 6.3.2 is employed as the test subject to compare the performances of MSF and GSPF-II. Backscattered signals of the tissue phantom array are acquired using the equipment described in Section 6.4.1. Twenty sets of 20002 samples of the backscattered signals are recorded. Each of the twenty sets is preprocessed by the bandpass filter described in Section 3.1. The averaged backscattered signals are shown in Figure 6.18. The amplitudes of the echoes are normalized with respect to the absolute maximum amplitude of the echo signals. The circle markers indicate the beginning of detected echoes.

The parameters used in MSF and GSPF-II are listed below.

- Measurement noise model: the statistical model obtained in Section 6.4.3
- Minimum and maximum of the slope of attenuation coefficient model: 2.45×10^{-6} and 2.51×10^{-6}(Hz m)$^{-1}$
- Minimum and maximum of the constant attenuation coefficient model: 3.00 and 78.00m^{-1}

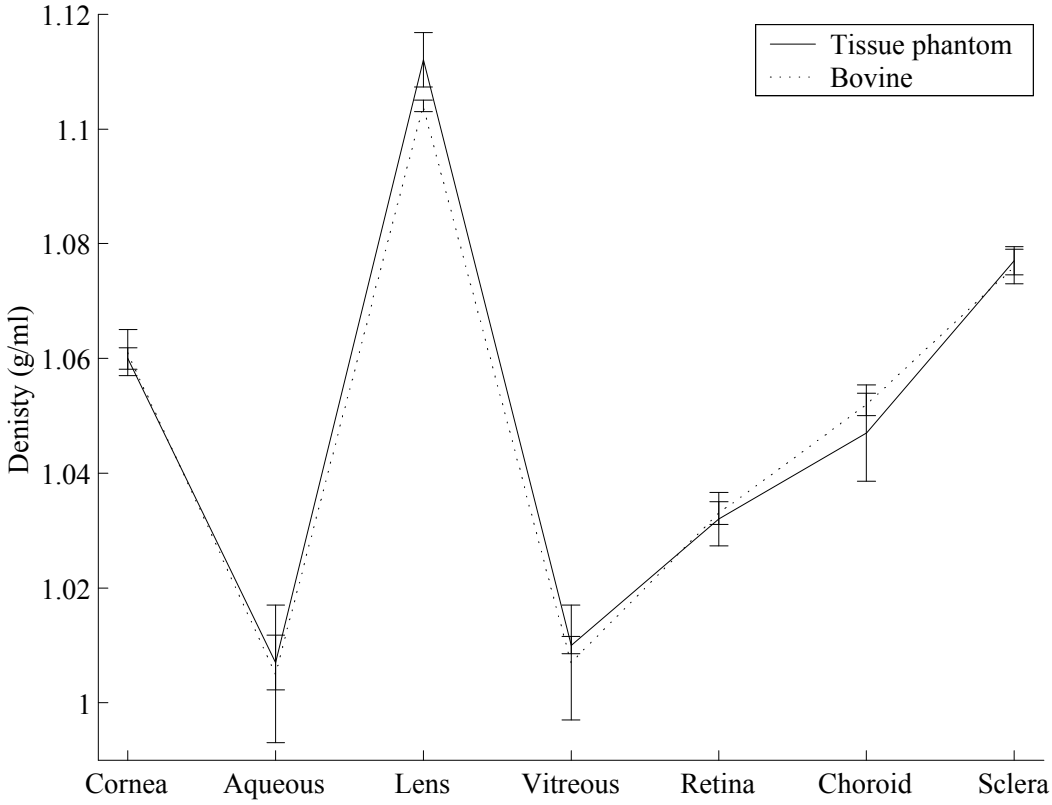

Figure 6.17: Comparisons between the density measurements of tissue phantoms and bovine ocular tissues

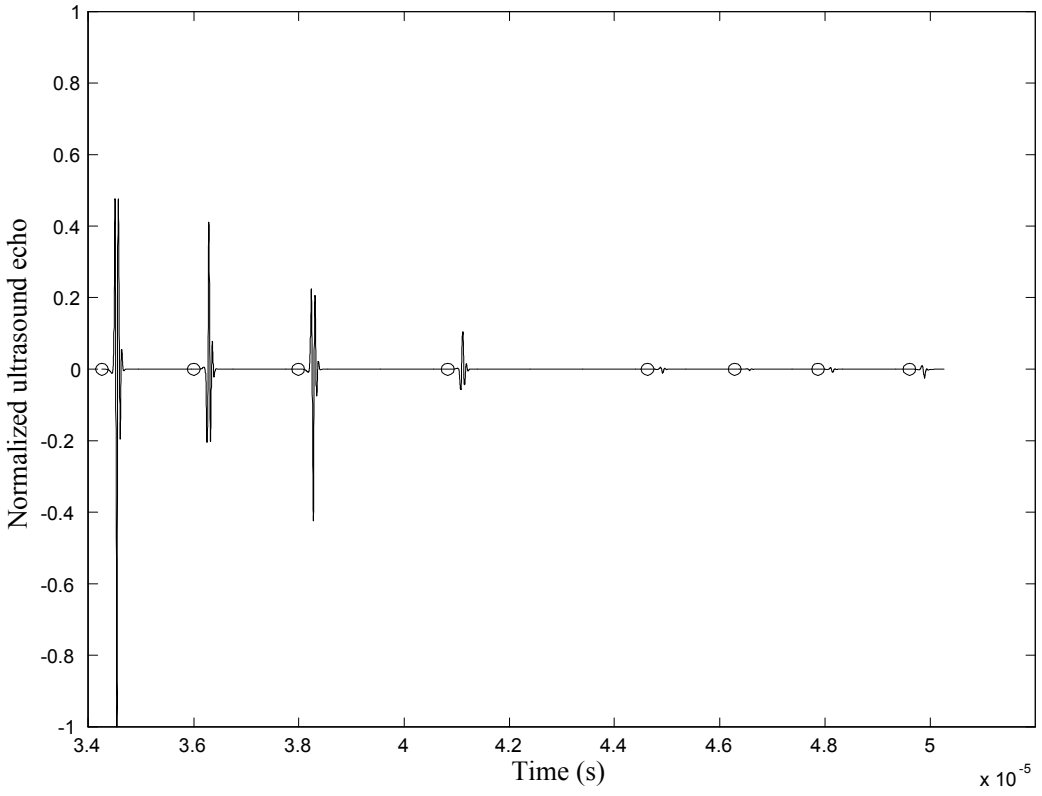

Figure 6.18: Backscattered signals of 7-layered tissue phantom

- Minimum and maximum of sound speed: 1500 and 1620m/s
- Minimum and maximum of acoustic impedance: 1.40×10^9 and 1.92×10^9g/(s m^2)
- Number of random samples: 50, 100 and 200. The number of random samples used in the experiments are chosen to be similar to that used by the state-of-the-art filter (i.e., GSPF-II) in [121]. The optimal number of random samples is dependent on the definition of optimality and may vary largely for different optimality definitions. Determining the optimal number of random samples is out of the scope of this research.
- Frequencies at which the estimations take place: 7 frequencies from 6.13 to 27.61MHz with 1.53MHz increments

The presentations of estimation results are organized as follows:

- The statistics of acoustic parameter estimation errors based on the three random sample sizes are listed in Tables 6.14, 6.15 and 6.16
- The measured and estimated acoustic parameters are in depicted Figures 6.19, 6.20, 6.21 and 6.22

6.4.6 Four-layered Tissue Phantom Array Acoustic Parameter Estimation

The 4x3x4 tissue phantom array described in Section 6.3.2 is employed as the test subject to compare the performances of MSF and GSPF-II. Backscattered signals of the tissue phantom array are acquired using the equipment described in Section 6.4.1. For each of the twelve four-layer array, twenty sets of 20002 samples of the backscattered signals are recorded. Each of the twenty sets is preprocessed by the bandpass filter described in Section 3.1. The averaged backscattered signals of each of the twelve four-layer array are shown from Figures 6.23 to 6.26. The amplitudes of the echoes are normalized with respect to the absolute maximum amplitude of the echo signals. The circle markers indicate the beginning of detected echoes.

The parameters used in MSF and GSPF-II are identical to that listed in Section 6.4.5. The estimation errors based on 100 random samples are shown in Figures 6.27, 6.28, 6.29 and 6.30.

MSF estimation error percentage								
No. of samples: 50	Attenuation coef. model				Sound speed		Density	
	Slope		Y-intercept					
Phantom layer	Mean	Std	Mean	Std	Mean	Std	Mean	Std
Cornea	0.167	0.418	-4.178	0.622	-1.168	0.477	1.184	0.489
Aqueous humor	0.149	0.419	16.988	3.138	1.154	0.292	-1.014	0.332
Lens	0.436	0.336	-3.710	1.468	0.178	0.833	-0.189	0.830
Vitreous humor	0.894	0.126	19.594	9.936	0.030	0.775	0.387	0.765
Retina	-0.423	0.071	14.278	6.337	0.620	0.588	-0.239	0.608
Choroid	-0.969	0.177	6.889	4.542	0.618	1.055	-0.235	0.971
Sclera	-0.780	0.304	-3.973	4.063	-2.400	1.166	2.913	1.329
Abs. average:	0.546	0.265	9.944	4.301	0.881	0.741	0.880	0.761
GSPF-II estimation error percentage								
No. of samples: 50	Attenuation coef. model				Sound speed		Density	
	Slope		Y-intercept					
Phantom layer	Mean	Std	Mean	Std	Mean	Std	Mean	Std
Cornea	0.053	0.255	0.352	0.628	0.381	1.752	-0.181	2.456
Aqueous humor	-0.027	0.814	1.736	17.560	-0.542	1.637	0.271	1.291
Lens	0.611	0.964	0.727	2.482	1.153	1.056	-0.495	1.299
Vitreous humor	1.030	0.172	3.728	20.773	0.180	2.199	0.018	1.177
Retina	-0.427	0.950	49.363	24.788	-0.948	2.048	1.845	3.469
Choroid	-1.023	0.495	72.477	10.743	5.889	2.861	1.976	2.313
Sclera	-0.629	0.755	63.254	1.186	0.602	2.066	5.483	2.812
Abs. average:	0.542	0.629	27.376	11.166	1.385	1.945	1.467	2.117

Table 6.14: MSF and GSPF-II acoustic parameter estimation errors based on 7-layered tissue phantom, focused wave and 50 random samples

MSF estimation error percentage								
No. of samples: 100	Attenuation coef. model				Sound speed		Density	
	Slope		Y-intercept					
Phantom layer	Mean	Std	Mean	Std	Mean	Std	Mean	Std
Cornea	0.087	0.224	3.031	3.162	-0.438	0.581	0.443	0.587
Aqueous humor	0.039	0.175	-1.665	8.821	0.326	0.514	-0.374	0.504
Lens	0.656	0.169	-4.154	2.253	0.906	0.815	-0.875	0.810
Vitreous humor	0.836	0.138	8.734	5.046	0.706	0.565	-0.494	0.474
Retina	-0.497	0.117	6.595	4.422	1.167	0.573	-0.957	0.554
Choroid	-0.920	0.255	5.315	4.143	0.895	0.597	-0.689	0.698
Sclera	-0.710	0.389	-5.052	0.773	-1.392	1.280	1.710	1.491
Abs. average:	0.535	0.210	4.935	4.089	0.833	0.704	0.792	0.731
GSPF-II estimation error percentage								
No. of samples: 100	Attenuation coef. model				Sound speed		Density	
	Slope		Y-intercept					
Phantom layer	Mean	Std	Mean	Std	Mean	Std	Mean	Std
Cornea	-0.062	0.451	-0.541	1.121	0.379	3.067	-0.186	0.621
Aqueous humor	0.070	0.729	9.547	10.354	0.454	1.766	-0.198	0.700
Lens	0.483	0.688	-2.127	2.163	0.464	1.008	-0.121	1.740
Vitreous humor	0.906	0.671	4.607	14.578	0.094	1.865	0.117	1.146
Retina	-0.549	0.445	41.484	18.216	0.922	2.298	0.781	2.231
Choroid	-0.913	0.214	62.276	9.261	4.771	0.264	1.803	2.496
Sclera	-0.583	0.557	63.952	1.075	0.405	1.721	4.876	4.787
Abs. average:	0.509	0.536	26.362	8.110	1.070	1.713	1.155	1.960

Table 6.15: MSF and GSPF-II acoustic parameter estimation errors based on 7-layered tissue phantom, focused wave and 100 random samples

MSF estimation error percentage								
No. of samples: 200	Attenuation coef. model				Sound speed		Density	
	Slope		Y-intercept					
Phantom layer	Mean	Std	Mean	Std	Mean	Std	Mean	Std
Cornea	0.094	0.320	3.434	1.051	-0.572	0.394	0.582	0.409
Aqueous humor	0.079	0.196	-2.364	1.009	0.111	0.575	-0.149	0.548
Lens	0.573	0.210	-0.791	0.665	0.468	1.132	-0.435	1.136
Vitreous humor	0.861	0.135	-2.757	7.043	-0.548	0.413	0.511	0.459
Retina	-0.439	0.144	0.941	4.381	0.066	1.012	-0.094	1.045
Choroid	-0.784	0.183	-3.585	2.368	0.295	0.602	-0.343	0.675
Sclera	-0.578	0.189	0.642	1.127	0.853	0.180	-0.940	0.351
Abs. average:	0.487	0.197	2.073	2.521	0.416	0.615	0.437	0.660
GSPF-II estimation error percentage								
No. of samples: 200	Attenuation coef. model				Sound speed		Density	
	Slope		Y-intercept					
Phantom layer	Mean	Std	Mean	Std	Mean	Std	Mean	Std
Cornea	-0.157	0.652	-0.654	0.918	-0.423	0.811	0.217	1.378
Aqueous humor	-0.148	0.315	7.238	4.400	0.095	0.916	-0.022	1.398
Lens	0.283	0.460	-0.494	2.599	-0.186	1.877	0.075	1.003
Vitreous humor	0.994	0.841	2.400	11.529	0.030	1.585	0.114	0.957
Retina	-0.453	0.707	29.799	14.152	0.219	3.250	0.761	2.020
Choroid	-0.850	0.510	65.515	18.368	4.761	1.226	2.084	1.761
Sclera	-0.671	0.220	61.857	1.507	0.823	1.326	5.164	1.368
Abs. average:	0.508	0.529	23.994	7.639	0.934	1.570	1.205	1.412

Table 6.16: MSF and GSPF-II acoustic parameter estimation errors based on 7-layered tissue phantom, focused wave and 200 random samples

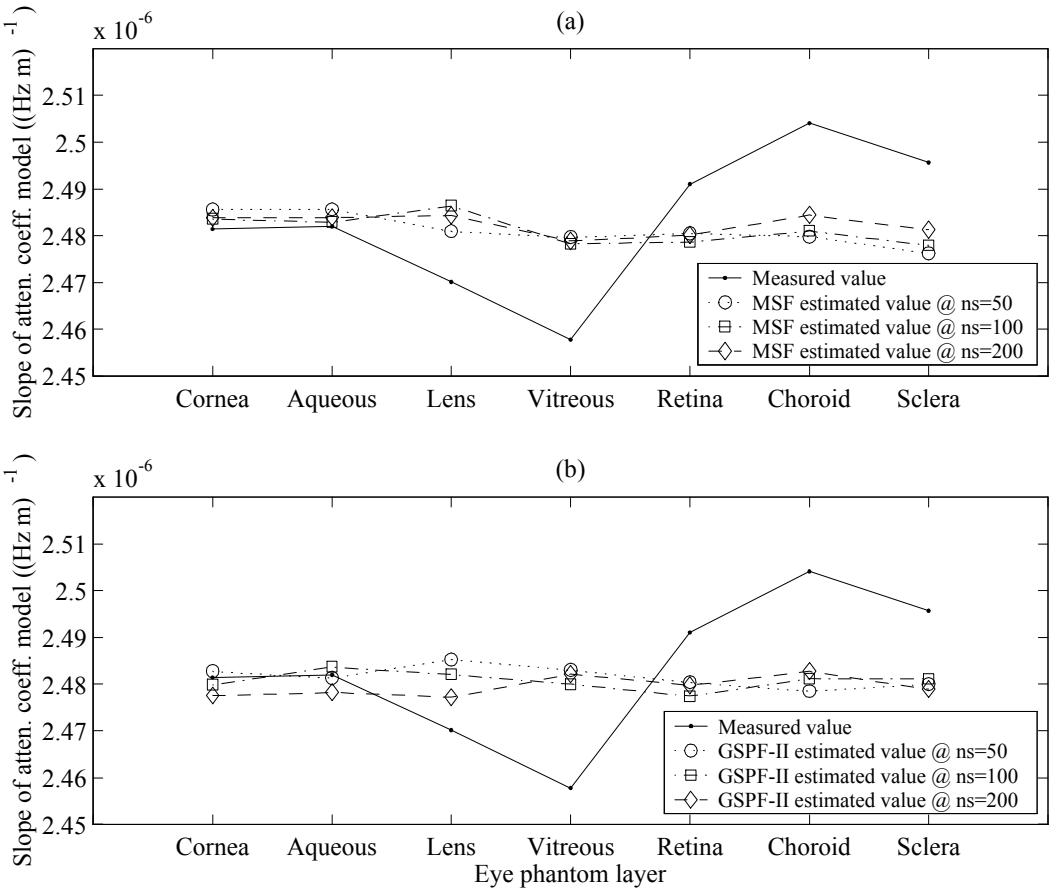

Figure 6.19: Comparison between the measured, (a) MSF and (b) GSPF-II estimated slope of attenuation coefficient model based on 7-layered tissue phantom and focused wave

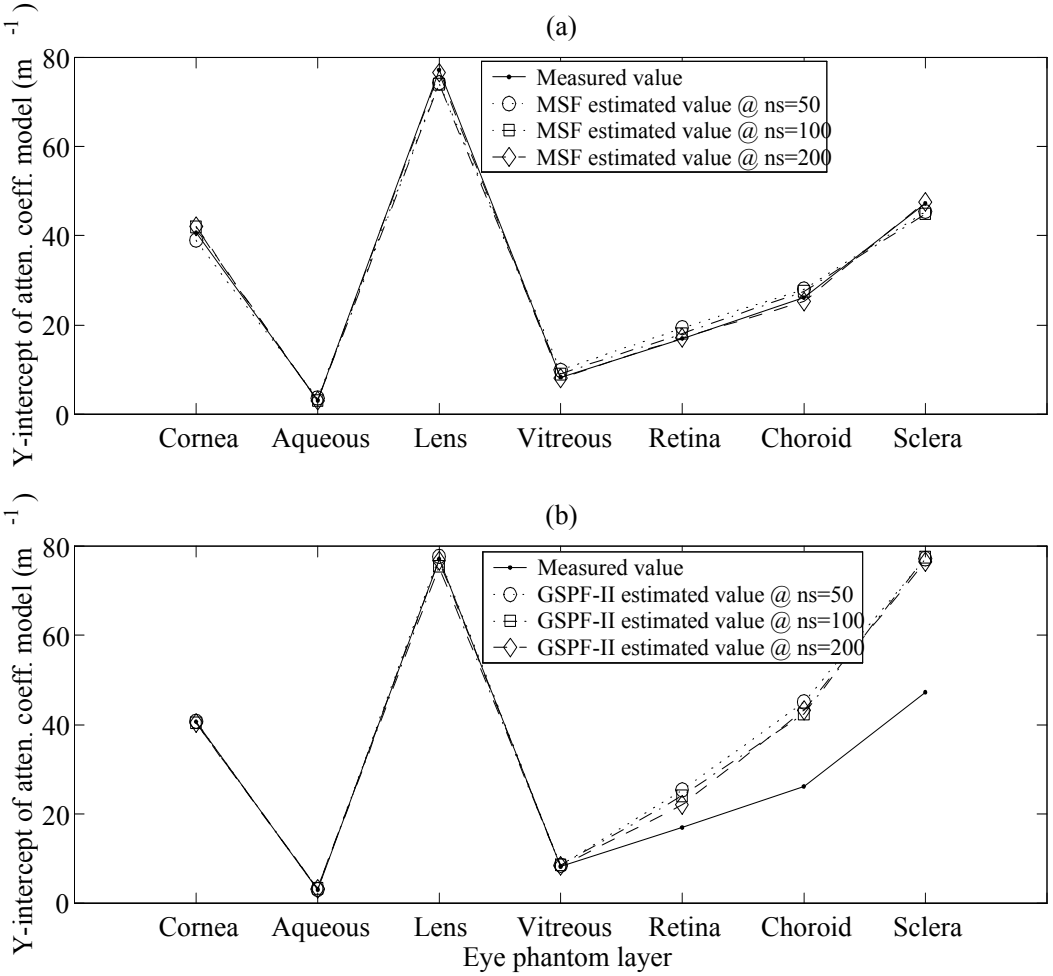

Figure 6.20: Comparison between the measured, (a) MSF and (b) GSPF-II estimated y-intercept of attenuation coefficient model based on 7-layered tissue phantom and focused wave

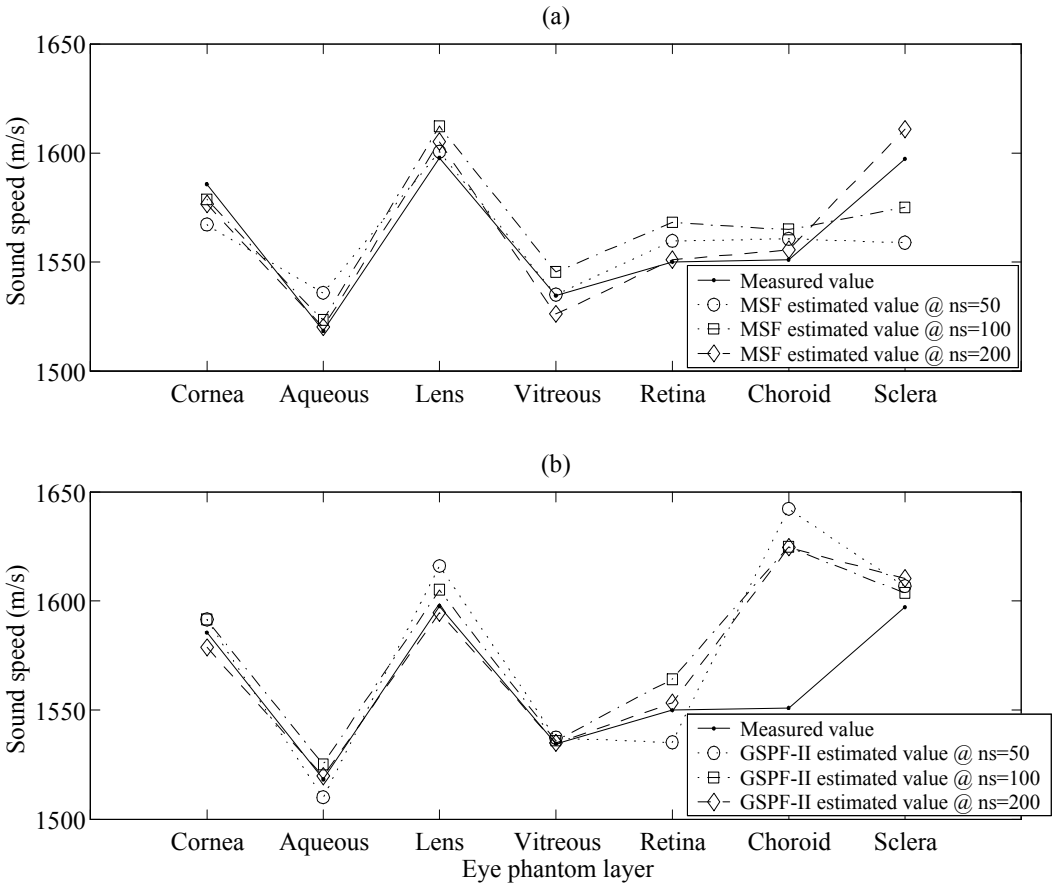

Figure 6.21: Comparison between the measured, (a) MSF and (b) GSPF-II estimated sound speed based on 7-layered tissue phantom and focused wave

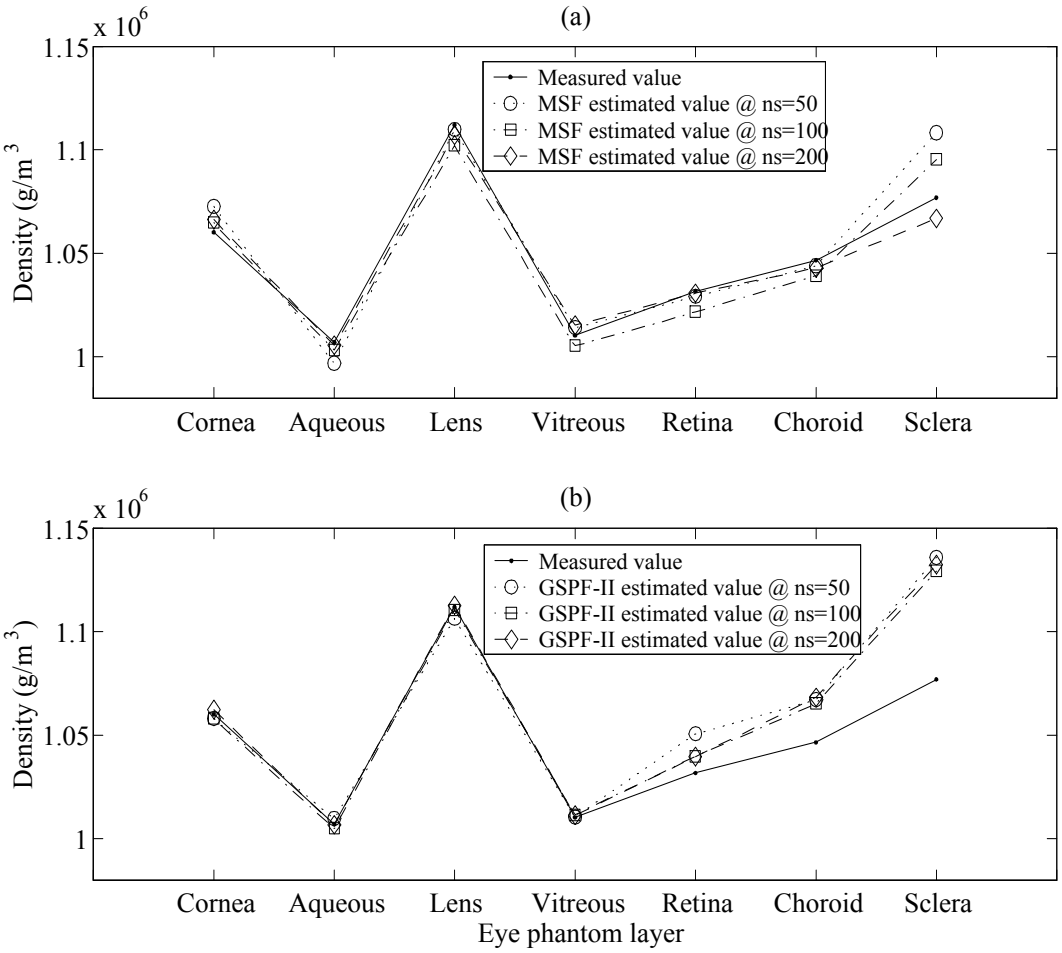

Figure 6.22: Comparison between the measured, (a) MSF and (b) GSPF-II estimated density based on 7-layered tissue phantom and focused wave

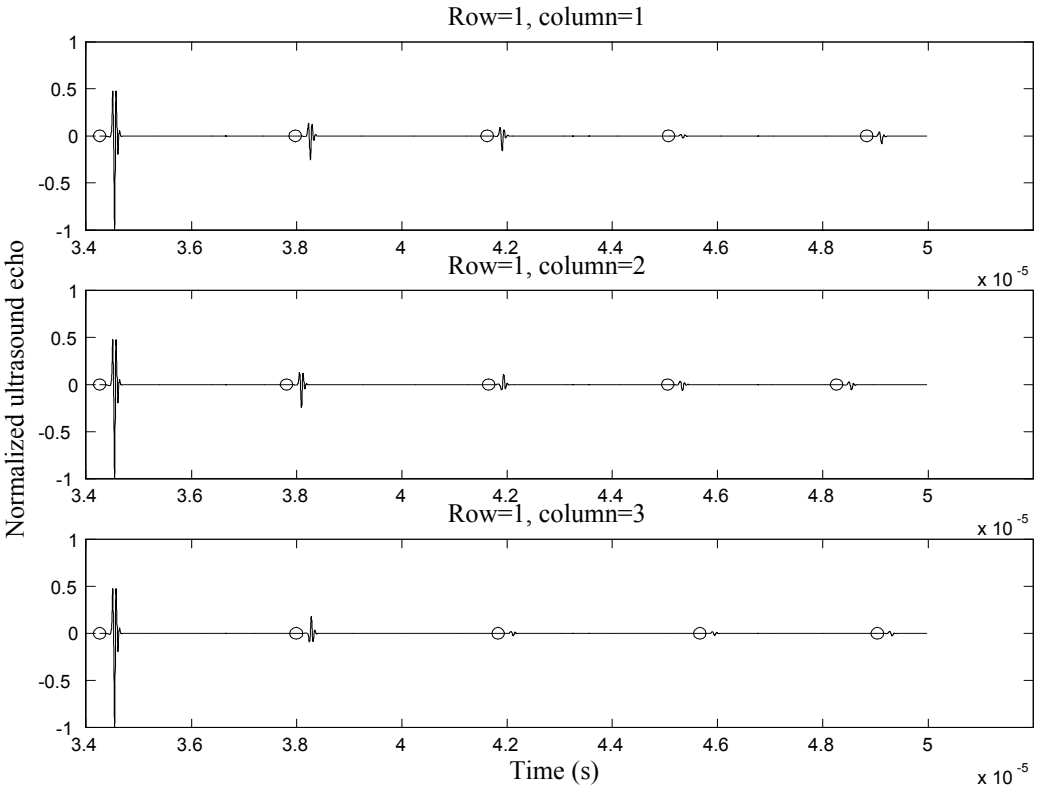

Figure 6.23: Backscattered signals of row 1 of 4-layered tissue phantom array

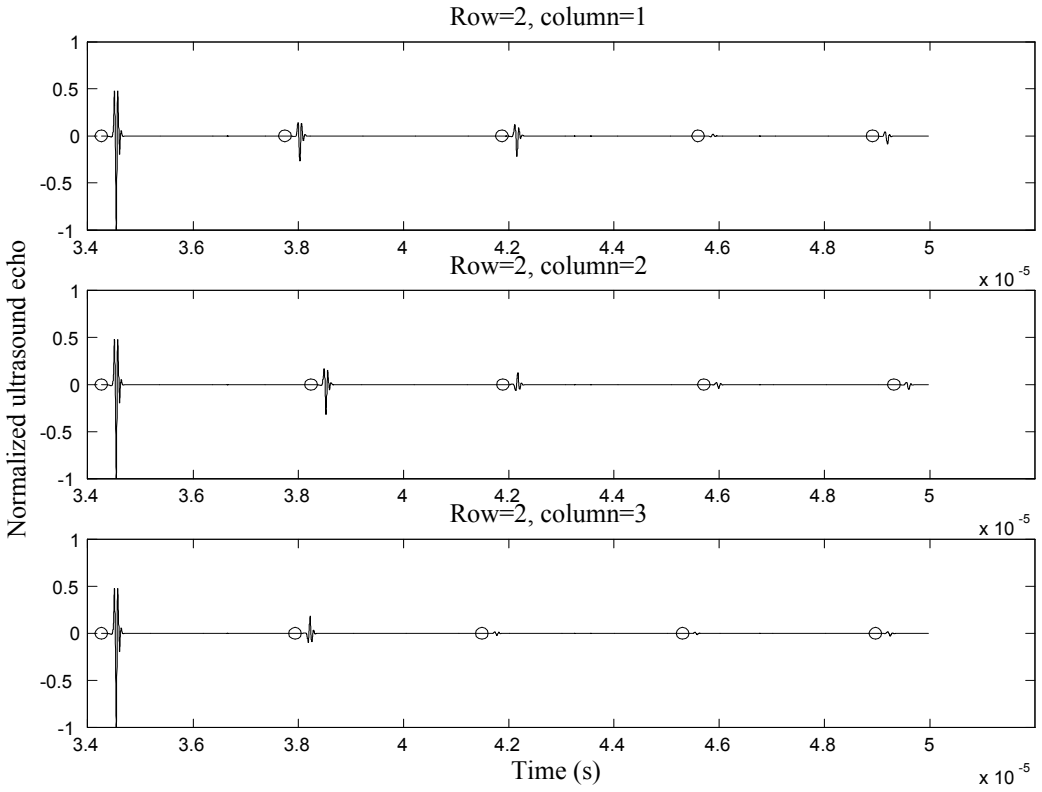

Figure 6.24: Backscattered signals of row 2 of 4-layered tissue phantom array

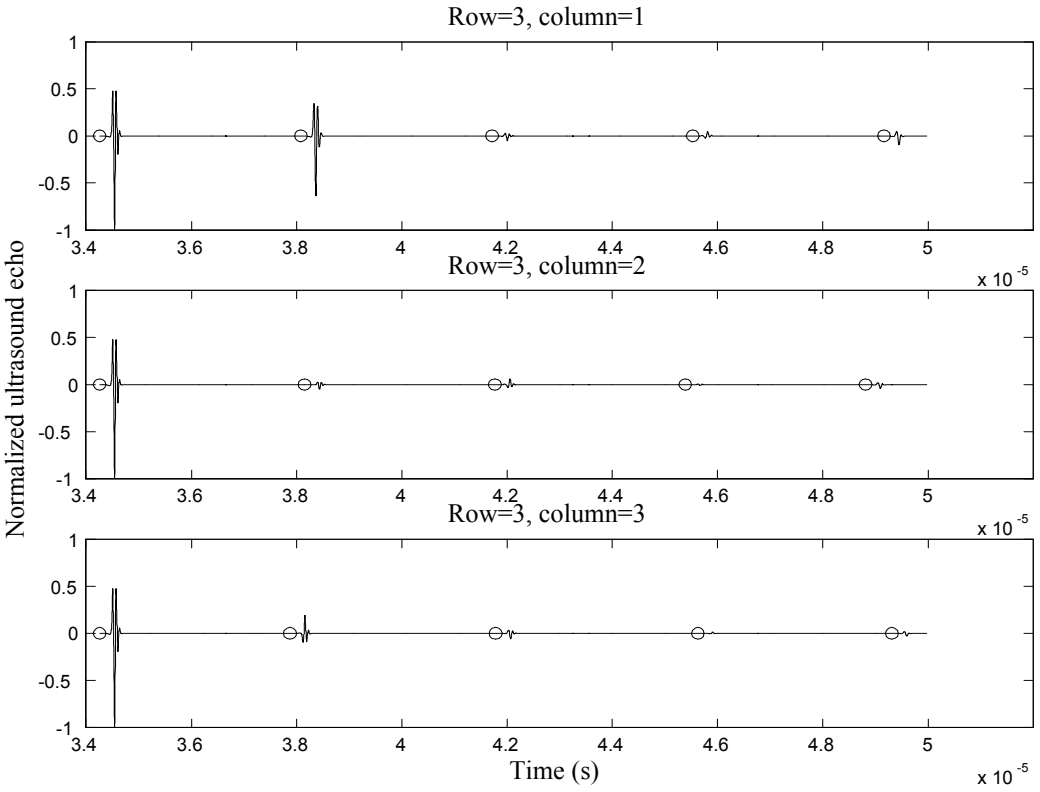

Figure 6.25: Backscattered signals of row 3 of 4-layered tissue phantom array

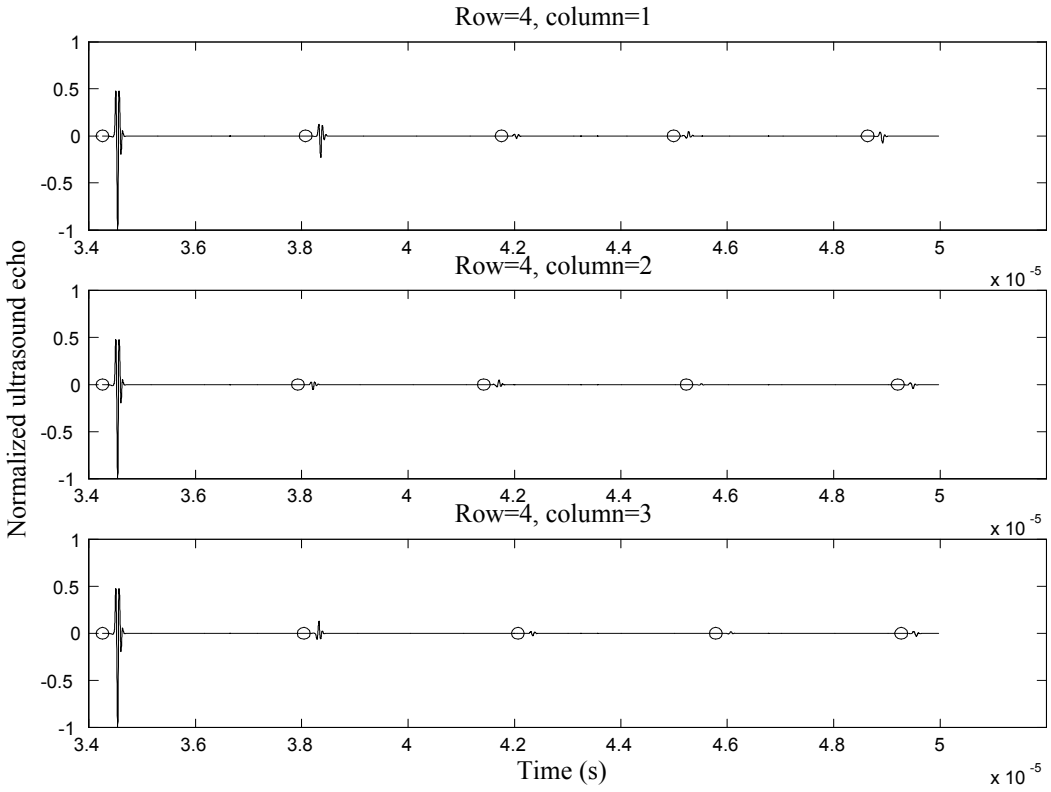

Figure 6.26: Backscattered signals of row 4 of 4-layered tissue phantom array

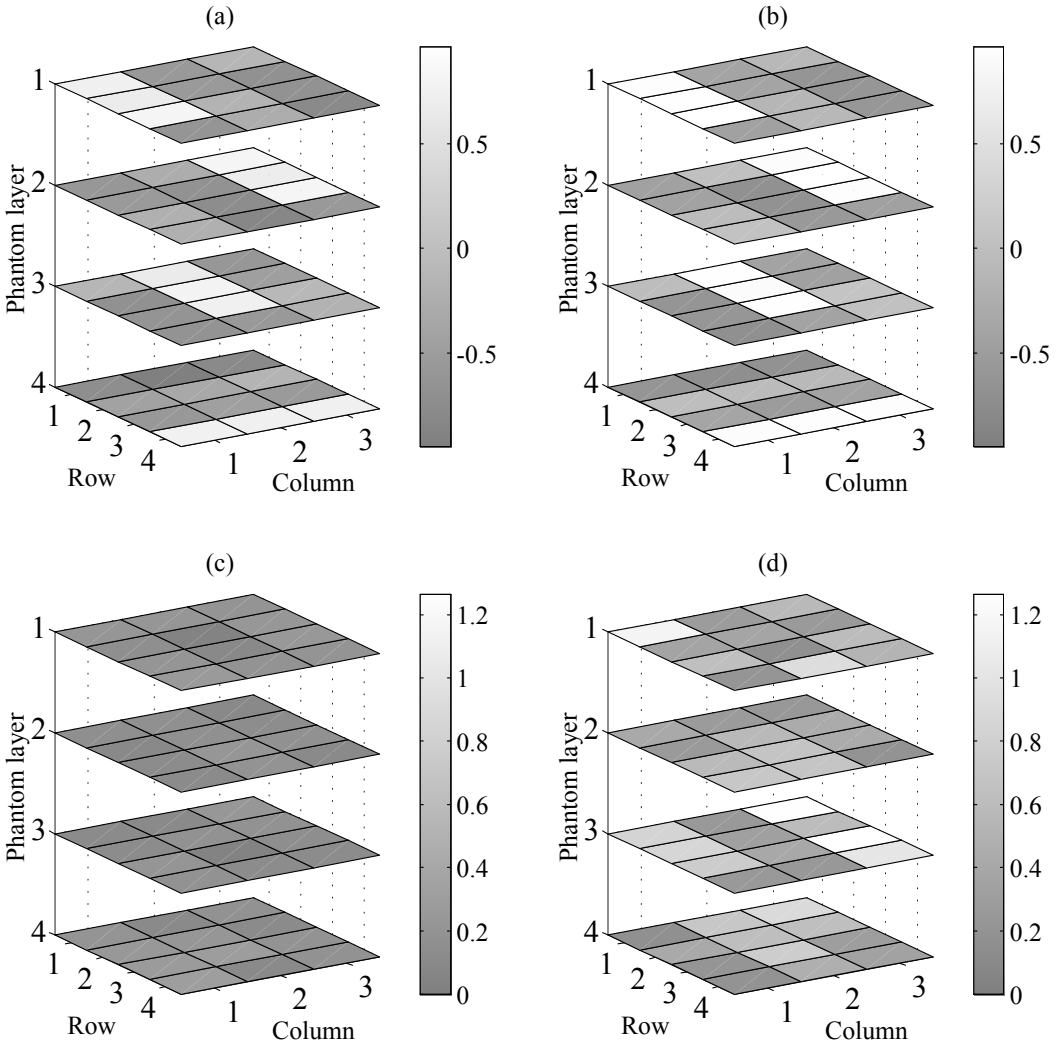

Figure 6.27: Estimation error percentage means of (a) MSF and (b) GSPF-II, and standard deviations of (c) MSF and (d) GSPF-II of the slopes of attenuation coefficient model based on 4-layered tissue phantom array, focused wave and 100 random samples

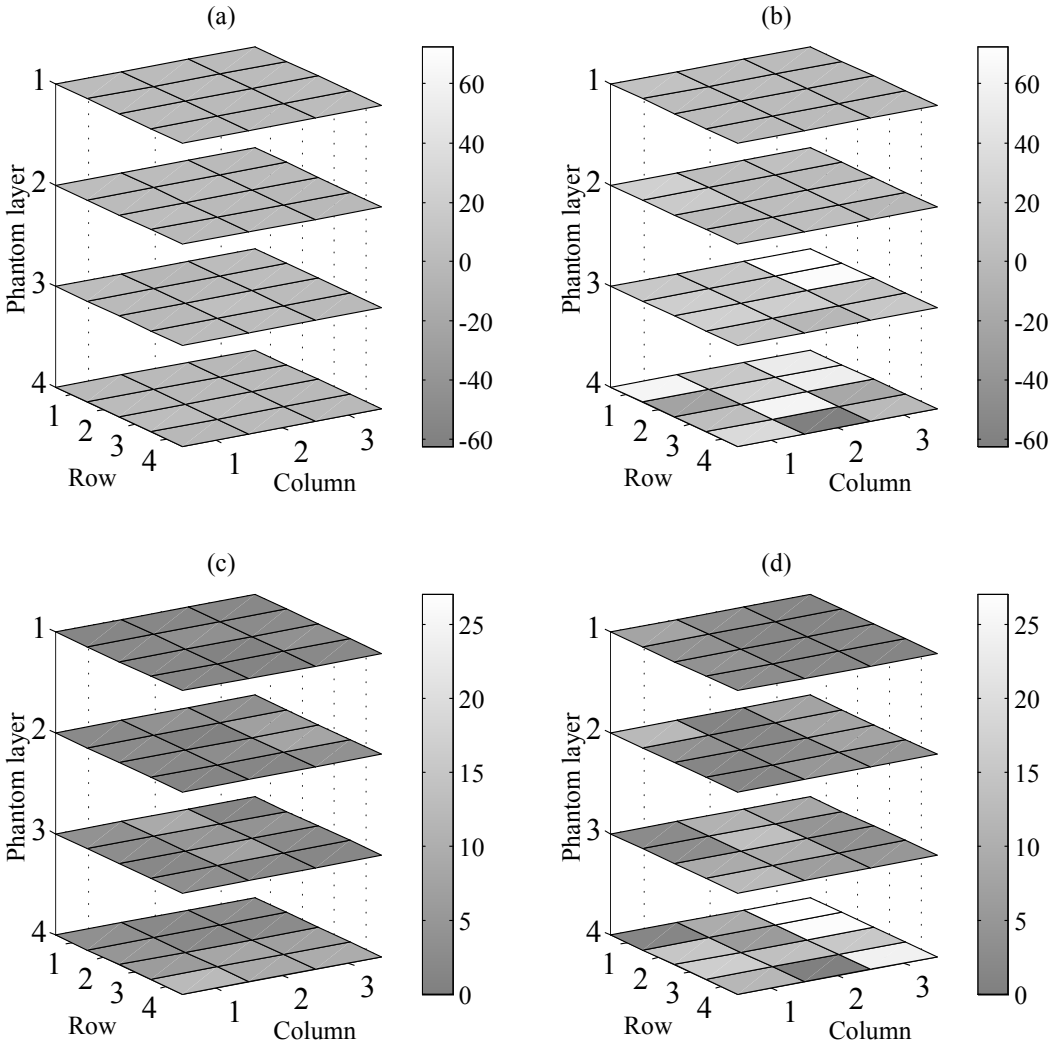

Figure 6.28: Estimation error percentage means of (a) MSF and (b) GSPF-II, and standard deviations of (c) MSF and (d) GSPF-II of the y-intercepts of attenuation coefficient model based on 4-layered tissue phantom array, focused wave and 100 random samples.

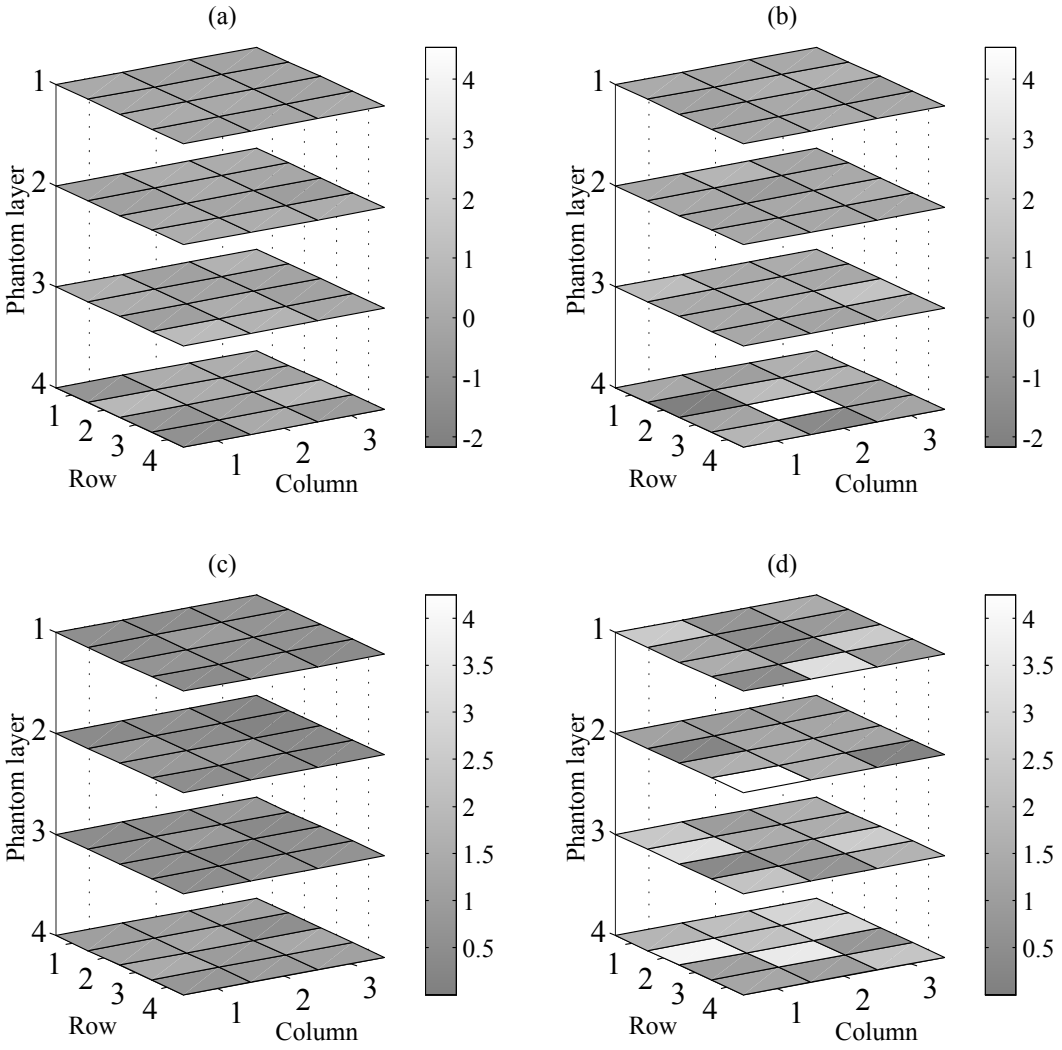

Figure 6.29: Estimation error percentage means of (a) MSF and (b) GSPF-II, and standard deviations of (c) MSF and (d) GSPF-II of sound speeds based on 4-layered tissue phantom array, focused wave and 100 random samples

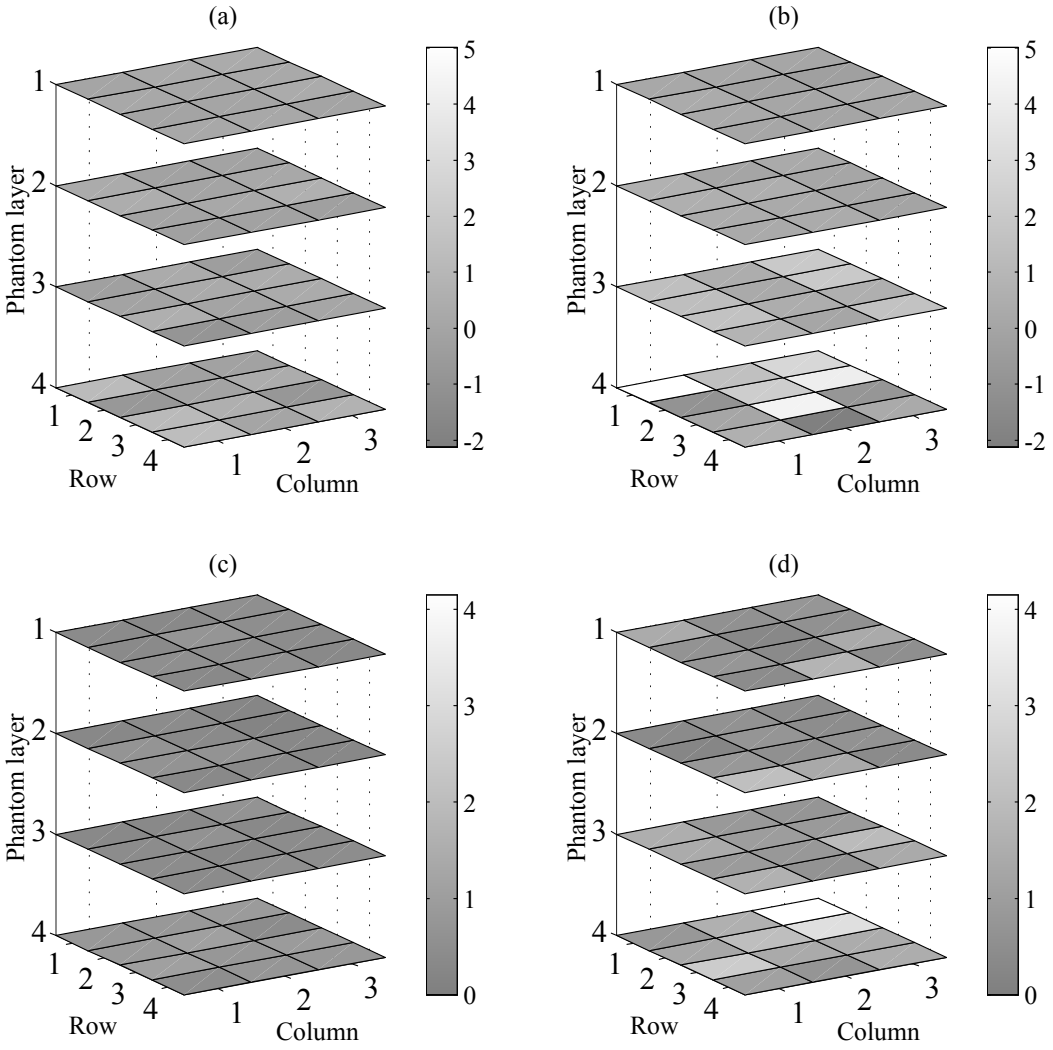

Figure 6.30: Estimation error percentage means of (a) MSF and (b) GSPF-II, and standard deviations of (c) MSF and (d) GSPF-II of densities based on 4-layered tissue phantom array, focused wave and 100 random samples

6.5 Analysis of Tissue Phantoms Echoes and MSF Performance

The characteristics of ultrasound echoes from tissue phantoms and the performance of MSF for tissue acoustic parameter estimation are analyzed in the following.

6.5.1 Characteristics of Ultrasound Echoes from Tissue Phantoms

Based on the backscattered signals of the tissue phantoms shown in Sections 6.4.5 and 6.4.6, for each multi-layered tissue phantom, the number of echoes is always one more than the number of its layers. Eight echoes are recorded from the seven-layered tissue phantom as shown in Figure 6.18, and five echoes are recorded from each of the 4×3 array of four-layered tissue phantoms as graphed in Figures 6.23 to 6.26. The first and last echoes of each tissue phantom are produced at the water-phantom interface and the phantom-container interface. The rest of echoes are produced at the layer interfaces within the phantoms. Although the amplitudes of some echoes are too small to be displayed, these echoes can be detected since amplitude ratio is used as the echo detection feature. The reasons of small amplitudes of these echoes are twofold. First, the echoes are produced at the interfaces between layers having similar acoustic impedances, so that the reflection coefficients of these layers are small relative to other layers. Second, the echoes are reflected from layer interfaces that are further away from the transducer. Since focused waves diffract as they travel away from the transducer, diffractions of waves reduce the energy of echoes sensed by the transducer. Diffraction is the main difference between plane waves and focused waves. Plane waves do not diffract, so that the amplitudes of plane wave echoes do not decrease rapidly as illustrated in Figure 5.1.

Wave reverberation in the phantoms is another issue of interest for analyzing the phantom ultrasound response. Wave reverberation is a physical phenomenon of wave propagation. When an ultrasound wave penetrates into phantom layers of various acoustic impedances, part of the wave energy is reflected at each layer interface and the rest is transmitted through the interface creating multiple waves with various propagation directions, phase characteristics and attenuated amplitudes. These waves are repeatedly divided into their reflection and transmission components when they encounter other interfaces. This process continues until the energy levels of the impulses become negligible. As a result, multiple reflected waves (i.e., echoes) may have similar phase characteristics, and the transducer registers

their superposition instead of individual echoes. Since many of these echoes do not uniquely correspond to the tissue structure, they are part of the backscattered signal noise. In fact, it is well-understood that the formation of speckle noise is both random and deterministic [20]. Wave reverberation can be considered as the deterministic component of speckle noise. Figures in Sections 6.4.5 and 6.4.6 show that all echoes in the backscattered signals of the phantoms are separated from each other, and the number of echoes is identical to the number of layers plus one. No reverberated echo is observed, which implies that the acoustic properties of the phantom layers yield negligible wave reverberation.

6.5.2 Number of Gaussian Components in the Estimation of Posterior PDF

Determining the optimal number of Gaussian components of the posterior PDF is out of the scope of this research. The number of Gaussian component, n_x, is commonly chosen by the user or determined experimentally. Instead of passing the responsibility of finding n_x to the user, our approach utilizes the measurements to guide the MSF algorithm to determine n_x autonomously. At each iteration, MSF generates n_s number of random samples, and they are weighted based on their likelihoods to produce the measurement. The samples with normalized weights less than n_s^{-1} are discarded. On the other hand, The samples with normalized weights greater than or equal to n_s^{-1} are retained for posterior PDF estimation. The value n_s^{-1} represents the average normalized weight of a set of n_s samples. The number of Gaussian component, n_x, is determined as the number the samples retained. The advantage of this approach is the flexibility to adapt to the measurements. For this application, the value of n_x is mostly below 8. It should be noted that the determined value n_x used by MSF is by no means optimal.

6.5.3 Effect of Random Sample Size on Estimation Accuracy

The number of random samples, n_s, used to estimate the posterior PDF and parameter estimates is of great practical interest. Based on data shown in Tables 5.4 to 5.12 and Tables 6.14 to 6.16, the average estimation error percentages consistently decrease as n_s increases. These results are expected, since more random samples increase the chance of finding more accurate parameters. In addition, the convergence of estimation requires large number of samples as suggested by Monte-Carlo integration and the law of large numbers. Moreover, the average reduction

of estimation error with respect to the increase of random samples is 18.7% per 50 samples for MSF considering both simulation and physical experiments. This error reduction is relatively small compared to 100% increase of n_s (i.e., increase from 50 to 100 and from 100 to 200). This implies that the estimation accuracy of MSF is not heavily dependent on n_s, so that smaller n_s may be used in MSF to relax computation power needed while maintaining the estimation accuracy.

6.5.4 Effect of Tissue Phantom Layer Sequence on Estimation Accuracy

In order to examine the effect of tissue phantom layer sequence on the tissue acoustic parameter estimation accuracy, the four-layered tissue phantom array is made with the four tissue phantoms layered in different sequences. The four selected tissue phantoms can be grouped in two pairs. The tissue phantom acoustic parameters are similar within each pair and are far apart across the pairs.

The results shown in Figures 6.27, 6.28, 6.29 and 6.30 reveal similar patterns of estimation errors between MSF and GSPF-II. For the slope of attenuation coefficient model (i.e., m), estimation errors for vitreous humor are the largest. Since the forward scattering model is relatively less sensitive to m, the estimates of m are determined as the mean of the random samples of m, which is the mid value of the range of m. The value of m for vitreous humor is much lower than the mid value of the range of m. Therefore, the estimation errors of m of vitreous humor become large.

For other three tissue acoustic parameters, no particular patterns of estimation errors among the tissue phantom array elements is observed. This indicates that the estimation accuracies of MSF and GSPF-II are independent of the tissue layer sequence. On the other hand, a trend of increasing estimation errors with respect to tissue phantom layers can be observed for y-intercept of attenuation coefficient model, sound speed and density. This is because echo waveforms are functions of the acoustic parameters of all layers in the propagation paths, so that the parameter estimate of a layer is affected by that of the previous layer. Therefore, the estimation errors are accumulated.

6.5.5 Posterior PDF Estimation and Analysis of Prior Information Dependency

The method of posterior PDF estimation is considered as one of the most critical elements in nonlinear stochastic filtering. Here brief comparisons of the posterior PDF estimation method are made between MSF and well known stochastic filters such as unscented particle filter (UPF) [118], Gaussian particle filter (GPF) [119, 120] and Gaussian sum particle filter (GSPF) [121]. UPF uses an unscented Kalman filter (UKF)[3] to estimate an importance density (ID)[4] as a Gaussian PDF for each particle. GPF employes an extended Kalman filter (EKF) or UKF for ID estimation for problems with Gaussian noise only. GSPF utilizes a bank of GPFs to filter systems with GMM noise processes. In effect, GSPF estimates the posterior PDF as a GMM, which is a general PDF representation. There are three types of GSPF. The second type, GSPF-II, is considered since it is designed for general noise model in the form of GMM. GSPF-II employes a bank of GPF to estimate the posterior PDF in parallel, and each GPF estimates one Gaussian component of the posterior PDF. The ID in each GPF is estimated as a Gaussian PDF using an UKF. In the GSPF-II algorithm, each ID is generated individually to capture local state statistics based on statistical linearization and without optimization. On the other hand, MSF estimates the posterior PDF using a sampling technique and optimizes the PDF to minimize estimation error variance in the sense of posterior Cramer-Rao bound based on multi-scale PDF reconstruction. In addition, all Gaussian components of the posterior PDF are collectively optimized to capture the state statistics globally.

Generally speaking, the prior PDF of the parameters to be estimated is required for stochastic filtering. Unfortunately, the prior PDF may be inaccurate or unknown in real world applications including tissue characterization. Therefore, the filter dependency on prior PDF is an important practical issue one must address. The results presented in Sections 6.4.6 and 6.4.5 demonstrate the estimation accuracy of MSF in the absence of the prior PDF. When the prior PDF is unknown, MSF employs the expectation maximization algorithm to estimate a GMM as the prior PDF based on random samples generated by an uniform distribution (or the coarsest scale PDF) and likelihood evaluations of the samples.

[3]UKF applies unscented transformation (UT) [173] in the extended Kalman filter framework to obtain a Gaussian PDF that represents local statistics of the parameters to be estimated based on statistical linearization.

[4]Importance density

6.6 Summary

This chapter reports a series of experiments performed to evaluate the tissue acoustic parameter estimation accuracy of MSF. The acoustic parameters of eye tissues are measured, and ocular tissue phantoms are fabricated based on these measurements. Ultrasound based measurements of the phantom acoustic parameters are obtained to compare to the MSF estimation results. MSF is applied to estimate the acoustic parameters of a seven-layered tissue phantom and a four-layered tissue phantom array. A state-of-the-art NSF (i.e., GSPF-II) is applied to the same estimation problems as MSF for comparison. Results show that MSF and GSPF-II, respectively, achieve average absolute estimation errors of 1.9% and 7.2%. MSF is 3.8 ($7.2/1.9 = 3.8$) times more accurate than GSPF-II for tissue acoustic parameter estimation. Estimation results and experimental setup used are also presented.

Chapter 7

Conclusions and Future Work

In this thesis, an inverse scattering approach is developed to tackle the problem of ultrasound tissue characterization. This approach estimates the tissue acoustic parameters based on ultrasound measurements of the tissues and a forward scattering model that maps the parameters to the measurements. This model is highly nonlinear with respect to the parameters and stochastic. In addition, inverting this model is an ill-posed problem. Thus, a nonlinear stochastic method that does not require inversion of this model is desirable for performing inverse scattering.

A multi-scale stochastic filter (MSF) is proposed to realize inverse scattering. MSF is formulated based on a multi-scale PDF analysis framework, which provides mechanisms for recursively decomposing (reconstructing) a PDF from a fine scale to the coarsest scale (from the coarsest scale to a fine scale). MSF generates a set of initial random samples of the parameters using the coarsest scale PDF (i.e., uniform distribution) of the parameters and evaluates the samples based on the forward scattering model, actual ultrasound measurement and measurement noise statistics. Some of the samples are then selected according to the evaluation results to estimate the posterior PDF. In order to minimize the estimation uncertainty of the parameters, the posterior PDF is optimized by reconstructing it from its current scale to a finer scale. PDF reconstruction minimizes the estimation uncertainty based on the posterior Cramer-Rao bound. The filtering process is repeated for each ultrasound measurement.

MSF satisfies the inverse scattering method design criteria by eliminating the dependence on prior statistics of the parameters, weak scattering assumption, linearization and mathematical inversion of the forward scattering model from its formulation. Model linearization and weak scattering assumption are the bases of many existing methods, which simplify the forward scattering process to enable

the mathematical inversion of the model. However, simplification of the process compromises the accuracy of parameter estimation. Instead of inverting the model to obtain the parameters, MSF estimates the PDF of the parameters by sampling the parameter solution space and evaluating the samples based on measurements. Therefore, no model linearization and no weak scattering assumption are needed. MSF does not depend on the prior statistics of the parameters, since the multi-scale formulation is designed to utilize a uniform distribution as the initial PDF.

The proposed inverse scattering method is validated on multi-layered soft tissues using pulse-echo mode focused ultrasound. A seven-layered eye phantom and a four-layered ocular tissue phantom array are developed as test subjects. MSF and a state-of-the-art NSF are applied to estimate the acoustic parameters of each layer of the tissue phantoms. Experimental results show that MSF achieves an average absolute estimation error of 1.9%, and MSF is 3.8 times more accurate than the state-of-the-art NSF. In addition, the estimation accuracy of MSF is independent of the tissue phantom layer sequence. Moreover, MSF do not rely on the prior statistics of the parameters, which may be unknown or inaccurate in practice. MSF is formulated to employ the coarsest scale PDF as the initial statistics of the parameters. Furthermore, it is shown that the estimation error of MSF is not heavily dependent on the number of random samples and signal-to-noise ratio.

7.1 Future work

Based on this research, suggestions of future research work are listed in the following:

1. Time series modelling and soft computing techniques can be applied to improve ultrasound signal deconvolution. Although, deconvolution of ultrasound signals has been a popular research field and many techniques have been developed including [174, 175, 176, 177]. These techniques are derived based on an assumption that the reflectivity of material is convolved with a point spread function (PSF) with some invariant assumptions. However, PSF in reality is different for each echo due to attenuation and/or dispersion of the ultrasound wave. Therefore, the accuracy of these techniques are limited. In our experiments, layers of retina and choroid in animal eyes are too thin to obtain separate echoes for clinical ultrasound systems. Ultrasound echoes from these layers are superimposed so that obtaining the time of arrival and waveforms of these echoes is a problem. Ultrasound echoes can be modelled

by time series methods and to predict echoes in backscattered signals. Experiments are performed to model echoes with various ARMA models. Genetic algorithm is employed to search for the best parameters of these models. Results show that the output-error (OE) model produces the best fit. The resulting OE model is able to accurately predict some echoes of backscattered signal, but fails to do so for echoes that are severely attenuated. Therefore, more investigation is needed to improve this deconvolution method.

2. Wavelet based ultrasound deconvolution methods have been developed [178, 175, 179]. In general, these methods exploit the similarity between ultrasound echo model and wavelet structure, as well as the suitability of wavelet for deconvolution applications. Although these methods demonstrate acceptable accuracy, they all seem to ignore one of the most important issue in using wavelet. That is, the selection of the optimal wavelet basis for the application. In [180], the critical issue of wavelet basis selection is addressed for ultrasound foreign body classification based on information theory. Results confirm that the classification accuracy yielded by the optimal wavelet basis is far more superior than that of the suboptimal one. Therefore, great enhancement to the existing wavelet based deconvolution methods is expected if the optimal wavelet basis selection is implemented. Furthermore, it would be interesting to design the optimal wavelet basis for the specific ultrasound transducer and/or system.

3. In ultrasound research, resolution of the media structure under test is still one of the biggest limiting factors. The resolution is greatly dependent on the echo frequency range. For time domain analysis, the frequency range of echo should be as wide as possible in order to obtain high resolution pulses. In the past few decades, wide band ultrasound transducers have been developed [181, 182, 183, 184]. Despite of the intensive research effort, there must be a limitation for physical devices. Realizing that ultrasound instrumentation consists of both the transducer and electronics system. Analog and/or digital filters can be developed to amplify the frequency contents outside of the transducer's range. A challenge of such filters is to reduce noise sensitivity and maintain stability. This type of filter is commonly known as the equalizer in the field of communication. One may wish to modify the design of equalizer for ultrasonic systems.

4. When the measurement model is nonlinear, obtaining the close-form solution of Fisher information matrix may not be possible as in the case of this research. The matrix can be computed numerically using Monte-carlo inte-

gration with good accuracy. However, it is a highly computational demanding process and is the computational bottleneck of MSF. Methods that relax the computational requirement are highly desirable. An idea is to approximate the nonlinear measurement model or related PDFs by multidimensional spline, which can differentiated and integrated analytically. This may be of great interests to mathematician and computer scientists

5. In addition to algorithmic computational speed enhancement as described above, dedicated hardware including FPGA or ASIC can be designed to handle the intense computation needs of MSF. Dedicated hardware has been developed for computational intensive stochastic filters including particle filtering [185, 186, 187, 188]. Since both MSF and particle filtering are sample based, it is expected that hardware implementation of MSF is a feasible research project.

6. The Echotree and reverberation filtering are developed to remove reverberated echoes for multi-layer media in general. The backscattered signals of the multi-layer tissue phantoms do not exhibit any reverberated echoes. Therefore, the performance of Echotree and reverberation filtering are not thoroughly examined. To ensure reverberated echoes are present in the backscattered signals, flat parallel glass pieces should be used as the test subjects under water since glass has much higher acoustic impedance than water in general. The advantages of glass are their smooth surfaces, stability in water and various temperatures, as well as incompressibility for the ease of accurate thickness measurements.

7. One of the challenges encountered in this research is the sound speed measurements of retina and choroid. As mentioned these ocular layers are too thin, so that the ultrasound echoes of their front and back surfaces are superimposed. Consequently, the time of arrival of these echoes cannot be identified to calculate the sound speed. Although research has been conducted to measure the sound speeds of human and porcine ocular tissues [22, 23], the measurements are done at much higher frequencies than the clinical ultrasound. Extrapolation can be used to estimate the speeds at lower frequencies. The estimation is prone to noise and errors. When the ultrasound deconvolution research discussed above is developed, clinical measurements of retina's and choroid's sound speeds are made possible by recovering the reflectivity function and the echo time of arrival.

Bibliography

[1] J. Thijssen, "Ultrasonic speckle formation, analysis and processing applied to tissue characterization," *Pattern Recognition Letters*, vol. 24, no. 4, pp. 659–675, 2003.

[2] R. A. Mountford and P. Wells, "Ultrasonic liver scanning: The a-scan in the normal and cirrhosis," *Physics in Medicine and Biology*, vol. 17, pp. 261–269, 1972.

[3] M. Linzer, Ed., *Ultrasonic tissue characterization I. Special Publication*, gaithersburg, Maryland, USA, 1976. National Bureau of Standards.

[4] Z. F. Lu, "Cardiovascular ultrasound imgaging - a survey of technical development," *Journal of X-Ray Science and Technology*, vol. 11, pp. 133–139, 2003.

[5] N. Kharin, D. Driscoll, and W. Tobocman, "Free of speckle ultrasonic imaging of soft tissue with account of second harmonic signal," *Physics in Medicine and Biology*, vol. 48, pp. 3239–3260, 2003.

[6] W. Tobocman, "In vivo biomicroscopy with ultrasound," *Current Topics in Acoustics*, vol. 1, pp. 247–265, 1994.

[7] T. D. Mast, Lin Feng, and R. C. Waag, "Time-domain ultrasound diffraction tomography," in *Ultrasonics Symposium*, Caesars Tahoe, NV, USA, October 1999, vol. 2, pp. 1617–1620, IEEE.

[8] S. J. Norton and M. Linzer, "Ultrasonic reflectivity imaging in three dimensions: Exact inverse scattering solutions for plane, cylindrical, and spherical apertures," *IEEE Transactions on Biomedical Engineering*, vol. BME-28, no. 2, pp. 202–220, 1981.

[9] J. Hadamard, *Lectures on the Cauchy Problem in Linear Partial Differential Equations*, Yale University Press, New Haven, 1923.

[10] Houssem Haddar David Colton and Michele Piana, "The linear sampling method in inverse electromagnetic scattering theory," *Inverse Problems*, vol. 19, pp. S105Ű S137, 2003.

[11] Peter Monk David Colton, Joe Coyle, "Recent developments in inverse acoustic scattering theory," *SIAM REVIEW*, vol. 42, no. 3, pp. 369–414, 2000.

[12] A. Tikhonov, "On the solution of incorrectly formulated problems and the regularization method," *Soviet Math. Dokl.*, vol. 4, pp. 1035–1038, 1963.

[13] M. Hadjinicolaou, "Non-destructive identification of spherical inclusions," *Advanced Composites Letters*, vol. 9, no. 1, pp. 25–33, 2000.

[14] R. Marklein, K. Mayer, R. Hannemann, T. Krylow, K. Balasubramanian, K. Langenberg, and V. Schmitz, "Linear and nonlinear inversion algorithms applied in nondestructive evaluation," *Inverse Problems*, vol. 18, no. 6, pp. 1733–1759, 2002.

[15] S. Tong, D. Downey, H. Cardinal, and A. Fenster, "Three-dimensional ultrasound prostate imaging system," *Ultrasound in Medicine and Biology*, vol. 22, no. 6, pp. 735–746, 1996.

[16] A. Fenster, D. Downey, and H. Cardinal, "Three-dimensional ultrasound imaging," *Physics in Medicine and Biology*, vol. 46, no. 5, pp. R67–R99, 2001.

[17] A. Fenstera, K. Surry, W. Smith, J. Gill, and D. Downey, "3d ultrasound imaging: applications in image-guided therapy and biopsy," *Computers and Graphics*, vol. 26, pp. 557–568, 2002.

[18] A. Fenster and D. Downey, "3-d ultrasound imaging: A review," *IEEE Engineering in Medicine and Biology*, vol. 15, no. 6, pp. 41–61, 1996.

[19] D. Boukerroui, O. Basset, A. Baskurt, and G. Gimenez, "Multiparametric and multiresolution segmentation algorithm of 3-d ultrasonic data," *IEEE Transactions on Ultrasonics, Ferroelectrics, and Frequency Control*, vol. 48, no. 1, pp. 64–77, 2001.

[20] Martin E. Anderson and Gregg E. Trahey, "A seminar on k-space applied to medical ultrasound," http://dukemil.egr.duke.edu/Ultrasound/k-space/bme265.htm, 2000.

[21] D. A Christensen, *Ultrasonic Bioinstrmentation*, John Wiley and Sons, New York, 1988.

[22] S.G. Ye, K.A. Harasiewicz, C.J. Pavlin, and F.S. Foster, "Ultrasound characterization of ocular tissue in the frequency range from 50 mhz to 100 mhz," *Ultrasonics Symposium, 1992. Proceedings., IEEE 1992*, pp. 1107–1112 vol.2, 20-23 Oct 1992.

[23] C.L. De Korte, A.F.W. Van Der Steen, and J.M. Thijssen, "Acoustic velocity and attenuation of eye tissues at 20 mhz," *Ultrasound in Medicine and Biology*, vol. 20, no. 5, pp. 471–480, 1994.

[24] L. E. Linsler, A. R. Frey, Coppens A. B., and J. V. Sanders, *Fundamentals of Acoustics*, John Wiley & Sons, New York, 1982.

[25] B. M. Lempriere, *Ultrasound and Elastic waves*, Academic Press, Amsterdam, 2002.

[26] K. K. Shung, "General engineering principles in diagnostic ultrasound," *IEEE Enegineering in Medicine and Biology Magazine*, pp. 7 – 13, December 1987.

[27] A. C. Kak and M. Slaney, *Principles of computerized tomographic imaging*, IEEE Press, New York, 1988.

[28] Michel Bruneau and Thomas Scelo, *Fundamentals of Acoustics*, ISTE, London, UK, 2006.

[29] J. F. Greenleaf, *Tissue Characterization with Ultrasound. Volume I*, CRC Press, Boca Raton, Florida, 1986.

[30] Albert Goldstein, "Steady state unfocused circular aperture beam patterns in nonattenuating and attenuating fluids," *Journal of Acoustical Soceity of America*, vol. 115, no. 1, pp. 99 – 110, 2004.

[31] Albert Goldstein, "Steady state spherically focused, circular aperture beam patterns," *Ultrasound in Medicine and Biology*, vol. 32, no. 10, pp. 1441 Ű 1458, 2006.

[32] Richard S. C. Cobbold, *Foundations of Biomedical Ultrasound*, Oxford University Press, New York, 2007.

[33] D. N. Ghosh Roy and L. S. Couchman, *Inverse Problems and Inverse of Plane Waves*, Academic Press, San Diego, 2002.

[34] J. B. Keller, "Accuracy and validity of the born and rytov approximations," *Journal of Optical Society of Ameria*, vol. 59, pp. 1003Ű1004, 1969.

[35] M. Kaveh, M. Soumekh, and R. K. Mueller, *A comparison of Born and Rytov approximations in acoustic tomography*, vol. 11 of *Acoustical Imaging*, pp. 100–119, Plenum Press, New York, New York, 1982.

[36] R. D. Murchr, "An extended born approximation," *Inverse Problem*, vol. 8, pp. L5–L11, 1992.

[37] F. W. J. Olver, *lntroducrion to Asymptotics and Special Functions*, Academic Press, New York, 1974.

[38] R. Parsons, B. Sigel, E. Feleppa, R. Golub, J. Justin, V. Swami, M. Rorke, A. Kalisz, C. Long, A. Can, F. Lizzi, and H. Kitamura, "Ultrasonic tissue characterization of experimental venous intimal hyperplasia," *Ultrasound in Medicine and Biology*, vol. 19, no. 4, pp. 299–308, 1993.

[39] G. Davison, C. Hall, J. Miller, M. Scott, and S. Wickline, "Ultrasonic tissue characterization of end-stage dilated cardiomyopathy," *Ultrasound in Medicine and Biology*, vol. 21, no. 7, pp. 853–860, 1995.

[40] P. Stetson and G. Sommer, "Ultrasonic characterization of tissues via backscatter frequency dependence," *Ultrasound in Medicine and Biology*, vol. 23, no. 7, pp. 989–996, 1997.

[41] T. Noritomi, B. Sigel, V. Swami, J. Justin, V. Gahtan, C. Xiaoli; E. Feleppa, A. Roberts, and K. Shirouzu, "Carotid plaque typing by multiple-parameter ultrasonic tissue characterization," *Ultrasound in Medicine and Biology*, vol. 23, no. 5, pp. 643–650, 1997.

[42] L. C. Lin, C. C. Wu, Y. L. Ho, C. W. Lin, W. J. Chen, M. F. Chen, C. S. Liau, and Y. T. Lee, "Ultrasonic tissue characterization for coronary care unit patients with acute myocardial infarction," *Ultrasound in Medicine and Biology*, vol. 24, no. 2, pp. 187–196, 1998.

[43] L. C. Lin, C. C. Wu, Y. L. Ho, M. F. Chen, C. S. Liau, and Y. T. Lee, "Ultrasonic tissue characterization in predicting residual ischemia and myocardial viability for patients with acute myocardial infarction," *Ultrasound in Medicine and Biology*, vol. 24, no. 8, pp. 1107–1120, 1998.

[44] L. C. Lin, H. L. Kao, C. C. Wu, Y. L. Ho, and Y. T. Lee, "Alterations of myocardial ultrasonic tissue characterization by coronary angioplasty in patients with chronic stable coronary artery disease," *Ultrasound in Medicine and Biology*, vol. 27, no. 9, pp. 1191–1198, 2001.

[45] D. Lee, B. Sigel, V. Swami, J. Justin, V. Gahtan, S. OŠBrien, L. Dwyer-Joyce, E. Feleppa, A. Roberts, and H. Berkowitz, "Determination of carotid plaque risk by ultrasonic tissue characterization," *Ultrasound in Medicine and Biology*, vol. 24, no. 9, pp. 1291–1299, 1998.

[46] G. Schmitz, H. Ermert, and T. Senge, "Tissue-characterization of the prostate using radio frequency ultrasonic signals," *IEEE Transactions on Ultrasonics, Ferroelectrics and Frequency Control*, vol. 46, no. 1, pp. 126–138, 1999.

[47] E. I. Cespedes, C. L. de Korte, and A. F. W. van der Steen, "Intraluminal ultrasonic palpation: assessment of local and cross-sectional tissue stiffness," *Ultrasound in Medicine and Biology*, vol. 26, no. 3, pp. 385–396, 2000.

[48] L. C. Lin, R. F. Yen, J. J. Hwang, F. T. Chiang, C. D. Tseng, and P. J. Huang, "Ultrasonic tissue characterization evaluates myocardial viability and ischemia in patients with coronary artery disease," *Ultrasound in Medicine and Biology*, vol. 26, no. 5, pp. 759–769, 2000.

[49] S. Huber, J. Danes, I. Zuna, J. Teubner, M. Medl, and S. Delorme, "Relevance of sonographic b-mode criteria and computer-aided ultrasonic tissue characterization in differential/diagnosis of solid breast masses," *Ultrasound in Medicine and Biology*, vol. 26, no. 8, pp. 1243–1252, 2000.

[50] I. Kondo, K. Mizushige, S. Nozaki, Y. Iwado, K. Hirao, S. Senda, M. Kohno, and H. Matsuo, "Ultrasonic tissue characterization can predict beta-blocker efficacy in dilated cardiomyopathy," *Ultrasound in Medicine and Biology*, vol. 27, no. 8, pp. 1079–1086, 2001.

[51] T. Masuyama, K. Yamamoto, N. Nishikawa, Y. Sakata, T. Mano, M. Hori, T. Sonoyama, T. Ito, and Y. Yoshikawa, "New attempt of ultrasonic tissue characterization: decreased chaos in myocardial echo in patients with dilated cardiomyopathy," *Ultrasound in Medicine and Biology*, vol. 28, no. 1, pp. 93–99, 2002.

[52] U. Scheipers, H. Ermert, H. Sommerfeld, M. Garcia-Schürmann, T. Senge, and S. Philippou, "Ultrasonic multifeature tissue characterization for prostate

diagnostics," *Ultrasound in Medicine and Biology*, vol. 29, no. 8, pp. 1137–1149, 2003.

[53] M. A. Kutay, A. P. Petropulu, and C. W. Piccoli, "Breast tissue characterization based on modeling of ultrasonic echoes using the power-law shot noise model," *Pattern Recognition Letters*, vol. 24, pp. 741–756, 2003.

[54] M. A. Kutay, A. P. Petropulu, and C. W. Piccoli, "On modelling biomedical ultrasound rf echoes using a power-law shot noise model," *IEEE Transactions on Ultrasonics, Ferroelectrics and Frequency Control*, vol. 48, pp. 953–968, 2001.

[55] C. Kechribaris, T. A. Maniatis, K. S. Nikita, and N. K. Uzunoglu, "Inverse scattering algorithms for biological tissue diffraction tomography: A comparative study," in *Proceedings of the 25th Annual International Conference of the IEEE Engineering in Medicine and Biology Society*, Cancun, Mexico, September 2003, vol. 4, pp. 3775–3778, IEEE.

[56] A. J. Devaney, "A filtered backpropagation algorithm for diffraction tomography," *Ultrasonics*, vol. 4, no. 4, pp. 336–350, 1982.

[57] M. M. Bronstein, A. M. Bronstein, M. Zibulevsky, and H. Azhari, "Reconstruction in diffraction ultrasound tomography using nonuniform fft," *IEEE Transactions on Medical Imaging*, vol. 21, no. 11, pp. 1395–1401, 2002.

[58] M. Slaney, A. C. Kak, and L. E. Larsen, "Limitations of imaging with first-order diffraction tomography," *IEEE Transactions on Microwave Theory and Techniques*, vol. 32, no. 8, pp. 860–874, 1984.

[59] R. F. Harrington, *Field computation by moment methods*, IEEE Press, Piscataway, NJ, 1993.

[60] D. T. Borup, S. A. Johnson, W. W. Kim, and M. J. Berggren, "Nonperturbative diffraction tomography via gaussian-newton iteration applied to the scattering integral equation," *Ultrasonic Imaging*, vol. 14, pp. 69–85, 1992.

[61] A. Roger, "Newton-kantorovitch algorithm applied to an electromagnetic inverse problem," *IEEE Transactions on Antennas and Propagation*, vol. 29, no. 2, pp. 232–238, 1981.

[62] Y. M. Wang and W. C. Chew, "An iterative solution of the two-dimensional electromagnetic inverse scattering problem," *International Journal of Imaging Systems and Technology*, vol. 1, pp. 100–108, 1989.

[63] W. C. Chew and Y. M. Wang, "Reconstruction of two-dimensional permittivity distribution using the distorted born iterative method," *IEEE Transactions on Medical Imaging*, vol. 9, no. 2, pp. 218–225, 1990.

[64] N. Joachimowicz, J. J. Mallorqui, J. Bolomey, and A. Broquets, "Convergence and stability assessment of newton-kantorovich reconstruction algorithms for microwave tomography," *IEEE Transactions on Medical Imaging*, vol. 17, no. 4, pp. 562–570, 1998.

[65] Lujiang Liu, Xiaodong Zhang, and S. L. Broschat, "Ultrasound imaging using variations of the iterative born technique," *IEEE Transactions on Ultrasonics, Ferroelectrics and Frequency Control*, vol. 46, no. 3, pp. 574–583, May 1999.

[66] O. S. Haddadin and E. S. Ebbini, "Imaging strongly scattering media using a multiple frequency distorted born iterative method," *IEEE Transactions on Ultrasonics, Ferroelectrics and Frequency Control*, vol. 45, no. 6, pp. 1485–1496, 1998.

[67] Y. Yang, O. A. Basir, and Y. Liu, "Estimation of high frequency scattered microwave electric field using the extended born approximation," in *IEEE Antennas and Propagation Society International Symposium*, Columbus, OH, USA, June 2003, vol. 2, pp. 215–218, IEEE.

[68] Y. Yang, O. A. Basir, and Y. Liu, "Wavelet based method for electromagnetic inverse scattering problem using extended born approximation," in *IEEE International Geoscience Remote Sensing Symposium*, Toulouse, France, Junly 2003, vol. 7, pp. 4220–4222, IEEE.

[69] E. L. Miller and A. S. Willsky, "Wavelet-based methods for the nonlinear inverse scattering problem using the extended born approximation," *Radio Science*, vol. 3, pp. 51–65, 1996.

[70] A. P. Berkhoff and J. M. Thijssen, "Correction of concentrated and distributed aberrations in medical ultrasound imaging," in *Ultrasonics Symposium*, San Antonio, TX, USA, 1996, vol. 2, pp. 1405–1410, IEEE.

[71] K. Santosh, W. Tobocman, E. M. Haacke, and F. Boada, "In vivo biomicroscopy with ultrasound," *Ultrasonics*, vol. 25, no. 5, pp. 274–282, 1987.

[72] K. Santosh, W. Tobocman, E. M. Haacke, and F. Boada, "In vivo biomicroscopy with ultrasound 2," *Ultrasonics*, vol. 28, no. 1, pp. 40–49, 1990.

[73] W. Tobocman, K. Santosh, J. R. Carter, and E. M. Haacke, "Tissue characterization of arteries with 4 mhz ultrasound," *Ultrasonics*, vol. 33, no. 4, pp. 331–339, 1995.

[74] A. Tarantola, *Inverse Problem Theory*, Elsevier, Amsterdam, 1987.

[75] D. Bedekar, A. Nair, and D. G. Vince, "Atherosclerotic plaque characterization by acoustic impedance analysis of intravascular ultrasound data," in *Ultrasonics Symposium*, D. E. Yuhas and S. C. Schneider, Eds., Honolulu, Hawaii, Oct. 2003, vol. 2, pp. 1524–1527, IEEE.

[76] A. Yamada, "High precision quasi 3d quantitative reconstruction of sound velocity image from the transmitted data around a single rotational axis," in *Ultrasonics Symposium*, San Antonio, TX , USA, Nov. 1996, vol. 2, pp. 1423–1426, IEEE.

[77] A. Yamada, "Quasi 3d quantitative computerized tomography for reconstructing sound velocity of a weakly scattering object," *Japanese Journal of Applied Physics, Part I*, vol. 35, no. 5, 1996.

[78] Sung-Jae Kwon and Mok-Kun Jeong, "Ultrasound inverse scattering determination of speed of sound, density, and absorption," in *Ultrasonics Symposium*, Sendai, Japan, October 1998, vol. 2, pp. 1631–1634, IEEE.

[79] P. M. Morse and K. U. Ingard, *Theoretical Acoustics*, Plenum, New York, 1968.

[80] S. A. Johnson, F. Stenger, C. Wilcox, J. Ball, and M. J. Berggren, "Wave equations and inverse solutions for soft tissue," *Acoustic imaging*, vol. 11, pp. 409–424, 1982.

[81] S. J. Norton, "Generation of separate density and compressibility images in tissue," *Ultrasonic imaging*, vol. 5, no. 3, pp. 240–252, 1983.

[82] A. J. Devaney, "Variable density acoustic tomography," *Journal of the Acoustic Society of America*, vol. 78, no. 1, pp. 120–130, 1986.

[83] S. Mensah and J. P. Lefebvre, "Enhanced compressibility tomography," *IEEE Transactions on Ultrasonics, Ferroelectrics and Frequency Control*, vol. 44, no. 6, pp. 1245–1252, 1997.

[84] M. Kuroiwa and A. Yamada, "Ultrasonic attenuation image of the biological tissues by using the diffraction tomographic technique," *Japanese Journal of Applied Physics, Part I*, vol. 37, no. 5, 1998.

[85] A. Yamada and M. Kuroiwa, "Quantitative ultrasonic attenuation image of the biological tissues using the inverse scattering technique," in *Ultrasonics Symposium*, Sendai, Japan, October 1998, vol. 2, pp. 1651–1654, IEEE.

[86] Akira Yamada, "Compensation of linearization approximation error in acoustic inverse scattering problem: Quantitative reconstruction of attenuation and sound speed images," *Jpn. J. Appl. Phys. Part 1*, vol. 38, no. 6, 1999.

[87] Jung-Soon Kim and Akira Yamada, "Inverse scattering image reconstruction from reflection and transmission data obtained using the mirror image theory," *Jpn. J. Appl. Phys. Part 1*, vol. 39, no. 5, 2000.

[88] M. J. Berggren, S. A. Johnson, B. L. Carruth, W. W. Kim, F. Stenger, and P. K. Kuhn, "Ultrasound inverse scattering solutions from transmission and/or reflection data," in *Proceedings of SPIE - The International Society for Optical Engineering*, Newport Beach, CA, USA, 1986, vol. 671, pp. 114–121, SPIE.

[89] J. C. Bamber and C. Daft, "Adaptive filtering for reduction of speckle in ultrasonic pulse-echo images," *Ultrasonics*, vol. 24, no. 1, pp. 41–44, 1986.

[90] C. B. Burckhardt, "Speckle in ultrasound b-mode scans," *IEEE Transactions on Sonics and Ultrasonics*, vol. 25, no. 1, pp. 1–6, 1978.

[91] R. F. Wagner, S. W. Smith, J. M. Sandrik, and H. Lopez, "Statistics of speckle in ultrasound b-scans," *IEEE Transactions on Sonics and Ultrasonics*, vol. 30, no. 3, pp. 156–163, May 1983.

[92] E. Jakeman and R. Tough, "Generalized k-distribution: A statistical model for weak scattering," *Journal of the Optical Society of America A*, vol. 4, no. 9, pp. 1764–1772, 1987.

[93] J. W. Goodman, "Statistical properties of laser speckle," in *Laser Speckle and Related Phenomena*, J. C. Dainty, Ed., pp. 9–75. Springer Verlag, Berlin, 1984.

[94] M. F. Insana, R. F. Wagner, B. S. Garra, D. G. Brown, and T. H. Shawker, "Analysis of ultrasound image texture via generalized rician statistics," *Optical Enginerring*, vol. 25, no. 6, pp. 743–748, 1986.

[95] J. W. Goodman, "Echographic image processing," in *Advances in Electronics and Electron Physics*, P. W. Hawkins, Ed., vol. 84, pp. 317–349. Academic Press, Boston, 1992.

[96] J. H. Hokland and T. Taxt, "Ultrasound speckle reduction using harmonic oscillator models," *IEEE Transactions on Ultrasonics, Ferroelectrics, and Frequency Control*, vol. 41, no. 2, pp. 215–224, 1994.

[97] M. Karaman, M. A. Kutay, and G. Bozdagi, "Adaptive speckle suppression filter for medical ultrasonic imaging," *IEEE Transactions on Medical Imaging*, vol. 14, no. 2, pp. 283–292, 1995.

[98] R. W. Prager, A. H. Gee, G. M. Treece, and L. H. Berman, "Analysis of speckle in ultrasound images using fractional order statistics and the homodyned k-distribution," *Ultrasonics*, vol. 40, pp. 133–137, 2002.

[99] N. Suhm, I. Zuna, M. Fein, and G. Weisser, "Effects of adaptive speckle filtering on the diagnostic accuracy of ultrasound in vivo tissue characterization," *European Journal of Ultrasound*, vol. 2, no. 1, pp. 57–64, 1995.

[100] W. Tobocman, D. Driscoll, N. Shokrollahi, and J. A. Izatt, "Free of speckle ultrasound images of small tissue structures," *Ultrasonics*, vol. 40, pp. 983–996, 2002.

[101] N. Kharin, D. Driscoll, and W. Tobocman, "Application of the born-approximation deconvolved inverse scattering (badis) method to second harmonic imaging," in *Proceedings of SPIE*, San Diego, CA, United States, Feb. 2002, vol. 4687, pp. 450–461, The International Society for Optical Engineering.

[102] R. K. Saha, S. K. Sen, S. K. Sharma, and B. Dutta-Roy, "Comments on free of speckle ultrasonic imaging of soft tissue with account of second harmonic signal," *Physics in Medicine and Biology*, vol. 49, pp. L11–L14, 2004.

[103] H. Ponnekanti, J. Ophir, and I. Cespedes, "Axial stress distributions between coaxial compressors in elastography: an analytic model," *Ultrasound in Medicine and Biology*, vol. 18, pp. 667–673, 1992.

[104] M. O'Donnell, A. R. Skovoroda, B. M. Shapo, and S. Y. Emelianov, "Internal displacement and strain imaging using ultrasonic speckle tracking," *IEEE Transactions on Ultrasonics, Ferroelectrics, and Frequency Control*, vol. 41, no. 3, pp. 314–325, May 1994.

[105] F. Yeung, S. F. Levinson, and K. J. Parker, "Multilevel and motion model-based ultrasonic speckle tracking algorithms," *Ultrasound in Medicine and Biology*, vol. 24, no. 3, pp. 427–441, 1998.

[106] T. Lawu and M. Ueda, "Simulation of ultrasonic displacement in random medium using ultrasonic speckle tracking," *Japanese Journal of Applied Physics, Part 1: Regular Papers and Short Notes and Review Papers*, vol. 39, no. 5B, pp. 3220–3224, 2000.

[107] G. Ohashi, T. Toyoda, A. Ohya, and I. Akiyama, "A study of speckle tracking method for three-dimensional ultrasonic imaging," *Electronics and Communications in Japan, Part III: Fundamental Electronic Science*, vol. 85, no. 12, pp. 1–8, 2002.

[108] B. S. Carmo, R. W. Prager, A. H. Gee, and L. H. Berman, "Speckle detection for 3d ultrasound," *Ultrasonics*, vol. 40, pp. 129–132, 2002.

[109] M. Jeong and S. Kwon, "Tissue stiffness imaging method using temporal variation of ultrasound speckle pattern," *IEEE Transactions on Ultrasonics, Ferroelectrics, and Frequency Control*, vol. 50, no. 4, pp. 457–460, 2003.

[110] J.H. McClellan and T.W. Parks, "A personal history of the parks-mcclellan algorithm," *IEEE Signal Processing Magazine*, vol. 22, no. 2, pp. 82 – 86, 2005.

[111] A. V. Oppenheim and R. W. Schafer, *Discrete-Time Signal Processing*, Prentice-Hall, Englewood Cliffs, NJ, 1989.

[112] L. M. Brekhovskikh, *Waves in Layered Media*, Academic Press, New York, 1980.

[113] L. M. Brekhovskikh and O. A. Godin, *Acoustics of Layered Media I Plane and Quasi-Plane Waves*, Springer-Verlag, Berlin, 1990.

[114] P. Ted Christopher and Kevin J. Parker, "New approaches to nonlinear diffractive field propagation," *Journal of Acoustical Soceity of America*, vol. 90, no. 1.

[115] Richard Croce, Pierre Calmon, and Luc Paradis, "Modeling of propagation and echo formation in a multilayered structure," *Ultrasonics*, vol. 38, pp. 537 Ű 541, 2000.

[116] J. Bilmes, "A gentle tutorial on the em algorithm and its application to parameter estimation for gaussian mixture and hidden markov models," Tech. Rep. ICSI-TR-97-021, University of Berkeley, 1997.

[117] B. Ristic, S. Arulampalam, and N. Gordon, *Beyond the Kalman Filter: Particle Filters for Tracking Applications*, Artech House, Boston and London, 2004.

[118] Rudolph van der Merwe, Arnauld Doucet, Nando de Freitas, and Eric Wan, "Unscented particle filter," Tech. Rep. CUED/F-INFENG/TR 380, Cambridge University, Engineering Department, Cambridge, UK, 2000.

[119] J. H. Kotecha and P. M. Djuric, "Gaussian particle filtering," *IEEE Transactions on Signal Processing*, vol. 51, pp. 2592–2601, 2003.

[120] Y. Wu, X. Hu, D. Hu, and M. Wu, "Comments on gaussian particle filtering," *IEEE Transactions on Signal Processing*, vol. 53, no. 8, pp. 3350–3351, 2005.

[121] J. H. Kotecha and P. M. Djuric, "Gaussian sum particle filtering," *IEEE Transactions on Signal Processing*, vol. 51, pp. 2602–2612, 2003.

[122] A. Doucet, S. Godsill, and C. Andrieu, "On sequential monte carlo sampling methods for bayesian filtering," *Statistics and Computing*, vol. 10, no. 3, pp. 197–208, 2000.

[123] A. Doucet, N. Gordon, and V. Krishnamurthy, "Particle filters for state estimation of jump markov linear systems," *IEEE Transactions on Signal Processing*, vol. 49, pp. 613–624, March, 2001.

[124] C. Andrieu, M. Davy, and A. Doucet, "Efficient particle filtering for jump markov systems application to time-varying autoregressions," *IEEE Transactions on Signal Processing*, vol. 51, no. 7, pp. 1762–1770, 2003.

[125] A. P. Witkin, Ed., *Scale-space filtering*, Karlsruhe, West Germany, 1983. IJCAI.

[126] R. N. Bracewell, *The Fourier Transform and Its Applications*, McGraw Hill, Boston, 2000.

[127] J. J. Koenderink, "The structure of images," *Biological Cybernetics*, vol. 50, pp. 363–370, 1984.

[128] T. Lindeberg, *Scale-space Theory in Computer Vision*, Kluwer Academic Publishers, Boston, 1994.

[129] A. L. Yuille and T. A. Poggio, "Scaling theorems for zero-crossings," *IEEE Transactions on Pattern Analysis and Machine Intelligence*, vol. 8, no. 1, pp. 15–25, 1986.

[130] J. Babaud, A. P. Witkin, M. Baudin, and R. O. Duda, "Uniqueness of the gaussian kernel for scale-space filtering," *IEEE Transactions on Pattern Analysis and Machine Intelligence*, vol. 8, no. 1, pp. 26–33, 1986.

[131] R. A. Hummel, *The scale-space formulation of pryramid data structures*, pp. 187–223, Parallel Computer Vision. Acdemic Press, New York, New York, 1987.

[132] T. Lindeberg, "Scale-space for discrete signals," *IEEE Transactions on Pattern Analysis and Machine Intelligence*, vol. 12, pp. 234–254, 1990.

[133] L. Florack, J. Koenderink B. ter Haar Romeny, and M. Viergever, "Scale and the differential structure of images," *Image and Vision Computing*, vol. 10, pp. 376–388, 1992.

[134] A. Doucet, N. de Freitas, and N. J. Gordon, "Sequential monte carlo methods in practice," 2001.

[135] A. Papoulis, *Probability, Random Variables, and Stochastic Processes*, McGraw-Hill Inc., New York, 1991.

[136] P. Tichavsky, C. Muravchik, and A. Nehorai, "Posterior cramer-rao bounds for discrete-time nonlinear filtering," *IEEE Transactions on Signal Processing*, vol. 46, no. 5, pp. 1386–1396, May 1998.

[137] S. J. Juiler, J. K. Uhlmann, and H. F. Durrant-White, "A new method for nonlinear transformation of means and covariances in filters and estimators," *IEEE Transactions on on Automatic Controls*, vol. 45, pp. 477–482, 2000.

[138] S. C. Nardone, A. G. Lindgren, and K. F. Gong, "Fundamental properties and performance of conventional bearings-only tracking motion analysis," *IEEE Transactions on Automatic Control*, vol. 29, no. 9, 1984.

[139] J. C. Hassab, *Underwater Signal and Data Processing*, CRC Press, Boca Raton, FL, 1989.

[140] S. Blackman and R. Popoli, *Design and Analysis of Modern Tracking Systems*, Artech House, Norwood, MA, 1999.

[141] T. Kirubarajan, Y. Bar-Shalom, and D. Lerro, "Bearings-only tracking for maneuvering targets using a batch-recursive estimator," *IEEE Transactions on Aerospace and Electronic Systems*, vol. 37, pp. 770–780, 2001.

[142] M. R. Morelande and S. Challa, "Manoeuvring target tracking in clutter using particle filters," *IEEE Transactions on Aerospace and Electronic Systems*, vol. 41, no. 1, pp. 252–270, 2005.

[143] G. Kitagawa, "Non-gaussian state-space modeling of nonstationary time series," *Journal of the American Statistical Association*, vol. 82, no. 400, pp. 1032–1063, 1987.

[144] N. Gordon, D. Salmond, and C. Ewing, "Bayesian state estimation for tracking and guidance using bootstrap filter," *Journal of Guidance, Control and Dynamics*, vol. 18, no. 6, pp. 1434–1443, 1995.

[145] E. R. Beadle and P. M. Djuric, "A fast weighted bayesian bootstrap filter for nonlinear model state estimation," *IEEE Transactions on Aerospace and Electronic Systems*, vol. 33, pp. 338–342, 1997.

[146] Richard E. Neapolitan and Kumarss Naimipour, *Foundations of Algorithms*, D. C. Heath and Company, Lexington, Massachusetts, Toronto, 1996.

[147] R. Van der Merwe and E.A. Wan, "The square-root unscented kalman filter for state and parameter-estimation," in *2001 IEEE International Conference on Acoustics, Speech, and Signal Processing*, Salt Lake City, Utah, USA, May 2001, vol. 6, pp. 3461–3464, IEEE.

[148] R. R. Seeley, T. D. Stephens, and Tate P., *Essentials of anatomy and physiology*, Mosby Year Book, St. Louis, 1991.

[149] R. L. Drake, Vogl W., and Mitchell A. W. M., *Gray's anatomy for students*, Elsevier, Philadelphia, 2005.

[150] R. C. Chivers and R. J. Parry, "Ultrasonic velocity and attenuation in mammalian tissues," *J. Acoust. Soc. Am.*, vol. 63, no. 3, pp. 940 – 953, 1978.

[151] S. A. Goss, R. L. Johnston, and F. Dunn, "Compilation of emperical ultrasonic properties of mammalian tissues ii," *J. Acoust. Soc. Am.*, vol. 68, no. 1, pp. 93 – 108, 1980.

[152] J. M. Thijssen, H. J. M. Mol, and M. R. Timmer, "Acoustic parameters of ocular tissues," *Ultrasound in Medicine and Biology*, vol. 11, no. 1, pp. 157 – 161, 1985.

[153] S. G. Ye, K.A. Harasiewicz, C.J. Pavlin, and F.S. Foster, "Ultrasound characterization of normal ocular tissue in the frequency range from 50 mhz to 100 mhz," *IEEE Transactions on Ultrasonics, Ferroelectrics, and Frequency Control*, vol. 42, no. 1, pp. 8 – 14, 1995.

[154] Xiao Su, Christina Vesco, Jacquelyn Fleming, and Vivian Choh, "The density of ocular components in the bovine eye," *Optometry and Vision Science*, p. (in press), 2009.

[155] Laura A. Negron, Francesco Viola, Cric P. Black, Cynthia A. Toth, and William F. Walker, "Development and characterization of a vitreous mimicking material for radiation force imaging," *IEEE Transactions on Ultrasonics, Ferroelectrics, and Frequency Control*, vol. 49, no. 11, pp. 1543Ű1551, 2002.

[156] Francesco Viola and William F. Walker, "Radiation force imaging of viscoelastic properties with reduced artifacts," *IEEE Transactions on Ultrasonics, Ferroelectrics, and Frequency Control*, vol. 50, no. 6, pp. 736Ű742, 2003.

[157] Jun Liu, Xiaoyin He, Xueliang Pan, and Cynthia J. Roberts, "Ultrasonic model and system for measurement of corneal biomechanical properties and validation on phantoms," *Journal of Biomechanics*, vol. 40, no. 5, pp. 1177 – 1182, 2007.

[158] K.V. Ramnarine, T. Anderson, and P.R. Hoskins, "Construction and geometric stability of physiological flow rate wall-less stenosis phantoms," *Ultrasound in Medicine and Biology*, vol. 27, no. 2, pp. 245 – 250, 2001.

[159] F. Kallel, C.D. Prihoda, and J. Ophir, "Contrast-transfer efficiency for continuously varying tissue moduli: simulation and phantom validation," *Ultrasound in Medicine and Biology*, vol. 27, no. 8, pp. 1115 – 1125, 2001.

[160] Seshadri Srinivasan, T. Krouskop, and Jonathan Ophir, "Comparing elastographic strain images with modulus images obtained using nanoindentation: Preliminary results using phantoms and tissue samples," *Ultrasound in Medicine and Biology*, vol. 30, no. 3, pp. 329 – 343, 2004.

[161] Steven J. Hammer, Judith Dineley, William J. Easson, and Peter R. Hoskins, "An arterial wall motion test phantom for the evaluation of wall motion software," *Ultrasound in Medicine and Biology*, vol. 33, no. 9, pp. 1504 – 1511, 2007.

[162] Manju Singh, H.R. Singh, Ashvani Kumar, V.R. Singh, K. Pant, and Poonam Sethi, "Development of tissue-equivalent phantoms for biomedical ultrasonic applications," *International Journal of Biomedical Engineering and Technology*, vol. 1, pp. 273 – 286, 2008.

[163] Linda K. Ryan and F. Stuart Foster, "Tissue equivalent vessel phantoms for intravascular ultrasound," *Ultrasound in Medicine and Biology*, vol. 23, no. 2, pp. 261 – 273, 1997.

[164] J. D'hooge, B. Bijnens, J. Nuyts, J.-M. Gorce, D. Friboulet, J. Thoen, F. van de Werf, and P. Suetens, "Nonlinear propagation effects on broadband attenuation measurements and its implications for ultrasonic tissue characterization," *Journal of the Acoustical Society of America*, vol. 106, no. 2, pp. 1126 – 33, 1999/08/.

[165] V. Khokhlova, O. Sapozhnikov, Yu. Pishchalnikov, T. Sinilo, E. Filonenko, M. Bailey, and L. Crum, "Enhancement of ultrasound-induced heating in tissue phantoms due to formation of shocks: Experimental measurements and numerical simulations," *Ultrasound in Medicine and Biology*, vol. 26, no. SUPPL 2, pp. 72 –, 2000.

[166] M.M. Doyley, J.C. Bamber, F. Fuechsel, and N.L. Bush, "A freehand elastographic imaging approach for clinical breast imaging: system development and performance evaluation," *Ultrasound in Medicine and Biology*, vol. 27, no. 10, pp. 1347 – 57, 2001.

[167] Ernest L. Madsen, Maritza A. Hobson, Hairong Shi, Tomy Varghese, and Gary R. Frank, "Tissue-mimicking agar/gelatin materials for use in heterogeneous elastography phantoms," *Physics in Medicine and Biology*, vol. 50, no. 23, pp. 5597 – 5618, 2005.

[168] Helen Morehouse, Harshada Pranav Thaker, and Chandowti Persaud, "Addition of metamucil to gelatin for a realistic breast biopsy phantom," *Journal of Ultrasound in Medicine*, vol. 26, no. 8, pp. 1123 – 1126, 2007.

[169] Y Yamamoto, R. Namiki, M. Baba, and M. Kato, "A study on the measurement of ocular axial length by ultrasound echography," *Acta Soc. Ophthal. Jap.*, vol. 64, pp. 1333–1341, 1960.

[170] M. Araki, "Studies on refractive elements of human eye by ultrasonic wave," *Jap. J. Clin. Ophthal.*, vol. 15, pp. 111 – 119, 1961.

[171] F. Jansson and E. Sundmark, "Determination of the velocity of ultrasound in ocular tissues at different temperatures," *Acta Ophtal.*, vol. 39, pp. 899 – 910, 1961.

[172] A. Rivarra and G. Sanna, "Determination of the speed of ultrasound in the ocular studies of humans and swine," *Ann. Ottal. Clin. Ocul.*, vol. 88, pp. 672 – 682, 1962.

[173] S. J. Juiler, J. K. Uhlmann, and H. F. Durrant-White, "A new method for nonlinear transformation of means and covariances in filters and estimators," *IEEE Transactions on Automatic Controls*, vol. 45, pp. 477–482, 2000.

[174] Oddvar Husby, Torgrim Lie, Thomas Lango, Jorn Hokland, and Havard Rue, "Bayesian 2-d deconvolution: A model for diffuse ultrasound scattering," *IEEE Transactions on Ultrasonics, Ferroelectrics, and Frequency Control*, vol. 48, no. 1, pp. 121 – 130, 2001.

[175] Dan Adam and Oleg Michailovich, "Blind deconvolution of ultrasound sequences using nonparametric local polynomial estimates of the pulse," *IEEE Transactions on Biomedical Engineering*, vol. 49, no. 2, pp. 118 – 131, 2002.

[176] Oleg V. Michailovich and Dan Adam, "A novel approach to the 2-d blind deconvolution problem in medical ultrasound," *IEEE Transactions on Medical Imaging*, vol. 24, no. 1, pp. 86 – 104, 2005.

[177] Liang Wei, Lei Hua-Ming, and Que Pei-Wen, "Sparsity enhancement for blind deconvolution of ultrasonic signals in nondestructive testing application," *Review of Scientific Instruments*, vol. 79, no. 1, pp. 014901 –, 2008.

[178] Henri-Pierre Valero, Stephanie Gautier, Ginette Saracco, and Matthias Holschneider, "Deconvolution from instrumental devices and source effect in acoustic experiments," *IEEE Transactions on Instrumentation and Measurement*, vol. 51, no. 2, pp. 268 – 276, 2002.

[179] Roberto Henry Herrera, Ruben Orozco, and Manuel Rodriguez, "Wavelet-based deconvolution of ultrasonic signals in nondestructive evaluation," *Journal of Zhejiang University: Science*, vol. 7, no. 10, pp. 1748 – 1756, 2006.

[180] P.P.C. Tsui and O.A. Basir, "Wavelet basis selection and feature extraction for shift invariant ultrasound foreign body classification," *Ultrasonics*, vol. 45, no. 1-4, pp. 1 – 14, 2006/12/.

[181] J. Souquet, P. Defranould, and J. Desbois, "Design of low-loss wide-band ultrasonic transducers for noninvasive medical application," *IEEE Transactions on Sonics and Ultrasonics*, vol. SU26, no. 2, pp. 75 – 81, 1979/03/.

[182] Kuniko Kimura, Kazuyuki Yoneya, and Hiroji Ohigashi, "Wide-band polymer ultrasonic transducer using acoustic impedance matching technique.," *Japanese Journal of Applied Physics, Part 1: Regular Papers and Short Notes*, vol. 27, no. 4, pp. 547 – 551, 1988.

[183] Yeon-Bo Kim and Yongrae Roh, "New design of matching layers for high power and wide band ultrasonic transducers," *Sensors and Actuators A (Physical)*, vol. A71, no. 1-2, pp. 116 – 22, 1998/11/01.

[184] G. Lypacewicz, A. Nowicki, R. Dynowski, and R. Tymkiewicz, "Wide-band circular ultrasonic transducers," *Acta Acustica (Stuttgart)*, vol. 88, no. 5, pp. 803 – 806, 2002.

[185] S. Hong, P.M. Djuric, and M. Bolic, "Simplifying physical realization of gaussian particle filters with block-level pipeline control," *EURASIP Journal on Applied Signal Processing*, vol. 2005, no. 4, pp. 575 – 87, 2005/03/15.

[186] Miodrag Bolic, Petar M. Djuric, and Sangjin Hong, "Resampling algorithms and architectures for distributed particle filters," *IEEE Transactions on Signal Processing*, vol. 53, no. 7, pp. 2442 – 2450, 2005.

[187] Akshay Athalye, Miodrag Bolic, Sangjin Hong, and Petar M. Djuric, "Generic hardware architectures for sampling and resampling in particle filters," *Eurasip Journal on Applied Signal Processing*, vol. 2005, no. 17, pp. 2888 – 2902, 2005.

[188] Sangjin Hong, Jinseok Lee, A. Athalye, P.M. Djuric, and We-Duke Cho, "Design methodology for domain specific parameterizable particle filter realizations," *IEEE Transactions on Circuits and Systems I: Fundamental Theory and Applications*, vol. 54, no. 9, pp. 1987 – 2000, Sept. 2007.

Appendix A - Derivations of PDF Low-pass Kernel Constraints

1. Derivations of contraint in Equation 4.20,

$$\int_{-\infty}^{+\infty} l_s(\tau)\ d\tau = 1$$

Proof. Substitute Equation 4.15 into Equation 4.16,

$$\begin{aligned}\int_{-\infty}^{+\infty}\int_{-\infty}^{+\infty} l_s(\tau)\ p_s(x-\tau)\ d\tau\ dx &= \int_{-\infty}^{+\infty} p_{s+1}(x)\ dx \\ \int_{-\infty}^{+\infty}\int_{-\infty}^{+\infty} l_s(\tau)\ p_s(x-\tau)\ d\tau\ dx &= 1 \end{aligned} \tag{7.1}$$

Rearrange the left-hand-side (LHS) of Equation 7.1 as,

$$\int_{-\infty}^{+\infty}\int_{-\infty}^{+\infty} l_s(\tau)\ p_s(x-\tau)\ dx\ d\tau = 1 \tag{7.2}$$

Since $l_s(\tau)$ is independent of x, $l_s(\tau)$ can be moved out of the inner integral as,

$$\int_{-\infty}^{+\infty} l_s(\tau) \int_{-\infty}^{+\infty} p_s(x-\tau)\ dx\ d\tau = 1 \tag{7.3}$$

Since $p_s(x-\tau)$ is a shifted version of the PDF $p_s(x)$, the inner integral is equal to one and Equation 7.3 can be expressed as,

$$\int_{-\infty}^{+\infty} l_s(\tau)\ d\tau = 1$$

■

2. Derivations of contraint in Equation 4.21,

$$l_s(x) \geqslant 0$$

Proof. Substitute Equation 4.15 into Equation 4.17,

$$\int_{-\infty}^{+\infty} l_s(\tau)\ p_s(x-\tau)\ d\tau \geqslant 0 \tag{7.4}$$

Since p_s is nonnegative, one way to satisfy Equation 7.4 is to restrict l_s to be nonnegative. ■

3. Derivations of contraint in Equation 4.22,

$$l_s(x) = l_s(-x)$$

Proof. The Fourier transform of Equation 4.15 is,

$$L_s(f)\ P_s(f) = P_{s+1}(f) \tag{7.5}$$

where L_s denotes the Fourier transform of l_s.

Expand Equation 7.5 in terms of real and imaginary terms,

$$\begin{aligned} & (\operatorname{Re}(L_s) + i\operatorname{Im}(L_s))(\operatorname{Re}(P_s) + i\operatorname{Im}(P_s)) \\ = \ & \operatorname{Re}(P_{s+1}) + i\operatorname{Im}(P_{s+1}) \end{aligned} \tag{7.6}$$

where $i = \sqrt{-1}$ is a complex number; f is omitted to maintain clarity.

Let $\operatorname{Im}(L_s)$ be zero, and collect the real and imaginary terms of Equation 7.6 separately,

$$\operatorname{Re}(L_s)\operatorname{Re}(P_s) = \operatorname{Re}(P_{s+1}) \tag{7.7}$$

$$\operatorname{Re}(L_s)\operatorname{Im}(P_s) = \operatorname{Im}(P_{s+1}) \tag{7.8}$$

It follows that the phase angles of P_{s+1} and P_s are identical when $\operatorname{Im}(L_s) = 0$,

$$\operatorname{Im}(P_s) / \operatorname{Re}(P_s) = \operatorname{Im}(P_{s+1}) / \operatorname{Re}(P_{s+1}) \tag{7.9}$$

Express $\operatorname{Im}(L_s)$ in terms of l_s,

$$\operatorname{Im}(L_s) = \int_{-\infty}^{+\infty} l_s(x)\sin(2\pi f x)\ dx \tag{7.10}$$

Since sine is an odd function (i.e. $\sin(f) = -\sin(-f)$), l_s must be an even function to make $\operatorname{Im}(L_s)$ equal to zero. ■

4. Derivations of contraint in Equation 4.23,

$$l'_s(x) = \begin{cases} \geq 0, & x < 0 \\ = 0, & x = 0 \\ \leq 0, & x > 0 \end{cases}$$

Proof. Express $p'_{s+1}(x)$ in Equation 4.19 as a convolution integral,

$$\int_{-\infty}^{+\infty} l'_s(\tau)\ p_s(x-\tau)\ d\tau = p'_{s+1}(x), \tag{7.11}$$

where l'_s is the 1^{st} derivative of l_s; it is important to note that l'_s is an odd function based on Equation 4.22,

$$\begin{aligned} l_s(x) &= l_s(-x) \\ \frac{\partial\ l_s(x)}{\partial x} &= \frac{\partial\ l_s(-x)}{\partial x} \\ l'_s(x) &= -l'_s(-x) \end{aligned} \tag{7.12}$$

Since $p_s(x)$ is non-negative by definition, in order for $p'_{s+1}(x) = 0,\ \forall x \in \{x_{peak}\} \cup \{x_{valley}\}$, l'_s must produce both positive and negative values. ■